



Human-Inspired Reflexes and Coordination in Soft Robot and Upper-Limb Prosthesis Control

Dipl.-Ing. Johannes Kühn

Vollständiger Abdruck der von der Fakultät für Elektrotechnik und Informationstechnik der Technischen Universität München zur Erlangung des akademischen Grades eines

Doktors der Ingenieurwissenschaften (Dr.-Ing.)

genehmigten Dissertation.

Vorsitzender:

Prof. Dr.-Ing. Eckehard Steinbach

Prüfende der Dissertation:

1. Prof. Dr.-Ing. Sami Haddadin
2. Prof. Dr. Antonio Bicchi

Die Dissertation wurde am 10.01.2022 bei der Technischen Universität München eingereicht und durch die Fakultät für Elektrotechnik und Informationstechnik am 16.05.2022 angenommen.

To my wife Anne-Sophie, my son Josua, “and perhaps more to follow”.

Acknowledgments

This dissertation is the result of my doctoral research, which I started at the Institute of Automatic Control at Leibniz Universität Hannover (LUH), and continued and completed at the Chair of Robotics and Systems Intelligence and the Munich Institute of Robotics and Machine Intelligence (MIRMI) at Technical University of Munich. I want to thank all the people who supported the successful completion of this personal project.

First of all, I would like to thank my supervisor and mentor Prof. Sami Haddadin. Sami taught me first-hand the basics of science, formulating and approaching research questions, developing solutions, and getting them published. He taught me never to stop pushing towards set goals while always complying with the highest standard. I will remember the countless inspiring and busy days, evenings, and nights working on projects or publications together. I am convinced that there is no other place where I would have developed more professionally and personally.

I would also like to thank Prof. Etienne Burdet and his team at Imperial College London. Etienne has broadened my scientific horizon significantly during our joint research. Special thanks to Dr. Carlo Bagnato, whom I mainly worked with during this period.

Furthermore, my thanks go to Prof. Antonio Bicchi from Università di Pisa and Istituto Italiano di Tecnologia. Antonio led the European Union research project SOFT-PRO (ICT 688857), through which I had the privilege of meeting and collaborating with leading robotics scientists from all over Europe.

This dissertation would certainly not have been completed without my esteemed colleagues. First, I thank my office mate Tingli Hu, with whom I pondered countless scientific and private issues. Next, I would like to thank Alexander Tödtheide and Johannes Ringwald with whom I fought several deadline battles. Furthermore, I want to thank Lars Johannsmeier, Jonathan Vorndamme, Dennis Knobbe, Ali Baradaranbirjandi, Erfan Shahriari, Edmundo Pozo Fortunić, and Dr. Elisabeth Jensen for the numerous interactions. Moreover, many thanks to the entire MIRMI team and the former team from LUH, Moritz Schappler, Dr.-Ing. Torsten Lilge, Andreas Kurz, Dr.-Ing. Christopher Schindlbeck and Dr.-Ing. Jumana Ma'touq. I also thank those not mentioned for sharing this unforgettable adventure with me. Furthermore, I would like to thank Tingli Hu, Nico Mansfeld, and Dr. Amartya Ganguly for proofreading this manuscript in part or whole.

Most importantly, I am deeply grateful to my close family and friends. They have been highly supportive and always encouraged me in my work. My deepest gratitude goes to my wife Anne-Sophie, who is such a wonderful wife and mother to our son Josua. I thank them both for their love and continuous support. This work is dedicated to them.

Abstract

A long-standing ambition of robotics is to enable soft robots and prostheses to safely and sensitively interact and manipulate the surrounding environment. The capabilities of biological organisms in this respect are unmatched. They perceive themselves and their environment through many sensors and interact with it through great dexterity and fine control while moving their limbs in a highly coordinated manner. A vital aspect is the self-protective mechanisms found in every living being. For example, pain helps humans avoid injuries by signaling the immediate threat and triggering relevant motor responses, often through withdrawal reflexes. Such behavior prevents further damage to an affected region by an automatic retraction from a noxious stimulus such as heat or pain. State-of-the-art robotics research developed technical antitypes only on a basic level, e.g., through engineered pre-programmed withdrawal patterns. However, this thesis aims to explore and understand human reflex behavior on a kinematic and muscular level. Based on the insights gained, the next generation of human-inspired self-protective reflexes is developed for soft robots and prostheses, resulting in a framework with superhuman performance. In addition to reflexes, this thesis develops new coordinated control concepts for upper limb prostheses for reach and grasp tasks. A novel control framework denoted Synergy Complement Control (SCC) is presented, allowing a prosthesis to complement the residual limb movement autonomously in accordance with human arm synergies. The hybrid system naturally renders intended movements for its carrier and adapts online to new tasks.

Firstly, this thesis analyzes humans' withdrawal reflexes and arm coordination. For this, two experiments are designed and conducted. The first focuses on finger reflexes and reveals a 5-phase reflex launch sequence that depends on the stimulus's shape, speed, and temperature and is further influenced by habituation. The second experiment investigates arm withdrawal coordination in the presence of concurrent potential pain sources: the arm must be withdrawn to avoid a slap on the hand while avoiding a painful elbow obstacle. The results show that the subjects learned to control the hand retraction movement to avoid potential pain. Subjects used individual motor strategies to modify the joint movement coordination to avoid hitting the obstacle with the elbow at the cost of increasing the risk of hand slap. Furthermore, they used a conservative strategy as if assuming an obstacle in all the trials.

Secondly, this thesis introduces self-protective reflexes for soft robots and prostheses. These are inspired by the above mentioned human withdrawal analysis and formalize into an artificial Robot Nervous System (aRNS). This mathematical framework unifies multi-modal physical stimuli sensation with robot pain-reflex reactions. Robot pain is formally introduced to interpret tactile and temperature sensation and proprioception. The severity of the impact adjusts the equilibrium position, stiffness, and feed-forward

Abstract

torque of an impedance controller. This framework is validated in simulation and experiments with several soft robotic systems, for example, arms and fingers with multiple degrees of freedom. Building on the aRNS, robot reflexes are designed based on different sensory feedback arrangements and subsequently compared to the quantified human performance. While the human remains superior in temperature-based reaction, the touch reflex performance of the robotic finger is superhuman with an unconventional configuration of proprioceptive forces and link segment acceleration. It also shows that the traditional tactile sensing or proprioceptive arrangements are sub-optimal, although they also have the potential to achieve superhuman performance.

Thirdly, this thesis introduces semi-autonomous and coordinated control methods for upper limb prostheses. After introducing basic coordination strategies relying on kinesthetic teaching or three dimensional computer vision, the SCC method is introduced. This novel residual limb-driven method inherently deals with complex multi-DoF motions, changing tasks and target locations, and outputs residual limb coordinated complementary prosthesis motions. The approach is experimentally validated for several daily living tasks using a novel four degrees of freedom prosthetic device operated by a human with preserved arm and an amputee operating a digital twin in virtual reality. Results show that lost movement capabilities can effectively be recovered through SCC.

In sum, this thesis contributes to the next generation of reflex-enabled soft robots and upper limb prostheses that harmonize with human coordinated motor control. This thesis may open up entirely new application domains for interactive, sensitive, and semi-autonomous robots in industry and service sectors, ranging from complex but intuitive human-robot collaboration to elderly-care applications at home.

Contents

Acknowledgments	v
Abstract	vii
Contents	ix
Notation	xiii
1 Introduction	1
1.1 Scientific objectives	2
1.2 State of the art	3
1.2.1 Human neuromechanics, motor control and learning	4
1.2.2 Human withdrawal reflexes	4
1.2.3 Soft robots and interaction control	5
1.2.4 Robot collision handling	6
1.2.5 Robot reflex control	7
1.2.6 Upper limb prostheses and control	8
1.3 Major open issues	10
1.4 Contributions and publication list	11
 Part I: Human reflex and motor coordination analysis	
2 Finger reflexes elicited by touch and heat	23
2.1 Experimental procedures	24
2.1.1 Participant	24
2.1.2 Design	24
2.1.3 Protocol	25
2.1.4 Apparatus	26
2.1.5 Finger temperature estimation	26
2.1.6 Contact force measurement	27
2.2 Measures	27
2.3 Results	28
2.3.1 Reflex launch sequence	28
2.3.2 Effect of stimulus shape	28
2.3.3 Effect of stimulus speed	29
2.3.4 Effect of stimulus temperature	30

CONTENTS

2.3.5	Finger retraction	32
2.3.6	Effect of habituation	33
2.4	Discussion	33
3	Arm withdrawal adaption to concurrent pain constraints	35
3.1	Experimental procedures	36
3.1.1	Participants	36
3.1.2	Design	36
3.1.3	Apparatus	37
3.1.4	Protocol	37
3.1.5	Kinematic calibration	39
3.1.6	Pain calibration	39
3.2	Measures	40
3.3	Data analysis	41
3.4	Results	41
3.4.1	Preliminary inspection of data	41
3.4.2	Effect of obstacle distance	43
3.4.3	Effect of obstacle presence uncertainty	47
3.4.4	Effect of obstacle nature (innocuous vs. painful)	48
3.5	Discussion	49

Part II: Protective robot reflexes

4	Foundations of soft robotics control	59
4.1	Rigid body dynamics	59
4.2	Joint impedance control	59
4.3	Momentum observer	60
5	Artificial robot nervous system	61
5.1	Concept	61
5.2	Virtual Nervous Robot-Tissue	62
5.3	Spiking Models	63
5.3.1	Principle aRN spiking characteristics	63
5.3.2	aRN types	64
5.4	Interpretation	67
5.5	Collision Control	68
5.5.1	Generalized Pain Spiking State	68
5.5.2	Reflex Control Strategies	69
5.5.3	Pain Reflex Graph	71
5.6	Results	72
5.6.1	Parameter dependency of aRNS control laws	72
5.6.2	Pain reactions on a 7 DoF robot arm	73
5.6.3	Pain responses on a pneumatically actuated finger prosthesis testbed	76

5.6.4	A proposal: Reflex stack for humanoids	80
5.7	Discussion	81
6	Superhuman finger reflexes for touch and heat	83
6.1	From human to robot	84
6.2	Robot finger testbed	85
6.2.1	Design	85
6.2.2	Rigid-body dynamics	86
6.2.3	Reflex control	86
6.3	Collision monitoring methods	87
6.3.1	Tactile sensing	87
6.3.2	Proprioception	88
6.3.3	Proprioception and link segment acceleration sensation	88
6.4	Experimental protocol	88
6.5	Performance metrics	89
6.6	Results	89
6.6.1	Robot vs human: touch reflexes	89
6.6.2	Robot versus human: temperature reflexes	91
6.7	Discussion	92
 Part III: Coordinated prosthesis control 		
7	A multi-modal database of human reach and grasp tasks	99
7.1	Experimental procedures	99
7.1.1	Participants	99
7.1.2	Design and protocol	99
7.1.3	Apparatus	99
7.2	Remarks	101
8	From sequential to semi-autonomous control	105
8.1	Methods	106
8.1.1	Exo-prosthesis	106
8.1.2	Prosthetic user apps	112
8.1.3	Sequential velocity control	113
8.1.4	Velocity control based on kinesthetic teaching	113
8.1.5	Velocity control based on 3D vision	114
8.2	Results	115
8.3	Conclusion	116
9	Synergy complement control	119
9.1	General framing	120
9.2	Concept	121

CONTENTS

9.3	Methods	122
9.3.1	Synergy dataset	122
9.3.2	Participants	122
9.3.3	Experimental protocol	122
9.3.4	Exo-Prosthesis	123
9.3.5	Soft controller used with SCC	125
9.3.6	EMG-based sequential control	125
9.3.7	Human template encoding	126
9.3.8	Phase variable decoding	127
9.3.9	Intention decoding	127
9.4	Results	128
9.4.1	Residual limb-prosthesis coordination	128
9.4.2	Reach and grasps tasks	130
9.4.3	Inter-task transitioning	130
9.4.4	Goal changes within a task	134
9.4.5	Pilot study with amputee	134
9.4.6	SCC versus sequential control	137
9.5	Discussion	138
10	Conclusion	141
10.1	Summary	141
10.2	Impact and future work	142
	List of Figures	145
	List of Tables	147
	Bibliography	149

Notation

The following list contains selected symbols that are frequently used in this dissertation. They are also introduced in the text together with other symbols. The reader is advised to refer to the specific definition in each context.

Symbol	Space	Unit	Description
x	\mathbb{R}	-	Scalar
\mathbf{x}	\mathbb{R}^n	-	n -dimensional vector
$\dot{\mathbf{x}}$	\mathbb{R}^n	-	First derivative of vector \mathbf{x} , $\dot{\mathbf{x}}(t) = \frac{d\mathbf{x}(t)}{dt}$, $\ddot{\mathbf{x}}(t) = \frac{d\dot{\mathbf{x}}(t)}{dt}$
$\ \mathbf{x}\ $	\mathbb{R}	-	Norm of vector \mathbf{x}
\mathbf{X}	$\mathbb{R}^{n \times m}$	-	$N \times M$ matrix
\mathbf{I}	$\mathbb{R}^{n \times n}$	-	Identity matrix
$\mathbf{0}$	$\mathbb{R}^{n \times m}$	-	Zero matrix

Part I

d	$\mathbb{R}_{>0}$	mm	Diameter
ϑ	\mathbb{R}	$^{\circ}\text{C}$, K	Temperature
v	\mathbb{R}	m/s	Stimulus speed
\mathbf{F}_c	\mathbb{R}^3	N	Contact force
$\sigma_{c,\max}$	\mathbb{R}	Pa	Maximum contact pressure
f	\mathbb{R}	%	Finger retraction frequentness or failure ratio
κ	\mathbb{R}	W/(K m)	Thermal conductivity
c	\mathbb{R}	J/(kg K)	Specific heat capacity
ρ	\mathbb{R}	kg/m ³	Material density
q_H	\mathbb{R}	rad	Joint angle of Metacarpophalangeal joint
ξ	\mathbb{R}	V	Mean muscle effort
Δt_c	\mathbb{R}	s	Contact duration
Δt_r	\mathbb{R}	s	Reaction time
φ, θ	\mathbb{R}	rad	Elbow angles
$\tilde{x}_{h,\max}$	\mathbb{R}	-	Normalized hand retraction

Part II

\mathbf{q}	\mathbb{R}^n	rad	Joint angles of n -DoF robot
$\boldsymbol{\tau}$	\mathbb{R}^n	Nm	Motor torques
$\boldsymbol{\tau}_f$	\mathbb{R}^n	Nm	Friction torques
\mathbf{M}	$\mathbb{R}^{n \times n}$	kg m ²	Joint inertia matrix
\mathbf{C}	$\mathbb{R}^{n \times n}$	kg m ² /s	Coriolis and centrifugal matrix
\mathbf{g}	\mathbb{R}^n	Nm	Gravity torques
$\boldsymbol{\tau}_{\text{ext}}$	\mathbb{R}^n	Nm	External torques
\mathbf{J}_c	$\mathbb{R}^{6 \times n}$	m/rad, -	Jacobian matrix
\mathbf{f}_{ext}	\mathbb{R}^3	N	External force
\mathbf{m}_{ext}	\mathbb{R}^3	Nm	External moments
\mathcal{F}_{ext}	\mathbb{R}^6	N, Nm	External contact wrench
\mathbf{u}_c	\mathbb{R}^6	-	Unit collision direction
\mathbf{q}_d	\mathbb{R}^n	rad	Desired joint angles
$\boldsymbol{\tau}_d$	\mathbb{R}^n	Nm	Desired joint torque
$\boldsymbol{\tau}_g$	\mathbb{R}^n	Nm	Gravity compensation torque
\mathbf{K}	$\mathbb{R}^{n \times n}$	Nm/rad	Joint stiffness matrix
\mathbf{K}_O	$\mathbb{R}^{n \times n}$	1/s	Observer gain matrix
\mathbf{D}	$\mathbb{R}^{n \times n}$	Nm s/rad	Joint damping matrix
\mathbf{a}	\mathbb{R}^3	m/s ²	Cartesian acceleration
\mathbf{R}	SO(3)	-	Rotation matrix
Δt_a	\mathbb{R}	s	Activation time
Δt_d	\mathbb{R}	s	Detection time
Δt_e	\mathbb{R}	s	Escape time

Part III

Δt_e	\mathbb{R}	s	Escape time
\mathbf{x}	\mathbb{R}^6	m,rad	Pose vector
\mathbf{F}	\mathbb{R}^6	N, Nm	Wrench
$\boldsymbol{\tau}$	\mathbb{R}^n	Nm	Torques
\mathbf{K}	$\mathbb{R}^{n \times n}$		Stiffness or gain matrix
\mathbf{D}	$\mathbb{R}^{n \times n}$	Nm s/rad	Joint damping matrix
\mathbf{r}	\mathbb{R}^3	m	Position vector

$\boldsymbol{\omega}$	\mathbb{R}^3	rad s^{-1}	Angular velocity
\boldsymbol{l}	\mathbb{R}^3	m	Residual limb position
\boldsymbol{m}	\mathbb{R}^m	-	Muscle activation of m muscles
\boldsymbol{p}	\mathbb{R}^6	m, rad	Prosthesis pose
ψ	\mathbb{R}	-	Phase variable
g	\mathbb{N}	-	Gesture state

1 Introduction

A grand challenge of robotics research is to achieve autonomous robots and semi-autonomous upper-limb prostheses that safely interact with and manipulate the surrounding environment. Human capabilities are still unmatched in this regard and thus often serve as an archetype for technical antitypes. Over the past decade, significant advances have been made in robotics research, taking the musculoskeletal properties of biological systems as inspiration. Soft control schemes [1] and soft actuators [2] have been developed, building the basis for the design of so-called *soft robots* [3]. They are capable of sensitive manipulation, and safe interaction with humans without needing safety barriers between man and machine [4]. This ability is based on lightweight mechatronics, tactile sensing, sophisticated interaction control algorithms such as impedance control, and fast collision handling [4, 5]. Thanks to these technological advancements, numerous soft robots are entering the market. Well-known commercial systems are the Franka Emika Panda robot arm [6] and qbrobotics' SoftHand [7, 8], see Fig. 1.1a and Fig. 1.1b. As robots move away from structured industrial environments into unstructured human environments, they face further challenges. Besides compliance, performance, and human safety, robots must also ensure their own physical integrity. However, a systemic framework for purposeful and intelligent collision reflex reactions for self-protection is still missing. So far, only hand-crafted heuristic algorithms exist that are not generalized yet.

Upper-limb prostheses share the same goals as soft robots. A human design and behavior are even explicitly desired for prostheses, as the artificial limbs are supposed to replace the missing natural limbs as best as possible. Therefore, some soft robotics methods have been transferred to upper limb prosthetics. A well-known example is APL's Modular Prosthetic Limb, as shown in Fig. 1.1c, which is impedance controlled and reflects the joint impedance of human arms [10]. However, most commercially avail-

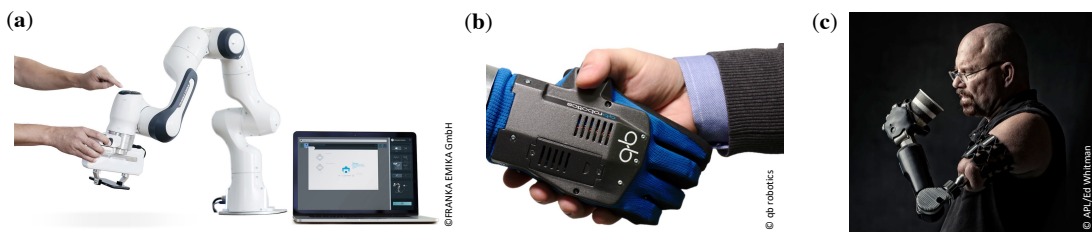


Figure 1.1: Examples of soft robotic and prosthetic systems. (a) Human interacts with Franka Emika Panda [6]. (b) Shaking hands with qbrobotics' SoftHand [7]. (c) Amputee uses APL's Modular Prosthetic Limb to take a drink [9].

1 Introduction

able upper-limb prosthetic devices are still rigid. The user needs significant practice to operate these tools. Although considerable efforts have been made in research to improve and enhance operability by myoelectric controls, sequential control is still today's commercial standard [11, 12]. Such control schemes often involve a finite state machine, allowing the user to select and actuate a single joint at a time using direct Electromyography (EMG)-based proportional control [13]. However, this approach is unintuitive and complex to use [14]. What is still missing is a robust control design that corresponds to natural human motion coordination and increases the intuitiveness and transparency of operation.

In both robotics and upper limb prosthetics disciplines, the human antitype, if understood well, may serve as a source of inspiration and technological guidance again. On the one hand, humans' sensitive, automatic, and intelligent reaction to desired and unforeseen contacts is unsurpassed. The human leverages proprioceptive force sensing in the tendons and tactile and nociceptive modalities. Based on this rich information, he can then detect, classify, and show meaningful reflexive reactions to contacts. On the other hand, the human moves his limbs in a highly coordinated manner performing smooth movements. Along this line of thought, future soft robotic/prosthetic hand-arm systems are sought to attain similar reflex and coordination capabilities. These devices will gain human-like interaction and manipulation capabilities by leveraging a thorough understanding of human reflexes and motor coordination.

1.1 Scientific objectives

This thesis takes an interdisciplinary approach between human, robotics, and prosthetics research. In particular, this thesis focuses on i) the analysis of human reflexes and motor coordination, ii) the development of protective robot/prosthesis reflexes, and iii) the development of coordinated prosthesis control schemes, see Fig. 1.2. This thesis aims to achieve the following concrete goals:

- G1 Deepen the understanding of human upper limb withdrawal reflexes and coordination in response to noxious stimuli.
- G2 Develop human-inspired self-protective reflexes for robots and prostheses.
- G3 Develop new coordinated control methods for upper-limb prosthesis.

The following specific research questions are posed to achieve these goals:

- Q1 How do stimulus's physical characteristics modulate the reflex response on a kinematic and muscular level?
- Q2 How do humans coordinate their arm movements to avoid concurrent pain sources?
- Q3 How can human-inspired robot reflexes be designed to achieve self-protective behaviors?

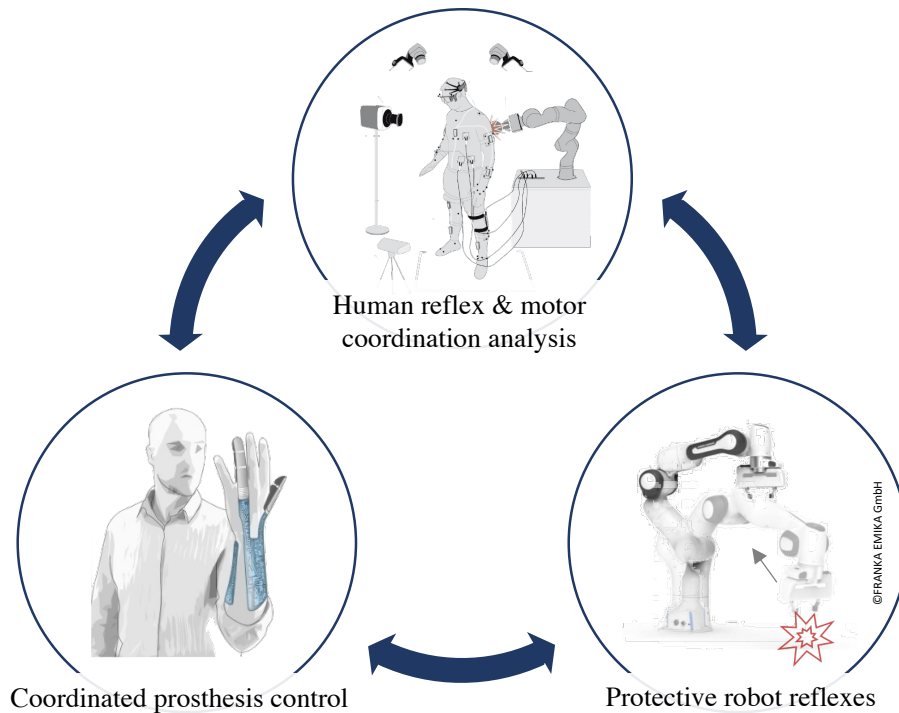


Figure 1.2: Scientific objectives of this thesis.

- Q4 Are the insights from the human reflex studies transferable to robot reflexes and which specific sensory setup enables the best robot reflex performance?
- Q5 How can new semi-autonomous coordinated control schemes for upper limb prostheses be achieved?
- Q6 How can upper-limb prosthesis control be reconciled with natural, coordinated motor control in humans?

In the next chapter, the research works are summarized that relate to the goals G1 to G3 and research questions Q1 to Q6. The following chapter then highlights major open issues and summarizes the thesis's contributions.

1.2 State of the art

This chapter provides a broad literature review of the primary research works related to the scientific objectives (Fig. 1.2), goals G1 to G3 and research questions Q1 to Q6. Related human research spans from human neuromechanics, motor control, and learning to human withdrawal reflexes. Robotics work spans the domain of physical Human-Robot Interaction (pHRI), focusing on soft robots and interaction control, robot collision handling, and reflex control. In addition to the following literature overview, specific research works are presented and discussed in the context of each chapter.

1.2.1 Human neuromechanics, motor control and learning

While the microscopic sliding filament and cross-bridge theory [15, 16, 17, 18, 19] well explains the dependence of isometric force on muscle length [20, 21, 22], the anisometric behaviour of skeletal muscles and the elastic behaviour of passive elements are macroscopically approximated by Hill’s formulation [23, 24, 25]. The *Hill-based muscle model* is widely used in modeling musculoskeletal systems [26, 27, 28, 29, 30, 31, 32, 33, 34] where the skeleton is a standard multi-body system [35, 36, 37, 38, 39]. Muscle and joint space are connected by a *muscle-path model*, which relates muscle lengths to joint angles [40, 41, 27, 29, 42, 43] and whose Jacobian connects muscle forces and joint torques [44, 40, 45, 46, 47, 39, 48, 49, 50, 51]. With electromyography (EMG) measurements and motion capture data, an individual-specific musculoskeletal model is identified via nonlinear least squares [30, 31, 32, 52]. In solving the inverse musculoskeletal dynamics, the encountering *force-sharing problem* (more muscles than joints) is solved by a general constrained optimization method [39, 53, 33, 34, 54]. Unlike the relatively simple kinematics of the arm [55, 16, 56, 57], hand kinematics exhibits higher complexity. Different hand kinematics models were developed and identified using optical motion capture techniques [58, 59, 60, 61, 62, 63, 64, 65, 66, 67].

The phenomenon of spring-like human arm behaviour in a slightly perturbing environment [68] stems from muscle viscoelasticity. Therefore, human motor control can be formulated as an impedance control with static and dynamic impedance [37], which increase with muscle activation [69] or joint torque [35]. In addition, the modulation of impedance can be learned gradually [70] in fast and slow processes [71] without visual feedback [72]. As a result, an optimal impedance [73] associated with movement and instability directions [74, 75] will be able to overcome perturbation. Furthermore, muscle activation [75, 76] and interaction force [77] can be learned as well. In general, human motor control can be summarized as a nonlinear adaptive control [78] and some hypotheses/theories such as Smith predictor [79, 80] hypothesis, computed torque control hypothesis [81], internal model control [82, 83, 84] and optimal feedback control [85, 86, 76] are rather popular nowadays. Besides, the experimentally identified task-specific muscle synergies from [87, 88, 89, 90] reflect an underlying task-dependent muscular control strategy.

1.2.2 Human withdrawal reflexes

Noxious stimuli are perceived and processed by human’s nervous system Human Nervous System (HNS). Consisting of millions of connected neurons, the HNS is the most powerful measurement and communication system of the human body. The HNS can be divided into the Central and Peripheral Nervous System (CNS, PNS). The CNS consists of the spinal cord, brain stem, and forebrain and is mainly responsible for forwarding and processing information coming from the PNS [91]. The PNS covers all the nerves located outside the CNS, gathering tactile and proprioceptive information with the help of a broad spectrum of receptors. If a stimulus is that strong that body injuries become possible, a highly unpleasant, but vitally important, the sensation is caused — *pain* [91].

The most responsible and contributing receptors to pain caused by physical contact are called nociceptors. When a mechanical stimulus affects nociceptors, distributed all over the skin, they become activated instantly. Depending on the stimulus strength, typically in terms of duration, penetration depth, and stress, the nociceptors send ionic electrical spikes decoded in a frequency modulated manner [91]. Once the stimulus surpasses a certain threshold, a nociceptor starts firing following the *all-or-nothing principle* at constant amplitude [91]. After the signal passes the first neural interconnection, it crosses to the other side of the spinal cord, following the spinothalamic tract, then through the medulla, pons, and midbrain to the thalamus. From there on, pain information is projected to different areas of the cerebral cortex. Pain is evoked, which may cause appropriate movements (pain-reflexes). Pain is also strongly an emotional experience, not only influenced by the signals coming from the nociceptors. Thus, one distinguishes between the emotional experience of pain and the nociceptive signals that may lead to pain experiences. This thesis focus on the latter.





The human Nociceptive Withdrawal Reflex (NWR) is an involuntary movement that results in the withdrawal of the perturbed limb from a stimulus [92, 93, 94, 95, 96]. The reflex response consists of a complex pattern of excited or inhibited extensors and flexors [92, 97, 98, 99, 100, 101, 102, 103]. On EMG level, two peaks with different latencies and functional adaptabilities can be identified in most muscles [93, 94, 104, 105]. In terms of intensity and direction, the NWR depends on the phase of movement and task [106, 107, 108, 95]. When applying electrical stimuli, the NWR shows frequency-modulated behaviour more elicited at 15 Hz than 30 Hz [109]. Investigations indicate a modular organization of the nociceptive motor system, each module controlling either a muscle or muscle group. Moreover, each of these modules has an inherent cutaneous receptive field, which overlap [93, 94, 110, 111, 112, 113, 114]. Studies of upper-limb NWRs at rest and movement show that the reflex-muscle pattern, reflex size and mechanical response adapt to movement type, phase (ac-/deceleration) and muscle activity (shortening, lengthening) [108, 84, 96, 115].

1.2.3 Soft robots and interaction control

The development of robots suitable for close physical interaction with humans is leading to a paradigm shift in mechanics: away from heavy, stiff and rigid designs towards lightweight mechatronics with low inertia and high (active) compliance [119]. Well-known actively compliant soft-robots are the Barrett arm [120], the DLR Lightweight Robot family [121, 122] and FRANKA EMIKA Panda [6]. Inspired by the elasticity contained in biological muscles, intrinsically compliant joints are recently designed with the aim of imitating human motions during various tasks. By storing and releasing energy in the joints, one hopes for improvement of tasks such as running or throwing [123, 124, 4, 125, 126]. In order to incorporate active reactions to external forces, the concept of force control has been introduced and extended to hybrid position/force control [127]. The most widely used control approach for robots to physically interact with humans or the environment is probably impedance control, introduced in [44] and extended to flexible joint robots e.g. in [128]. This type of controller imposes a desired physical

1 Introduction

Table 1.1: Human upper-limb neuromechanics, motor control and protective reflexes.

Clinical Evaluation	Reflex data	Neuromechanics	Motor control & learning models
 <p>Green: studied part Red: stimulation</p>			
State of the art			
Protective reflexes [116] <ul style="list-style-type: none"> • Nociceptive reflex • Biceps stretch reflex 	Isolated investigations of <ul style="list-style-type: none"> • Excited/inhibited muscle patterns [101, 102] • Characteristic peaks in EMG response [93, 94] • Reflex motions [108] • Receptive fields [114] • The modular nociceptive motor system [111] • Reflex dependent parameters, e.g. movement type or phase [115] 	Existing models: <ul style="list-style-type: none"> • Muscle model [23, 24] • Hand kinematic models: Digit I-IV [58], Digits I-V & wrist [59], Digit I-IV & wrist [64], Digit I & V [67] • Arm kinematic models [55, 56] • EMG to muscle activation model [117, 28] • Muscle path models: polynomial [40, 41], trigonometric [27, 29], 3D geometric [42, 43] • Musculoskeletal dynamics and identification [52, 31] • Force-sharing problem solver [39, 33] 	Motor control findings: <ul style="list-style-type: none"> • Viscoelastic behavior [68] • Impedance control with static and dynamic stiffness [37] • Impedance is related to muscle activation [69], joint torque [35] • Interaction learning of impedance [70, 73], force [77], muscle activation [75, 76] • Learning: fast + slow processes [71] • Nonlinear adaptive control [78] • Smith predictor [118, 80] • Computed torque control [81] • Internal model control [83, 84] • Optimal feedback control [85, 76] • Identified muscle synergies from [87, 88, 89, 90]

behaviour with respect to external forces acting on the robot. In [129], a passivity based, unified force/impedance control has been presented, which was successfully applied to a safe adaption to contacts in [130]. An approach to simultaneously adapt force, trajectory and impedance based on studies in neuroscience has been presented in [131].

1.2.4 Robot collision handling

In general, one can consider up to seven elementary phases in the so called collision event pipeline [5]. Multiple monitoring signals can be used to obtain information about the event [5]:

- 1) Pre-collision phase: The primary goals are collision avoidance and anticipatory robot motion to minimize impact effects.
- 2) Collision detection: The collision detection phase, whose binary output denotes whether a collision occurred or not, is characterized by the transmission of contact wrenches. The occurrence of a collision, happening anywhere along with the robot structure, shall be detected as fast as possible [123, 132, 133].

- 3) Collision isolation: Knowing which robot part is involved in the collision is a piece of important information that can be exploited for robot reaction. One way to obtain both collision detection and isolation is to use sensitive skins [134, 135].
- 4) Collision identification phase: Other relevant quantities about a collision are the generalized collision force, either in terms of the acting Cartesian wrench at the contact or of the resulting joint torque [136, 135, 137].
- 5) Collision classification phase: Based on the information from previous phases, one can interpret the collision nature in a context-dependent way (accidental or intentional, light or severe, permanent, transient, or repetitive).
- 6) Collision reaction phase: Indeed, the robot should react purposefully in response to a collision event [4], using information from previous phases. Some examples of successful collision reflex reaction strategies have been given in [138, 139, 140].
- 7) Post-collision phase: Once a safe condition has been reached after the collision, the robot should autonomously decide whether to try to recover the original task and how, or to abandon it [140].

1.2.5 Robot reflex control

Various approaches to reflexes in legged robot locomotion were developed with the focus on stabilizing the gait of humanoids in [141, 142, 143]. A quadruped robotic platform was used in [144] to study reflex networks in cats for locomotion. Reflexes in manipulation tasks differ since they are less cyclic and rather asymmetric. In [145], the humanoid “Cog” was taught reflexive behaviors by generating movements from biologically pre-defined inspired postural primitives. Through the superposition of these primitives, it was possible to imitate reflex-like withdrawal behavior. In [146], a similar approach was used by overlaying different movement patterns triggered by a tactile (force) sensor and was implemented on a 7 DoF robot arm. Different reflex types were realized based on single neuron firing models. They focus on manipulation and specific rather abstract high-level reflexes such as grasping or catching in case of slipping. The basic implementation of mechanically triggered reflexes is based on force sensing only. No deeper “mechano-physiologica” contact dynamics were involved, nor does their human-like neuron firing imply human topological design. It rather represents a switching strategy that may trigger different events. In [147], withdrawal movements of the human arm were recorded, and a force-distance relation was established to model this behavior. In order to trigger reflexes, an elastic robot tissue was introduced, additionally mitigating the impact force through inherent damping properties. In [148], authors proposed a new concept for online trajectory generation to react to unforeseen events. Moreover, in [4], based on the work in [149, 138], various collision reflex controls were proposed in the framework of proprioceptive collision detection and reflex reaction. Further approaches to reflex control based on optimal control can be found in [150] and [151].

1.2.6 Upper limb prostheses and control

In the early 20th century the first powered prostheses [160, 161] and around 1950 the first myoelectric prostheses emerged [162, 163, 164] with the goal of regaining the lost scope of human arm movement and manipulation capabilities [165, 166, 3, 167, 168, 169, 170, 171]. Many mechatronic developments have transpired in the decades since. Nowadays, several upper-limb prostheses are commercially available [153, 9, 156, 155, 154] as well as under experimental and clinical research [171, 172, 173, 159]. Electrically powered prostheses are strongly linked to light-weight robotic arm manipulators or humanoids [3, 174] where torque, position, current and temperature sensors are equipped [3, 173, 175, 173, 175]. The prosthetic devices are either position [153, 9, 156, 155, 154] or impedance controlled [173, 159], where surface electromyography (sEMG) [176, 177, 178, 177, 179] usually serves as user input to control a single DoF [180], finger forces [181], movement trajectories or switch between control modes [153, 154]. Also other sensors have been developed for the user interface, algorithms for decoding user intention, and control strategies for handling the many DoFs of the hand-arm system. Sensor systems that have so far been explored besides surface EMG (single- and multi-channel as well as high density), are inertial measurement units (IMUs), electroencephalography (EEG), and camera systems.

Several criteria for ideal upper-limb prosthesis control have been previously defined [182, 183]. For example, control schemes should enable




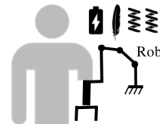

- natural and intuitive use,
- smooth and continuous movement (transitions) with minimal error buildup,
- coordinated, human-like movement of multiple DoFs,
- diverse movement patterns with minimal increase in complexity, and
- regulated dynamic response during physical interaction.

Furthermore, the system should be characterized by

- robustness to day-to-day changes,
- minimal training/retraining requirements, and
- fast user responsiveness.

Although direct neural interfacing would be ideal, several factors make this approach impractical for transhumeral prostheses in particular. Firstly, there are up to four DoFs to control for just the elbow and wrist. Moreover, barring invasive methods such as targeted muscle reinnervation for signal “amplification” of transected forearm and hand nerves [184] or implanted Microelectrode Arrays [185, 186], only the biceps (BIC) and triceps (TRI) muscles are available for electromyography (EMG) based control. Also, non-invasive myoelectric control has disadvantages, such as muscle fatigue, electrode displacement, difficulties in decoding complex patterns, or dealing with coordinated joint movements [14, 187]. Thus, there is an increased interest in limb-driven control concepts [187].

Table 1.2: Samples of state of the art of upper limb prostheses and control

	Passive or body powered	Electrically powered	Soft prosthetic	Soft exo- prosthetic I (robot- based)	Soft exo- prosthetic II
Icon legend:					
Exemplary references	[152]	[153, 154, 155, 156]	[157, 10, 158, 159]	Test-bed I developed in this thesis	Test-bed II/Target
Weight	< 1.5 kg	1.5 – 5 kg	4.8 kg	5.7 kg for prosthesis	<3 kg for prosthesis
Payload	5.0 kg	3.5 – 5.0 kg	6.8 kg	> 8.0 kg	> 10.0 kg
Sensory setup	n.a.	Position sensors	Position and joint-torque sensors	Position and joint-torque sensors	Position and joint-torque sensors
Low-level control	–	Position control	Joint impedance control	Joint impedance control	Joint & Cartesian impedance control
Collision handling	n.a.	n.a.	n.a.	Collision handling (stop, switch control mode, ...)	Collision handling with protective reflexes
Motion control strategies	–	Sequential	Sequential and one heuristic coordinated skill	Sequential and semi-autonomous coordinated skills	Residual limb-driven synergy complement control
Perceptual support	n.a.	n.a.	n.a.	Object recognition / tracking via 3D vision pipeline	Object recognition / tracking via 3D vision pipeline
Gravity support	n.a.	n.a.	n.a.	Mechanical stump relief via robot-based exoskeletal substitute	Lightweight exoskeleton: sacrifice residual limb loads for body reaction forces
Human Machine Interface	Mechanic	EMG	EMG	Intention from EMG and proprioception	Intention from EMG, eye-tracking and residual limb measurements

1 Introduction

Here, the residual limb (RL) movement rather than muscle activation measurements are used as a continuous control input for the device. Several RL-driven methods exist for upper limb prostheses that are still considered to be basic and primarily focus on simulation, virtual reality, or single DoF elbow coordination (e.g., [188, 189, 187]). At its core, they share one fundamental idea: simultaneously learn the coordination between the upper and lower arm for a wide spectrum of possible motion variants based on captured human templates. For this, regression techniques are applied involving linear regression such as Principal Components Analysis (PCA) [190, 187, 191] or non-linear regression such as Artificial Neural Networks (ANN), Radial Basis Function Networks (RBFN), or Locally Weighted Regression (LWR) [192, 193, 194, 187, 195, 191, 196, 197, 198, 189, 188]. However, the mapping between low dimensional upper arm movement and high dimensional total limb movement is highly underdetermined. Consequently, these methods output prosthesis motions that are inaccurate, not smooth (jerky), are of unnatural shape, and often delayed [187]; in sum, still quite far from solving the original problem.

1.3 Major open issues

Three major unresolved issues arise from the state of the art described above:

1. **Human reflexes and motor coordination:** The systemic and experimentally investigation of protective reflex responses to foreseen and unforeseen mechanical stimuli is still open in human research. How stimulus properties affect the kinematic and muscular reflex response is not understood. Moreover, it is unclear how humans deal with simultaneously occurring sources of pain and how they coordinate their movements to avoid them.
2. **Protective robot reflexes:** Soft robots still respond quite primitively to physical contact, for example, by simply stopping or switching to gravity compensation mode. A solution for a reflex framework, which provides more intelligent, meaningful reactions, has not yet been found. Furthermore, it is unclear which sensory enables the highest performance of robotic reflexes and whether human performance can be matched or surpassed.
3. **Coordinated prosthesis control:** An intuitive, robust method for controlling upper arm prostheses has not yet been found. Modern methods often use error-prone EMG measurements to control prosthetic joints individually and sequentially. On the other hand, limb-driven approaches use the motion of the residual limb to generate prosthesis motion. However, existing methods are not robust or precise enough to replay movements of human nature and often focus on single DoF tasks. In sum, they are not yet a valid replacement of missing motor capabilities. This calls for a new method that compensates for existing drawbacks.

1.4 Contributions and publication list

This thesis aims to close the open gaps highlighted in Sec. 1.3 by taking an interdisciplinary approach: Deepen the understanding of human protective reflexes and arm coordination and use gained insights as a source of inspiration and technical guidance for developing robotic and prosthetic counterparts. The main contributions of this thesis are briefly summarized below and put into context with the research questions Q1 to Q6 posted in Sec. 1.1:

- Analysis of human finger reflexes elicited by touch and heat (Q1).
- Analysis of human arm withdrawal adaption to concurrent pain constraints (Q2).
- Development of a human-inspired reflex framework denoted artificial Robot Nervous System for the self-protection of soft robots and prostheses (Q3).
- Development of superhuman protective robot reflexes based on tactile perception, proprioceptive forces, and proprioceptive forces with measurements of link-segment acceleration (Q4).
- Development of semi-autonomous coordinated prosthesis control schemes based on the new concept of exo-prosthetics (Q5).
- Development of a novel limb-driven prosthesis control method denoted Synergy Complement Control (Q6).

Contributions to Q1: Analysis of human finger reflexes elicited by touch and heat

An exploratory case study investigates human finger reflexes elicited by mechanical and thermal stimuli with varying properties. Reflex responses are analyzed on joint and muscle levels. The subject's motor reactions unveiled a 5-phase reflex launch sequence composed of three characteristic events: a muscle twitch reflex, a hold period, and finger retraction. Results also show that the reflex response depends on stimulus's shape, speed, and temperature and also is affected by habituation.

Contributions to Q2: Analysis of human arm withdrawal adaption to concurrent pain constraints

An exploratory study investigates a motor task in the presence of concurrent potential pain sources. Subjects needed to withdraw their arm to avoid a slap on the hand while avoiding an elbow obstacle with noxious electrical stimulation. The results show that the subjects learned to control the hand retraction movement to avoid potential pain. Subject-specific motor strategies were used to modify the joint movement coordination to avoid hitting the obstacle with the elbow at the cost of increasing the risk of hand slap. Furthermore, they used a conservative strategy as if assuming an obstacle in all trials.

Contributions to Q3: An artificial robot nervous system

A reflex framework—denoted artificial Robot Nervous System (aRNS)—is introduced to generate self-protective withdrawal movements for soft robots and prostheses. Its basic concept is inspired by state-of-the-art human reflex (neuro-)physiology and robot-human collision studies. The aRNS enables a robot or prosthesis to sense, interpret and react to potentially harmful collisions in analogy to a human’s NWR. The framework is experimentally validated for simulated and physical contacts using the KUKA LWR4+ and the BioTac sensor. Furthermore, the aRNS is applied to a pneumatically actuated prosthesis finger testbed and a proposal for a aRNS-based humanoid reflex stack is made.

Contributions to Q4: Superhuman protective robot reflexes

Human-inspired robot finger reflexes are introduced and evaluated based on the aRNS framework (see contribution to Q3) and the human finger reflex case study (see contributions to Q1). Robot reflexes are implemented on a custom-developed robot finger testbed. While the human remains superior in temperature reaction, touch reflex performance is superhuman with an unconventional configuration of proprioceptive forces and link segment acceleration. It also shows that the traditional tactile sensing or proprioceptive arrangements are suboptimal, though having the potential to be superhuman.

Contributions to Q5: Semi-autonomous coordinated control schemes based on the new concept of exo-prosthetics

The concept of semi-autonomous exo-prosthetics is introduced, unifying exoskeletons and prostheses. The exoskeleton minimizes unnecessary interaction forces on the residual limb and serves as a measurement device of the residual limb’s kinematic data. The soft-robotics design of a prototype consisting of a transhumeral prosthesis and a robot-based exoskeleton substitute is presented. A coupled human-prosthesis-exoskeleton dynamics model and semi-autonomous coordinated control schemes are derived for this class of hybrid systems. The user sets task goals via kinesthetic teaching combined with an app-based programming framework or autonomously via 3D computer vision. Experiments with a human with preserved arm show that the new schemes are intuitive and enable fast task execution.

Contributions to Q6: The synergy complement control approach

A new residual limb-driven control framework denoted Synergy Complement Control (SCC) is introduced based on human arm coordination in everyday tasks. This new method adds contextual task and goal information, is expressed in terms of natural human synergies, and allows seamless transitions between these. An experimental validation with a human with preserved arm and a pilot study with an amputee in virtual reality confirms that lost coordinated motor capabilities are reliably recovered by SCC.

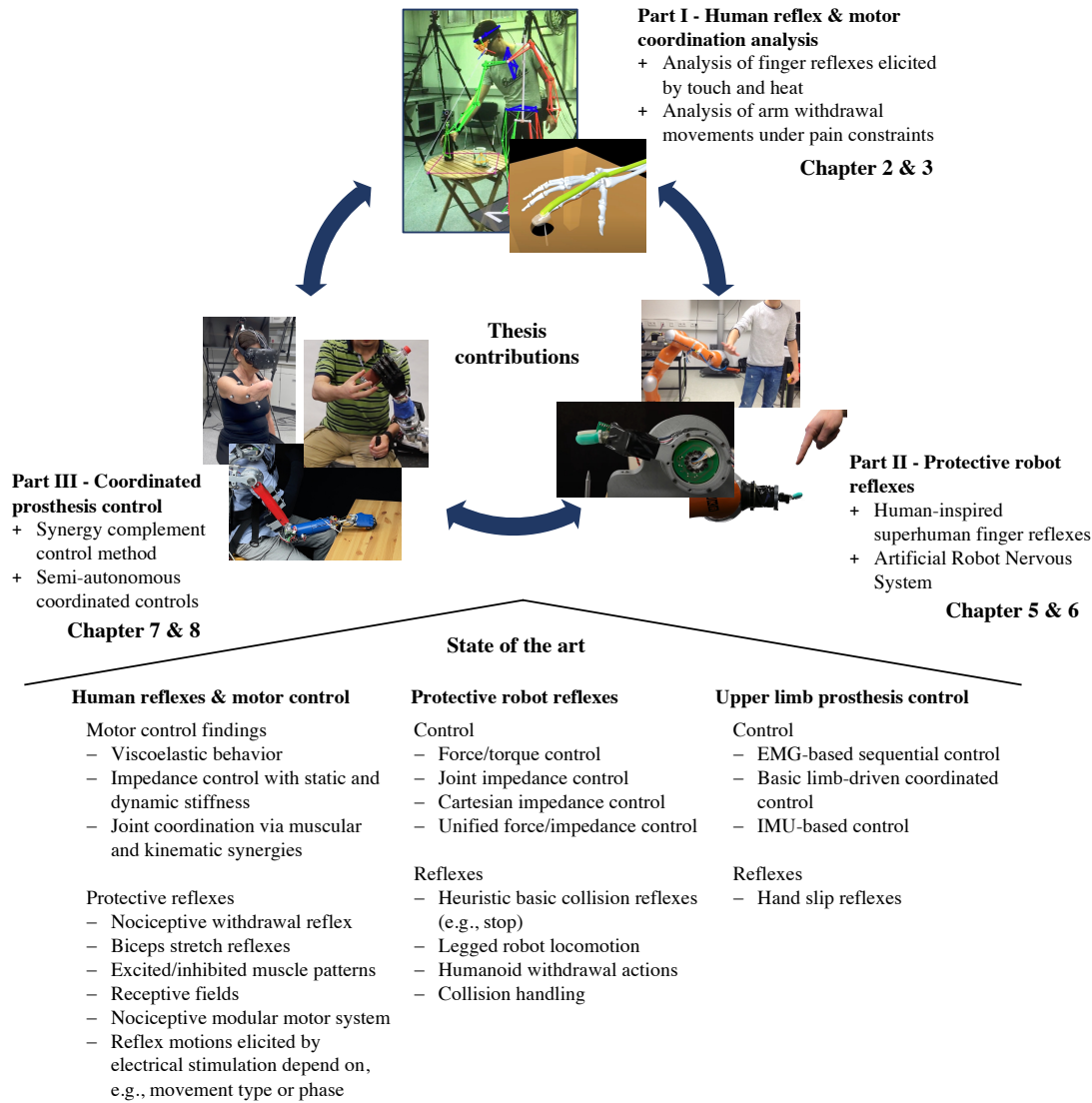


Figure 1.3: The thesis' contributions to state of the art and structure.

Publication list

The contents of this dissertation have been published in international peer-reviewed journals, conferences, and workshops, are under review or will be submitted shortly. The publications of the first author represent the main contribution of this thesis. The following list is arranged by publication type and in descending chronological order.

International Journals

- T. Hu, **J. Kühn**, S. Haddadin, “The muscle-activation observer: a computationally efficient method for solving musculoskeletal inverse dynamics”, *to be submitted*, 2022.
- A. Tödtheide, E. Pozo Fortunić, **J. Kühn**, E. Jensen, S. Haddadin, “Mechatronics, Modeling and Impedance Control of a Force Sensitive Arm Prosthesis with a Tendon Actuated Wrist”, *International Journal of Robotics Research*, *submitted*, 2022.
- A. Tödtheide, E. Pozo Fortunić, **J. Kühn**, E. Jensen, S. Haddadin, “A New Concept for Helping Transhumeral Amputees: Mechatronics of a Force Sensitive and Floating Base Aware Exo-prosthesis with Dorsal Actuator Placements”, *Transactions on Robotics*, *submitted*, 2022.
- **J. Kühn**, A. Tödtheide, E. Pozo Fortunić, T. Hu, E. Jensen, S. Haddadin, “Seamless Limb-Driven Prostheses: The Synergy-Complement Control Approach”, *Nature Machine Intelligence*, *submitted*, 2022.
- N. Seppich, N. Tacca, K. Chao, M. Akim, D. Hidalgo-Carvajal, E. Pozo Fortunić, A. Tödtheide*, **J. Kühn***, S. Haddadin*, “CyberLimb - A Novel Robotic Prosthesis Concept With Shared and Intuitive Control”, *Journal of Neuro-Engineering and Rehabilitation*, Springer Nature, 2021, *Senior authors.
- **J. Kühn**, T. Hu, A. Tödtheide, E. Pozo Fortunic, E. Jensen, S. Haddadin, “Approaching Asimov’s 3rd law: Superhuman protective robot reflexes for touch and heat”, *submitted*, 2021.
- **J. Kühn**, C. Bagnato, E. Burdet, S. Haddadin, “Arm movements adaptation to concurrent pain constraints”, *Scientific Reports*, Springer Nature, 2021.
- G. Averta, F. Barontini, V. Catrambone, S. Haddadin, G. Handjaras, J. Held, T. Hu, E. Jakubowitz, C. M. Kanzler, **J. Kühn**, O. Lamercy, A. Leo, A. Obermeier, E. Ricciardi, A. Schwarz, G. Valenza, A. Bicchi, M. Bianchi, “U-Limb: A multi-modal, multi-center database on arm motion control in healthy and post-stroke conditions”, *GigaScience*, 2021.
- T. Hu, **J. Kühn**, S. Haddadin, “Forward and Inverse Dynamics Modeling of Human Shoulder-Arm Musculoskeletal System with Scapulothoracic Constraint”, *Computer Methods in Biomechanics and Biomedical Engineering*, 2020.
- S.A.B. Birjandi, **J. Kühn**, S. Haddadin, “Observer-Extended Direct Method for Collision Monitoring in Robot Manipulators Using Proprioception and IMU Sensing”, *IEEE Robotics and Automation Letters (RA-L)*, 2020.
- **J. Kühn**, S. Haddadin, “An artificial robot nervous system to teach robots how to feel pain and reflexively react to potentially damaging contacts”, *IEEE Robotics and Automation Letters (RA-L)*, 2016.

International Conferences

- E. Jensen, T. Hu, H. Xing, Z. Chen, M. Tröbinger, S. Knebel, A. Costinescu, **J. Kühn**, M. Porzenheim, C. Günter, D. W. Franklin, D. Burschka, A. Naceri, L. Figueredo, S. Haddadin, “The Human Digital Twin Room”, *to be submitted*, 2022.
- A. Tödtheide, **J. Kühn**, E. Pozo Fortunić, S. Haddadin, “An Integrated, Force-Sensitive, Impedance Controlled, Tendon-Driven Wrist: Design, Modeling, and Control”, *IEEE-RAS International Conference on Humanoid Robots (Humanoids)*, Munich, Germany, July 19-21, 2021.
- **J. Kühn**, J. Ringwald, M. Schappler, L. Johannsmeier, S. Haddadin, “Towards Semi-Autonomous and Soft-Robotics Enabled Upper-Limb Exoprosthetics: First Concepts and Robot-Based Emulation Prototype”, *IEEE International Conference on Robotics and Automation (ICRA)*, Montreal, Canada, May 20-24, 2019.
- S.A.B. Birjandi, **J. Kühn**, S. Haddadin, “Joint velocity and acceleration estimation in serial chain rigid body and flexible joint manipulators”, *IEEE/RSJ International Conference on Intelligent Robots and Systems (IROS)*, Macau, China, November 4-8, 2019.
- **J. Kühn**, T. Hu, M. Schappler, S. Haddadin “Dynamics simulation for an upper-limb human-exoskeleton assistance system in a latent-space controlled tool manipulation task”, *IEEE International Conference on Simulation, Modeling, and Programming (SIMPAN)*, Brisbane, Australia, May 16-19, 2018.
- T. Hu, **J. Kühn**, S. Haddadin “Identification of Human Shoulder-Arm Kinematic and Muscular Synergies During Daily-Life Manipulation Tasks”, *IEEE International Conference on Biomedical Robotics and Biomechatronics (BioRob)*, Twente, The Netherlands, August 26-29, 2018.
- T. Hu, **J. Kühn**, J. Ma'touq, S. Haddadin “Learning and Identification of human upper-limb muscle synergies in daily-life tasks with autoencoders”, *OTWorld Congress*, Leipzig, Germany, May 15-18, 2018.

Workshops

- A. Tödtheide, **J. Kühn**, S. Haddadin, “Proprio- and exteroceptive reflexes for a pneumatically actuated finger based on the artificial robot nervous system”, *IEEE International Conference on Robotics and Automation (ICRA), Workshop on “The robotic sense of touch: from sensing to understanding”*, May 29 to July 3, Marina Bay Sands, Singapur, 2017.
- **J. Kühn**, J. Vorndamme, M. Schappler, S. Haddadin, “Humanoid Collision Reflex Sequences based on an artificial Robot Nervous System including Contact Location and Direction”, *IEEE International Conference on Robotics and Automation (ICRA), Workshop on Legged Robot Falling: Fall Detection, Damage Prevention, and Recovery Actions*, May 16-21, Stockholm, Sweden, 2016.

1 Introduction

- L. Johannessmeier, J. Ringwald, **J. Kühn**, S. Haddadin, “Teleoperated Semi-Autonomous Control of the LWR and a Humanoid Hand via the Myo Armband”, IEEE International Conference on Robotics and Automation (ICRA), *Workshop on Human-robot interfaces for enhanced physical interactions*, May 16-21, Stockholm, Sweden, 2016.
- **J. Kühn**, S. Haddadin, “Pain Reflexes For Robots To Evade Noxious Contact Events”, *8th International Workshop on Human-Friendly Robotics*, München, Germany, October 21-23, 2015.



René Descartes' conception of how a painful thermal stimulus is transmitted to the brain, L'Homme, 1664.

Part I

Human reflex and motor coordination analysis

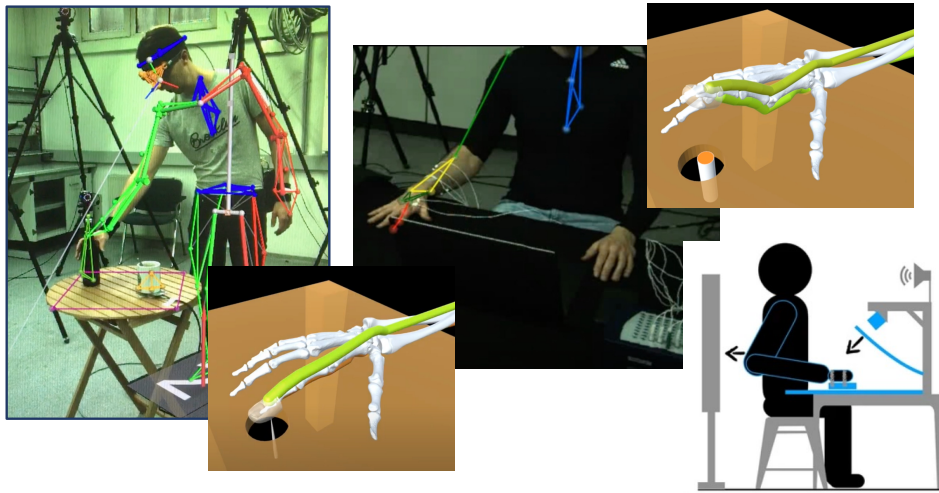


Figure 1.4: Impressions from the work carried out in Part I.

Part I examines human upper limb reflexes and motor coordination in response to noxious stimuli. Two exploratory studies are presented, relating to Q1 and Q2. Chapter 2 deals with study I (Q1), which is published in [199]. Chapter 3 deals with study II (Q2), which is published in [200]. Both studies are briefly summarized below. Fig. 1.4 shows some impressions from these works.

Chapter 2: Human finger reflexes (Q1) How do stimulus' physical characteristics such as shape, speed, or temperature modulate reflex responses of joints and muscles? This work sheds light on this open question through an exploratory case study. Human finger reflexes elicited by mechanical and temperature stimuli with varying properties at kinematic and muscular levels were studied. Analyzing the subject's motor reactions unveiled a 5-phase reflex launch sequence that changes with shape, speed, and temperature of the stimulus, as well as habituation.

Chapter 3: Arm withdrawal adaption (Q2) How do humans coordinate their movements to avoid concurrent pain sources? This exploratory study investigates the kinematic characteristics of withdrawal movements of the human upper limb that are triggered by a threatening source at hand level. The experimental task included the presence of an obstacle at different distances along the direction of withdrawal. Assigning the participants to two different groups, one of which would execute the experiment with an innocuous obstacle and the other one with a painful one, allowed for investigation of the effect of pain as an extra layer of motivation to prevent collision. The results show that the subjects learned to control the hand retraction movement in order to avoid the potential pain. Subject-specific motor strategies were used to modify the joint movement coordination to avoid hitting the obstacle with the elbow at the cost of increasing the risk of hand slap.

2 Finger reflexes elicited by touch and heat

Humans have a fascinating built-in embodied intelligence that is indispensable for survival. A central ability is the protection reflex such as the nociceptive withdrawal reflex (NWR) [201], defined as an automatic retraction of an extremity from a noxious stimulus such as heat or pain. Such noxious stimuli are detected by a wide spectrum of receptors in the skin and viscera [202], which transmit this information to the spinal cord and brain in the form of electrical impulses [203, 204, 205] (Fig. 2.1).

Although some works focused on the NWR elicited by *electrocutaneous* stimulation on upper limb level [108, 206], no literature has systematically investigated such protection reflex triggered by *noxious mechanical* stimuli (to the best of my knowledge). It is unknown how stimulus's physical characteristics such as shape, speed, or temperature modulate reflex responses on joint and muscle levels in the neuromusculoskeletal system. Moreover, despite the already astonishing performance in biological systems, there may exist limits and potential weaknesses, which, if well understood, could be addressed and

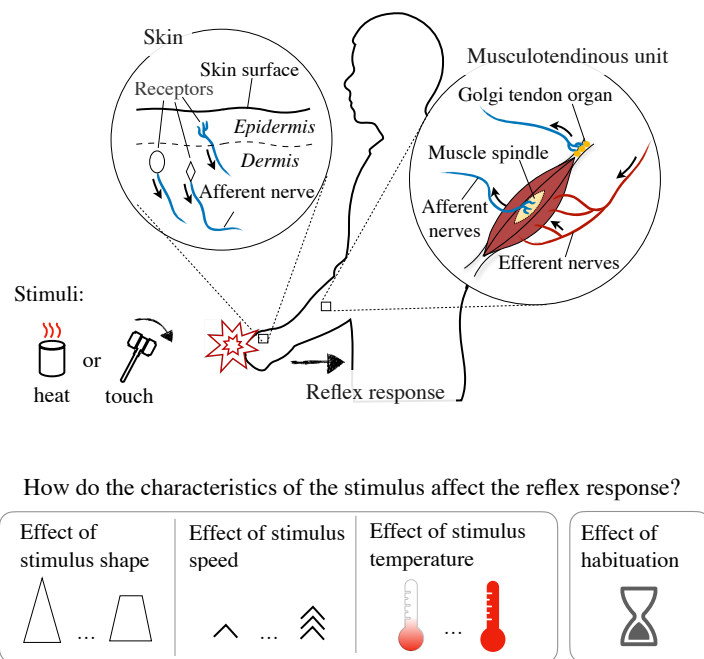


Figure 2.1: Protective reflexes in humans. Noxious stimuli are perceived by many receptors in the skin, processed by the spinal cord and brain, and trigger protective reflexes via musculotendinous units.

overcome in a robotic implementation. Thus, this work aims to answer the following research question (Fig. 2.1):

Can a distinct reflexive motor pattern on a kinematic and muscular level be found?
If yes, how do shape, speed and temperature of a mechanical stimuli modulate it,
and what role does habituation play? (Fig. 2.1)

To address this research question, a reflex case study is conducted in which human finger withdrawal is elicited through a threatening mechanical source with varying properties. The human reflex response is investigated on a kinematic and muscular level.

2.1 Experimental procedures

2.1.1 Participant

A case study is conducted with a subject who is part of the research team¹. The experiments took place at the Munich Institute of Robotics and Machine Intelligence (MIRMI) of Technical University of Munich (TUM). All experiments were conducted according to the principles in the Declaration of Helsinki. The subject—male, 32 years old, and right-handed as was assessed using the Edinburgh Handedness Inventory [207]—gave written informed consent before participating in the study. No neuromuscular disorder or recent injury at hand level was known. The subject performed reflex movements with the index finger triggered by pointed metal frustums or a heated cylinder.

2.1.2 Design

Figure 2.2a shows a schematic of the experimental setup. The subject is seated comfortably on a stool and remains upright during the experiment. The right hand is placed flat on the table with the elbow at approximately 90° to the upper arm. Below the fingertip of the index finger is a small hole in the table through which a *stimulus*, a conical frustum or a heated cylinder, is applied. The stimulus and a *force sensor* are fixed to the *stimulator*, i.e., the end effector of a robotic arm. To prevent the subject from visually or aurally anticipating an impending collision, the subject watches television on a *screen* and listens to it through *headphones*. In this case study, stimulus shape is considered as pointedness of conical frustums with diameter $d \in \{0.2 \text{ mm}, 0.5 \text{ mm}, 1.0 \text{ mm}, 1.6 \text{ mm}\}$. Diameters 0.2 mm and 1.6 mm are used to investigate how the subject deals with a *pointed* versus *blunt* contact, while diameters 0.5 mm and 1.0 mm shed light on the blurred scale in between. Note that the blunt frustum was shaped like a pyramidal frustum (width 1 mm, length 2 mm), and the diameter $d = 1.6 \text{ mm}$ is representative of a conical frustum of same contact area. The effect of temperature was analysed using a cylinder made of aluminium with 5 mm diameter that was approximately heated to mean temperature $\vartheta \in \{35^\circ\text{C}, 45^\circ\text{C}, 55^\circ\text{C}\}$. The temperature 35°C , corresponding to body temperature, was introduced to verify that the reflexes, possibly seen under the *warm* (45°C)

¹This experiment was done during an early stage of the COVID-19 pandemic. A participant from the research team was selected to support the COVID-19 pandemic containment measures.

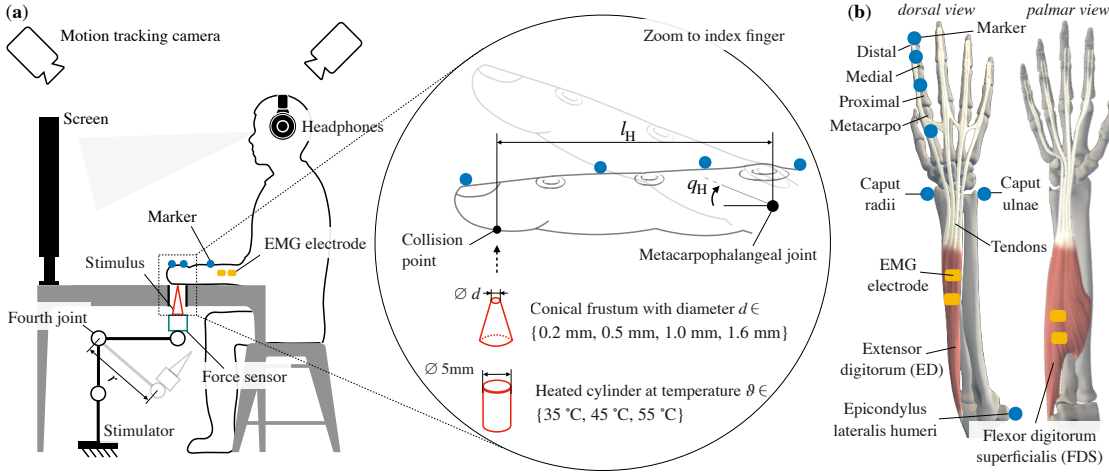


Figure 2.2: Human reflex case study. (a) Schematic of experimental setup. (b) Marker and EMG electrode placement.

and *hot* ($55\text{ }^{\circ}\text{C}$) conditions, were triggered by heat and not purely mechanical. The effect of stimulus speed was investigated by applying each of these seven conditions—a conical frustum with four different diameters and a cylinder with three different temperatures—at speed $v \in \{0.01\text{ m/s}, 0.025\text{ m/s}, 0.05\text{ m/s}, 0.1\text{ m/s}\}$, respectively. The speeds 0.1 m/s and 0.01 m/s are used to investigate how the subject behaves in a relatively *fast* versus a *slow* condition, while 0.05 m/s and 0.025 m/s investigates the range in between. Thus, a total of 28 conditions are examined.

2.1.3 Protocol

The experiment consisted of $N = 56$ trials divided into *Block 1* and *Block 2*. Each block had 28 trials corresponding to the 28 conditions, occurring in an unpredictable order to minimize bias. The subject is asked to sit comfortably on a stool and keep the back upright during the experiment. After the motion tracking markers and EMG electrodes are accurately positioned (Fig. 2.2b), the subject is asked to place the hand in the starting position and watch television. From there on, the stimulus could hit the finger pad. An experimenter observes the experiment, controls the stimulator, and changes the stimulus after each trial. The stimulator, i.e., the robotic arm, follows a pre-programmed motion so that the stimulus hits the finger pad perpendicular at a constant speed. If a collision triggered a finger reflex, the subject was instructed to return to the starting position when he felt ready. Each block lasted approximately one hour, and a 15-minute break was introduced between them. However, the markers and EMG electrodes remained attached to the subject during the break.

2.1.4 Apparatus

A real-time *Lock Sync box* (Vicon Motion Systems Ltd, UK) was used to synchronize a motion tracking system, an EMG device, a force sensor, and the stimulator.

Sixteen infrared *Vicon Vero* cameras (Vicon Motion Systems Ltd, UK) tracked the movement trajectories of passive reflected markers in a predefined Cartesian coordinate system at 200 Hz. Four essential markers (4 mm diameter) were placed on significant anatomical landmarks of the right index finger: at the middle of the *medial, proximal* and *metacarpal phalanx*, and at the distal end of the *distal phalanx* as shown in Fig. 2.2b. In order to capture possible arm movements as part of reflex response, five additional markers (15 mm diameter) were placed at significant anatomical landmarks: *Caput ulnae*, *Caput radii*, *Epicondylus lateralis humeri*, *Acromion*, and *Fossa jugularis sternalis* as (partially) indicated in Fig. 2.2b.

A *Refa system* (TMSi B.V., the Netherlands) and bipolar surface microelectrodes (1 mm diameter) were used to record muscle activities of the *Flexor digitorum superficialis* (*FDS*) and *Extensor digitorum* (*ED*) at 2 kHz. These muscles are mainly responsible for flexion and extension of the index finger and are measurable by surface EMG. Electrode placement (indicated in Fig. 2.2b) was performed in line with SENIAM guideline [208], whereas the muscles were palpated according to [16].

The stimulator was realized by a seven DoF *Panda robot arm* (FRANKA EMIKA GmbH, Germany) with a force sensor and the stimulus attached to its end effector. A joint impedance controller [209] is applied with high stiffness (3 kNm/rad) to control the fourth joint. It performed a circular motion at constant tangential speed; the radius ($r = 0.384$ m, see Fig. 2.2a) was sufficiently large so that the movement of the stimulus can be considered as a straight-line motion with constant speed v , perpendicular to the fingertip. The robot was programmed to stop at ≈ 3 mm above the tabletop. After 1.5 s it returned to the starting position.

In order to measure the contact force, a three-component force sensor *Typ 9327C* (Kistler Instrumente GmbH, Germany) is deployed. This piezoelectric sensor was calibrated to measure forces up to 100 N with a resolution of 1.3 mN and a natural frequency of ≈ 3.2 kHz.

Furthermore, an *ETC-200+ thermostat* (Conrad Electronic AG, Germany) consisting of a heating element, a thermistor, and a bang-bang controller was used to heat the cylindrical stimulus. In addition, the temperature at the cylinder surface was checked using a laboratory alcohol thermometer.

2.1.5 Finger temperature estimation

When the finger pad touches an object, the thermal interaction is a transient process dominated by heat conduction. Given a temperature difference between the skin and an object in contact with the skin—in this work, the initial temperature $\vartheta_{\text{skin},0}$ at the skin surface is lower than that of the cylinder $\vartheta_{\text{obj},0} > \vartheta_{\text{skin},0}$ —heat flows from the object to the skin through a thermal contact resistance $R \in \mathbb{R}_{>0}$. The temperature $\vartheta_{\text{skin}}(t)$ at

skin surface evolves over time t as [210]

$$\begin{aligned} \vartheta_{\text{skin}}(t) &= \frac{A}{B} \left(1 - \exp\left\{(\alpha_{\text{skin}} B^2 t)\right\} \operatorname{erfc}(B\sqrt{\alpha_{\text{skin}} t}) \right) + \vartheta_{\text{skin},0}, \\ A &= \frac{\vartheta_{\text{obj},0} - \vartheta_{\text{skin},0}}{\kappa_{\text{skin}} R}, \quad B = \frac{1}{\kappa_{\text{skin}} R} \left(1 + \frac{\sqrt{\kappa_{\text{skin}} \rho_{\text{skin}} c_{\text{skin}}}}{\sqrt{\kappa_{\text{obj}} \rho_{\text{obj}} c_{\text{obj}}}} \right), \end{aligned} \quad (2.1)$$

where κ is thermal conductivity, c is specific heat capacity, ρ is material density, $\alpha = \kappa/(\rho c)$, and $\operatorname{erfc}(\cdot)$ is the complementary error function. Subscripts “skin” and “obj” refer to the skin and the object. The thermal contact resistance between the finger pad and an object is approximated by $R = (0.37 + \kappa_{\text{obj}})/(1870\kappa_{\text{obj}})$ ($\text{m}^2\text{K}/\text{W}$) [211].

2.1.6 Contact force measurement

Throughout this work, the contact force $\mathbf{F}_c(t) \in \mathbb{R}^3$ refers to the force exerted by the stimulus on the finger pad and is derived from force measurements (Fig. 2.2a). $\mathbf{F}_c(t)$ is obtained by

$$\mathbf{F}_c(t) = \mathbf{F}_{\text{sensor}}(t) - \mathbf{F}_{\text{ref}}(t), \quad (2.2)$$

where $\mathbf{F}_{\text{sensor}}(t) \in \mathbb{R}^3$ denotes the sensor signal. To calibrate the measurements, the reference force profile $\mathbf{F}_{\text{ref}}(t)$ prior experimentation for each $v \in \{0.01 \text{ m/s}, 0.025 \text{ m/s}, 0.05 \text{ m/s}, 0.1 \text{ m/s}\}$ is recorded. Eventually, $\mathbf{F}_c(t)$ is denoised by using a zero-lag 4-th order Butterworth low-pass filter with cut-off frequency 50 Hz. Note that in “Results” section, the magnitude of the vector $F_c(t) = \|\mathbf{F}_c(t)\|$ is used, since the direction is always perpendicularly to the finger pad.

2.2 Measures

Finger retraction frequentness is defined as

$$f = \frac{N_r}{N_{\text{total}}} \times 100\%, \quad (2.3)$$

where $N_{\text{total}} \in \mathbb{N}^+$ denote the total number of trials, and $N_r \in \mathbb{N}$ represents the total number of trials in which the subject retracted the finger.

The *maximum contact pressure* is obtained by

$$\sigma_{c,\max} = \max_{t \in [t_c, t'_c]} \frac{\|\mathbf{F}_c(t)\|}{\pi(d/2)^2} \quad (2.4)$$

where t_c, t'_c (see Fig. 2.3) denote, respectively, the time of contact and loss of contact between the finger pad and the stimulus, and d is stimulus diameter.

The *maximum finger retraction* is defined as

$$q_{H,\max} = \max_{t \in [t_c, t_{\text{end}}]} q_H(t), \quad (2.5)$$

2 Finger reflexes elicited by touch and heat

where $q_H(t)$ is the angular position of the *Metacarpophalangeal joint* (Fig. 2.2a) and t_{end} denotes the time of the end of a trial.

Mean muscle effort with time period $[t_1, t_2] \neq \emptyset$ is defined as

$$\xi(t_1, t_2) = \frac{1}{t_2 - t_1} \int_{t_1}^{t_2} |\eta(t)| dt, \quad (2.6)$$

where $\eta(t) \in \mathbb{R}$ is the measured EMG signal of a muscle.

Lastly, the total *contact duration* is obtained by

$$\Delta t_c = t'_c - t_c \quad (2.7)$$

where t_c, t'_c (see Fig. 2.3) denote, respectively, the time of contact and loss of contact between the finger pad and the stimulus.

2.3 Results

2.3.1 Reflex launch sequence

Figure 2.3 shows data from a representative trial after a collision with a pointed frustum ($d = 0.2$ mm) at a rather slow speed ($v = 0.025$ m/s). The temporal progression can be divided into five characteristic phases, which are elucidated in detail in Table 2.1. Briefly, the subject responds to the pointed frustum with a muscle twitch (Phase II)—a time-shifted excitation/inhibition of extensor and flexor, here defined as *muscle twitch reflex (MTR)*—followed by a *hold* period (Phase III) in which extensor activity is slightly increased compared to the baseline activity observed in the pre-collision phase (Phase I). Subsequently, the subject retracts (Phase IV), causing the finger to lose contact with the frustum, and eventually returns to the initial pose (Phase V). Similar behavior was observed in the responses to temperature stimulus. The accompanying video shows an animation of the trial shown in Figure 2.3.

2.3.2 Effect of stimulus shape

A more pointed frustum is more likely to cause finger withdrawal (upper plot in Fig. 2.4a). While the *pointed* frustum ($d = 0.2$ mm) always leads to finger retraction, finger retraction frequency f (2.3) decreases with a larger diameter ($d = 0.5$ mm), and almost vanishes ($d = 1.0$ mm and $d = 1.6$ mm) for maximum contact pressures $\sigma_{c,\text{max}} < 10^0$ MPa (2.4) (middle plot in Fig. 2.4a). It is noteworthy that the *DIN EN 12203* standard [212] for the manufacture of footwear machines specifies a safety limit of 0.3 MPa for the protection of fingers and hands (see the middle plot of Fig. 2.4a). In contrast to f and contrary to intuitive interpretation, maximum finger retraction $q_{H,\text{max}}$ (2.5) does not appear to correlate with pointedness (bottom plot in Fig. 2.4a).

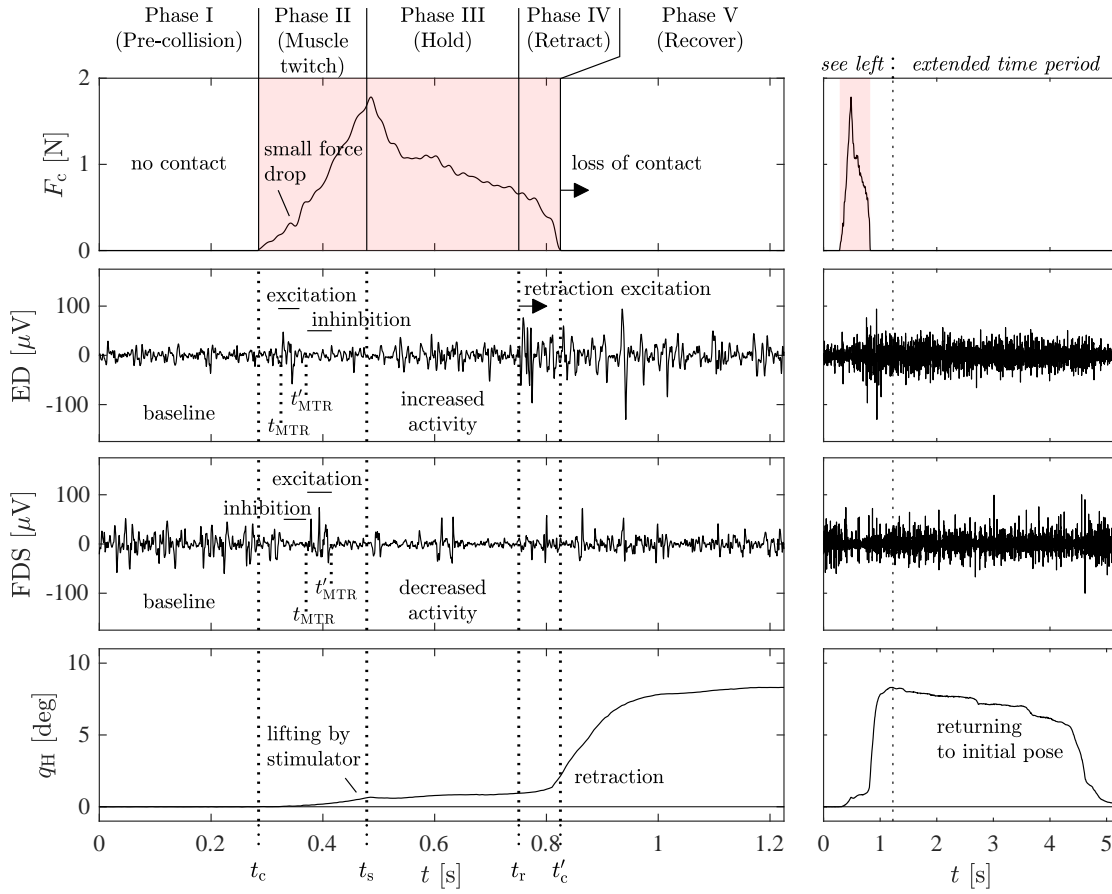


Figure 2.3: Reflex launch sequence. Data of a representative trial after a collision between a pointed frustum at slow speed and human finger. The temporal progression is divided into five characteristic phases, which are elucidated in Table 2.1.

2.3.3 Effect of stimulus speed

The faster the stimulus approaches, the higher finger retraction frequentness f is observed (upper plot in Fig. 2.4b). Notably, two retractions were triggered by the fastest stimulus ($v = 0.1$ m/s), even though the corresponding maximum pressure was below the safety limit (middle plot of Fig. 2.4b). Maximum finger retraction $q_{H,\text{max}}$, like pointedness, does not seem to correlate with speed (bottom plot in Fig. 2.4b). The mean muscle effort $\xi(t_1, t_2)$ (2.6) is calculated using characteristic time intervals such as $\xi(t_c - 100\text{ms}, t_c)$ (cf. Phase I in Fig. 2.3), $\xi(t_{\text{MTR}}, t'_{\text{MTR}})$ (cf. Phase II in Fig. 2.3), and $\xi(t'_{\text{MTR}}, t_r)$ (cf. Phase III in Fig. 2.3). Time instant t_c denotes the start of contact, and t_r denotes the start of finger retraction (as shown in Fig. 2.3). Time instants t_{MTR} and t'_{MTR} (see also Fig. 2.3) mark the start and the end of MTR excitation for each muscle, respectively, and were visually and independently identified by two reviewers (average

2 Finger reflexes elicited by touch and heat

Table 2.1: Explanations of Phase I to V (see Fig. 2.3).

Illustration	Phase I (Pre-collision)	Phase II (Muscle twitch)	Phase III (Hold)	Phase IV (Retract)	Phase V (Recover)
Time	$t \in [0, t_c[$	$t \in [t_c, t_s]$	$t \in]t_s, t_r[$	$t \in [t_r, t'_c]$	$t > t'_c$
Stimulator	Stimulator approaches finger at constant speed.	Stimulator contacts skin at t_c , compresses tissue and stops at t_s .	Stimulator interacts with skin receptors.	Stimulator interacts with skin receptors until loses contact at t'_c .	Stimulator is programmed to return to starting position at $t = t_s + 1.5$ s.
Finger muscles	Extensor (ED) and flexor (FDS) show baseline activity.	Time-shifted excitation and inhibition of ED and FDS (<i>muscle twitch reflex</i> (MTR)).	Slightly increased activity of ED is supported by inhibition of FDS.	Retraction excitation in ED and FDS start at t_r .	As in Phase IV, until subject returns to initial pose.
Finger skeleton	Skeleton is in starting pose, i.e., $q_H(t = 0) = 0$ deg.	Passively lifted by stimulator, while MTR leads to a small, brief drop in force.	Skeleton tends to remain in a constant position, but is slightly lifted and bent, resulting in a continuous decrease in force.	Skeleton is moving corresponding to muscle excitation.	As in Phase IV, until subject returns to initial pose.

values were used). Analysis of mean muscle effort of extensor and flexor reveals that the MTR grows as the stimulus speed increases (Fig. 2.4c). Extensor mean activity (left plot in Fig. 2.4c) appears to be slightly higher for *Hold* compared with *Baseline*, while flexor mean activity (right plot in Fig. 2.4c) appears to be slightly lower for *Hold* compared with *Baseline* (cf. Phase III in Fig. 2.3).

2.3.4 Effect of stimulus temperature

To estimate finger pad's surface temperature—resulting from the contact with the heated cylinder—the thermal model in (2.1) is applied using the parameters shown in Table 2.2. The upper plot in Fig. 2.5a reveals that the subject retracted his finger starting at skin surface temperatures $\vartheta_{\text{skin}}(t = t'_c) \gtrsim 48^\circ\text{C}$ (for the definition of t'_c see Fig. 2.3) with contact duration $\Delta t_c \gtrsim 1$ s, cf. (2.7). Maximum finger retraction height h_{max} , defined as the maximum distance between the table and the marker attached to

Table 2.2: Parameters used in the thermal model. Values for specific heat capacity c , thermal conductivity κ , and material density ρ are taken from literature [211, 213, 214], while the initial temperature ϑ_0 was set for the stimulus, and measured for the subject.

	ϑ_0 [K]	c [J/(kg K)]	κ [W/(K m)]	ρ [kg/m ³]
Aluminium	$\vartheta_{\text{obj},0} = \vartheta$	897	247	2710
Epidermis	$\vartheta_{\text{skin},0} = 303.15$	3598	0.255	1200

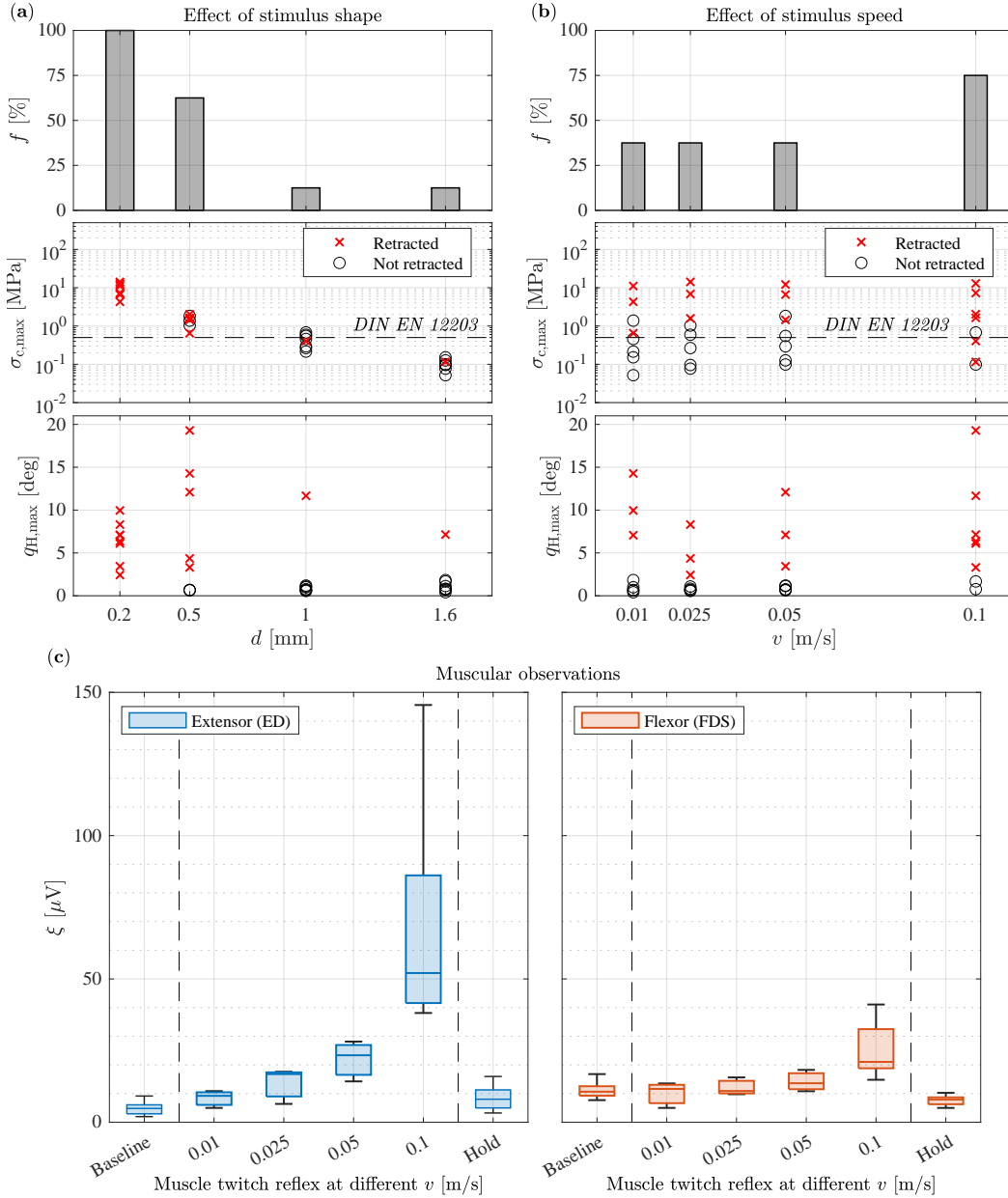


Figure 2.4: Effect of stimulus shape and speed. **(a)** Finger retraction frequentness f (2.3), maximum contact pressure $\sigma_{c,max}$ (2.4), and maximum finger retraction $q_{H,max}$ (2.5) at stimulus diameter d . **(b)** Same measures as shown in **a** but at stimulus speed v . **(c)** Mean muscle effort ξ (2.6) of “Baseline”, “Muscle twitch” and “Hold” (cf. Phases I to III in Fig. 2.3).

the medial phalanx (Fig. 2.2b), reveals that for one trial the reflex response included the elevation of the wrist (see $h_{max} \approx 200$ mm in the bottom plot in Fig. 2.5a). Notably, this trial was the very first trial the subject was confronted with.

2 Finger reflexes elicited by touch and heat

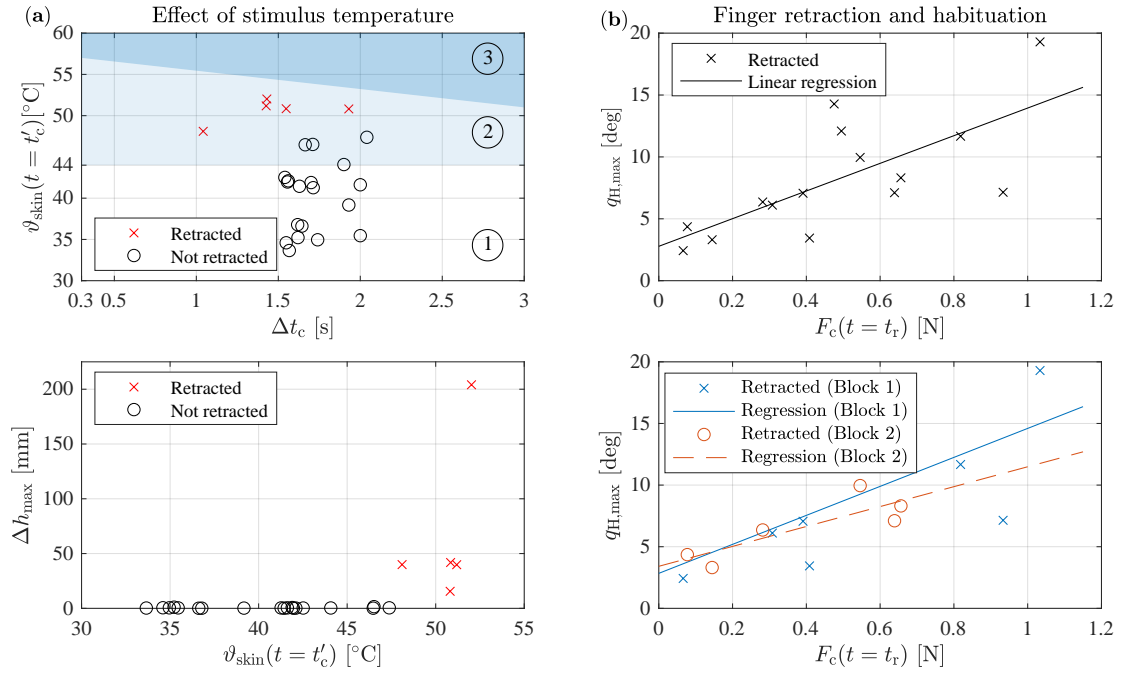


Figure 2.5: Effect of stimulus temperature, and finger retraction and habituation. **(a)** Estimated skin surface temperature $\vartheta_{\text{skin}}(t = t'_c)$ (2.1) over contact duration Δt_c (2.7) (upper plot). Colored areas are known from literature [215] and refer to *no tissue change* Φ , *1st Degree burns* \mathcal{Q} , and *transition zone* towards 2nd Degree burns \mathcal{B} . Maximum finger retraction height h_{max} over $\vartheta_{\text{skin}}(t = t'_c)$ (lower plot). **(b)** Maximum finger retraction $q_{H,\text{max}}$ (2.5) could be explained by compression depth of the tissue, which is approximated here by contact force $F_c(t)$ at time instant $t = t_r$ (upper plot). Effect of habituation on $q_{H,\text{max}}$ across trials of Block 1 and 2 in comparison (bottom plot).

2.3.5 Finger retraction

Stimulus shape and speed do not seem to be sufficient to explain the observed maximal finger retraction $q_{H,\text{max}}$ (2.5) in response to the conical frustums (see bottom plots in Fig. 2.4a and Fig. 2.4b). Rather, it appears that the contact force imminent to withdrawal start, i.e., $F_c(t = t_r)$, determines $q_{H,\text{max}}$ (upper plot in Fig. 2.5b). Regression of Fig. 2.5b (see solid line) indicates a linear relationship (slope= 11.17 deg/N, $R^2 = 0.512$). The interpretation of this is discussed in the “Discussion” section. Note that the small number of observed retraction movements elicited by the heated cylinder (only five out of a total of 24 trials (cf. Fig. 2.5a), in contrary to 15 out of a total of 32 trials with the conical frustum (cf. Fig. 2.5b)) does not allow further analysis of maximum finger retraction with respect to the temperature stimulus.

2.3.6 Effect of habituation

Habituation effects are analyzed by comparing measures between *Block 1* and *Block 2* (the experiment was divided into two blocks of trials, each containing the same conditions in an unpredictable order with a 15-minute break in between.). With respect to the experiments with the conical frustum, finger retraction frequentness f (2.3) across all trials for each block decreases from $f = 56.25\%$ (*Block 1*) to $f = 37.5\%$ (*Block 2*). The bottom plot in Fig. 2.5b shows the regression of maximum finger retraction $q_{H,\max}$ (2.5) and contact force $F_c(t = t_r)$ (definition of t_r see Fig. 2.3) for each block, respectively, revealing a decrease in slope from 11.76 deg/N ($R^2 = 0.462$, *Block 1*) to slope = 8.08 deg/N ($R^2 = 0.702$, *Block 2*). Considering only the trials in which the subject retracted the finger for each block, respectively, the contact duration increases from $\Delta t_c = 344.8 \pm 169.5$ ms (*Block 1*) to $\Delta t_c = 531.3 \pm 156.2$ ms (*Block 2*). This indicates that the subject can sustain the stimulus for a longer period of time in *Block 2*, before withdrawing the finger. Furthermore, with respect to the experiments with the heated cylinder, one can observe a flexion of the wrist as part of the reflex response only in one trial, which was the very first trial of *Block 1* (cylinder temperature was $\vartheta = 58.53^\circ\text{C}$).

2.4 Discussion

Humans protect their bodies by autonomous [108] as well as voluntary [200] withdrawal actions. While the withdrawal reflex [201] was extensively studied using electrocutaneous or non-noxious mechanical stimulation on the lower [216, 217] and upper limbs [218, 108], little or no literature has investigated withdrawal actions that were triggered by noxious mechanical stimulation. The presented exploratory case study investigated the muscular and kinematic characteristics of the human index finger's withdrawal movements triggered by pointed frustums or heated objects.

Results show that the withdrawal response of the subject follows a *5-phase reflex launch sequence* composed of three characteristic events: the muscle twitch reflex (MTR), a hold period, and finger retraction. After the stimulus contacts the skin surface, the subject responds with the MTR, a temporally shifted excitation/inhibition of the extensor and flexor muscle leading to a slight drop in contact force. The MTR appears to be dominated by low-level control circuits in the spinal cord, as reaction times suggest [219] and correlates with stimulus speed. Extensor activity slightly increases during the hold period, while the flexor decreases activity. From a control theory perspective, this can be interpreted as the central nervous system maximizes control authority, preparing the finger to be withdrawn. Reaction times suggest that finger retraction is dominated by intermediate spinal/supra-spinal circuits [220]. Note also that the muscle activity of the MTR and finger retraction overlapped in two trials.

Stimulus shape and speed do not seem to be sufficient to account for the observed maximum finger retraction in response to the conical frustums. The question then arises as to what determines the amplitude. The subject's data show a linear relationship between the maximum retraction amplitude and the contact force at the very time instant before finger retraction. Here, contact force might be a proportional indicator

2 Finger reflexes elicited by touch and heat

of compression depth of the skin tissue caused by the frustum. Simply put, the higher the contact force, the more the tissue is compressed. This compression depth appears to result from the subject's reaction to the contact, comprising the MTR and the hold period. The more the MTR and the hold period counteracted tissue compression, the less the tissue is compressed, thus, the lower the finger retraction amplitude, and vice versa.

Conical frustums of various diameters are applied to investigate the effect of stimulus shape on the reflex response. It seems that contact pressure dominates the frequentness of finger retraction: the pointier, the more likely the finger is withdrawn. Also, the stimulus speed appears to affect the frequentness: the faster, the more likely the finger is withdrawn.

A blunt cylinder that was heated to various temperatures was also applied. Results show that the subject retracted his finger starting at skin surface temperatures $>48^{\circ}\text{C}$ with contact duration $>1\text{ s}$. These values can be considered the subject's individual, critical temperature reflex conditions. The number of trials in which the subject retracted the finger is too low to conclude finger retraction amplitude. More trials with higher cylinder temperatures should be considered in future experiments.

Furthermore, effects of habituation were observed. In the case of the conical frustum, finger retraction frequency and amplitude decrease over time. Desensitization of the skin contact area can explain this. Regarding the temperature reflexes, an elevation of the hand as part of the reflex response only in the first trial of human experiments was observed. This might be explained by the subjects' fear of the unknown, which subsequently decreased. The results of this work have inspired the robot reflex design presented in Chapter 6.

3 Arm withdrawal adaption to concurrent pain constraints

Pain helps humans to avoid injuries by signaling the immediate threat and triggering relevant motor responses, e.g. the withdrawal reflex. While the withdrawal reflex is defined as an automatic retraction of an extremity from a noxious stimulus such as heat or pain, it is also common to initiate withdrawal actions prior to any physical stimulation, for instance when we visually spot the threatening event. This is what would happen when our hand is about to get slammed into the heavy cutlery drawer, as our cheerful son suddenly pushes it with force. To prevent pain and injury, we would retract the hand from inside the drawer as fast as possible. Additionally, we may have to consider several constraints and pain sources simultaneously. Imagine that our son is exactly located along the direction of withdrawal at that point in time. The motor control dilemma arises on how to preserve physical integrity and at the same time modulate the instinctive withdrawal of the hand in such a way that the kid is not hit by the retraction of the arm. How do humans deal with such constraints during motor tasks?

Corresponding to this scenario (Fig. 3.1a):

1. Effect of obstacle distance: Do we — and, if yes, how do we — use the mechanical redundancy of our upper limb when a constraint (i.e. an obstacle behind us) is introduced that limits the room for withdrawal?
2. Effect of obstacle presence uncertainty: Does our motor strategy change when the environmental conditions are subject to uncertainty? Specifically, if an obstacle may or may not be present behind us, do we adopt a conservative strategy and plan the movement according to the worst-case scenario or do we rather take risks?
3. Effect of obstacle nature: How does the introduction of pain — as a consequence of the possible impact with the obstacle — affect the way we avoid the obstacle when withdrawing our arm?

To address these questions, a paradigm is developed where sudden withdrawal of the upper limb is elicited through a threatening mechanical source at the hand level. At the same time, they could hit an obstacle on the back with the elbow. To escape pain at the hand, subjects necessarily had to retract the arm while an obstacle impedes the path of the elbow during hand retraction. Their withdrawal actions were compared across different geometric and pain conditions.

3 Arm withdrawal adaption to concurrent pain constraints

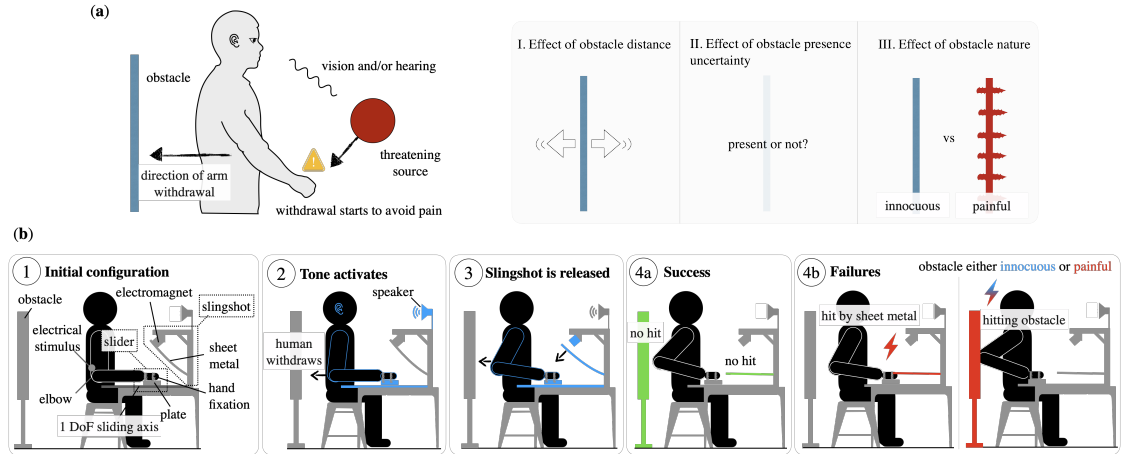


Figure 3.1: (a) Study focus. (b) Experimental setup and sequence. [200]

3.1 Experimental procedures

3.1.1 Participants

The experiments took place at the Institute of Automatic Control of Gottfried Wilhelm Leibniz Universität Hannover (LUH). The study was approved by the ethics committee of LUH, and all experiments were conducted according to the principles in the Declaration of Helsinki. Each of the 23 subjects gave their written informed consent prior to participating in the study. The subjects were all male and right-handed (as was assessed using the Edinburgh Handedness Inventory [207]), and no subject had a known neuromuscular disorder or recent injury at arm level. All subjects had normal or corrected to normal vision at the time point of experiment.

A group of 11 subjects (aged 27.36 ± 2.29 years) used their dominant arm to perform a withdrawal task, escaping a slap on their hand while avoiding a collision between their elbow and an *innocuous* obstacle. A second group of 12 subjects (aged 26.5 ± 4.5 years) performed the same task under the same conditions while contact with the obstacle at elbow level was *painful*.

3.1.2 Design

The experiment took place in a sound-isolated and electromagnetically shielded measuring chamber. Fig. 3.1b shows sketches of the experimental setup and sequence. The subject is seated comfortably on a chair and remains in an upright position during the experiment. In order to reduce complexity, the hand is fixed on a one DoF *slider* mechanism, i.e. a moving plate on a rail that is orthogonal to the coronal plane. Above the hand is a preloaded *slingshot*, a flexible sheet metal (Fig. 3.1b ①) retained by an electromagnet. An acoustic signal — aired 500 ms before the electromagnet is switched off (Fig. 3.1b ②) — warns the subject, who is prompted to retract the hand and so avoid the impact with the sheet metal (Fig. 3.1b ③).

An innocuous or painful *obstacle* is placed behind the elbow. This thin and flexible metallic panel will not harm a subject accidentally hitting it with the elbow while withdrawing the hand to avoid the slap. The goal for all subjects (Fig. 3.1b ④) is to withdraw the hand in such a way that they can (i) escape the mechanical pain threat by the slingshot mechanism by retracting their elbow and (ii) also avoid collision with the obstacle. For subjects in the *painful* group, an electrical stimulation is released to their elbow when they touch the panel.

3.1.3 Apparatus

A real-time measurement computer was used together with a *National Instrument 9144 EtherCAT chassis* to control and synchronize the slingshot mechanism, a motion tracking system, and an electrical stimulator device. A *Vicon MXT10s* (Vicon Motion Systems Ltd, UK) system with eight infrared cameras tracking positions of passive reflected markers (15 mm diameter) at 500 Hz was used to capture human upper limb motions in Cartesian space. Six *essential* markers were placed on significant anatomical landmarks: *Os metacarpale tertium (Caput metacarpi)*, *Caput ulnae*, *Caput radii*, *Epicondylus lateralis humeri*, *Acromion* and *Fossa jugularis sternalis* as shown in (Fig. 3.2b). Note that the marker on the *Fossa jugularis sternalis* remains unused in this work, but can be employed in e.g. future analysis based on human musculoskeletal models [221].

For the *painful* group of participants, a computer controlled *Single Constant Current Stimulator* of *Dantec™Keypoint® G4 Workstation* (Natus Medical Incorporated, USA) was used to percutaneously stimulate the *Nervus cutaneus brachii posterior*, a sensory branch of the *Nervus radialis*, through a 2-point-bipolar electrode placed three finger widths above the *Humerus coronoid fossa* on the dorsal side of the upper limb. A single burst consisting of ten rectangular pulses with 0.2 ms duration at 300 Hz is applied when the elbow contacts the obstacle, as detected by the experimenter following a visually-unequivocal vibration by the thin metallic panel.

3.1.4 Protocol

Fig. 3.2a shows the protocol sequence. Each subject is asked to sit comfortably on a chair and keep the back in an upright position during the experiment. After motion tracking markers (and also the electrical stimulator for the *painful* group of subjects) are positioned accurately, the hand is fixed to the slider mechanism using straps tightened at the wrist, ring finger and index finger (Fig. 3.2c ①). A calibration procedure is then performed to determine (i) the starting position of the hand and (ii) the distance between the obstacle and the elbow (see Kinematic calibration). Furthermore, (iii) a pain calibration is conducted so that the level of pain from hand slap is normalized across all subjects (see Pain calibration). A complementary calibration protocol is undertaken by the *painful* group of participants in order to ensure a comparable perception level when hitting the obstacle with the elbow as when the hand is slapped (see Pain calibration). Before the experiment started, all subjects conducted two training blocks of 4 trials each to get used to the system and to minimize in-study learning effects (Fig. 3.2a).

3 Arm withdrawal adaption to concurrent pain constraints

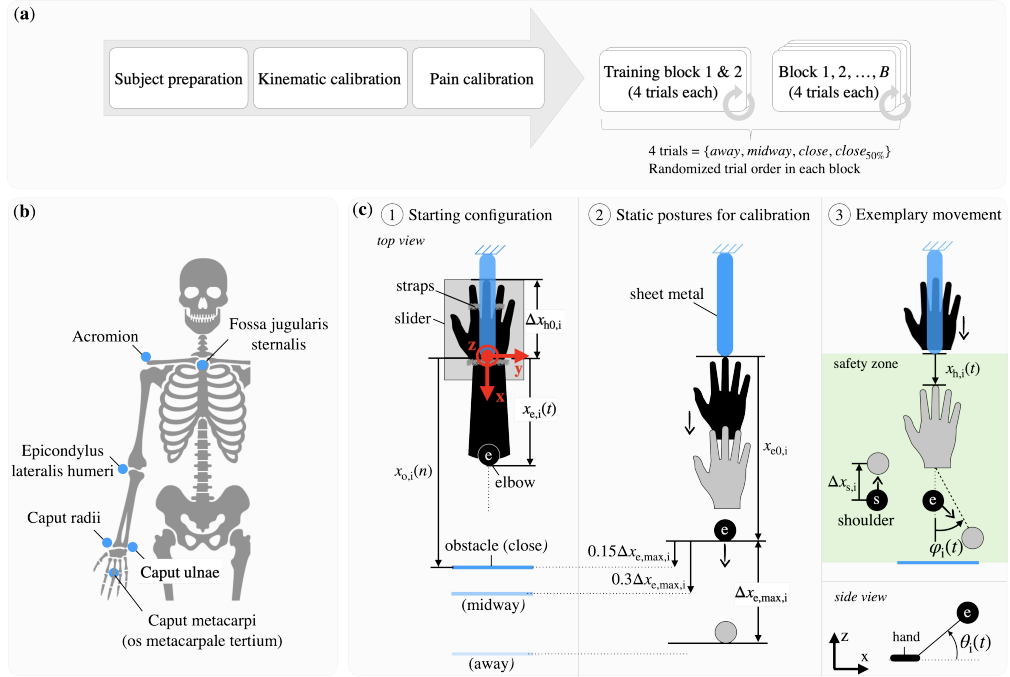


Figure 3.2: (a) Experimental protocol sequence. (b) Marker placement. (c) Measurements for data analysis of subject i . [200]

For the *painful* group of subjects, the experiment consisted of $N = 24$ trials divided in $B = 6$ blocks. For the *innocuous* group it consisted of $N = 16$ trials divided in $B = 4$ blocks (Fig. 3.2a). After having completed the experiments with the *innocuous* group, the total number of trials for the *painful* group was increased as the *innocuous* experiment duration was not altering the quality of data, i.e. did not cause fatigue to subjects nor affected their attention. Each block had 4 trials with conditions $\{away, midway, close, close_{50\%}\}$, where these denominations correspond to the respective distance between the elbow position at the start of the trial and the position of the obstacle (Fig. 3.2c ①). The conditions *close* and *midway* could be used to investigate how subjects deal with a challenging versus moderate difficulty level, relative to the *away* condition without obstacle. In the *close_{50%}* condition, participants were informed that there would be an obstacle in 50% of the cases. The trials in each block were randomized to minimize any bias and in-study time effects (Fig. 3.2a). However, the same random sequence of trials was used for all subjects.

The subjects wear blinkers during the experiment in order to avoid visual feedback of the obstacle. They are informed of which specific condition would be presented before each trial and could (haptically) explore the surroundings at their back and locate the obstacle in order to plan the withdrawal movement. Subjects are then asked to reach the starting position and tell the experimenter when they were ready. Any time during 30s after a vocal “Start” cue, an acoustic signal is emitted, 500 ms after which the slingshot mechanism would attempt to slap the subject’s hand.

3.1.5 Kinematic calibration

For each participant, the starting position of the hand $x_{h,i}(t=0) = \Delta x_{h0,i}$ is selected so that the dorsum can be hit by the sheet metal, adjacent to the wrist strap (Fig. 3.2c ①). To ensure repeatability across trials, the position is marked by a screw on the slider rail. In order to determine the individual obstacle distances *away*, *midway* and *close*, each subject is asked to place the hand in the first position along the longitudinal axis of the sheet metal, such that the sheet metal itself no longer reaches the hand (Fig. 3.2c ②), keeping the elbow aligned to the same axis (i.e. $\varphi_i \approx 0^\circ$). In this static configuration, the position of the elbow $x_{e0,i}$ is measured and $x_{h,i} := 0$ m defined. The maximum elbow displacement $x_{e,max,i} = x_{e0,i} + \Delta x_{e,max,i}$ is then identified by asking the subject to simulate the withdrawal movement, maximizing the elbow travel and maintaining $\varphi_i \approx 0^\circ$.

3.1.6 Pain calibration

Pain underlies sensory-discriminatory, cognitive-evaluative and affective-motivational processes [222], and is by definition subjective [223]. While it is not possible to measure pain objectively [224], efforts have been made to develop reliable methods and tools [225] to estimate it. In this context, a pain calibration procedure was included with the aim to remove high-granular bias in our exploratory study.

In order to normalize the pain intensity caused by the slingshot across all subjects, a verbal *Visual Analogue Scale* (VAS) of 100 mm length is used, graded by *no pain* (0-4 mm), *mild pain* (5-44 mm), *moderate pain* (45-74 mm) and *severe pain* (75-100 mm)[226]. The subject is asked to place the *distal interphalangeal joint* of the middle finger underneath the slingshot. Three paddings of varying thickness $\{2, 3, 4\}$ mm are attached to the sheet metal starting with 4 mm. Then, the slingshot is activated and the subject rates the perceived pain on the VAS. The padding whose VAS value is closest to the middle of the scale is then chosen.

To verify that hitting the obstacle does not harm the subjects, the obstacle is set at $x_{e0,i}$ and each subject is asked to withdraw the elbow and hit the obstacle first slowly and then at increasing speeds. The VAS is again used to confirm that the impacts are harmless.

A complementary calibration is undertaken by the *painful* group of participants in order to ensure comparable perception levels of pain between the electrical stimulation at the elbow and the hand slap. A staircase method [227] is used to calibrate the pain stimulation. First, the sensory threshold (ST) is determined by gradually increasing the current in steps of 0.1 mA (starting from 0 mA) until the subject notices the stimulus. Then, the *pain threshold* (PT) is determined by further increasing the current until the subject perceives the stimulus as painful. To verify the PT, the current is then increased to around 1 mA and gradually decreased afterwards till the subject marks the intensity as innocuous.

In order to relate the pain experienced at the elbow (caused by the *electrical* stimulus) to the one at the hand (caused by a *mechanical* stimulus), the intensity of the electrical

3 Arm withdrawal adaption to concurrent pain constraints

stimulus is then subsequently increased times PT, until the participant reports that the resulting pain perception matches with the one induced by the slingshot mechanism at the hand.

3.2 Measures

The normalized *hand retraction* for each trial is defined as

$$\tilde{x}_{h,\max} := \frac{x_h(t^*)}{|\Delta x_{h0}|}, \quad (3.1)$$

where t^* is the time instant when $x_h(t)$ reaches its maximum retraction during the withdrawal movement (Fig. 3.2c ③). The maximum hand retraction $x_h(t^*)$ is normalized to the individual distance $|\Delta x_{h0}|$. Such distance corresponds to the span of retraction necessary for subjects to exit the slingshot impact range with their hand (Fig. 3.2c ①). This normalization yields an intuitive way to interpret the extent of the hand retraction length. For example, $\tilde{x}_{h,\max} > 1$ means that the hand successfully escaped impact with the slingshot mechanism. In the analysis the maximum velocity $\dot{x}_{h,\max}$ and acceleration $\ddot{x}_{h,\max}$ of hand retraction is also considered.

The *reaction time* is defined as

$$\Delta t_r := t' - t_{\text{beep}}, \quad (3.2)$$

where t_{beep} is the time instant when the acoustic signal starts to ring and t' is the time instant when the Cartesian acceleration of the hand marker *Os metacarpale tertium* (*Caput metacarpi*) reaches 0.1 m/s^2 . This threshold, determined empirically, was introduced to filter out any hand movements taking place prior to the withdrawal action.

Furthermore, the *failure ratio* is defined as

$$f := \frac{N_{\text{failed}}}{N_{\text{total}}} 100\%, \quad (3.3)$$

where $N_{\text{total}}, N_{\text{failed}} \in \mathbb{N}^+$ denote, respectively, the total number of trials and the total number of failed trials within a group $\{\textit{innocuous}, \textit{painful}\}$, across a condition $\{\textit{away}, \textit{midway}, \textit{close}, \textit{close}_{50\%}\}$.

Other measures appearing in the results are the *elbow angles* $\varphi(t^*), \theta(t^*)$, and *Cartesian shoulder positions* (Fig. 3.2c ③)

$$\Delta x_s = x_s(t') - x_s(t^*), \quad (3.4)$$

$$\Delta z_s = z_s(t') - z_s(t^*). \quad (3.5)$$

3.3 Data analysis

The data of recorded measures were analyzed using a linear mixed-effects model [228]

$$r_{ij} = \begin{bmatrix} 1 \\ a_{1,ij} \\ a_{2,ij} \\ a_{1,ij}a_{2,ij} \end{bmatrix}^\top \begin{bmatrix} \alpha_0 \\ \alpha_1 \\ \alpha_2 \\ \alpha_3 \end{bmatrix} + \begin{bmatrix} 1 & a_{1,ij} \end{bmatrix} \begin{bmatrix} \beta_{0,j} \\ \beta_{1,j} \end{bmatrix} + \epsilon_{ij}, \quad (3.6)$$

where subscript $j = 1, \dots, N$ denotes the observation (i.e. one for each trial) for subject i . As fixed effects an intercept, two explanatory variables $a_{1,ij}$ and $a_{2,ij}$, and the interaction $a_{1,ij}a_{2,ij}$ is introduced. Parameter $\beta_{0,j}$ denotes the random effect for the by-subject intercepts and $\beta_{1,j}$ is the random effect for by-subject slopes for the effect of $a_{1,ij}$.

In order to understand the effect of varying *obstacle distance* on the subject's behavior, the model in (3.6) is applied with explanatory variables $a_{1,ij} \in \{away, midway, close\}$ and $a_{2,ij} \in \{innocuous, painful\}$ on maximum hand position $\tilde{x}_{h,max}$ (3.1), $\dot{x}_{h,max}$, $\ddot{x}_{h,max}$, $\varphi(t^*)$, $\theta(t^*)$, Δx_s (3.4), Δz_s (3.5) and reaction time Δt_r (3.2). Pairwise comparisons (paired t-tests) with Bonferroni corrections were performed to compare average measures within each group $\{innocuous, painful\}$ across the different obstacle distance $\{away, midway, close\}$.

In order to understand the effect of varying *obstacle presence uncertainty* on the subject's behavior, the model in (3.6) is applied with explanatory variables $a_{1,ij} \in \{0\%(away), 50\%(close_{50\%}), 100\%(close)\}$ and $a_{2,ij} \in \{innocuous, painful\}$ on maximum hand position $\tilde{x}_{h,max}$ (3.1), $\dot{x}_{h,max}$, $\ddot{x}_{h,max}$, $\varphi(t^*)$, $\theta(t^*)$, Δx_s (3.4), Δz_s (3.5) and reaction time Δt_r (3.2). Pairwise comparisons (paired t-tests) with Bonferroni corrections were performed to compare average measures within each group $\{innocuous, painful\}$ across the different obstacle presence probabilities $\{0\%, 50\%, 100\%\}$.

Following the application of those linear mixed-effects models, in order to understand the effect of varying *obstacle nature*, single t-tests were performed over distances $\{away, midway, close\}$ between groups $\{innocuous, painful\}$ and over probabilities $\{0\%, 50\%, 100\%\}$ between groups $\{innocuous, painful\}$ for values of $\tilde{x}_{h,max}$, $\dot{x}_{h,max}$ and $\ddot{x}_{h,max}$. Bonferroni corrections were performed here as well.

For all linear mixed-effects models, no obvious deviation from homoscedasticity and normality was observed from the inspection of residual plots and the p-values were obtained by likelihood ratio tests of the full model with the effect in question against the model without the effect in question [229]. A 5% significance level was used in all tests.

3.4 Results

3.4.1 Preliminary inspection of data

Fig. 3.3 shows raw data from representative subjects of each group. Visual inspection of trajectories reveals that the hand retracts less when the obstacle gets closer (Fig. 3.3a).

3 Arm withdrawal adaption to concurrent pain constraints

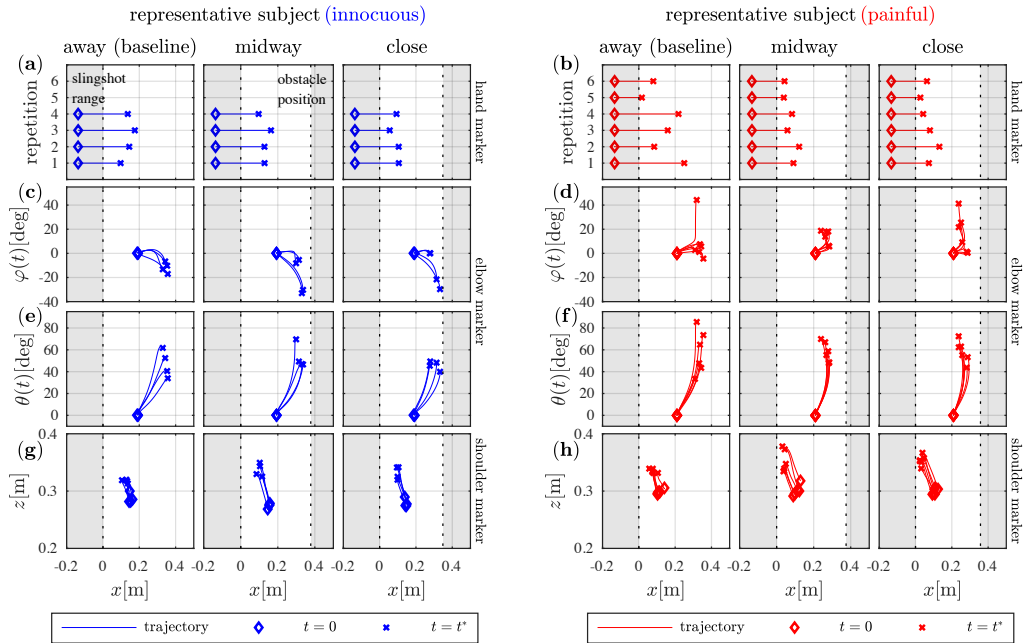


Figure 3.3: Raw data of representative subjects from each group. (a/b) Trajectories of hand marker (x -coordinate) for all trials of one representative subject from each group. (c/d) Lateral elbow displacement $\varphi(t)$ over x -coordinate values of the elbow marker for all trials of one representative subject from each group. (e/f) Upward elbow displacement $\theta(t)$ over x -coordinate values of the elbow marker for all trials of one representative subject from each group. (g/h) Cartesian trajectories of shoulder marker in xz -plane. The definition of $\varphi(t)$, $\theta(t)$ and the right-handed coordinate system are depicted in Fig. 3.2c. [200]

By retracting the hand, subjects bend their elbows sideways to the right of the longitudinal axis of the hand, to the left of or along it (Fig. 3.3c). Reviewing all subjects individually reveals that subjects who bend their elbow to the inside ($\varphi(t) < 0$) retract the hand less, while other subjects opt for longer spans of hand retraction, but bend their elbow to the outside ($\varphi(t) > 0$) and with more displacement. When the obstacle is introduced, the lateral movement of the elbow seems to increase. As the elbow moves sideways during hand retraction, it also shifts upwards (Fig. 3.3e). Such combined movement is more accentuated for the subjects who bend their elbow to the outside (the ones with greater hand retraction and lateral elbow displacement). During the withdrawal action, the shoulder moves upwards and forward (Fig. 3.3g). Comparing the representative subjects from the two groups, the hand seems to retract less when subjects are presented with the painful obstacle, in contrast to the innocuous one (Fig. 3.3a vs. Fig. 3.3b). With respect to the lateral elbow displacement $\varphi(t)$, no systematic differences between the *painful* and *innocuous* groups could be seen (Fig. 3.3c vs. Fig. 3.3d). Upward elbow

displacement $\theta(t)$ versus hand retraction appears to be steeper for the *painful* group (Fig. 3.3e vs. Fig. 3.3f). With respect to the shoulder movement, no remarkable differences could be seen between the *painful* and *innocuous* groups (Fig. 3.3g vs. Fig. 3.3h).

3.4.2 Effect of obstacle distance

Placing an obstacle closer leads to more hits with the obstacle (Tab. 3.1). This shows that the task was challenging enough to represent limit cases. Although more task errors were recorded when the obstacle distance was reduced, the percentage of failures collected in Tab. 3.1 suggests that the task, although challenging, was achievable in most of the occurrences.

condition	obstacle type	f [%]			
		obstacle only	slingshot only	both	sum
away	innocuous	-	0	-	0
	painful	-	1.39	-	1.39
midway	innocuous	9.09	4.55	0	13.64
	painful	2.78	4.17	1.39	8.34
close	innocuous	25.00	2.27	2.27	29.54
	painful	8.33	15.28	0	23.61
close _{50%}	innocuous	6.82 [†]	4.55	0 [†]	11.37 [†]
	painful	5.56 [†]	15.28	0 [†]	20.84 [†]

[†]Note that, in the *close*_{50%} condition, errors were only possible when the obstacle was present.

Table 3.1: Failure ratios f (3.3). [200]

Results exhibit no significant differences for reaction times (Tab. 3.2) among the *away*, *midway* and *close* conditions tested.

	innocuous	painful
away	214.2 ± 20.8 ms	214.8 ± 40.9 ms
midway	224.4 ± 30.9 ms	218.9 ± 39.2 ms
close	210.9 ± 25.8 ms	226.8 ± 53.6 ms
close _{50%}	209.3 ± 22.2 ms	229.4 ± 51.8 ms

Table 3.2: Reaction time Δt_r (3.2). [200]

The hand retracts less when the obstacle gets closer, as showed by the significant differences of $\tilde{x}_{h,\max}$ (Fig. 3.4a). The linear mixed-effects analysis showed significant

3 Arm withdrawal adaption to concurrent pain constraints

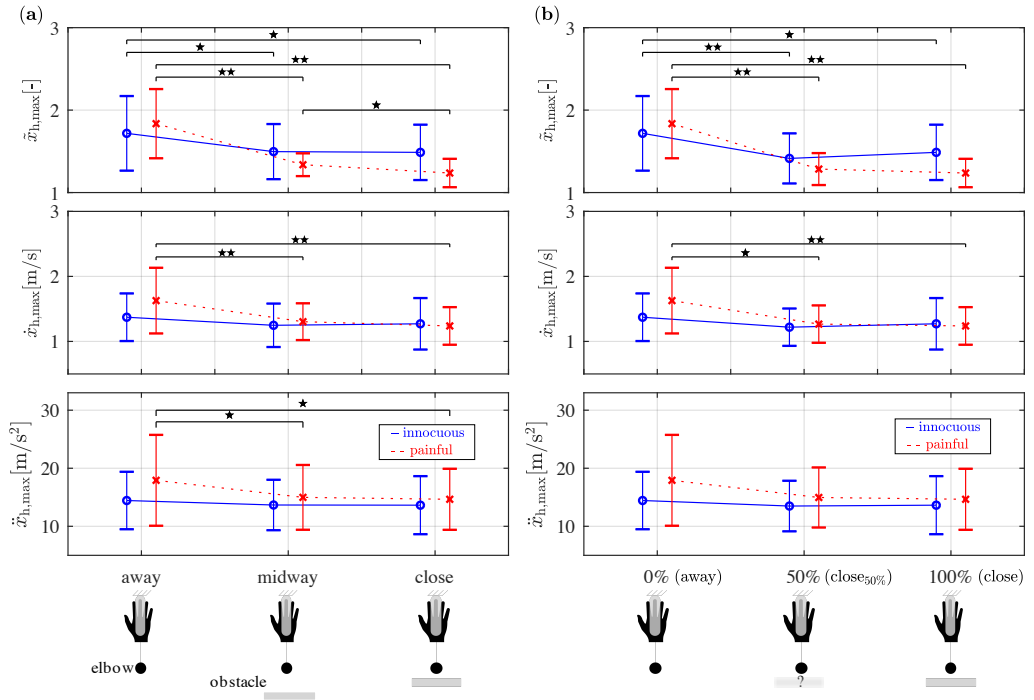


Figure 3.4: (a) Maximum hand retraction $\tilde{x}_{h,max}$ (3.1), $\dot{x}_{h,max}$ and $\ddot{x}_{h,max}$ over varying obstacle distances $\{away, midway, close\}$, for both *innocuous* (blue) and *painful* (red) groups. The closer the wall, the less the hand retracts. This effect is more remarkable for obstacle type *painful* (red). Only when the painful obstacle is presented (red), subjects slow down speed and decrease acceleration of hand retraction. $\star = p < 0.05$, $\star\star = p < 0.01$; corrected. (b) Maximum hand retraction $\tilde{x}_{h,max}$, $\dot{x}_{h,max}$ and $\ddot{x}_{h,max}$ over varying probabilities of obstacle presence $\{0\%, 50\%, 100\%\}$, for both *innocuous* (blue) and *painful* (red) groups. Probabilities were made explicit to subjects prior to the start of each trial. In the trials when the obstacle was present, it was positioned in the *close* configuration. No differences were found between the 50% (i.e. condition *close_{50%}*, when the obstacle was present in half of the trials) and 100% (i.e. *close* condition) probabilities. $\star = p < 0.05$, $\star\star = p < 0.01$; corrected. [200]

effects of the interaction between distances $\{away, midway, close\}$ and obstacle types $\{innocuous, painful\}$, on $\tilde{x}_{h,max}$ ($\chi^2(1) = 5.70, p < 0.05$), $\dot{x}_{h,max}$ ($\chi^2(1) = 7.04, p < 0.01$), and $\ddot{x}_{h,max}$ ($\chi^2(1) = 4.96, p < 0.05$). Paired t-tests applied on the mean values of $\tilde{x}_{h,max}$, $\dot{x}_{h,max}$ and $\ddot{x}_{h,max}$ revealed significant differences (Fig. 3.4a) of $\tilde{x}_{h,max}$ for the obstacle type *innocuous*: $\tilde{x}_{h,max}$ decreases from condition *away* to *midway* ($p < 0.05$), and also from *away* to *close* ($p < 0.05$). No significant differences were found on $\dot{x}_{h,max}$ and $\ddot{x}_{h,max}$. Within group *painful* paired t-tests revealed significant differences (Fig. 3.4a): $\tilde{x}_{h,max}$ decreases from condition *away* to *midway* ($p < 0.01$), from *away* to *close* ($p < 0.01$), and from *midway* to *close* ($p < 0.05$). Significant differences were found concerning $\dot{x}_{h,max}$ that decreases from condition *away* to *midway* ($p < 0.01$), and from *away* to

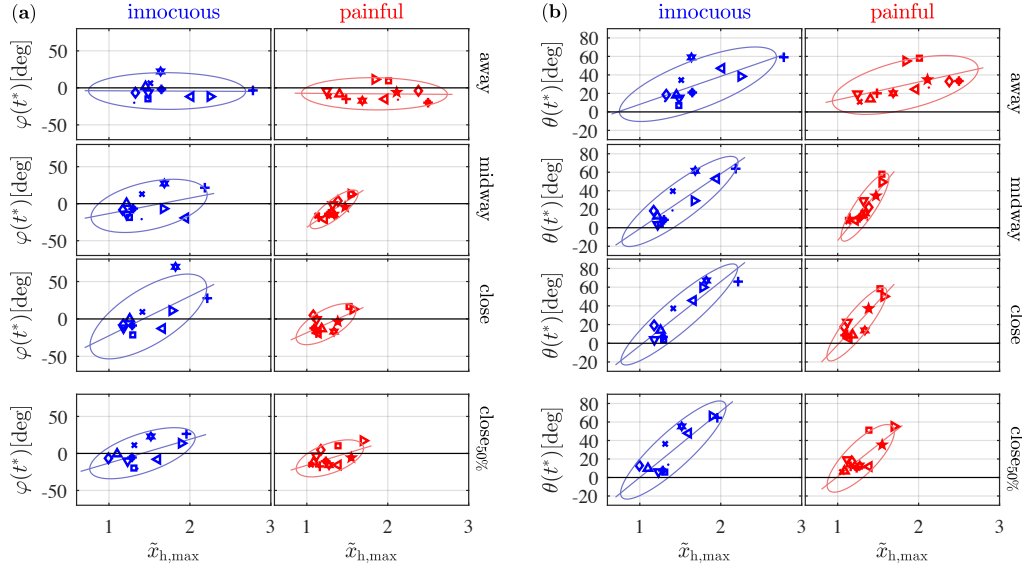


Figure 3.5: The figure shows values of sideways displacement $\varphi(t^*)$ of the elbow (a) and values of upward displacement $\theta(t^*)$ of the elbow (b) at the point of maximum hand retraction $\tilde{x}_{h,\max}$ (3.1). Each symbol represents the mean of such dyad for one individual subject. $\varphi(t^*)$ distributes evenly along the axis of hand retraction, and subjects seem to stick to one specific strategy (left, right or straight) over the different conditions, with only one exception (see \blacktriangleright for innocuous). Ovals denote confidence ellipses with confidence interval 90%. Introducing a painful obstacle (red) reduces the area of the confidence ellipses. Solid lines denote the fitted linear models. Their slope increases as obstacles are introduced. [200]

3 Arm withdrawal adaption to concurrent pain constraints

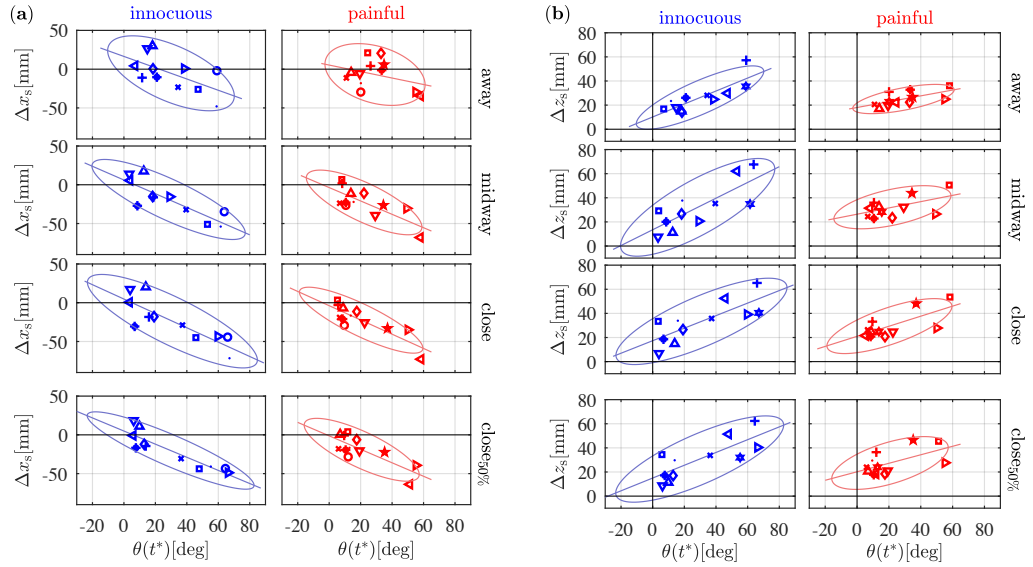


Figure 3.6: The figure shows mean values of shoulder displacement in the x -direction Δx_s (a) and in the z -direction Δz_s (b) at the time t^* over the elbow upward displacement $\theta(t^*)$. Each symbol represents the mean of such dyad for one individual subject. Ovals denote confidence ellipses with confidence interval 90 %. Introducing a painful obstacle (red) reduces the area of the confidence ellipses. Solid lines denote the fitted linear models. In both cases, slopes do not change over conditions. [200]

close ($p < 0.01$). Furthermore, significant differences were found concerning $\ddot{x}_{h,\max}$ that decreases from condition *away* to *midway* ($p < 0.05$), and from *away* to *close* ($p < 0.05$).

The linear mixed-effects analysis showed no significant differences for $\varphi(t^*)$ and $\theta(t^*)$. However, values of mean $\tilde{x}_{h,\max}$ for each subject, at all conditions, were visually inspected by plotting them with $\varphi(t^*)$ and $\theta(t^*)$, respectively (Fig. 3.5). Different symbols were used for individual subjects to enable tracking of any change in motor behavior, as the conditions of the experiment vary. By retracting the hand, subjects bend their elbow sideways (Fig. 3.5a), either to the right of, to the left of, or along the longitudinal axis of the hand, in any case sticking to one of such strategies over the different distance conditions they are presented with. The linear regression of Fig. 3.5a (solid lines) exhibit slopes steeper as the obstacle distance decreases, indicating that a certain value of hand retraction corresponds to a bigger lateral displacement of the elbow (see Tab. 3.3 for the R^2 and slope values of linear regression). This behavior is coherent with task requirements, as subjects tend to keep away from collision by bending the elbow more when the obstacle is closer. The same tendency is observed for $\theta(t^*)$. As the elbow moves sideways during hand retraction, it also shifts upwards (Fig. 3.5b), with such effect becoming more emphasized as the obstacle gets closer.

To further analyze the kinematic chain of the upper limb, the shoulder front and upwards movements were displayed against the values representing the elbow upward movements. Although the linear mixed-effects analysis showed no significant differences

condition	Fig. 3.5a				Fig. 3.5b			
	innocuous		painful		innocuous		painful	
	R^2	slope	R^2	slope	R^2	slope	R^2	slope
away	0.00	-0.48	0.00	-0.81	0.53	30.2	0.30	19.2
midway	0.18	21.0	0.67	71.6	0.76	59.3	0.74	106.9
close	0.45	53.0	0.43	48.4	0.84	68.5	0.76	92.7
close _{50%}	0.37	32.2	0.30	32.9	0.77	71.4	0.62	69.0

condition	Fig. 3.6a				Fig. 3.6b			
	innocuous		painful		innocuous		painful	
	R^2	slope	R^2	slope	R^2	slope	R^2	slope
away	0.37	-0.73	0.11	-0.42	0.68	0.54	0.40	0.24
midway	0.70	-0.88	0.58	-0.86	0.62	0.65	0.29	0.26
close	0.69	-0.93	0.72	-0.92	0.62	0.52	0.52	0.44
close _{50%}	0.81	-0.85	0.61	-0.87	0.62	0.53	0.35	0.35

Table 3.3: Results of linear regression in Fig 3.5 and Fig 3.6. [200]

for Δx_s and Δz_s , one can see in Fig. 3.6a and Fig. 3.6b that the higher $\theta(t^*)$, the more forward the shoulder moves. Similarly, the higher $\theta(t^*)$, the more upwards the shoulder moves.

3.4.3 Effect of obstacle presence uncertainty

While no significant differences were found with the analysis of reaction times (Tab. 3.2), the results of Tab. 3.1 reveal that the failure ratio in the *close*_{50%} condition matches the one recorded for the *close* condition. While subjects consistently escape impact from the slingshot stimulation at their hand when the *away* condition is presented, more errors occur when they know that there is an obstacle behind them (*close* condition), with the ratio of failure registered for the *close*_{50%} condition comparable to the one in the *close* condition. The same reasoning cannot be applied fully to study the failure ratios regarding the collisions with the obstacle, as no obstacle is present by definition in the *away* condition (0%), and the obstacle is present only in half of the trials in the *close*_{50%} condition. However, the number of errors recorded for such 50% of trials when the obstacle was in place suggests that, also in this regard, the participants of our experiment responded to the *close*_{50%} condition similarly to how they did when they were certain about the presence of the obstacle behind them.

The conservative approach by humans to deal with uncertainty under our experimental scenario is also confirmed by the extent and velocity of hand retraction (i.e. $\tilde{x}_{h,\max}$ and $\dot{x}_{h,\max}$), as can be seen in Fig. 3.4b. The linear mixed-effects analysis revealed significant effects of the interaction between probabilities {0%, 50%, 100%} and obstacle

3 Arm withdrawal adaption to concurrent pain constraints

types $\{\textit{innocuous}, \textit{painful}\}$ on $\tilde{x}_{h,\max}$ ($\chi^2(1) = 3.89, p < 0.05$) and $\dot{x}_{h,\max}$ ($\chi^2(1) = 4.59, p < 0.05$). Paired t-tests revealed significant differences on $\tilde{x}_{h,\max}$ for the obstacle type *innocuous*: $\tilde{x}_{h,\max}$ decreases from condition 0% to 100% ($p < 0.05$) and from 0% to 50% ($p < 0.01$). No significant differences were found on $\dot{x}_{h,\max}$. For the *painful* group, significant differences were found on $\tilde{x}_{h,\max}$, that decreases from condition 0% to 50% ($p < 0.01$) and from condition 0% to 100% ($p < 0.01$). Significant differences were found concerning $\dot{x}_{h,\max}$ that decreases from condition 0% to 50% ($p < 0.05$) and from condition 0% to 100% ($p < 0.01$). This means that no significant difference divides the *close*_{50%} and the *close* (100%) condition, while significant difference was indeed found between these two conditions and the *away* (0%) condition.

The linear mixed-effects analysis revealed no significant differences on $\varphi(t^*)$, $\theta(t^*)$, Δx_s and Δz_s . However, the distribution of data points in Fig. 3.5a and Fig. 3.5b reveal that both sideways displacement of the elbow and its upward movement at the point of maximum hand retraction $\tilde{x}_{h,\max}$, for condition *close*_{50%}, are comparable with condition *close* (100%), whereas they are considerably different from the values of condition *away* (0%).

Additionally, while the shoulder front and upward movements in relation to the upward movement of the elbow (Fig. 3.6a and Fig. 3.6b) did not reveal remarkable differences across the experimental conditions, the slopes of the linear fitted models describing the relationship between values of $\varphi(t^*)$ (lateral elbow displacement) and $\theta(t^*)$ (upward elbow displacement) with hand retraction length (Fig. 3.5a and Fig. 3.5b) show that condition *close*_{50%} is, also in such regard, comparable with condition *close* (100%).

3.4.4 Effect of obstacle nature (innocuous vs. painful)

No significant differences in reaction time were found between the two groups (Tab. 3.2). Examination of Tab. 3.2 reveals that, when the obstacle was placed in the position corresponding to the *midway* condition, subjects collided their elbow more often when the obstacle itself was innocuous (*innocuous* 9.09% vs *painful* 2.78%). The same difference also holds true for the more challenging *close* condition (*innocuous* 25.00% vs *painful* 8.33%).

Analysis of the values of failure ratio for the errors at the hand level (caused by the hand not retracting back enough to avoid impact with the slingshot mechanism) shows that, while the number of failures is comparable in the position corresponding to the *midway* condition (*innocuous* 4.55% vs *painful* 4.17%), such balance shifts when the obstacle is placed in the *close* condition (*innocuous* 2.27% vs *painful* 15.28%). Note that the pain experience elicited by the slingshot mechanism and obstacle were calibrated prior to the start of the experiment to generate comparable perception of pain. Therefore, although not consistently successful, subjects aimed to plan and execute their withdrawal action in a way such as to escape both painful sources. Only in a very small number of cases, subjects made errors at both hand and elbow levels (see last column of Tab. 3.1).

Another effect of placing a painful obstacle can be observed by the analysis of the extent, velocity and acceleration of hand retraction (i.e. $\tilde{x}_{h,\max}$, $\dot{x}_{h,\max}$ and $\ddot{x}_{h,\max}$), as it can be seen in Fig. 3.4a and Fig. 3.4b. While the direct comparison — between subjects

who were presented with the painful versus the ones who encountered the innocuous obstacle — revealed no significant differences, values of $\tilde{x}_{h,\max}$ show that the hand retracts significantly less when subjects are presented with the painful obstacle, in comparison to the innocuous one. Furthermore, only the group of participants who performed the task in the presence of the painful obstacle shows significant decrease of $\dot{x}_{h,\max}$ and $\ddot{x}_{h,\max}$ as the obstacle gets closer (see section Effect of obstacle distance).

The linear mixed-effects analysis showed no significant differences for $\varphi(t^*)$, $\theta(t^*)$, Δx_s and Δz_s . However, the distribution of data points in Fig. 3.5a and Fig. 3.5b reveal that introducing a painful obstacle reduces the area of the confidence ellipses that are indicative for the variance of both sideways displacement of the elbow $\varphi(t^*)$ and its upward movement $\theta(t^*)$ at the point of maximum hand retraction $\tilde{x}_{h,\max}$. Such effect is likely to be caused by the lower values of hand retraction in participants who were presented with the painful obstacle, as lower values of $\tilde{x}_{h,\max}$ also require lower displacement of the elbow to succeed in the task. When the painful versus the innocuous obstacle is present, also the areas of the confidence ellipses encapsulating values of front and upward movement of the shoulder at the point t^* of elbow upward displacement is systematically smaller (Fig. 3.6a and Fig. 3.6b). This effect is again likely due to the lower values of hand retraction in subjects belonging to the *painful* group, as lower values of $\tilde{x}_{h,\max}$ require lower displacement of the elbow, and thereby less prominent movement of the shoulder to accommodate the overall withdrawal action. Interestingly, smaller variance was recorded in the *away* condition too, although this experimental condition did not differ between the *painful* and *innocuous* group, as no obstacle was present for either group. Such smaller variance could derive from learning effects, i.e. subjects from the *painful* group may have retained — in the *away* trials — part of the motor behavior developed in the trials when the painful obstacle was or could be present.

Ultimately, while analysis of the linear relationship between values of $\varphi(t^*)$ (lateral elbow displacement) with hand retraction length (Fig. 3.5a), as well as of shoulder front and upward movements in relation to the upward movement of the elbow (Fig. 3.6a and Fig. 3.6b) do not reveal systematic differences between the *painful* and *innocuous* groups, it appears for $\theta(t^*)$ (upward elbow displacement) (Fig. 3.5b) that slopes are steeper in the *painful* group.

3.5 Discussion

Pain signals immediate threats [230] and triggers relevant motor responses [231], including the ones elicited by the withdrawal reflex [108]. While the withdrawal reflex [201] — defined as an automatic retraction of an extremity from a noxious stimulus such as heat or pain — was extensively studied, little or no literature has investigated withdrawal actions that start even prior to any physical stimulation, for instance when we visually spot or hear a threatening event. This exploratory study investigate the kinematic characteristics of withdrawal movements of the human upper limb that are triggered by a threatening source at hand level. The experimental task further included an obstacle behind the subject’s arm, positioned at different distances along the direction of with-

drawal. Results show that humans do not simply regulate the retraction of the hand alone to avoid both the original threatening source and the collision with the obstacle, but they make use of the degrees of freedom of their upper limb (which can be considered as 12 DoF serial kinematics) [221, 55] — in a highly coordinated manner. Specifically, in the presence of an obstacle placed behind us, not only do we stop our rapid withdrawal action earlier than what we would do in the absence of the obstacle, but we also complement this action by bending the elbow sideways, keeping it away from collision. While some participants bend their elbow to the inside and retract the hand less, others opt for longer spans of hand retraction, but bend their elbow to the outside, where they can count on a more abundant range of possible displacement. Therefore, different subjects use distinct motor strategies [232, 233]. Subjects tend to stick to bending their elbow either to the right of, to the left of, or along the longitudinal axis of the hand, across trials and conditions. To accommodate such withdrawal action, we raise the elbow and move the shoulder forward and upwards — with such coordinated movement more accentuated for the subjects who bend their elbow to the outside (i.e. with greater hand retraction and lateral elbow displacement). The closer the obstacle, the more discernible this behavior appears. It is likely that the overall withdrawal movement originates from a highly coordinated action between hand, elbow and shoulder [234], although the shoulder movement could also be due to the physical constraint placed at hand level (i.e. its fixation to the slider). Another interesting interpretation is that the subjects may utilize the mechanical coupling of the upper limb’s joints to accelerate the hand, specifically by using the inertia of the shoulder, whereby the shoulder is “thrown” forward and upwards in order to facilitate acceleration of the hand, to keep it away from the slingshot range.

Retraction movements have been studied from the traditional perspective of motor control, with sensory information together with self-intention leading to a motor action via a planning process [68]. The overall success demonstrated by our participants to deal with a task that requires a prompt and explosive reaction shows how such complex action needs to be planned in advance. While the planning phase is fundamental in similar tasks, continuously shaping the withdrawal trajectory during the task is also crucial, with results from a study that investigated object throwing [235] suggesting that creating a timing window for determining tolerance for variability, and consequently accuracy, requires shaping the arm trajectory not only before, but even after the critical release moment.

To investigate whether and how the withdrawal strategy changes when humans are subject to uncertainty, a condition where participants were informed that the obstacle may or may not be present behind them was introduced. They were made explicitly aware that the chance corresponded to a 50 % probability. Specifically, results were examined to ascertain whether humans adopt a conservative strategy and plan the movement according to the worst-case scenario (i.e. *close* condition), or they rather take risks and behave more similarly to the *away* condition, in the attempt to save the mental workload required for planning a more constrained, demanding movement. Mental workload was recently defined to include perceptual, motor and also cognitive components [236], with anticipation of cognitive effort relying on the cortico-limbic network via activation in the anterior cingulate cortex and the striatum [237]. In particular, results

were expected to reveal a relatively more conservative strategy for participants who were possibly presented with a painful obstacle behind them. Anticipation of pain, i.e. the activation of mechanisms to prevent future harm by learning to recognize signals of impending pain [238] prepares the organism for a potentially painful outcome, as pain can be suppressed or enhanced by factors such as immediate threat and predicted reward [239, 240]. While these physiological studies have explored the brain neural systems underlying pain, and motivation, the experiment of this present work has investigated the effect of pain anticipation on subjects' decision-making from a behavioral standpoint. In this, our findings reveal that humans always adopt a conservative strategy and plan the movement according to the worst-case scenario, regardless of the painful or innocuous nature of the obstacle. In contrast, a previous study [241] investigating the effect of pain probability on human motor behavior during an exploration task showed that the explicit probability that subjects may encounter an object does not influence their approach speed when the object is innocuous, whereas the probability of encountering a noxious object decreases their approach velocity. Crucially, it could be observed that the speed of the reaching movement decreased gradually as the probability that the participants could encounter a noxious object increased, in a trade-off between safety and time to complete the task. The difference between the results from these two studies could be explained by the intrinsic task motivation in our present experiment, where the explicit goal to avoid impact with the obstacle could have by far exceeded our subjects' will to modulate their motor behavior efficiently. Furthermore, although subjects could plan the movement in advance, the impulsive and challenging nature of the motor task itself could have allowed little cognitive resources for developing a trade-off like behavior.

Such a conservative approach was also likely to prevent participants from making more errors under the condition of uncertainty, especially when the obstacle behind was painful. While pain anticipation is generally associated with stress and correlates with the degree of uncertainty [242] — and motor performance is known to depend on the level of stress according to an inverse-U relationship [243] — the same error ratio was recorded between the uncertain and the certain *close* condition.

The effect of introducing a painful obstacle was systematically studied by assigning the participants of our experiment to two different groups, one of which executed the experiment with an innocuous obstacle and the other one with a painful one, as in the latter case collision triggered electrical stimulation. This painful event was meant to introduce an additional layer of motivation. While subjects from both groups *innocuous* and *painful* were asked to avoid impact with the obstacle behind them (i.e. they were motivated by the definition of the task goal itself), the group *painful* was additionally subject to the motivation of avoiding the electrical pain. It was found that, when the impact with the obstacle is painful, success rate at elbow level increases. This is achieved by controlling retraction more carefully, i.e. decreasing velocity and acceleration of hand retraction. Furthermore, we modulate the elbow movement (i.e. we raise the elbow more for the same extent of hand retraction) such that it is as far away as possible from the obstacle. However, such strategy increases the chance to fail at hand level. The increased failure ratio at the level of the hand for the *close* condition — only for the group subject to the painful obstacle — is likely to be due to the attempt by participants to minimize

3 Arm withdrawal adaption to concurrent pain constraints

hand retraction, thus avoiding collision with the painful obstacle. This strategy resulted in over-minimization of hand retraction, thereby exposing them to the impact with the slingshot mechanism.

These results indicate that, in contrast to what it could be concluded by observing group *innocuous* alone, the twofold objective of avoiding both hand- and elbow-level collisions could not be decoupled in the present task. Therefore, it is unlikely that a subset of joints and movement range were primarily responsible for the completion of one and the other goal, as is used to control complex robotic systems [244, 245]. Reducing the number of elbow collisions at the cost of hand collisions could underlie hierarchical processes [246], on the basis of which participants switched from one motor strategy to another, given the perceived consequence of the immediate threats (i.e. pain at the hand versus elbow). Although the neural correlates of pain and its effect on motor behaviour under the scenarios presented to our subjects can only be reliably identified with purposely designed versions of our experiment, literature suggests that neural control of movement of higher vertebrates is organized into a distributed set of structures that are both anatomically and functionally hierarchical [246]. Withdrawal from noxious threats could be mainly driven by low-level controllers that function autonomously, whereas the switch from one strategy to another could be regulated by higher-level control layers [247, 248], and mediated by the activity of sub-cortical structures such as the basal ganglia, which have been proposed as motor program selectors among different modes of coordinated behavior [249].

In summary, humans — when aware of the incoming threat — plan the retraction movement and make use of the degrees of freedom of their upper limb in a highly coordinated manner, adopting a conservative approach. Furthermore, introducing pain at the elbow level as an extra layer of motivation does modify behavior. Specifically, the tendency by subjects to reduce elbow collisions at the cost of hand collisions reveals our inability to decouple the motor task, and underlies hierarchical processes. Such results further reveal how humans prevent damage, pain and injury [231, 241], adding to our fundamental understanding of motor control.

First Law

A robot may not injure a human being or, through inaction, allow a human being to come to harm.

Second Law

A robot must obey the orders given it by human beings except where such orders would conflict with the First Law.

Third Law

A robot must protect its own existence as long as such protection does not conflict with the First or Second Law.

— Three Laws of Robotics, Isaac Asimov, *Runaround*, 1950 [250].

Part II

Protective robot reflexes

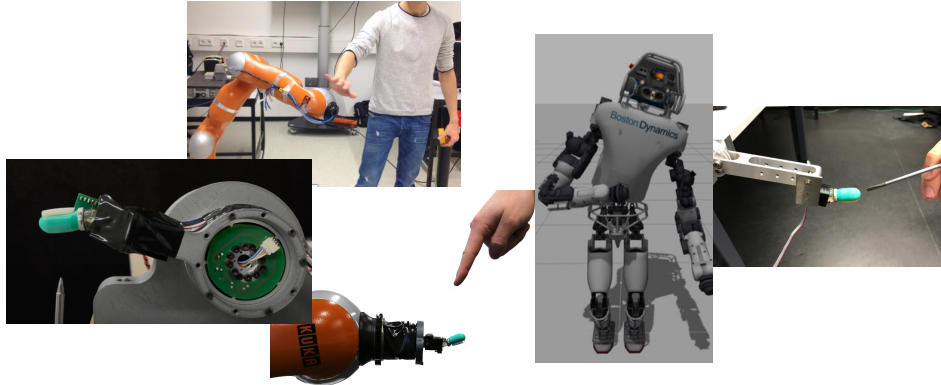


Figure 3.7: Impressions from the work carried out in Part II.

Part II presents protective robot reflexes relating to research questions Q3 and Q4. First, the foundations of soft robot control are summarized in Chapter 4 (which is part of the publication in [251]). Chapter 5 introduces the artificial robot nervous system, which is a human-inspired generalized reflex framework for soft robots. The content of this chapter was published in [251, 252, 253]. Chapter 3 presents then superhuman finger reflexes, which is part of the publication in [199]. All three chapters are briefly summarized below, while Fig. 3.7 shows some impressions from these works.

Chapter 4: Foundations of soft robotics control This chapter provides an overview of the fundamentals of soft robotics control in the context of this thesis. This includes rigid-robot dynamics, joint-level impedance control and a momentum observer.

Chapter 5: Artificial robot nervous system (Q3) This work introduces the concept of an artificial Robot Nervous System (aRNS) as a novel way of unifying multi-modal physical stimuli sensation with robot pain-reflex movements. This work focus on the formalization of robot pain, based on insights from human pain research, as an interpretation of tactile sensation. Specifically, pain signals are used to adapt the equilibrium position, stiffness, and feed-forward torque of a pain-based impedance controller. The schemes are experimentally validated with the KUKA LWR4+ for simulated and physical collisions using the BioTac sensor.

Chapter 6: Superhuman robot reflexes (Q4) This work introduces novel human-inspired robot reflex algorithms based on the aRNS framework and evaluates them with a custom-developed robot finger testbed. While the human remained superior in temperature reaction, touch reflex performance was superhuman with an unconventional configuration of proprioceptive forces and link segment acceleration. It also shows that the traditional tactile sensing or proprioceptive arrangements are suboptimal, though having the potential to be superhuman.

4 Foundations of soft robotics control

This chapter outlines the basics of soft robotics control concerning this thesis. Sec. 4.1 describes the robot dynamics, Sec. 4.2 a joint impedance controller, and Sec. 4.3 a momentum observer. Extended methods, such as the floating-base dynamics model, are discussed in the following chapters.

4.1 Rigid body dynamics

The dynamics an n -DoF serial chain rigid robot in contact can be described in Lagrangian form by

$$\mathbf{M}(\mathbf{q})\ddot{\mathbf{q}} + \mathbf{C}(\mathbf{q}, \dot{\mathbf{q}})\dot{\mathbf{q}} + \mathbf{g}(\mathbf{q}) = \boldsymbol{\tau} - \boldsymbol{\tau}_f + \boldsymbol{\tau}_{\text{ext}}, \quad (4.1)$$

where \mathbf{q} , $\dot{\mathbf{q}}$, and $\ddot{\mathbf{q}}$ denote joint angle, velocity and acceleration, respectively. Furthermore, $\boldsymbol{\tau} \in \mathbb{R}^n$ denotes the actuator torques, $\boldsymbol{\tau}_f \in \mathbb{R}^n$ denote the friction torques, $\mathbf{M}(\mathbf{q}) \in \mathbb{R}^{n \times n}$ is the symmetric joint inertia matrix, $\mathbf{C}(\mathbf{q}, \dot{\mathbf{q}}) \in \mathbb{R}^{n \times n}$ the Coriolis and centrifugal matrix, $\mathbf{g}(\mathbf{q}) \in \mathbb{R}^n$ the gravity vector, and $\boldsymbol{\tau}_{\text{ext}}$ the external joint torques. Let us consider a single-area contact with associated contact Jacobian matrix $\mathbf{J}_c(\mathbf{q})$. This maps the physically acting contact wrench $\mathcal{F}_{\text{ext}} \in \mathbb{R}^6$, which is caused by the local compression and tensile stress distribution, into the respective external joint torques via

$$\boldsymbol{\tau}_{\text{ext}} = \mathbf{J}_c^\top(\mathbf{q})\mathcal{F}_{\text{ext}} = \mathbf{J}_c^\top(\mathbf{q}) \begin{bmatrix} \mathbf{f}_{\text{ext}} \\ \mathbf{m}_{\text{ext}} \end{bmatrix} \quad (4.2)$$

Throughout Part II, the unit collision direction \mathbf{u}_c of \mathcal{F}_{ext} and \mathbf{J}_c is assumed to be known. In general this information could be derived from various sources such as e.g. proprioceptive information or suitable tactile sensors.

4.2 Joint impedance control

A joint-level impedance controller can be written as

$$\boldsymbol{\tau}_d = \mathbf{K}_d(\mathbf{q}_d - \mathbf{q}) + \mathbf{D}(\mathbf{q})(\dot{\mathbf{q}}_d - \dot{\mathbf{q}}) + \boldsymbol{\tau}_g(\mathbf{q}), \quad (4.3)$$

where $\mathbf{K}_d \in \mathbb{R}^{n \times n}$, $\mathbf{q}_d \in \mathbb{R}^n$, and $\dot{\mathbf{q}}_d \in \mathbb{R}^n$ are the desired closed-loop stiffness and the desired equilibrium position. The vector $\boldsymbol{\tau}_g \in \mathbb{R}^n$ denotes the gravity compensation torque and $\mathbf{D} \in \mathbb{R}^{n \times n}$ the configuration dependent joint damping matrix

$$\mathbf{D}(\mathbf{q}) = \mathbf{A}(\mathbf{q})\mathbf{D}_\xi\mathbf{K}_{d1} + \mathbf{K}_{d1}\mathbf{D}_\xi\mathbf{A}(\mathbf{q}),$$

where $\mathbf{D}_\xi = \text{diag}\left(\frac{1}{\sqrt{2}}\right) \in \mathbb{R}^{n \times n}$ is the desired joint damping ratio matrix. According to [254], $\mathbf{A}(\mathbf{q})$ and \mathbf{K}_{d1} are defined by $\mathbf{A}(\mathbf{q})\mathbf{A}(\mathbf{q}) = \mathbf{M}(\mathbf{q})$ and $\mathbf{K}_{d1}\mathbf{K}_{d1} = \mathbf{K}_d$.

4.3 Momentum observer

The goal is to derive an estimate $\hat{\boldsymbol{\tau}}_{\text{ext}} \in \mathbb{R}^n$ of $\boldsymbol{\tau}_{\text{ext}}$. To achieve this, the well-known momentum observer in [136] can be deployed, which can be written as

$$\hat{\boldsymbol{\tau}}_{\text{ext}} = \mathbf{K}_O \left(\int_0^t (\boldsymbol{\tau} - \hat{\boldsymbol{\tau}}_g - \hat{\boldsymbol{\tau}}_f - \hat{\boldsymbol{\tau}}_{\text{ext}}) dt^* - \mathbf{M}(\mathbf{q})\dot{\mathbf{q}} \right), \quad (4.4)$$

where $\mathbf{K}_O = \text{diag}\{k_{O,i}\} > \mathbf{0}$ is the observer gain. The $\hat{\square}$ denotes the estimate of the respective terms.

5 Artificial robot nervous system

Physical human-robot interaction (pHRI) has become an increasingly major discipline in robotics research. With regard to human safety, considerable research was carried out in [255], [256] and the results reached real-world applications and international standards. However, little effort was undertaken to ensure the robot's own safety via appropriate controls, and a systematic approach is still missing. For this, a robot needs to be able to detect and classify unforeseen physical states and disturbances, rate the potential damage they may cause to it, and initiate appropriate countermeasures, i.e., reflexes. In turn, enhanced robot reflexes may improve human safety in case of human-robot collisions. In order to tackle this demanding requirement, the human antitype serves as inspiration, meaning that human pain-reflex movements are used for designing according to robot pain sensation models and reaction controls.

5.1 Concept

In general, the schematic concept of a collision between any suitably controlled (via the desired torque τ_d) robot and a collision object (mass m_c , local radius r_c) can be described by its corresponding contact dynamics, see Fig. 5.1. In generalized coordinates, the contact dynamics between a robot arm and a colliding object with state \mathbf{x}_c and its derivative $\dot{\mathbf{x}}_c$ are determined by the robot joint configuration \mathbf{q} , the joint velocity $\dot{\mathbf{q}}$, and the external torque vector $\boldsymbol{\tau}_{ext}$. This torque is caused by the contact wrench \mathcal{F}_c or the stress σ_c (single point contact) acting on the collision object and the robot, respectively.

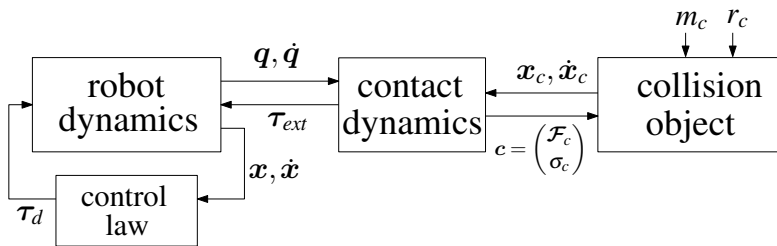


Figure 5.1: Dynamics of a collision between a controlled robot and a collision object. ©2016 IEEE [251]

In order to rate potentially painful collisions and activate proper pain-reflexes, using information about $\boldsymbol{\tau}_{ext}$ only may not be sufficient. Humans are known to utilize further information, e.g., in terms of penetration depth δ or stress, into their controls, using the multitude of information provided by the skin, and not only from their proprioceptive

torque measurement via the *Golgi tendon organs*. In this work, the goal is to enhance robots with similar capabilities by introducing the concept of an *artificial Robot Nervous System* that the HNS inspires. It enables a robot to not only sense but also to interpret and react to “painful” collisions, see Fig. 5.2. The aRNS can be subdivided into four major components: the *nervous robot-tissue*, the *spiking model*, the *interpretation* layer of generated spiking signals, and the *motor control law*. In the following, each component is separately elucidated, while the proposed *control laws* are introduced in Sec. 5.5.

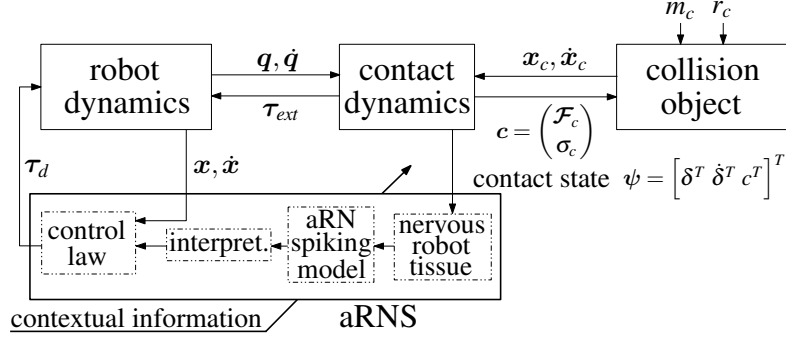


Figure 5.2: Collision between a controlled robot and a collision object including the aRNS.
© 2016 IEEE [251]

5.2 Virtual Nervous Robot-Tissue

A hypothetical nervous robot-tissue model is assumed that is inspired by the human skin structure. In analogy to the human skin, the nervous robot-tissue into is split in three distinct layers filled with *artificial Robot Neurons* (aRNs) that replicate the principles of human receptors, see Fig. 5.3. The parameters $b_{1,2,3}$ denote the thickness of each layer and are set to $b_1 = 0.002$ m, $b_2 = 0.004$ m, and $b_3 = 0.014$ m, resulting in a total tissue thickness $b_t = 0.02$ m. The contact with an object is described by the contact radius d , the penetration volume V_c , and the object radius r_c . The material constants $E_{1,2,3}$ and $\nu_{1,2,3}$ represent Young’s modulus and the Poisson’s ratios. In this work, they are chosen to be $E_1 = E_2 = E_3 := 50$ MPa and $\nu_1 = \nu_2 = \nu_3 := 0.25$. $E_{1,2,3}$ and $\nu_{1,2,3}$ correspond to polystyrene (soft) material that may be a suitable choice for a mechanical implementation. Based on [257], b_t is chosen to be thick enough to prevent the material from full compression during contact events. $b_{1,2,3}$ are chosen in terms of a scaled ratio that approximately corresponds to the standard thickness ratio of human skin layers [91]. The parameters $\rho_{1,2,3}$ represent the homogenous density of the aRNs and were chosen to be $\rho_1 < \rho_2 < \rho_3$ with $\rho_1 = 10^7$ m⁻³, $\rho_2 = 1.05 \cdot 10^7$ m⁻³, and $\rho_3 = 1.1 \cdot 10^7$ m⁻³. These density values approximately correspond to the density of the human fingertip mechanoreceptors [258].¹

This contact structure has two main properties. First, the deeper a collision object penetrates the nervous robot tissue, the more stimulated aRNs. Second, when a collision

¹For more details on suitable contact models, please refer to [257].

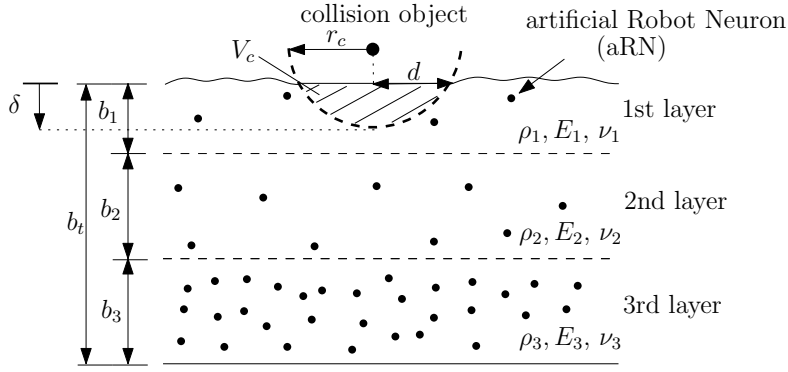


Figure 5.3: Mechanical model of the proposed nervous robot-tissue. ©2016 IEEE [251]

object reaches the next tissue layer, the rate of stimulated aRN rises. Note that the distribution of aRN does not necessarily reflect the distribution of human skin receptors.

5.3 Spiking Models

5.3.1 Principle aRN spiking characteristics

The aRN reflect the essential function of human receptors. If the stimulus of human neurons exceeds a certain threshold, they start to send spike-like signals. One spike is constant at amplitude, duration, and refractory time, which denotes the duration the receptor cannot fire again regardless of present stimuli. A significant amount of information is thus encoded by changing the frequency of the firing rate. To imitate such behavior, aRN firing can be modeled as a finite-state machine (FSM) consisting of the three states *idle*-, *firing*- and *rest-state*, see Fig. 5.4.

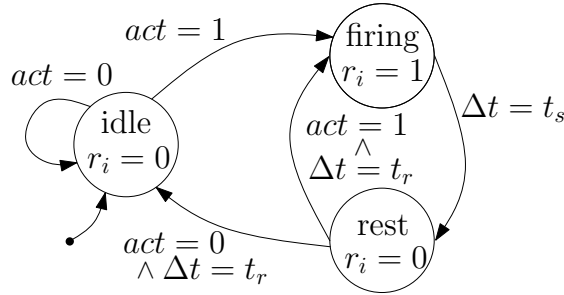


Figure 5.4: Modeling aRN firing as a finite-state machine. ©2016 IEEE [251]

Initially, the aRN is in *idle-state*, i.e., in case of no contact ($act = 0$) leading to $r_i = 0$. Subscript $i \in \mathbb{N}$ denotes the individual aRN. If stimulation occurs ($act = 1$) the aRN switches to the *firing-state*, i.e., it starts firing by setting $r_i = 1$ for a fixed time duration t_s . Thereafter, it switches to *rest-state*. The output is then set to $r_i = 0$ for the refractory time t_r , regardless of possibly present stimuli. After this silent period, the aRN switches

either back to firing-state ($act = 1$) or remains silent by switching to idle-state ($act = 0$), depending on the stimulus. In the following, the aRN types modeled in this work are outlined.

5.3.2 aRN types

Here, aRN types that respond to *penetration depth*, *penetration velocity* and *compressive stress*, including their spiking models, are elaborated as they correlate with pain sensation as described in [259, 260].² Each aRN type is assumed to be equally distributed over the robot-tissue with according density $\rho_{1,2,3}$, respectively. In addition to the “instantaneous” aRN types, aRN types are introduced encoding the *repetitiveness* of contacts, since it is known that this influences pain level as well [261].

5.3.2.1 Penetration depth spike train

Under the assumption that the higher the penetration depth δ , the more aRN types are activated, the total number of activated aRN types $r(\delta)$ is

$$r(\delta) = \begin{cases} V_1(\delta)\rho_1 & \delta \leq b_1 \\ V_2(\delta - b_1)\rho_2 + r(b_1) & b_1 < \delta \leq b_{t2} \\ V_3(\delta - b_{t2})\rho_3 + r(b_{t2}) & b_{t2} < \delta, \end{cases} \quad (5.1)$$

with $b_{t2} = b_1 + b_2$. $V_1(\delta)$, $V_2(\delta - b_1)$ and $V_3(\delta - b_{t2})$ denote the instantaneous effective volumes that envelop the stimulated aRN types. Due to tissue compression, those aRN types that were placed at penetration volume V_c (see Fig. 5.3) push against neighboring ones and may stimulate them as well. Therefore, some affected aRN types lie outside the penetration volume V_c . To take this effect into account, the instantaneous effective volumes are approximated to be cylindrical as a reasonable simplification. Accordingly, each respective volume of layer i is obtained by

$$V_i(\delta) = \Delta\delta_i\pi d^2 = \Delta\delta_i\pi (2r_c\Delta\delta_i - \Delta\delta_i^2), \quad (5.2)$$

where $\Delta\delta_i$ is the penetration depth in layer i and d the radius of the cylindrical volume (see Fig. 5.3).

5.3.2.2 Penetration velocity spike train

The velocity-dependent spike generation is defined in a straight forward manner as the absolute value of the first time derivative of penetration depth based firing

$$r_v := |\dot{r}(\delta)|. \quad (5.3)$$

²This work adds penetration velocity, which obviously strongly correlates with potential danger, as an important metric for an aRNS. It is anticipated that such a modality will become technologically available.

5.3.2.3 Compressive stress spike train

The stress-dependent spiking is computed as

$$p(\sigma) = \begin{cases} V_1(\delta^*)\rho_1 & \delta^* \leq b_1 \\ V_2(\delta^* - b_1)\rho_2 + r(b_1) & b_1 < \delta^* \leq b_{t2} \\ V_2(\delta^* - b_{t2})\rho_3 + r(b_{t2}) & b_{t2} < \delta^*. \end{cases} \quad (5.4)$$

Due to the physically decaying impact characteristics of pressure the effective penetration depth δ^* is introduced as

$$\delta^* := \begin{cases} c_e \delta & \delta \leq \frac{b_t}{2} \\ b_t & \frac{b_t}{2} < \delta \leq b_t, \end{cases} \quad (5.5)$$

since not only the aRNs within the penetration depth δ are activated, but also significant portions below. If $c_e \approx 2$ is chosen, then, as a result δ^* covers 99 % of the impact decay, i.e., the tissue stress has reduced to < 1 % of the maximum surface stress. In analogy to (5.2) the instantaneous stress volumes are

$$V_i(\delta^*) = \Delta\delta_i^* \pi d^2, \quad i = 1, 2, 3, \quad (5.6)$$

where $\Delta\delta_i^*$ is the effective penetration depth of layer i .

5.3.2.4 Repetitiveness spike train

The repetitiveness ξ is defined as

$$\xi := \int_{t_c} \dot{\xi} dt, \quad (5.7)$$

where t_c is the time instant at which the collision occurs. The *repetitiveness rate* $\dot{\xi}$ is defined as

$$\dot{\xi} := \begin{cases} aF(\delta)\dot{\delta} & \dot{\delta} > 0 \\ - \int_{t_v} \ddot{\xi}_r dt & \dot{\delta} \leq 0 \wedge \xi > 0 \\ 0 & \dot{\delta} \leq 0 \wedge \xi = 0, \end{cases} \quad (5.8)$$

where $a > 0$ and $\ddot{\xi}_r > 0$ are the growth and decay factors. t_v denotes the time when penetration velocity gets negative. The contact force $F(\delta)$ is assumed to follow Hertzian theory, see [257].

Figure 5.5 depicts the sensory response of the nociceptive aRNs given the true compressive stress σ under the following collision parameters. The contact occurs between a 2-shell 1-DoF robot with $m_r = 4.5$ kg, $r_r = 0.1$ m and a 1-shell collision object with $m_c = 4.5$ kg, $r_c = 0.1$ m at impact speed $v_c = 0.4$ m/s. The robot is assumed to be at rest and the object approaches at v_c . After a single contact event a repetitive decaying impact follows. The response of the respective aRN-type to penetration depth $r(\delta)$, velocity r_v , impact stress $p(\sigma)$ and repetition frequency ξ are displayed. One can see that each aRN type correlates with the respective (physical) modality.

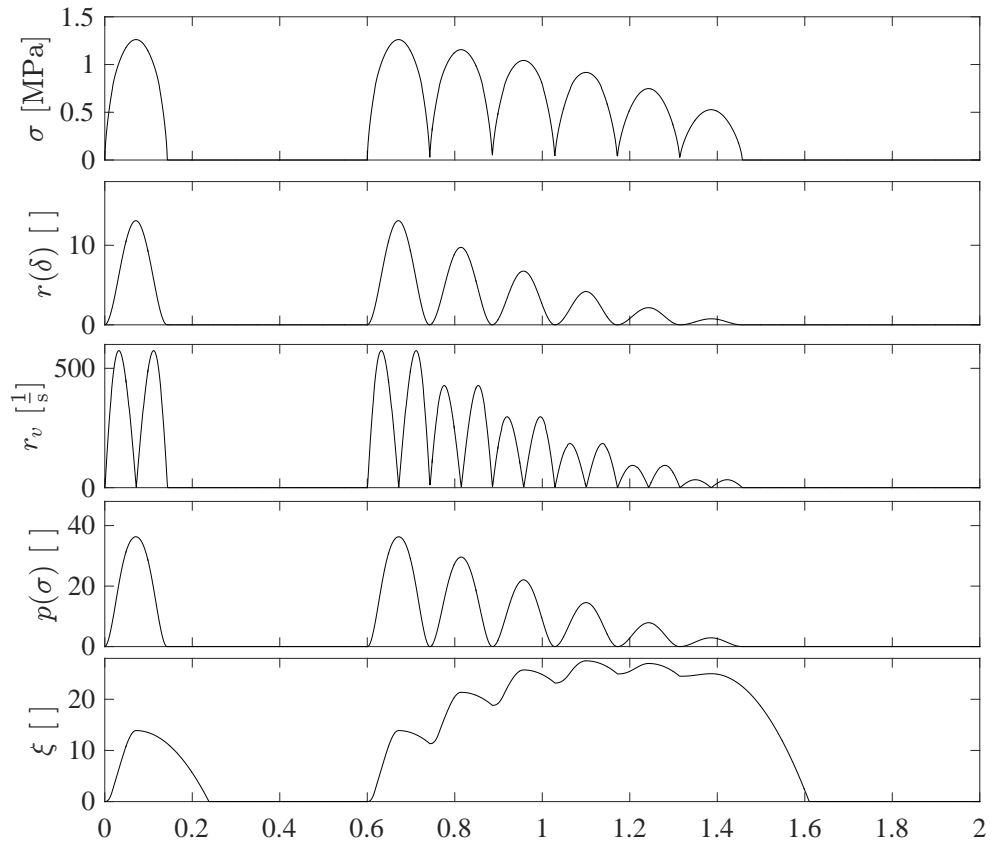


Figure 5.5: Cumulated spike signals of aRN-types penetration depth r , velocity r_v , stress p , and repetitiveness ξ . ©2016 IEEE [251]

5.3.2.5 Implementation remarks

For convenience, a time discretisation $t = kT_s$ is introduced, with sampling time T_s and time step $k \in \mathbb{N}$, in the implementation. During the refractory time t_r (see Fig. 5.4) aRNs do not fire. Thus, the number of stimulated aRNs $r(\delta, kT_s)$ in (5.1) reduces to an effective number r_{eff} . This is the sum of aRNs currently being in firing-state. By setting $t_r = t_s = T_s$ the stimulated aRNs can be either in firing or silent mode for every k . Consider the stimulated aRNs at time step k fire. Then they pause in time step $k+1$ and fire again in $k+2$ (assuming the stimulus is still present, i.e., $act = 1$, see Fig. 5.4). The increment of stimulated aRNs in time step k is therefore

$$\Delta r_i(\delta, kT_s) = r(\delta, kT_s) - r(\delta, (k-1)T_s), \quad i = 1, 2, \dots, l, \quad (5.9)$$

where subscript i is the incremental counter during contact. All $\Delta r_i(\delta, kT_s)$ form the elements of the stacked vector

$$\Delta R = [\Delta r_1 \ \dots \ \Delta r_l]^\top \quad \Delta R \in \mathbb{R}^l, \quad \Delta r_i > 0 \quad (5.10)$$

of length l that increases as long as $\Delta r_i > 0$. It follows that for even and odd time steps one can separately compute r_{eff} as

$$r_{eff}(kT_s) = \begin{cases} \sum_{j=0}^{\lfloor l/2 \rfloor} \Delta R_{2j+1} & k = 2m + 1 \\ \sum_{j=1}^{\lfloor l/2 \rfloor} \Delta R_{2j} & k = 2m \end{cases}, \quad m = 0, 1, 2, \dots \quad (5.11)$$

If Δr_i is negative ($\Delta r_i^- := \Delta r_i \leq 0$) the number of stimulated aRNs decreases. This means that the object's collision velocity turns into the opposite direction and thus moves away from the robot. Therefore, Δr_i^- is deleted from ΔR in reverse order such that the aRNs stimulated last are deactivated first. Algorithm 1 shows the pseudo code of this firing reduction algorithm.

Algorithm 1 Pseudocode for modeling firing reduction.

```

c = Δrl + Δrl+1-
while c ≤ 0 do
  Δrl = 0
  l = l - 1
  c = Δrl + c
end while
Δrl = c

```

5.4 Interpretation

In this work, *robot pain* is defined as the interpretation of spike trains generated by the aRNs involving contextual information. Inspired by the human pain system, robot pain is

divided into four verbal pain classes: *no*, *light*, *moderate*, and *severe pain*. They represent a simplification of the *Verbal Rating Scale (VRS)* of pain measurement in humans, see Tab. 5.1. The first pain class contains no contact and contacts that are not painful, here referred to as “soft contacts”. Consider, e.g., the robot fulfills a certain task such as holding a desired configuration \mathbf{q}_d . Obviously, in case of no contact the robot shall hold its position. In case of soft contact, the robot experiences an external torque $\boldsymbol{\tau}_{ext}$ that results in a deviation from its desired equilibrium position \mathbf{q}_d . Since the contact is not harmful the robot shall treat the contact as a disturbance, compensate for it, and focus on the desired task. In the second pain class, such contacts occur that may harm the robot or prevent it from performing the task. The robot “feels” uncomfortable and shall smoothly retract until the contact event is over and return thereafter. Strong collisions

Table 5.1: Robot pain classes and corresponding reaction strategies. © 2016 IEEE [251]

Robot pain class	Collision severity	Strategy	\mathbf{q}_d -adapt.	\mathbf{K}_d -adapt.	$\boldsymbol{\tau}_{ff}$ -adapt.
I no pain	no/soft contact	fulfill task/compensate	(5.14), with $\dot{\mathbf{q}}_p(\mathbf{k}_q^I)$	(5.17), with $\mathbf{K}_d(I\mathbf{K}_d^*, \mathbf{k}_K^I)$	(5.19), with $\boldsymbol{\tau}_{ff}(\mathbf{k}_\tau^I, \mathbf{W} > \text{diag}(\mathbf{0}))$
II light pain	light	smoothly retract	(5.14), with $\dot{\mathbf{q}}_p(\mathbf{k}_q^{II})$	(5.17), with $\mathbf{K}_d(II\mathbf{K}_d^*, \mathbf{k}_K^{II})$	(5.19), with $\boldsymbol{\tau}_{ff}(\mathbf{k}_\tau^{II}, \mathbf{W} = \text{diag}(\mathbf{0}))$
III moderate pain	strong	quickly retract	(5.14), with $\dot{\mathbf{q}}_p(\mathbf{k}_q^{III})$	(5.17), with $\mathbf{K}_d(III\mathbf{K}_d^*, \mathbf{k}_K^{III})$	(5.19), with $\boldsymbol{\tau}_{ff}(\mathbf{k}_\tau^{III}, \mathbf{W} = \text{diag}(\mathbf{0}))$
IV severe pain	hard	abort task	n.a.	n.a.	n.a.

are covered in the third pain class. The robot “feels” moderate pain, shall quickly retract, and more distant until the contact event is over. Then, it may move back towards \mathbf{q}_d . The last pain class covers all contacts in which the robot may be damaged and thus needs some sort of “help”. In order to prevent making the damage worse, the robot switches to gravity compensation with additional damping for dissipation, improving the safety of the robot and the environment by its strictly passive behavior. The desired interpretation is realized by the control laws that are elucidated in the following.

5.5 Collision Control

5.5.1 Generalized Pain Spiking State

In order to involve the spiking signals into the overall control strategy, this work introduces the *generalized pain spiking state* as

$$\mathbf{s} = [p(\sigma) \ r(\delta) \ r_v(\delta) \ \xi]^\top \geq \mathbf{0}, \quad (5.12)$$

which is defined as the stacked vector of all cumulated spike signals from Sec. 5.3.2. Note that for a possibly real-world implementation of the aRNS using conventional sensors, i.e., providing analog outputs, one can use this spiking state vector as an entry point to incorporate those signals. For example, in this work, the BioTac analog outputs are subsequently used to replace the cumulated spike signals, leading to a sensor-related spiking vector \mathbf{s}_{BT} , see Sec. 5.6.2.

5.5.2 Reflex Control Strategies

The proposed control strategy adapts the overall impedance and feed-forward characteristics of a joint level impedance controller, as well as the reference trajectory based on the Cartesian pain sensation and interpretation. This *pain-based joint level impedance controller* is defined by

$$\boldsymbol{\tau}_d = \mathbf{K}_d(\mathbf{s})(\mathbf{q}_d(\mathbf{s}) - \mathbf{q}) + \mathbf{D}(\mathbf{q})\dot{\mathbf{q}} + \boldsymbol{\tau}_{ff}(\mathbf{s}) + \boldsymbol{\tau}_G(\mathbf{q}), \quad (5.13)$$

where $\mathbf{K}_d \in \mathbb{R}^{n \times n}$, $\mathbf{q}_d \in \mathbb{R}^n$ and $\boldsymbol{\tau}_{ff} \in \mathbb{R}^n$ are the desired closed-loop stiffness, the desired equilibrium position and the feedforward torque. They all depend on the generalized pain spiking state \mathbf{s} . The vector $\boldsymbol{\tau}_G \in \mathbb{R}^n$ denotes the gravity compensation torque and $\mathbf{D} \in \mathbb{R}^{n \times n}$ the configuration dependent joint damping matrix

$$\mathbf{D}(\mathbf{q}) = \mathbf{A}(\mathbf{q})\mathbf{D}_\xi\mathbf{K}_{d1} + \mathbf{K}_{d1}\mathbf{D}_\xi\mathbf{A}(\mathbf{q}),$$

where $\mathbf{D}_\xi = \text{diag}\left(\frac{1}{\sqrt{2}}\right) \in \mathbb{R}^{n \times n}$ is the desired joint damping ratio matrix. According to [254], $\mathbf{A}(\mathbf{q})$ and \mathbf{K}_{d1} are defined by $\mathbf{A}(\mathbf{q})\mathbf{A}(\mathbf{q}) = \mathbf{M}(\mathbf{q})$ and $\mathbf{K}_{d1}\mathbf{K}_{d1} = \mathbf{K}_d$.

5.5.2.1 q_d -adaptation

Equilibrium position adaptation after the collision event, occurring at collision time t_c , shall cause faster evading from external contacts the larger $\mathbf{s}(t)$. After the contact, an exponential recovery behavior towards the original equilibrium $\mathbf{q}_d(t_c)$ shall be achieved. Specifically, the desired equilibrium position \mathbf{q}_d is adapted via

$$\mathbf{q}_d := \mathbf{q}_d(t_c) + \int_{t_c} \dot{\mathbf{q}}_p(\mathbf{s}) dt, \quad (5.14)$$

where $\mathbf{q}_d(t_c)$ denotes the desired joint configuration at t_c and $\dot{\mathbf{q}}_p$ is the *pain reflex equilibrium rate*, which is integrated from collision time t_c on. The generalized *virtual pain force* \mathbf{f}_v is defined as

$$\mathbf{f}_v := (\mathbf{k}_q^\top \mathbf{s}) \mathbf{u}_c, \quad (5.15)$$

where $\mathbf{k}_q > \mathbf{0}$ is a gain vector. The pain reflex equilibrium rate is then obtained by

$$\dot{\mathbf{q}}_p := \begin{cases} \mathbf{J}_c^\top \mathcal{F}_v := \mathbf{J}_c^\top [\mathbf{f}_v^\top \mathbf{0}]^\top & \mathbf{s} > \mathbf{0} \\ -\text{sign}\{\mathbf{q}_d - \mathbf{q}_d(t_c)\} \int_{t'} \ddot{\mathbf{q}}_r dt & \mathbf{s} = \mathbf{0} \wedge \mathbf{q}_d \neq \mathbf{q}_d(t_c) \\ \mathbf{0} & \mathbf{s} = \mathbf{0} \wedge \mathbf{q}_d = \mathbf{q}_d(t_c), \end{cases} \quad (5.16)$$

where $\ddot{\mathbf{q}}_r > \mathbf{0}$ is the constant equilibrium recovery acceleration. t' is the time at contact loss.

5.5.2.2 K_d -adaption

The stronger the stimulus, stiffness adaptation shall cause faster stiffness increase, while after the collision recovery to the original constant *reference stiffness* $\mathbf{K}_d^* > \mathbf{0}$ shall be moderately fast. For simplicity, the stiffness entries are chosen to be equal for all joints. The desired diagonal closed-loop stiffness $\mathbf{K}_d > \mathbf{0}$ is adapted by

$$\mathbf{K}_d := \mathbf{K}_d^* + \min \left[\Delta \mathbf{K}_{d,\max}, \int_{t_c} \dot{\mathbf{K}}_p(\mathbf{s}) dt \right], \quad (5.17)$$

where $\dot{\mathbf{K}}_p$ is the *pain stiffness rate*. The stiffness increase (as reasoned in Sec. 5.5.3), which is bounded from above by $\Delta \mathbf{K}_{d,\max} = \mathbf{K}_{d,\max} - \mathbf{K}_d^*$, starts at t_c . The according stiffness adaptation rate $\dot{\mathbf{K}}_p(\mathbf{s})$ is defined as

$$\dot{\mathbf{K}}_p(\mathbf{s}) := \begin{cases} \text{diag}(\mathbf{k}_K^\top \mathbf{s}) & \mathbf{s} > \mathbf{0} \\ - \int_{t'} \dot{\mathbf{K}}_r dt & \mathbf{s} = \mathbf{0} \wedge \mathbf{K}_d > \mathbf{K}_d^* \\ \mathbf{0} & \mathbf{s} = \mathbf{0} \wedge \mathbf{K}_d = \mathbf{K}_d^*, \end{cases} \quad (5.18)$$

where $\mathbf{k}_K > \mathbf{0}$ represents the stiffness rate gain vector and $\dot{\mathbf{K}}_r > \mathbf{0}$ the constant stiffness relaxation acceleration.

5.5.2.3 τ_{ff} -adaptation

The feed forward torque τ_{ff} is adapted according to the same principle as the equilibrium position behavior. It consists of the *pain reflex torque* τ_p and the *compensation torque* τ_{comp} :

$$\tau_{ff}(\mathbf{s}) := \tau_p(\mathbf{s}) + \tau_{comp} \quad (5.19)$$

Let us start at the generalized *pain force* \mathbf{f}_p , which is defined as

$$\mathbf{f}_p := (\mathbf{k}_\tau^\top \mathbf{s}) \mathbf{u}_c, \quad (5.20)$$

where $\mathbf{k}_\tau > \mathbf{0}$ is the gain vector of the pain reflex torque. The pain reflex torque is then obtained via

$$\tau_p(\mathbf{s}) := \begin{cases} -\mathbf{J}_c^\top \mathcal{F}_p := \mathbf{J}_c^\top [\mathbf{f}_p \mathbf{0}]^\top & \mathbf{s} > \mathbf{0} \\ -\text{sign}\{\tau_p\} \iint_{t'} \ddot{\tau}_r dt & \mathbf{s} = \mathbf{0} \wedge \tau_p \neq \mathbf{0} \\ \mathbf{0} & \mathbf{s} = \mathbf{0}, \end{cases} \quad (5.21)$$

where \mathcal{F}_p denotes the pain wrench and $\ddot{\tau}_r > \mathbf{0}$ the constant pain torque recovery acceleration. The compensation torque is computed as

$$\tau_{comp} := \mathbf{W} \int_{t_c} (\mathbf{q} - \mathbf{q}(t_c)) dt, \quad (5.22)$$

where $\mathbf{W} \in \mathbb{R}^{n \times n}$ represents a diagonal and positive definite gain matrix. Note that the compensation torque does not depend on the spiking state vector \mathbf{s} . It is only active in the first pain class to compensate unintended (and painless) contacts.

deeper and faster the collision object penetrates, the stronger the feedforward torque. As the respectively growing intensities increase with the order of pain class according to the gain vectors, the decaying rates decrease, i.e., the time of recovering grows with the order of pain class. In pain class IV, controls are set to gravity compensation with a constant diagonal damping matrix $\mathbf{D} > \mathbf{0}$ only. Since \mathbf{f}_p in (5.20) depends on two aRN types, the respective gain constants $k_{\tau,2}$ and $k_{\tau,3}$ are set such that they equally contribute to the maximally possible pain force $\mathbf{f}_{p,max}$. Thus, the torque gain vector becomes

$$\mathbf{k}_\tau = \begin{bmatrix} 0 \\ (2 r_{max}(\delta))^{-1} \mathbf{f}_{p,max} \\ (2 r_{v,max}(\delta))^{-1} \mathbf{f}_{p,max} \\ 0 \end{bmatrix}, \quad (5.23)$$

where $r_{max}(\delta)$ and $r_{v,max}(\delta)$ denote the respective maximum spiking magnitude.

5.6 Results

In the following, the aRNS framework is applied to a 7-DoF light-weight robot and a pneumatically actuated finger prosthesis testbed. Furthermore, based on the aRNS, a humanoid reflex stack is proposed.

5.6.1 Parameter dependency of aRNS control laws

The parameter dependency of aRNS control laws is investigated during simulated single and multiple collision event(s) between a 2-shell 1-DoF robot ($m_r = 4.5$ kg, $r_r = 0.1$ m) and a 1-shell collision object ($m_c = 4.5$ kg, $r_c = 0.1$ m at $v_c = 0.5$ m/s.³ The task of the robot is to hold $q_d = 0$ m at $K_d^* = 5000$ N/m. Please note that for this one-dimensional collision, q denotes the Cartesian position. The influence of the respective key parameters is investigated regarding the equilibrium, stiffness, and feedforward torque adaption.

Figure 5.7 depicts the q_d -adaptation during a single collision.

The top chart shows the collision's stress spiking $p(\sigma)$. In the middle plot, q_d -adaptation based on $p(\sigma)$ and $k_{q,1}$ from the gain vector \mathbf{k}_q is shown at fixed recovery acceleration \ddot{q}_r . Obviously, $k_{q,1}$ can be used for varying the magnitude of the set point. The lower chart shows the reverse case at fixed value of $k_{q,1}$. This means that for a given collision the distal response does not change, while the recovery acceleration \ddot{q}_r varies, allowing to influence the decay time before the robot proceeds with the task. In Fig. 5.8 the variation of stiffness rate adaptation is shown during repetitive contacts.

³The radii $r_{r,c}$ are equally chosen, since the used contact model is only valid for radii greater than the contact radius d , see Fig. 5.3. Reasonable values are chosen for $m_{r,c}$ that correspond to typically reflected mass values found during human-robot collisions [257].

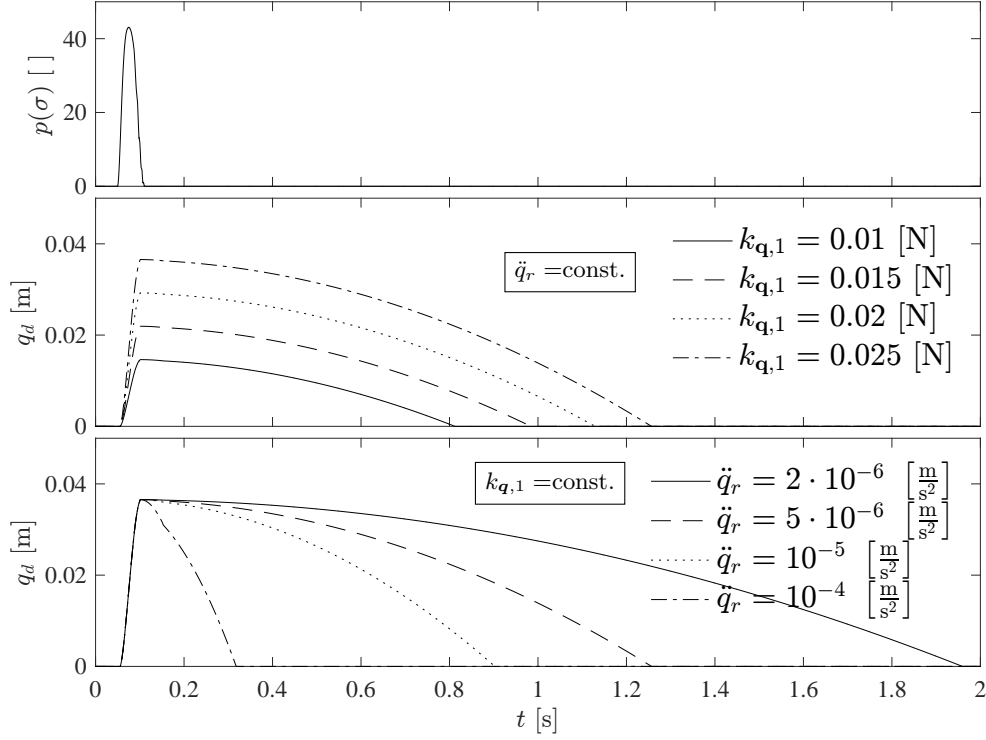


Figure 5.7: q_d -adaptation for single contact for different k_q and \ddot{q}_r . ©2016 IEEE [251]

The top diagram depicts the repetitiveness spiking ξ . The middle and lower diagrams show \mathbf{K}_d -adaptation for different $k_{\mathbf{K},4}$ at fixed recovery acceleration $\ddot{K}_r = \text{const.}$ (middle) and vice versa (bottom). The stiffness magnitude increases with the number of contacts (indicated by ξ) at different rates depending on the particular choice of $k_{\mathbf{K}}$ until $K_{p,max} = 5500$ N/m is reached. When the contact event is over \mathbf{K}_d recovers to the nominal stiffness K_d^* with \ddot{K}_r . Figure 5.9 shows feedforward torque adaption for $r_{max}(\delta) = 16$, $r_{v,max}(\delta) = 2200$ s⁻¹, and $f_{p,max} = 100$ N.

The first and middle charts depict the penetration depth and velocity spiking $r(\delta)$ and r_v for three consecutive collisions. To separately emphasize the contribution of the two spiking signals, only $r(\delta)$ is activated for the first collision. Only r_v is considered during the second collision, while the last collision shows the combined response. The decay acceleration is set to $\ddot{r}_r = 50$ N/s².

To sum up, the aRNS controller adaption can be separately set up for \mathbf{q}_s , \mathbf{K}_d , and $\boldsymbol{\tau}_{ff}$, which should be done carefully, while considering the used robot, its task, and foreseeable environments.

5.6.2 Pain reactions on a 7 DoF robot arm

The pain-reflex control is experimentally demonstrated using a KUKA LWR4+ equipped with the BioTac[®] sensor as an implementation of the artificial robot neuron concept.

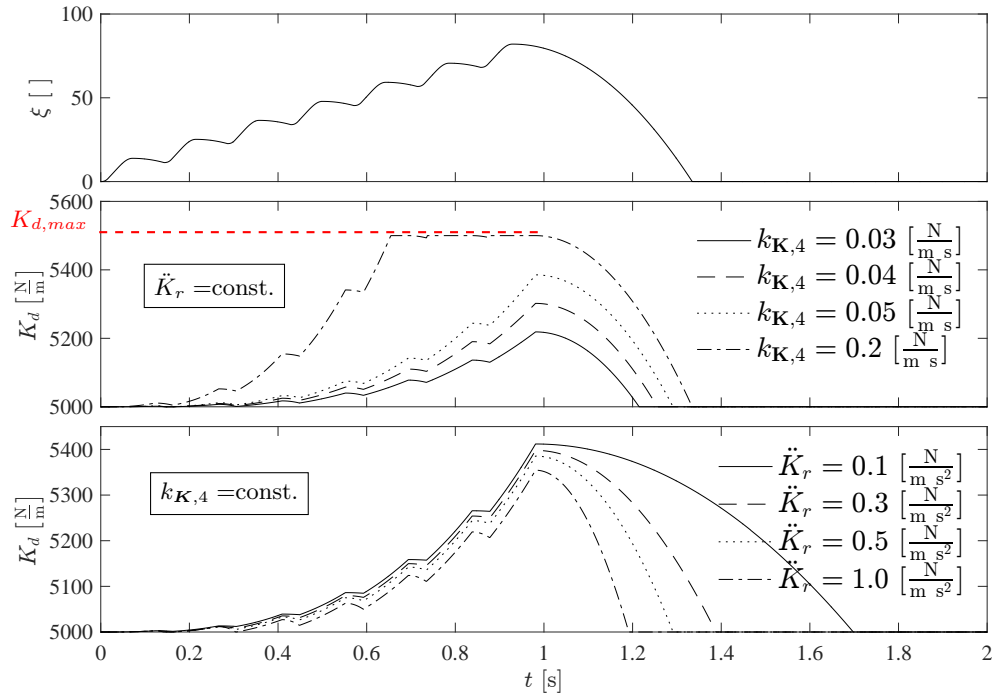


Figure 5.8: K_d -adaptation for repetitive contacts for different $k_{\mathbf{K}}$ and \ddot{K}_r . ©2016 IEEE [251]

The sensor is mounted at the end effector, and pressure is induced by a human finger, leading to the respective pain class and reflex reaction, see Fig. 5.10. The BioTac can sense multiple modalities such as pressure, vibration, temperature, or spatial contact forces. In this work, e.g., the pressure signal σ_{BT} is utilized as the cumulated spiking signal adapting \mathbf{q}_d .

A counter realizes the repetitiveness spiking ξ with constant gradient and exponential decay characteristics that is activated for $\sigma_{BT} > 0$, directly influencing \mathbf{K}_d . The particular relation can be derived from (5.8) by replacing $aF\delta$ with $T_{inc} = 0.1$ and $\dot{\delta}$ with σ_{BT} . In addition, the spiking state vector \mathbf{s} in (5.12) is extended by the modality of temperature sensing, utilizing the *analog derivative* of temperature T_{AC} of the BioTac.⁴ Due to the larger time constants of temperature measurement, a separate *temperature pain class* is introduced that is activated as soon as a threshold of $H = 1920$ kbits is exceeded. Its formal definition and reflex behavior is equivalent to the other contact classes. However, only two reaction classes are defined for this particular case. The robot retracts with a change of 5 deg in every joint and waits for 4 s until recovery, provided that T_{AC} does not drop any further. These values were empirically found to successfully avoid contact with a plastic cup filled with hot boiled water ($\vartheta_c \approx 100^\circ C$).

The cup was only slightly touched during the experiment to avoid unwanted retraction due to pressure sensing. The spiking state vector used in the experiment is $\mathbf{s}_{BT} =$

⁴For more information about the BioTac and signal interpretation see [262].

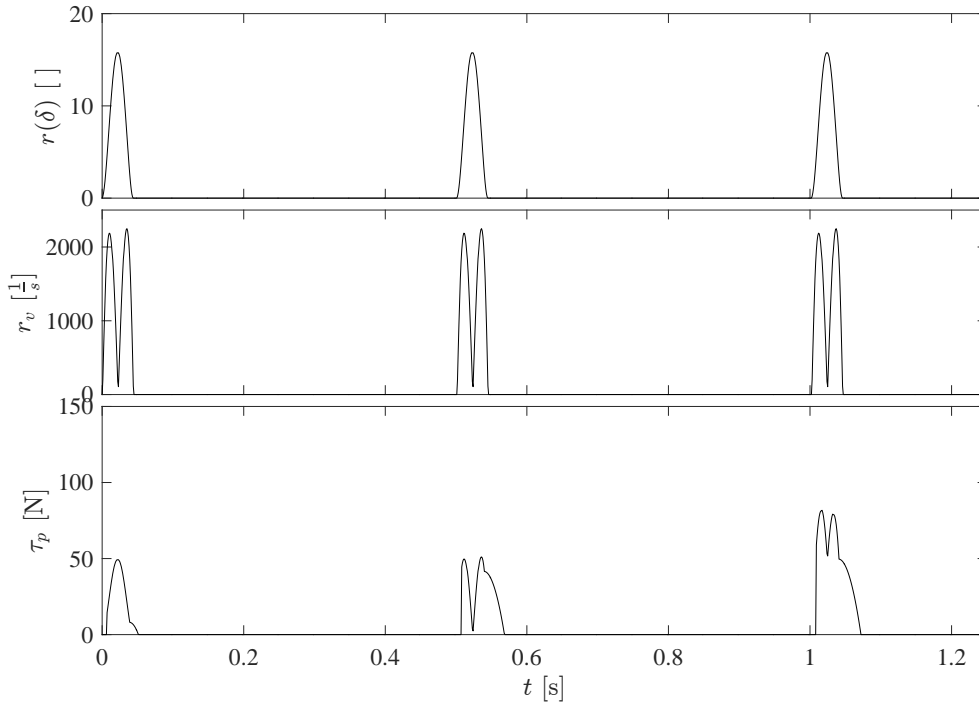


Figure 5.9: Contribution of $r(\delta)$ and r_v to τ_p -adaptation for given \mathbf{k}_τ . ©2016 IEEE [251]

$[\sigma_{BT}, T_{AC}, \xi]^\top$ and the controller parameters can be found in Tab. 5.2. The equilibrium position-related parameters are empirically chosen such that for the given contact events, the robot does not violate a predefined workspace. Furthermore, the stiffness parameters comply with the specifications of the KUKA LWR4+. The robot task is to maintain $\mathbf{q}_d = [0, 30, 0, -50, 0, 10, 0]^\top$ [deg]. In Figure 5.11 one can see an increase in desired equilibrium position and a slight increase in stiffness for *light pain*. For *moderate pain* one observes a reinforced version of light pain. Note that since the appropriate reflex behavior in this particular experimental setup was mainly observed in axis 2 and 4, the other traces are omitted for clarity. The corresponding gains were selected to be

Table 5.2: Gain vectors and parameters for collision between BioTac and human finger (see Fig. 5.10). ©2016 IEEE [251]

pain class	\mathbf{q}_d -adapt.		\mathbf{K}_d -adapt.		
	\mathbf{k}_q^\top [N -]	$\ddot{\mathbf{q}}_r$ [$\frac{\text{rad}}{\text{s}^2}$]	\mathbf{k}_K^\top [- - $\frac{\text{Nm}}{\text{rad}\cdot\text{s}}$]	\mathbf{K}_d^* [$\frac{\text{Nm}}{\text{rad}}$]	$\dot{\mathbf{K}}_r$ [$\frac{\text{Nm}}{\text{rad}\cdot\text{s}^2}$]
I	$\mathbf{0}^\top$	$\mathbf{0}$	$\mathbf{0}^\top$	diag{500}	$\mathbf{0}$
II	$[0.05 \ 0 \ 0]^\top$	diag{ 10^{-5} }	$[0 \ 0 \ 60]^\top$	diag{500}	diag{0.02}
III	$[0.075 \ 0 \ 0]^\top$	diag{ $5 \cdot 10^{-6}$ }	$[0 \ 0 \ 80]^\top$	diag{500}	diag{0.02}

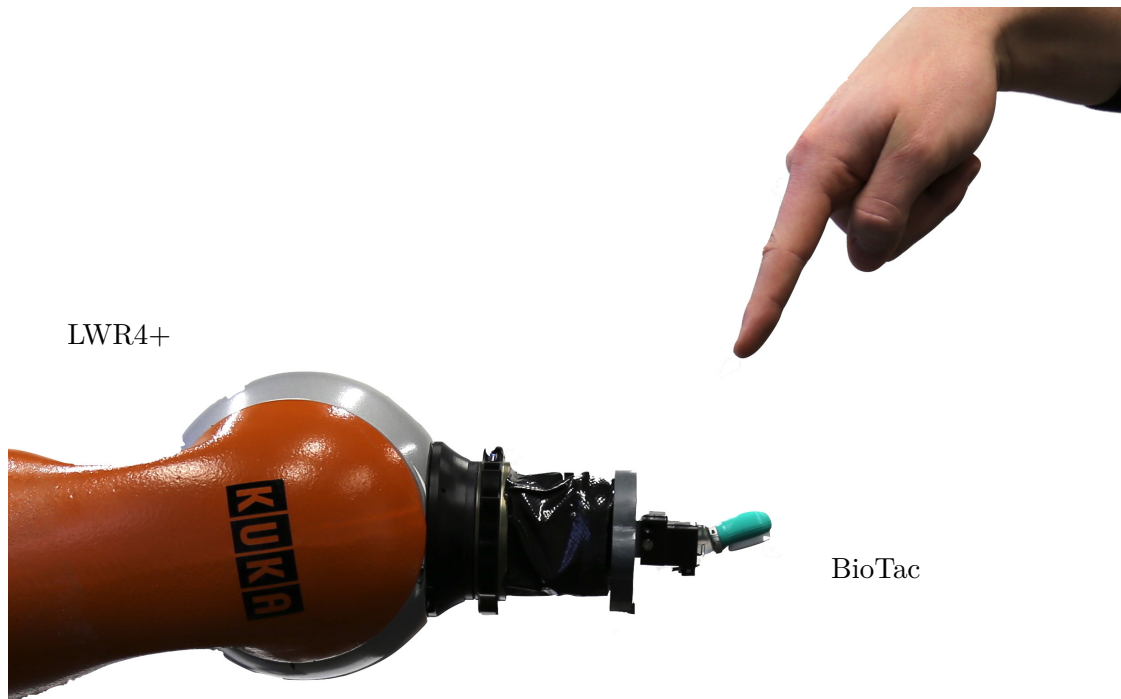


Figure 5.10: Experimental setup consisting of KUKA LWR4+ equipped with BioTac sensor and controlled by the aRNS. ©2016 IEEE [251]

larger, and the recovery rates decreased. The collision that causes *severe pain* represents a special case where the controller switches to pure gravity compensation mode with some additional damping, see Fig. 5.6. The pain controls are deactivated, and without human intervention, the robot cannot return to the task. Most noticeably, the setpoint adaption and stiffness rise until contact is lost during repetitive contacts. Finally, the robot retracts to avoid more prolonged contact with a hot object for the temperature reflexes.

5.6.3 Pain responses on a pneumatically actuated finger prosthesis testbed

This section shows possible reflex behaviors for blunt/sharp contacts as well as based on proprio- and exteroceptive information for a simplified prosthesis, realized by a pneumatically actuated and impedance controlled finger joint [263]. The reflexes are generated using aRNS. The Biotac sensor serves as input for the exteroceptive reflexes, whereas a joint momentum observer is used for proprioceptive reflexes.

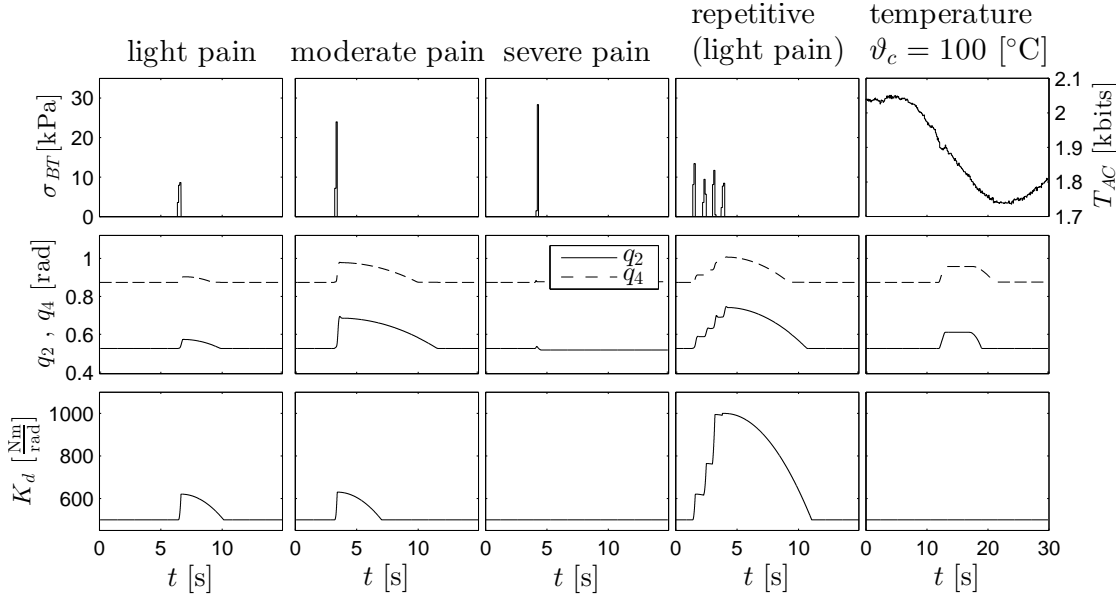


Figure 5.11: Physical collision for the KUKA LWR4+ equipped with the aRNS/BioTac and a human finger that applies varying pressure. ©2016 IEEE [251]

Figure 5.12 shows the experimental setup of the antagonistic and pneumatically actuated finger joint. A Biotac sensor is mounted at the fingertip, which is used for pressure sensing. The system uses a cascaded joint-level impedance controller with underlying piston-level force control (see [263]).

The aRNS based joint-level impedance controller applied to the finger joint is defined as

$$\tau_d = K_d(\mathbf{s})(q_d(\mathbf{s}) - q) + D_d(q, \mathbf{s})\dot{q} + \tau_{ff}(\mathbf{s}) + \tau_g(q), \quad (5.24)$$

with τ_d being the desired torque and τ_g the gravity compensation term. q , q_d and \dot{q} denote the actual, desired joint position and velocity. Furthermore, the stiffness K_d , damping D_d , feedforward torque τ_{ff} and q_d can be adapted depending on the *generalized pain spiking state* vector $\mathbf{s} = [\sigma, \xi]$ with ξ being the repetitiveness rate. The contact pressure is determined by

$$\sigma = \max[\sigma_{BT}, c_0 \hat{\tau}_{\text{ext}}], \quad (5.25)$$

where σ_{BT} is the internal pressure value of the Biotac sensor and c_0 being a scaling factor. The external torque τ_{ext} is estimated by a *generalized momentum observer* [264]

$$\hat{\tau}_{\text{ext}} = K_O \left(\int_0^T (\tau_m - M_j l_{\text{CM}} \cos(q)g - \hat{\tau}_{\text{ext}}) dt - J_c \dot{q} \right) \quad (5.26)$$

where K_O is the observer gain. The joint torque τ_m is measured by the pressure sensors of the cylinders. Mass, inertia and center of gravity of the joint link are M_j , J_c and l_{CM} . In this work, only q_d is adapted by

$$q_d := q_d(t_c) + \int_{t_c}^t \dot{q}_p(s_1) dt, \quad (5.27)$$

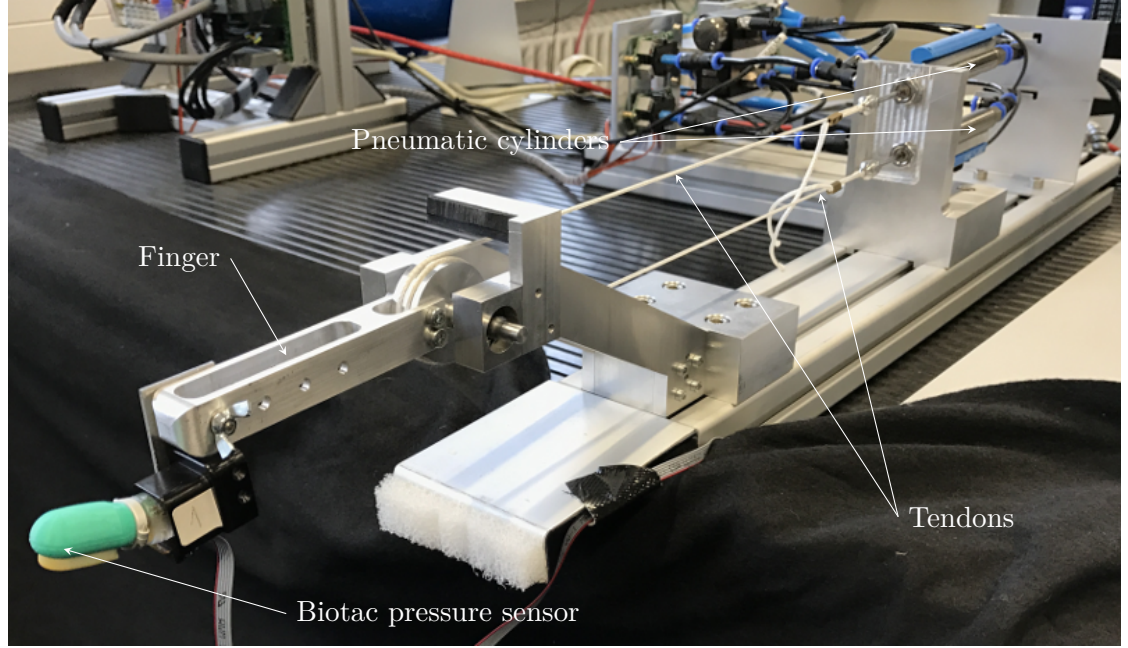


Figure 5.12: Experimental setup. ©2017 IEEE [253]

$$\dot{q}_p := \begin{cases} -c_1 l s_1 & s_1 > 0 \\ -\text{sign}\{q_d - q_d(t_c)\} \int c_2 dt, & s_1 = 0 \wedge q_d \neq q_d(t_c) \\ 0 & s_1 = 0 \wedge q_d = q_d(t_c), \end{cases} \quad (5.28)$$

and K_d by

$$K_d := K_d^* + \min[\Delta K_{d,max}, \int_{t_c} \dot{K}_p(s_2) dt] \quad (5.29)$$

$$\dot{K}_p := \begin{cases} c_3 s_2, & s_2 > 0 \\ -\int c_4 dt, & s_1 = 0 \wedge K_d > K_d^* \\ 0, & s_1 = 0 \wedge K_d = K_d^* \end{cases} \quad (5.30)$$

where c_{1-4} define constants, l is the center of collision, t_c the time instant of collision, K_d^* the nominal and $K_{d,max}$ the maximum stiffness.

Two experiments were performed. The first experiment investigates the reflex behavior for blunt and sharp contacts, see Fig. 5.13 and Fig. 5.14a.

The blunt contacts represent nominal interaction behavior, i.e., no reflex is triggered. In the case of sharp contacts, the finger follows the desired trajectory of the aRNS reflex generator. Stiffness increases with the level of signal strength or repetitiveness (see also Fig. 5.14b) that occur usually for highly accelerative motions.

The second experiment compares the aRNS based on exteroceptive (Biotac) and proprioceptive (momentum observer) information. Here either the Biotac sensor or the finger structure is touched. The fusion of the two signals is given by (5.25). Fig. 5.14

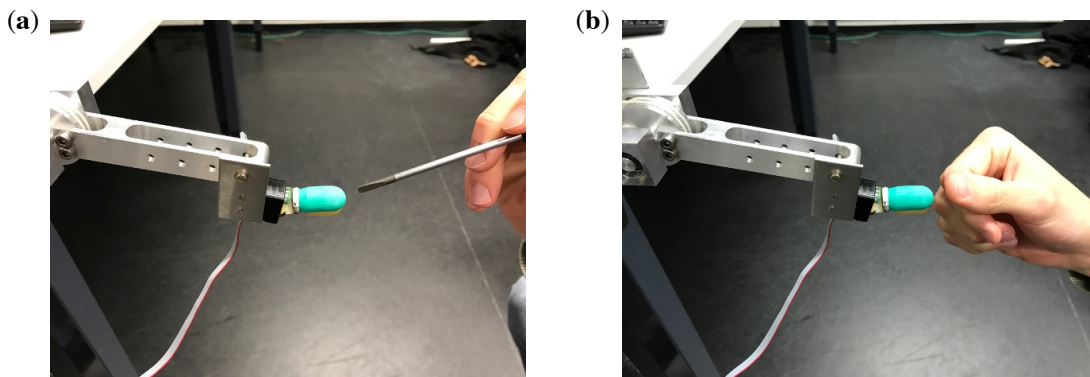


Figure 5.13: Contact types of the experiment shown in Fig. 5.14. (a) Sharp contact. (b) Blunt contact. © 2017 IEEE [253]

shows corresponding experimental results. The aRNS was configured to adapt to stiffness for the exteroception case only. It was chosen freely and be easily transferred to proprioception as well.

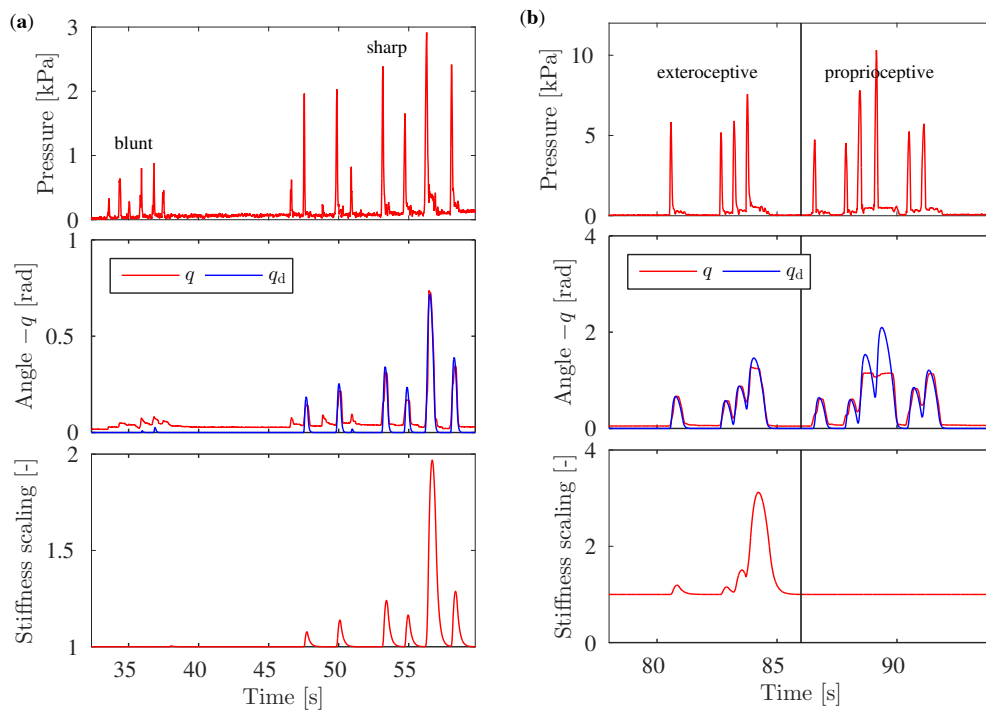


Figure 5.14: (a) aRNS reflex response for blunt and sharp contacts. (b) aRNS reflex response based on extero- (Biotac) and proprioceptive (momentum observer) information. © 2017 IEEE [253]

5.6.4 A proposal: Reflex stack for humanoids

The aRNS can also be extended to humanoid robots. For this, a humanoid reflex stack is proposed, see Fig. 5.15.

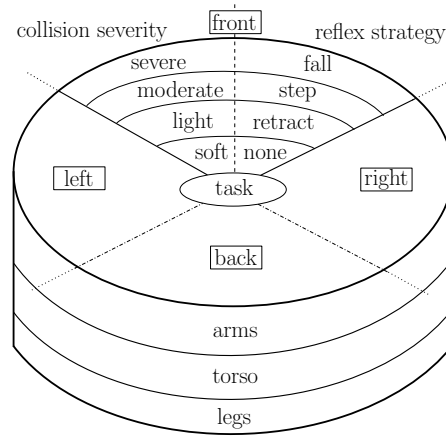


Figure 5.15: Humanoid reflex stack. © 2016 IEEE [252]

Contacts are classified by suitable algorithms into the classes *soft*, *light*, *moderate* and *severe*. Note that other schemes are possible as well. In correspondence to these classes and based on collision location and orientation, context-dependent reflex strategies can be designed (see “reflex strategy” in Fig. 5.15).

The reflex movements are visualized using a dynamic simulation model of the Atlas robot. Two examples of possible collisions and according reflex movements at the leg and the arm are shown, see Fig. 5.16. In Fig. 5.16a, one moderate contact at the right knee results in a step to the left away from the contact direction. In Fig. 5.16b, one light contact at the right lower arm leads to a retraction of the upper body and weight-shifting to the left leg, away from the collision.

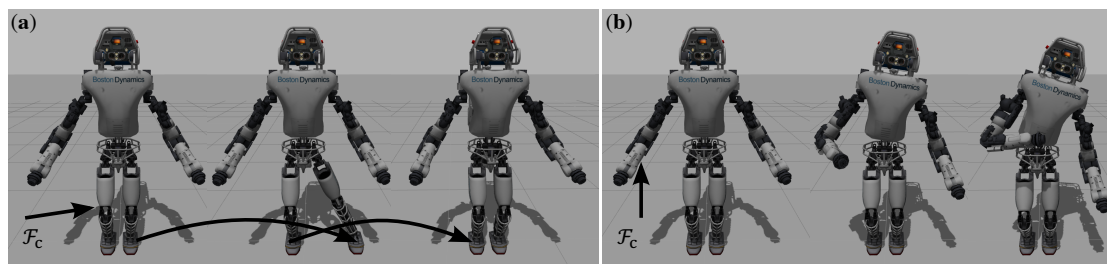


Figure 5.16: (a) Moderate collision at the right knee and according reflex reaction. (b) Light collision at the right arm and according reflex reaction. © 2016 IEEE [252]

5.7 Discussion

This work enables soft robots to not only measure or estimate contacts but also to sense and interpret them based on novel bio-inspired controls. For this, the concept of an aRNS was developed, which architecture and basic functionality mimic its human antitype. The concept is designed to unify different sensing modalities and let the robot respond in a human-inspired way to perceived stimuli. Specifically, this work introduces a sensory pathway from mechanical collision quantities such as contact forces and stresses to *artificial Robot Neuron* firing caused by quantities such as penetration depth, contact timing, and aRN density in the involved tissue layers. This concept makes it possible to design new and interesting collision reflex reaction behaviors. Depending on the spiking rate, the robot executes protective behavior of varying intensity as an escape strategy before trying to re-engage into the previous task again. The aRNS framework was experimentally validated using a 7-DoF light-weight robot and a pneumatically actuated finger prosthesis testbed. Furthermore, a humanoid reflex stack was proposed based on the aRNS.

6 Superhuman finger reflexes for touch and heat

In robotics, Asimov's First Law states that “*A robot may not injure a human being or, through inaction, allow a human being to come to harm.*” [250]. Recently, the first robots were equipped with an engineered proprioceptive reflex system for establishing safe human-robot contacts [4][5] and left the safety cages even in the real world. With the recent rise of artificial intelligence and sophisticated interaction control, more than ensuring human safety alone becomes necessary and within reach. Robots need to purposefully and sensitively interact with the world, including humans. In this sense, Asimov's Third Law states that “*A robot must protect its own existence...*” [250], suggesting to give robots similar abilities to humans. In Chapter 5, the first artificial Robot Nervous System [251] generating protective reflex motions for robots was introduced, motivated by the human NWR. It proves that robots are in principle able to protect themselves from physical sources of danger, such as high force or temperature, through adequate artificial pain-induced retraction movements.

However, it remains unclear how such a framework should be parameterized and which sensory configuration may, in the end, achieve superhuman performance. Therefore, to develop novel human-inspired reflex capabilities to a full scale, it is essential to thoroughly understand the reflex mechanism of humans on an algorithmic and systemic level. Thus, this work aims to answer the following research questions (Fig. 6.1b):

Are the insights from Chapter 2 transferable to robot reflexes and which specific sensory setup, ranging from traditional *tactile* (Method A) and *proprioceptive* (Method B) to *proprioceptive forces and link segment acceleration* (Method C) is performing best? (Q4)

The selection of sensors in Methods A, A2, and B is based on human models, e.g., touch and heat receptors in the skin, and position and torque sensors by means of muscle spindles and Golgi tendon organs, respectively. Motivated by the human sense of acceleration in the vestibular system, in Method C this concept is transferred to the limbs by adding accelerometers to the link segments.

To address this research question (Fig. 6.1b), in this chapter novel human-inspired reflex controls are designed based on the aRNS and considering the results from Chapter 2. They are experimentally validated on a robot finger system, having similar inertial properties to the human one for reasons of quantitative comparability.

6 Superhuman finger reflexes for touch and heat

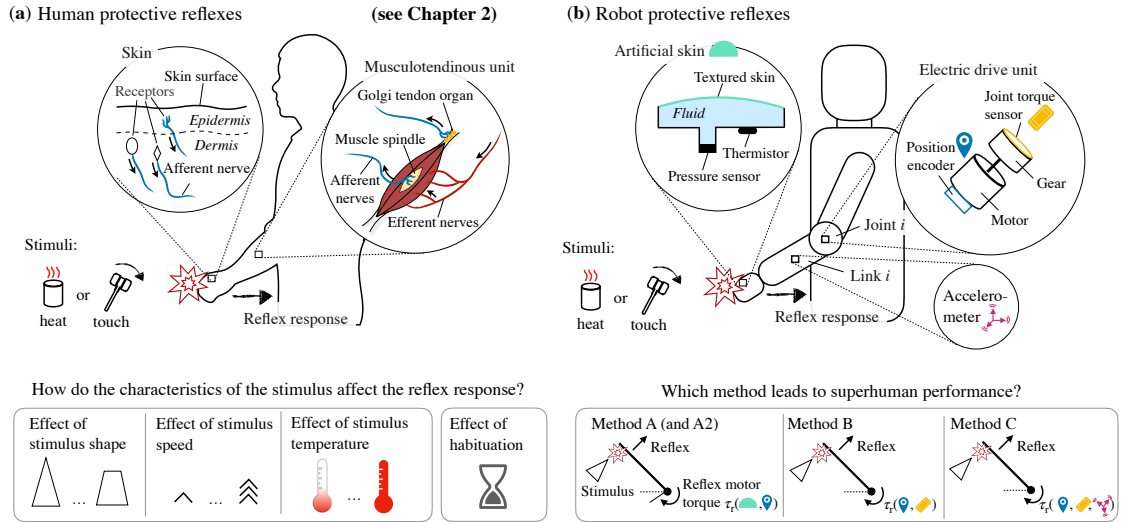


Figure 6.1: Protective reflexes in humans and robots. **(a)** Noxious stimuli are perceived by a multitude of receptors in the skin, which are processed by the spinal cord and brain and trigger protective reflexes via musculoskeletal units (**covered in Chapter 2**). **(b)** In this chapter, protective robot reflexes are triggered based on tactile perception (Method A), proprioceptive forces (Method B), or proprioceptive forces with measurements of link segment acceleration (Method C). Method A2 refers to robot temperature reflexes based on thermistor measurements.

6.1 From human to robot

Inspired by the results of the human finger reflex case study (Chapter 2) and building on the idea of an aRNS framework (Chapter 5), this chapter introduces a human-inspired robot reflex control system compatible with different sensory arrangements. Inspired by the subject's 5-phase reflex launch sequence (Chapter 2), this work introduces a biologically plausible robot reflex response composed of

- i) a short and instant *feed-forward joint torque* (corresponding to the MTR observed in phase II in Fig. 2.3),
- ii) a retraction *equilibrium position* adaptation (corresponding to the retraction observed in phase IV in Fig. 2.3), and
- iii) a recovery *equilibrium position* adaptation (corresponding to the recovering observed in phase V in Fig. 2.3).

To maximize robot reflex performance, the “Hold” phase (cf. phase III in Fig. 2.3) was removed. A custom-built, one degree of freedom (DoF) robot finger serves as a testbed (Fig. 6.2a and Fig. 6.2b). Three sensory arrangements for reflexes elicited by the conical frustum are employed. They are based on tactile sensation (Method A), proprioception in combination with a momentum observer (Method B), and proprioception with link

segment acceleration measurements (Method C) (Fig. 6.2c). The same tactile sensor as in Method A is used to trigger temperature reflexes, which is referred to as Method A2 throughout this chapter (Fig. 6.2c). For methods Method A, B and C, the estimate $\hat{\tau}_{\text{ext}}(t)$ (6.2) of the external torque above a constant threshold is considered to be harmful to the robot (Fig. 6.2c). In Method A2, the measured temperature ϕ above a constant temperature is considered to be harmful to the robot. Robot experiments were designed in analogy to the human case study using the same experimental setup (Fig. 2.2a), except that the robot finger substituted the human. A detailed description of the robot finger testbed, the reflex control approach and the methods can be found in the ‘‘Materials and Methods’’ section.

6.2 Robot finger testbed

6.2.1 Design

Figure 6.2a shows a schematic of the robot finger and the communication between its components. The finger is composed of an integrated *robot joint*, a *finger phalanx*, a

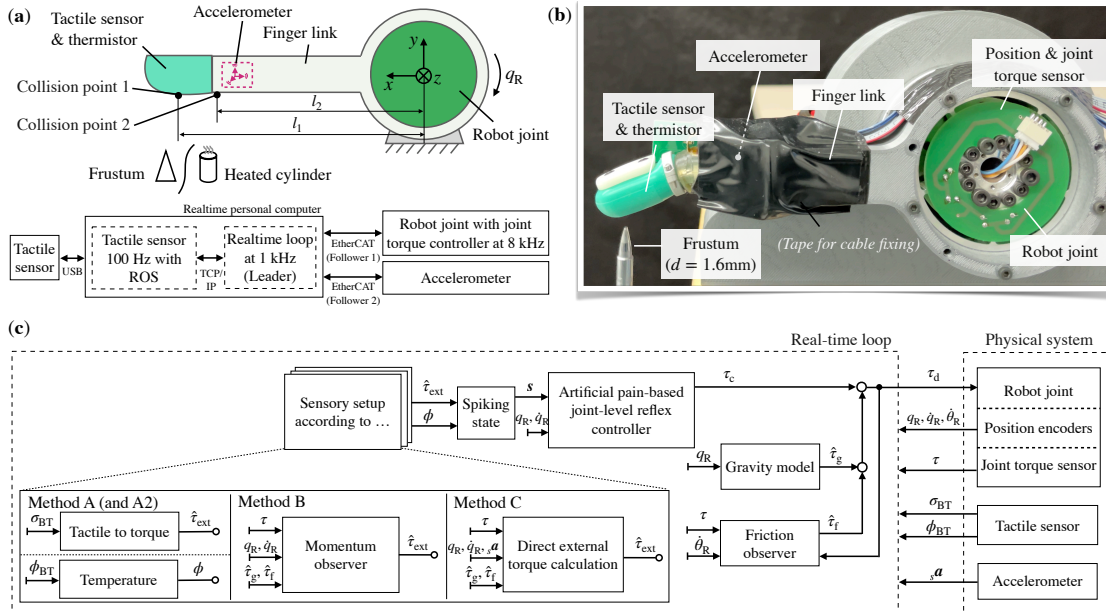


Figure 6.2: Robot finger testbed. (a) Schematic of robot finger testbed and communication. (b) Physical system. (c) Control diagram.

tactile sensor, and an *accelerometer*. The robot joint integrates a servo motor *ILM50x08* (TQ-System GmbH, Germany), which is connected to a 50:1 *strain wave gear* (Harmonic Drive SE, Germany), a self-developed *articulated joint torque sensor* based on strain gauges, and corresponding printed circuit boards (PCBs). Motor position is measured by a rotary absolute encoder *AksIM-2* (RLS d.o.o, Slovenia). At the heart of the embedded electronics is a *Microchip ARM-cortex-M0+ microcontroller* (Microchip

Technology Inc., USA) that runs a closed-loop joint torque control at 8 kHz. The finger phalanx is 3D printed, made of polylactic acid (PLA) filament, and carries a biomimetic tactile *BioTac sensor* (SynTouch Inc., USA). This sensor is capable of sensing forces, microvibrations and temperature. Furthermore, an accelerometer *BMI055* (Robert Bosch GmbH, Germany) is firmly attached to the side of the phalanx. It is configured to measure accelerations up to $\pm 2 \times 9.81 \text{ m/s}^2$ at a sample rate of 1 kHz. A high-level joint impedance controller is implemented on a real-time personal computer (Leader) that communicates with the robot joint (Follower 1) via EtherCAT at 1 kHz (Fig. 6.2a). The accelerometer (Follower 2) is also connected via EtherCAT. The BioTac’s software driver provides the data at 100 Hz running with the Robot Operating System (ROS), which is integrated into the real-time loop using a TCP/IP-based ROS-realtime interface. An image of the physical robot finger is shown in Fig. 6.2b.

6.2.2 Rigid-body dynamics

The equation of motion of the fixed-base single DoF robot finger is

$$\tau = M\ddot{q}_R + \tau_g(q_R) + \tau_f(\dot{q}_R) - \tau_{\text{ext}}, \quad (6.1)$$

where $q_R, \dot{q}_R, \ddot{q}_R \in \mathbb{R}$ are joint position, velocity and acceleration, respectively. Furthermore, $M = \text{const.} \in \mathbb{R}_{>0}$ accounts for inertia, and $\tau, \tau_g(q_R), \tau_f(\dot{q}_R) \in \mathbb{R}$ are motor, gravity and friction joint torque, respectively. The external torque is $\tau_{\text{ext}} = \mathbf{J}_c^\top(q_R)\mathcal{F}_{\text{ext}}$, where $\mathbf{J}_c \in \mathbb{R}^6$ is the contact Jacobian and $\mathcal{F}_{\text{ext}} \in \mathbb{R}^6$ denotes the contact wrench.

6.2.3 Reflex control

To execute protective reflexes, novel human-inspired reflexes are introduced that build on the general artificial Robot Nervous System (aRNS) framework (Fig. 5). While aRNS’s mathematical framework is utilized, the sensory input and parameters inspired by the human reflex study results are chosen. Concretely, the *feed-forward joint torque* and *equilibrium position* of a *joint-level impedance controller* based on artificial pain sensation is adapted. *Artificial pain* is defined by the pain state vector $\mathbf{s} \in \mathbb{R}^n$, which is also the input to the controller. This vector contains—depending on the robot sensory configuration— $n \in \mathbb{N}^+$ usually physical quantities suitable to detect dangerous contacts for the robot. Here, the estimate $\hat{\tau}_{\text{ext}}(t)$ of the external torque and the temperature $\phi(t)$ above constant thresholds $\mathbf{s}_0 \in \mathbb{R}^2$ are considered to be harmful to the robot, and thus define the pain state vector to be

$$\mathbf{s}(t) = \begin{pmatrix} \hat{\tau}_{\text{ext}}(t) & \phi(t) \end{pmatrix}^\top. \quad (6.2)$$

The artificial pain-based *joint level reflex controller* is defined as

$$\begin{aligned} \tau_c(t) &= K(q_{R,d} - q_R(t)) - D\dot{q}_R(t) + \tau_{\text{ff}}(\mathbf{s}(t)), \\ q_{R,d} &= \int_0^t p(\mathbf{s}(t^*))dt^* + q_{R,0} \end{aligned} \quad (6.3)$$

where $K, D \in \mathbb{R}_{>0}$ denotes the desired joint stiffness and damping, respectively, and $q_{R,0}$ is robot's position prior withdrawal. Damping is set to $D = 0.7\sqrt{4KM}$. The desired equilibrium position $q_{R,d}$ is obtained by integrating the pain-driven speed

$$p(\mathbf{s}) = \begin{cases} \mathbf{k}_q^\top \mathbf{s} & \mathbf{s} > \mathbf{s}_0 \\ -\text{sign}(q_R(t) - q_{R,0}) \iint_t b_q dt^* & \mathbf{s} < \mathbf{s}_0 \wedge q_R(t) \neq q_{R,0} \\ 0 & \mathbf{s} < \mathbf{s}_0 \wedge q_R(t) = q_{R,0}, \end{cases} \quad (6.4)$$

where $\mathbf{k}_q \in \mathbb{R}^2$ is a gain vector. In a nutshell, the robot retracts the finger as a function of \mathbf{s} if $\mathbf{s} > \mathbf{s}_0$ and returns to its initial position $q_{R,0}$ at constant acceleration b_q if $\mathbf{s} < \mathbf{s}_0$. In analogy to (6.4), the pain-driven *feed-forward torque* is defined as

$$\tau_{ff}(\mathbf{s}) = \begin{cases} \mathbf{k}_{ff}^\top \mathbf{s} & \mathbf{s} > \mathbf{s}_0 \\ -\text{sign}(\tau_{ff,0}) \iint_{t^*} b_{ff} dt & \mathbf{s} < \mathbf{s}_0 \wedge q(t) \neq q_{R,0} \\ 0 & \mathbf{s} < \mathbf{s}_0 \wedge q_R(t) = q_{R,0}, \end{cases} \quad (6.5)$$

where $\mathbf{k}_{ff} > \mathbf{0} \in \mathbb{R}^2$ is a suitable gain vector, $b_{ff} > 0$ is a constant and $\tau_{ff,0}$ is the feed-forward torque at first time instant of $\mathbf{s} > \mathbf{s}_0$. Eventually, the desired motor torque is chosen to be

$$\tau_d = \tau_c + \hat{\tau}_g(q_R) + \hat{\tau}_f, \quad (6.6)$$

where $\hat{\tau}_g(q_R)$ denotes the modelled gravity torque. Furthermore, frictional effects are compensated using the friction observer in [265], whose output $\hat{\tau}_f$ is derived from the motor speed $\dot{\theta}$ and corresponds to the low-pass filtered friction torque. Figure 6.2C shows the overall control diagram.

6.3 Collision monitoring methods

In this work, the external torque is estimated or algebraically calculated for joint level control based on tactile sensation (Method A), proprioception (Method B), and proprioception with link segment acceleration measurements (Method C).

6.3.1 Tactile sensing

In *Method A*, BioTac's measured fluid pressure $\sigma_{BT}(t)$ is used, which highly correlates with contact force to estimated the external torque by

$$\hat{\tau}_{ext}(t) = (k_\sigma \sigma_{BT}(t) + F_0) l_1, \quad (6.7)$$

where the moment arm $l_1 \in \mathbb{R}_{>0}$ (Fig. 6.2a), and the constant parameters $k_\sigma, F_0 \in \mathbb{R}$ are determined in prior robot experiments. The same multi-modal sensor is also used to trigger temperature reflexes based on the signal

$$\phi(t) = \phi_{BT}(t) + \phi_0, \quad (6.8)$$

where the constant parameter $\phi_0 \in \mathbb{R}$ is determined prior robot experiments. $\phi_{BT}(t)$ is measured by the BioTac and correlates with temperature. Throughout this work, the temperature-based method is referred to as *Method A2* (Fig. 6.2c).

6.3.2 Proprioception

Method B is based on the momentum observer in ((4.4). In the single DoF case, this observer can be written as

$$\hat{\tau}_{\text{ext}}(t) = K_O \left(\int_0^t (\tau(t^*) - \hat{\tau}_g(t^*) - \hat{\tau}_f(t^*) - \hat{\tau}_{\text{ext}}(t^*)) dt^* - M \dot{q}_R(t) \right), \quad (6.9)$$

where $K_O > 0$ is the observer gain, and $\tau(t)$ is measured joint torque.

6.3.3 Proprioception and link segment acceleration sensation

In *Method C*, the external torque is calculated based on a link segment accelerometer attached to the robot finger phalanx (Fig. 6.2a). Considering the fixed-base system, the Cartesian acceleration ${}_w \mathbf{a} \in \mathbb{R}^3$ —expressed in world frame $\{w\}$ —at sensor location ${}_w \mathbf{r}(q_R) \in \mathbb{R}^3$ can be decomposed into

$${}_w \mathbf{a} = \begin{pmatrix} 0 \\ 0 \\ \ddot{q}_R \end{pmatrix} \times {}_w \mathbf{r}(q_R) + \begin{pmatrix} 0 \\ 0 \\ \dot{q}_R \end{pmatrix} \times \left(\begin{pmatrix} 0 \\ 0 \\ \dot{q}_R \end{pmatrix} \times {}_w \mathbf{r}(q_R) \right) \quad (6.10)$$

${}_w \mathbf{a}$ is calculated from sensor readings ${}_s \mathbf{a} \in \mathbb{R}^3$ by

$${}_w \mathbf{a} = {}^s \mathbf{R}_w^\top(q_R) ({}_s \mathbf{a} - {}_s \mathbf{a}_{\text{bias}} - {}^s \mathbf{R}_w(q_R) {}_w \mathbf{g}), \quad (6.11)$$

where the rotation matrix ${}^s \mathbf{R}_w(q_R) \in \text{SO}(3)$ from $\{w\}$ to sensor frame $\{s\}$, as well as sensor bias ${}_s \mathbf{a}_{\text{bias}} = \text{const.} \in \mathbb{R}^3$ are calibrated by sinusoidal reference trials and optimization prior experiments. By combining (6.10) and (6.11), one is able to obtain \ddot{q}_R from ${}_s \mathbf{a}$. Consequently, one obtains the estimate $\hat{\tau}_{\text{ext}}$ algebraically from (6.1), given that $\hat{\tau}_g(q_R)$, $\hat{\tau}_f$, τ are known from the model, friction observer and joint torque sensor, respectively. Eventually, the estimate $\hat{\tau}_{\text{ext}}(t)$ is denoised by applying a second-order Butterworth low-pass filter with cut-off frequency 25 Hz.

6.4 Experimental protocol

Robot experiments were designed in analogy to the human case study (see Chapter 2). The same experimental setup was used (Fig. 2.2a), except that the human was substituted by the robot finger. Only the blunt conical frustum ($d = 1.6$ mm) is applied (to protect sensor's skin) at *Collision point 1* (Method A) and at *Collision point 2* (Method B/C) with highest speed $v = 0.1$ m/s (Fig. 6.2a). This work distinguishes between these two collision points as the tactile sensor is assumed not to be present in Method B/C, and moreover, the sensor would change the contact dynamics. With respect to the temperature reflexes (Method A2), the same metal cylinder was used as in the human case study, heated to $\vartheta \approx 55^\circ\text{C}$ at speed $v = 0.1$ m/s. The experiments were repeated three times in a row for Method A, A2, B, and C, respectively.

Table 6.1: Human and robotic finger parameters. While the mass of the robot finger was measured, the human finger mass density is estimated to be 1.09 g/cm^3 [266]. The parameters relate to finger phalanxes modelled as cuboids.

	Length×Width×Height [cm×cm×cm]	Mass [g]	Moment of inertia [kg cm ²]
Human finger	9.5×2.1×1.8	39.1	1.19
Robot finger	12.5×1.78×1.78	55	58.66

6.5 Performance metrics

The performance of robot and human reflexes is compared based on three characteristic time intervals: detection time Δt_d , activation time Δt_a , and escape time Δt_e . For the human, the detection time is defined as $\Delta t_d := (t_{\text{MTR}} - t_c)/2$ (t_{MTR} refers to the start of the muscle twitch excitation of the extensor muscle, cf. Phase II in Fig. 2.3). Activation time is defined as $\Delta t_a := (t_r - t_c) - \Delta t_d$, and escape time is defined as $\Delta t_e := t'_c - t_r$ (time instants t_c , t_r , and t'_c are illustrated in Fig. 2.3). For the robot, the detection time Δt_d is defined as the time when the signal—the estimate $\hat{\tau}_{\text{ext}}(t)$ of the external torque or the measured temperature $\phi(t)$ (cf. 6.2)—reaches six times the standard deviation of its noise calculated in the time window $t \in [t_c - 100\text{ms}, t_c]$. The robot activation time Δt_a is defined as the time interval between contact detection and the first time instant of positive actuation torque $\tau_c(t) > 0$ (cf. 6.3). The robot escape time Δt_e is defined as the time interval between activation and contact loss. In the following, the reflexes triggered by the conical frustum is referred to as *mechanical/touch reflex*, and the reflex triggered by the heated cylinder as *temperature reflex*.

6.6 Results

6.6.1 Robot vs human: touch reflexes

To ensure comparability between the subject and robot finger, the robotic finger was designed to approximately match the geometric dimensions and mass of the human finger (Tab. 6.1). To compensate for any modeling errors in favor of the human, the moment of inertia is larger for the robot (Tab. 6.1).

For all three Methods A, B and C, the reflex controller defined in (6.3) to (6.6) is used. The reflex controller of the robot is configured in such a way that a mechanical reflex is elicited if the estimated external torque $\hat{\tau}_{\text{ext}}(t)$ (6.2) exceeds the threshold $s_{0,1} = 0.4 \text{ Nm}$, which corresponds twice the external torque experienced by the subject (i.e. $2F_c l_H \approx 0.4 \text{ Nm}$, where l_H is shown in Fig. 2.2a). The control parameters are set to $K = 15 \text{ Nm/rad}$ (6.3), $\mathbf{k}_q = [800 \text{ rad/sNm} \quad 0 \text{ rad/s}^\circ\text{C}]^\top$ and $b_q = 0.05 \text{ rad/s}^2$ (6.4), and $\mathbf{k}_{\text{ff}} = [25 \quad 0 \text{ Nm}/^\circ\text{C}]^\top$ and $b_{\text{ff}} = 100 \text{ Nm/s}^2$ (6.5). A comparison of the reflex trajectories between robot and human in terms of lowest activation time Δt_a unveils that the robot reflexes are superior to the human mechanical reflex regardless of Method A, B, or C used

6 Superhuman finger reflexes for touch and heat

(upper plot in Fig. 6.3a). For those trials, the maximum angular speed is slightly lower

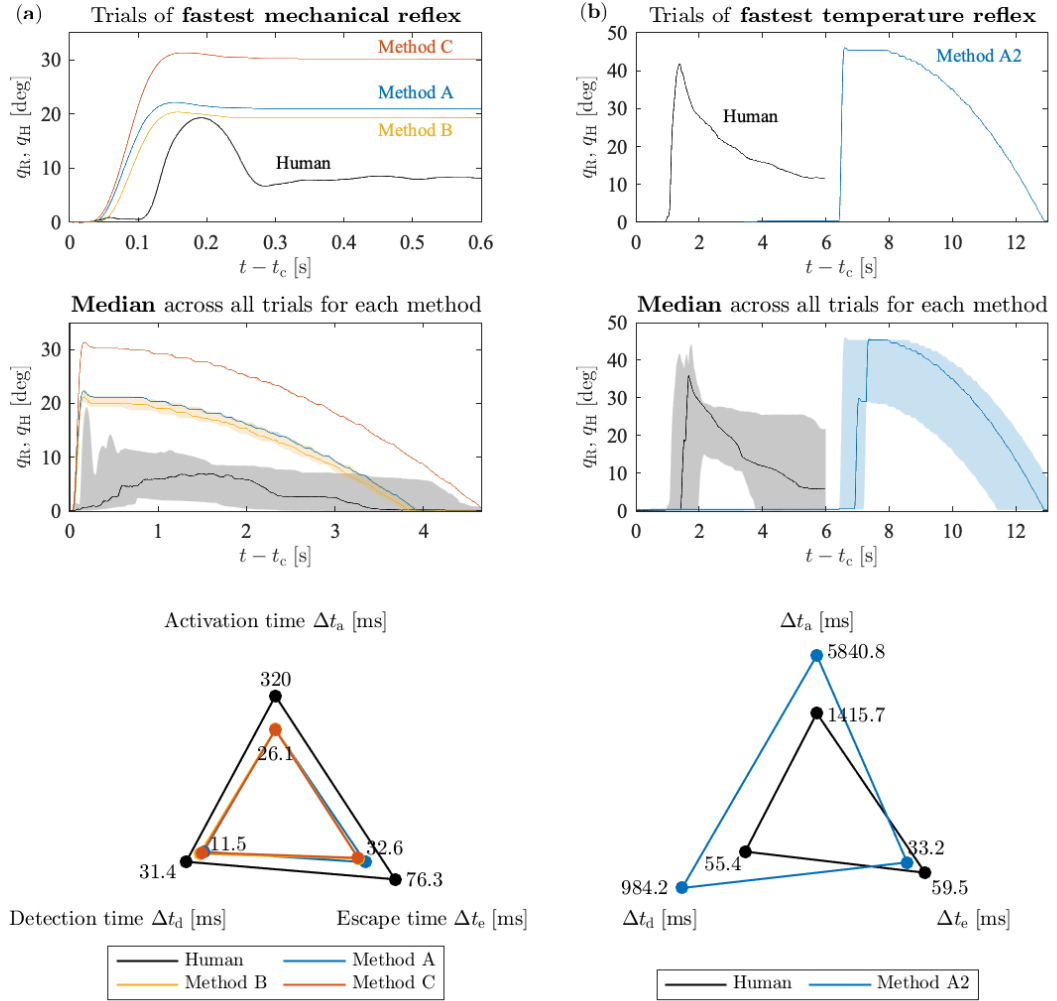


Figure 6.3: Robot versus human protective reflexes. (a) Robot joint angle q_R and human joint angle q_H of mechanical reflex with lowest activation time Δt_a (upper plot). Time 0s marks the start of contact. The median (solid lines) and the envelope of maximum/minimum values (colored areas) of human and robot trials, respectively, over an extended time period (middle plot). Mean of detection time Δt_d , activation time Δt_a , and escape time Δt_e (bottom plot), which are defined in the text (see “Performance metrics” section). (b) Same as in a but for temperature reflexes.

for the robot reflexes (Method A: $\dot{q}_{R,\max} = 5.95$ rad/s, Method B: $\dot{q}_{R,\max} = 6.06$ rad/s, Method C: $\dot{q}_{R,\max} = 7.83$ rad/s) compared to the human ($\dot{q}_{H,\max} = 8.02$ rad/s). Note that higher robot speeds can be easily achieved by increasing aRNS parameter gains, like the finger retraction amplitude. Displaying the median (solid lines) and the envelope of the maximum/minimum (colored areas) across all trials for each Method A, B, C and the human underline that robot reflexes show superior performance and are more predictable

compared to human (middle plot in Fig. 6.3a). The robot does not only show lower activation time, but also lower detection and escape time (bottom plot in Fig. 6.3a). Comparing Methods A, B, and C with each other based on the performance metrics reveals that Method A has lowest detection time, and Method C lowest activation and escape time (Table 6.2). Comparing the best mechanical reflex performance of the robot (mean values in Tab. 6.2 highlighted in bold) with those of the human unveils that the robot detects contact ≈ 5 times faster, activates withdrawal ≈ 15 times faster, and escapes contact ≈ 3.5 times faster.

6.6.2 Robot versus human: temperature reflexes

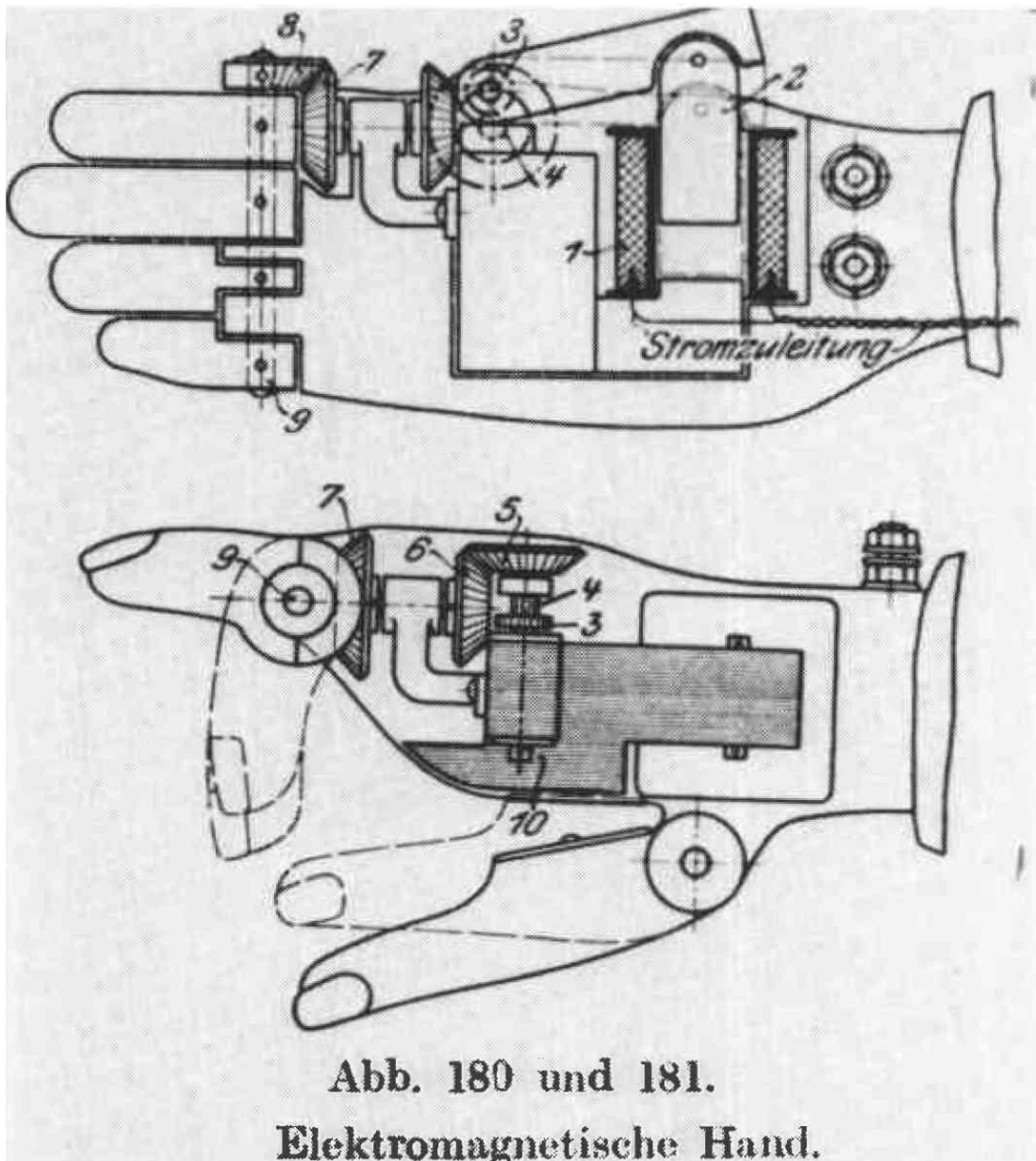
Here, the reflex controller in (6.3) to (6.6) is applied. The reflex controller is configured in such a way that a robot temperature reflex is elicited if the sensed temperature $\phi(t)$ (6.2) exceeds $s_{0,2} = 48$ °C, which corresponds to the same temperature that triggered a reflex in the subject (upper plot in Fig. 2.5a). The control parameters are set to $K = 15$ Nm/rad (6.3), $\mathbf{k}_q = [0 \text{ rad/s Nm} \quad 10 \text{ rad/s}^\circ\text{C}]^\top$ and $b_q = 0.05 \text{ rad/s}^2$ (6.4), and $\mathbf{k}_{ff} = [0 \quad 0 \text{ Nm}/^\circ\text{C}]^\top$ and $b_{ff} = 0 \text{ Nm/s}^2$ (6.5). A comparison of the reflex movements between robot and human in terms of lowest activation time Δt_a shows that the robot reflexes are inferior to the human temperature reflex (upper plot in Fig. 6.3b). Displaying the median (solid lines) and the envelope of the maximum/minimum (colored areas) across all trials for the robot (Method A2) and the human confirms that the robot reflexes are inferior to the human (middle plot in Fig. 6.3b). Although the robot shows lower detection and activation time, it is faster in escaping the contact (cf. Δt_e in the bottom plot in Fig. 6.3b, and Table 6.2). Also for the fastest trials (upper plot in Fig. 6.3b) the maximum angular speed is higher for robot reflexes (Method A2: $\dot{q}_{R,\max} = 7.88 \text{ rad/s}$, compared to human $\dot{q}_{H,\max} = 6.03 \text{ rad/s}$). Comparing the best temperature reflex performance of the robot (mean values in Tab. 6.2 highlighted in bold) with those of the human unveils that the robot detects contact ≈ 17 times slower, activates withdrawal ≈ 4 times slower, and escapes contact ≈ 1.8 times faster.

Table 6.2: Performance metrics. Mean and standard deviation of detection time Δt_d , activation time Δt_a , and escape time Δt_e (definitions see ‘‘Performance metrics’’ section) for human and robot trials. Lowest values are highlighted in bold.

Stimulus	Method	Δt_d [ms]	Δt_a [ms]	Δt_e [ms]
	Human	31.42 ± 9.23	257.27 ± 174.96	76.27 ± 23.62
Conical frustum	Method A	5.88 ± 3.84	23.00 ± 5.00	32.63 ± 0.25
	Method B	11.50 ± 1.08	26.13 ± 1.93	23.12 ± 0.25
	Method C	7.75 ± 1.32	16.38 ± 0.75	21.62 ± 0.75
Heated cylinder	Human	55.90 ± 15.32	1415.70 ± 322.83	59.50 ± 15.86
	Method A2	984.17 ± 398.20	5840.83 ± 673.68	33.17 ± 5.48

6.7 Discussion

Inspired by the results of the human finger reflex case study (Chapter 2) and building on the idea of an aRNS framework (Chapter 5), this chapter introduced a human-inspired robot reflex control system compatible with different sensory arrangements. To compare human and robot reflex performance, the human-inspired reflex controls were experimentally validated on a robot finger system, having similar inertial properties to the human one for reasons of quantitative comparability. This system was designed to match the geometric and mass dimensions of the human finger. At the same time, the robot moment of inertia was even selected higher to ensure a rather conservative comparison. Three sensory arrangements were investigated; two classical ones *tactile sensation* and *proprioception*, as well as the rather unconventional one *proprioception with link segment accelerometer*. Thanks to well-engineered robot sensors, low signal transmission delays, and a high controller update rate, all methods turned out to be superhuman concerning detection, activation, and escape time for the collisions with the frustums. Results also show that in the case of temperature reflexes, the human is still superior to the robot in terms of detection and activation time but has lower dynamics in escaping the threat. This means that the robot's mechanics showed higher performance but still lag behind humans in sensing. However, equipping the robot with non-human-inspired temperature sensors, such as thermal imaging cameras, could even improve sensory performance in the future.



Mechanical drawing of perhaps the first electrically powered hand prosthesis, Ersatzglieder und Arbeitshilfen (Substitute Limbs and Work Aids) 1919 [160, 161].

Part III

Coordinated prosthesis control

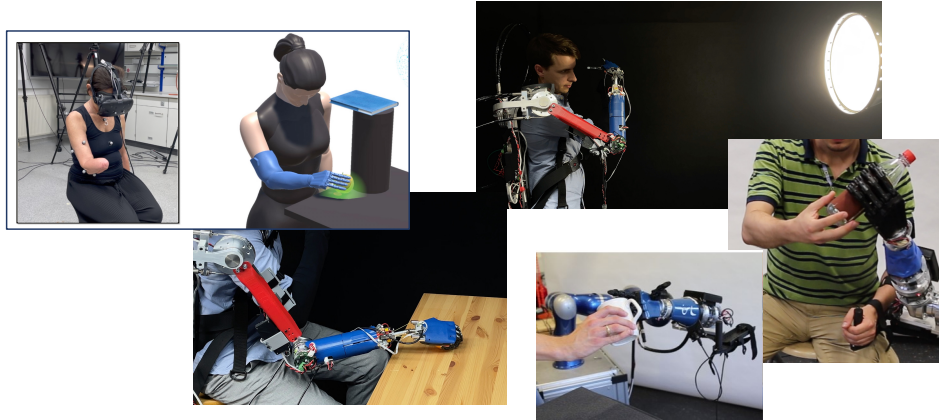


Figure 6.4: Impressions from the work carried out in Part III.

Part III presents novel coordinated upper limb prosthesis control schemes relating to research questions Q5 and Q6. Chapter 7 presents a database of human arm coordination in everyday tasks, the content of which is published in [234, 267]. Secondly, semi-autonomous controls are presented based on a custom developed exo-prosthesis prototype Chapter 8, which is published in [268]. Thirdly, a more advanced synergy complement control approach is presented in Chapter 9. This work is part of the publication in [269]. All three chapters are briefly summarized below, while Fig. 6.4 shows some impressions from these works.

Chapter 7: Database of coordinated human arm motion (used in Chapter 9) This chapter outlines the experimental design of a user study with healthy subjects. The goal is to generate a database of human upper limb trajectories for daily life tasks to serve the coordinated controls developed in Chapter 9.

Chapter 8: From sequential to coordinated control (Q5) In this work, the concept of a semi-autonomous upper-limb exo-prosthesis is presented. The exoskeleton provides the residual limb's kinematic data to design more intelligent coordinated control concepts. Here, in contrast to established standard *sequential* strategies, all joints are moved simultaneously according to a desired task. In combination with an app-based programming framework, task goals are set either via kinesthetic teaching or autonomously via 3D visual perception.

Chapter 9: Synergy complement control (Q6) Limb-driven upper-limb prosthesis control promises to allow direct control solely by residual limb movements instead of unnatural and complex to use muscle activation. In this work, human arm coordination in everyday tasks (from Chapter 7) served the design of a novel control framework denoted synergy complement control. It allows a prosthesis to complement residual limb movements autonomously. Thus, the hybrid system naturally renders intended movements for its carrier and adapts online to new tasks.

7 A multi-modal database of human reach and grasp tasks

This chapter outlines the experimental design of a user study with healthy subjects for daily life reach and grasp tasks. These tasks were selected within the European Union’s Horizon 2020 “SOFTPRO” project (No. 688857) consortium as a joint effort. The resulting database serve the design of coordinated controls developed in Chapter 9.

7.1 Experimental procedures

7.1.1 Participants

The experiments were approved by the ethics committee of Leibniz Universität Hannover, Germany, and were conducted with respect to the Declaration of Helsinki. Six healthy human subjects (age: 30 ± 5.81 , right-handed, male) participated in the experiments.

7.1.2 Design and protocol

The goal was to perform *30 daily-life table-top manipulation tasks* involving upper-limb movements (Tab. 7.1 and Tab. 7.2). These tasks were selected within the European Union’s Horizon 2020 “SOFTPRO” project (No. 688857) consortium as a joint effort. Each task was repeated three times in a row. The experiments took place in an electromagnetically isolated chamber to avoid disturbing signal interferences. The human subject was seated upright on a stool in front of a table, without any fixation or constraints on any body parts. On the table various objects were located, see Fig. 7.1. Motion trajectories, surface EMG, and scalp EEG were recorded simultaneously and synchronized.

7.1.3 Apparatus

Motion Tracking A Vicon MXT10s (Vicon Motion Systems Ltd, UK) system was used to capture the motion of the upper limb at 500 Hz. *Essential* markers were placed on significant skin landmarks, see Fig. 7.2, while several *redundant* markers were used to facilitate data postprocessing (not shown in Fig. 7.2 for simplicity). The Cartesian positions of all m essential markers are gathered in a stacked vector $\mathbf{x}_m \in \mathbb{R}^{3m}$.

Surface Electromyography EMG was measured via a Refa system (TMSi, Netherlands) in a bipolar manner at 2 kHz. Following the SENIAM guideline [208], the microelectrodes were placed on the muscles that were palpated according to [16]. The

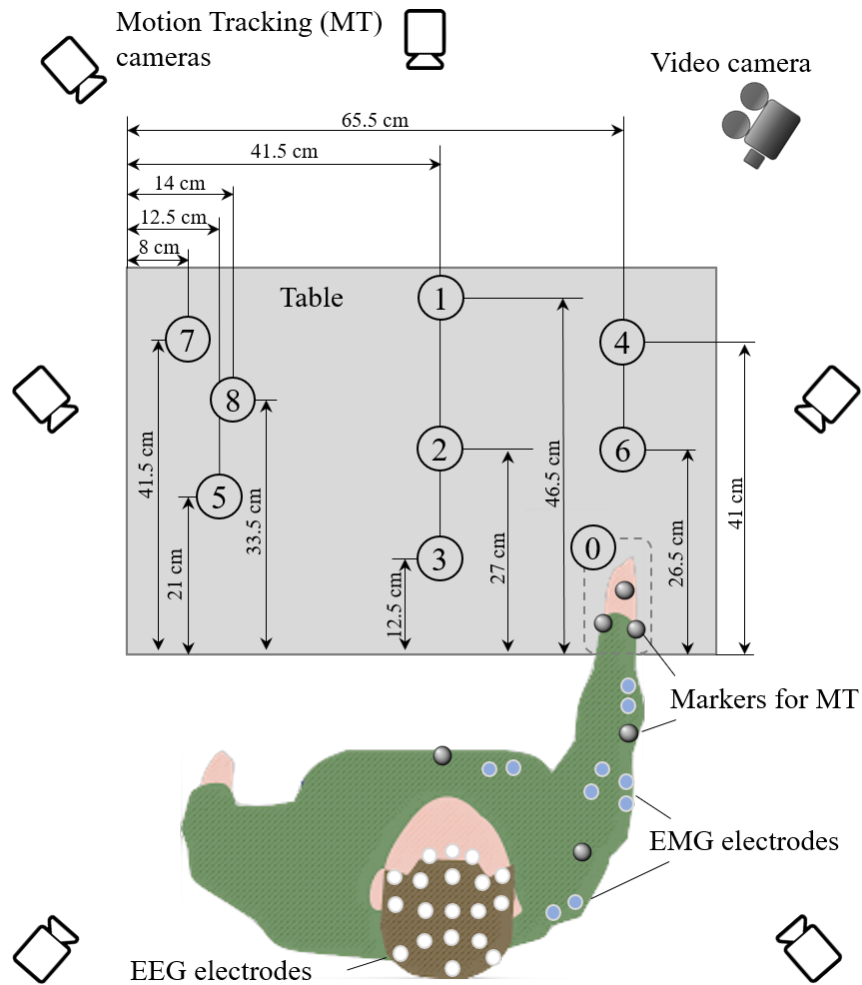


Figure 7.1: Schematic experimental setup. Numbers ①–⑧ refer to characteristic locations of involved objects / tools. The camera, electrode and marker placement does not correspond to the true positions and are only shown for clarity. ©2018 IEEE [234]

innervation zones were avoided if possible, see [270]. In total, 29 shoulder, arm and forearm muscles were recorded, see Tab. 7.3.

Scalp Electroencephalography An actiCHamp active EEG electrode net of 32 unipolar channels (Brain Products GmbH, Germany), was used at 10 kHz to record brain activity. As already mentioned, the EEG synergy analysis is out of the scope of this work and left for future work.

Table 7.1: The *intransitive* and *transitive* daily-life tasks, which were selected within the SOFT-PRO project consortium as a joint effort. ①–⑧ denote locations illustrated in Fig. 7.1. ©2018 IEEE [234]

No.	Task	Description
0	Initial	Place the forearm on the table at approximately ① with an open palm facing downwards and relax, flex the elbow to $\approx 90^\circ$. This posture defines the start and end posture of task 1 – 30.
1	OK gesture	Lift the hand from the table, and gesture an OK at the face height.
2	Thumb down	Extend the arm along the sagittal plane, and direct the extended thumb downwards.
3	Exultation	Extend the arm up in the air with a closed fist.
4	Hitchhiking	Extend the arm laterally in the frontal plane and parallel to the floor, with a closed fist and an extended thumb.
5	Block sun light	Bring the hand to the forehead, which should be touched by the thumb and the index finger, and the palm faces downwards.
6	Hello wave	Greet someone by waving hand.
7	Military salute	Bring the flat hand to the head and keep the upper arm parallel to the floor.
8	Stop gesture	Extend the arm along the sagittal plane and parallel to the floor, with an open palm facing forward.
9	Pointing	Extend the arm forward and point at something straight ahead with the index finger.
10	Silence gesture	Bring the index finger on the lips, with the other part of the hand being closed.
11	Suit case	Reach and grasp a small suitcase (placed at ① along the frontal plane, weight 2.7 kg) from the handle, lift it and place it on the floor close to the stool, along the sagittal plane.
12	Glass	Reach and grasp a glass (0.17 kg, at ②), drink from it for ≈ 3 s and place it back to ②.
13	Phone receiver	Reach and grasp a phone receiver (0.15 kg, ②, along the sagittal plane), carry it to the right ear for ≈ 3 s and place it back to ②.
14	Book	Reach and grasp a book (0.98 kg) on a shelf (between ① and ②, height: 61.6 cm from the table), put it on the table and open it (from the right side to the left side).
15	Small cup	Reach and grasp a small cup (0.17 kg, at ②, the handle directs rightwards) from the handle, drink from it for ≈ 3 s and place it back to ②.
16	Apple	Reach and grasp an apple (at ②), mimic biting and put it back to ②.
17	Hat	Reach and grasp a hat (at ④) from its top and place it on the head.
18	Cup	Reach and grasp a cup (0.24 kg, at ②) from its top, lift it and put it to ⑤.
19	Tray	Receive a tray (0.10 kg) from one-thirty (clock position) and place it to ②.
20	Key	Reach and grasp a key in a lock (at ②, the key faces the subject), extract it (without turning) from the lock and place it to ⑤.

7.2 Remarks

This generated database is part of the publication in [267]. The data can be downloaded together with the generated databases of the other project partners. In this dissertation, this database is used for the design of the syngery complement control method in Chapter 9. An analysis of kinematic and muscular synergies based on this database can be found in [234].

Table 7.2: The *tool-mediated* daily-life tasks, which were selected within the SOFTPRO project consortium as a joint effort. ①–⑧ denote locations illustrated in Fig. 7.1. ©2018 IEEE [234]

No.	Task	Description
21	Pour water	Reach and grasp a bottle (at ⑥, 500 mL full of water), mimic pouring water into a glass (at ②) for ≈ 3 s and put the bottle back to ②.
22	Smart phone	Reach and grasp a smart phone (at ②), unlock the screen, dial number, and put it back to ②.
23	Brush teeth	Reach and grasp a toothbrush (at ②, along the sagittal plane), mimic brushing teeth along horizontal axis, and put the toothbrush into a cylindrical holder (at ⑦).
24	Laptop	Reach for a laptop (between ② and ③) and open it without changing its position; the left hand can hold the laptop.
25	Pen	Reach and grasp a pen (at ⑥, along the sagittal plane) and draw a vertical line from the top to the bottom on the table.
26	Pencil	Reach and grasp a pencil (at ⑥, along the frontal plane) and put it into a squared pencil holder (at ⑧).
27	Tea bag	Reach for a tea bag in a cup (at ②), remove it from the cup and place it on the table.
28	Open a door	Reach for a door handle (at ②, height: 24.5 cm from the table) and grasp it with the whole hand, turn it, open the door (extend the arm), and release the handle.
29	Ball	Reach and grasp a ball (at ②), place it into a basket on the floor (close to the stool).
30	Unscrew	Unscrew a bottle (at ③) using the right hand, while the left hand is holding the bottle, and place the cap on a shelf (between ① and ②, height: 61.6 cm from the table).

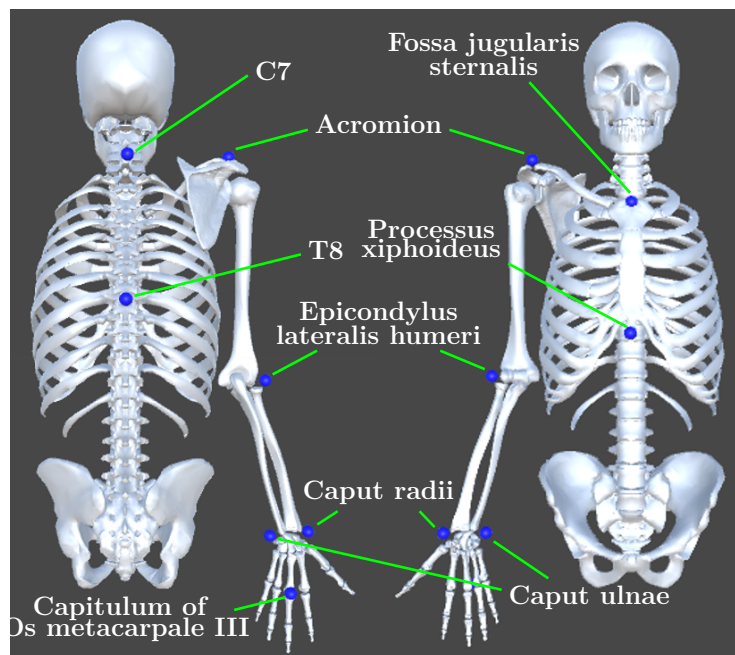


Figure 7.2: The anatomical landmarks (*blue spheres*) that define the placement of essential markers for motion tracking. ©2018 IEEE [234]

Table 7.3: List of measured muscles (IZ: innervation zone). ©2018 IEEE [234]

Muscles	Subregions	Abbreviation	IZ avoidance
<i>M. trapezius</i>	<i>Pars descendens</i>	TRPc	✓
	<i>Pars transversa</i>	TRPt	✓
	<i>Pars ascendens</i>	TRPa	✓
<i>M. deltoideus</i>	<i>Pars clavicularis</i>	DLTc	✓
	<i>Pars acromialis</i>	DLTa	✓
	<i>Pars spinalis</i>	DLTs	✓
<i>M. latissimus dorsi</i>		LTDt	✓
<i>M. pectoralis major</i>	<i>Pars clavicularis</i>	PMJc	✓
	<i>Pars sternocostalis</i>	PMJs	✓
	<i>Pars abdominalis</i>	PMJr	✓
<i>M. biceps brachii</i>	<i>Caput longum</i>	BICl	✓
	<i>Caput breve</i>	BICs	✓
<i>M. triceps brachii</i>	<i>Caput longum</i>	TRClg	✓
	<i>Caput laterale</i>	TRClt	✓
<i>M. pronator teres</i>		PRNT	✓
<i>M. flexor carpi radialis et</i> (if present) <i>M. palmaris longus</i>		FCR	probably not avoided
<i>M. flexor carpi ulnaris</i>		FCU	IZ unknown
<i>M. flexor digitorum superficialis</i>		FDS	IZ unknown
<i>M. flexor pollicis longus</i>		FPL	IZ unknown
<i>M. extensor digitorum</i>		EDT	IZ unknown
<i>M. extensor digiti minimi</i>		EDM	IZ unknown
<i>M. extensor carpi ulnaris</i>		ECU	IZ unknown
<i>M. abductor pollicis longus et</i> <i>M. extensor pollicis brevis</i>		APL&EPB	IZ unknown
<i>M. brachioradialis</i>		BRD	✓
<i>M. extensor carpi radialis</i>		ECR	✓
<i>M. abductor digit minimi</i>		ADM	cannot be avoided
<i>M. flexor pollicis brevis</i>		FPB	cannot be avoided
<i>M. abductor pollicis brevis</i>		APB	cannot be avoided
<i>M. interosseus dorsalis I</i>		DI1	IZ unknown
Electrocardiography		ECG	–

8 From sequential to semi-autonomous control

Semi-autonomous upper limb prostheses that can sensitively interact with their environment are one of the main goals of current prosthetics research. Available, mostly rigid upper-limb prosthetic devices allow affected persons to regain functional parts of lost abilities, enabling them to grasp and manipulate again. However, upper-limb state-of-the-art prostheses have rather low autonomy and are quite insensitive to the environment from a haptic perspective. A major issue in terms of wearability is the mechanical stump-prosthesis interface. For almost all available upper limb prosthetic devices skin abrasions occur due to high loads on the residual limb. Furthermore, the widely used sequential motion control in available prostheses is rather unintuitive and difficult to use in contrast to the natural coordinated movement strategies of humans, in which the joints of the limbs are moved simultaneously.

In robotics research, force and joint-torque controlled soft robots [271], which are capable of sensitive and safe interaction with their environment, have advanced the field of manipulation and interaction to a new level. This technology is regarded as a key enabler for a new generation of sensitive and safe machines and allows for new applications, including safe human-robot co-working [4].

In this work, the novel concept of semi-autonomous *exo-prosthetics* first introduced in [129] together with a full dynamics model of this new system class is formally introduced. An *exo-prosthesis* is defined as a unified hybrid between *exoskeleton* and *prosthesis*, see Fig. 8.1. To minimize stump reaction forces, gravity effects of the prosthesis shall be compensated via the exoskeleton part. Furthermore, the exoskeleton measures or at least estimates position, velocity and acceleration of the human residual limb, which is used to design more intelligent coordinated control.

An early robot-based prototype is presented, which consists of a newly developed soft-robotics enabled 2 DoF transhumeral prosthesis and an exoskeleton substitute, a joint level torque controlled lightweight robot. This intermediate step with a robot as exoskeleton replacement enables the early validation of a simplified form of system dynamics as well as the development of semi-autonomous control methods. The core contributions are (see Fig. 8.1):

- Formal introduction of upper-limb exo-prosthetics with human embodied exo-prosthesis dynamics model.
- Early robot-based prototype emulating several aspects of the future target system. The prosthesis is designed according to a mechatronic low-cost and lightweight

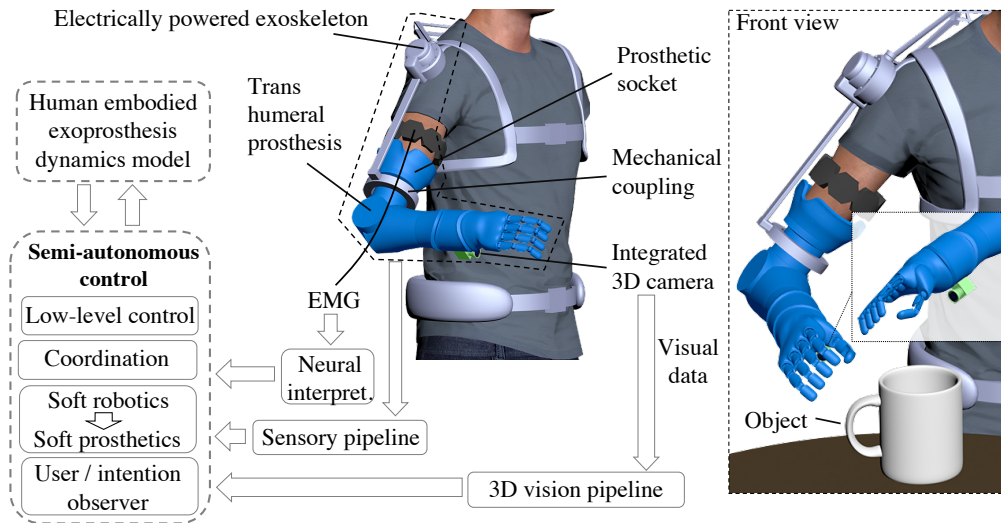


Figure 8.1: Towards a semi-autonomous exo-prosthesis system. © 2019 IEEE [268]

approach, equipped with soft-robotics key technologies such as flexible impedance control.

- Semi-autonomous kinesthetic coordinated prosthesis control strategy. The kinesthetic teaching can additionally be replaced by a visual tracking approach.
- First experimental evaluation of current exo-prosthesis system with an unimpaired subject.

8.1 Methods

8.1.1 Exo-prosthesis

8.1.1.1 Exo-prosthesis dynamics

In this section, the dynamics formulation of the coupled exo-prosthesis system is introduced, see Fig. 8.2. First, the dynamical description of the subsystems *prosthesis*, *exoskeleton* and *human* are separately derived. Then, the state space representation of the coupled system is formulated. Based on this, the simpler model of the intermediate robot-based version is derived, see Fig. 8.2.

Prosthesis A rigid-body upper-limb prosthesis can be described as a floating base articulated system. The $n = n_j + 6$ DoF system configuration is represented by $\mathbf{q} = (\mathbf{x}_b^\top \mathbf{q}_j^\top)^\top$, where $\mathbf{q}_j \in \mathbb{R}^{n_j}$ contains n_j joint angles, and $\mathbf{x}_b \in \mathbb{R}^6$ denotes the base pose,

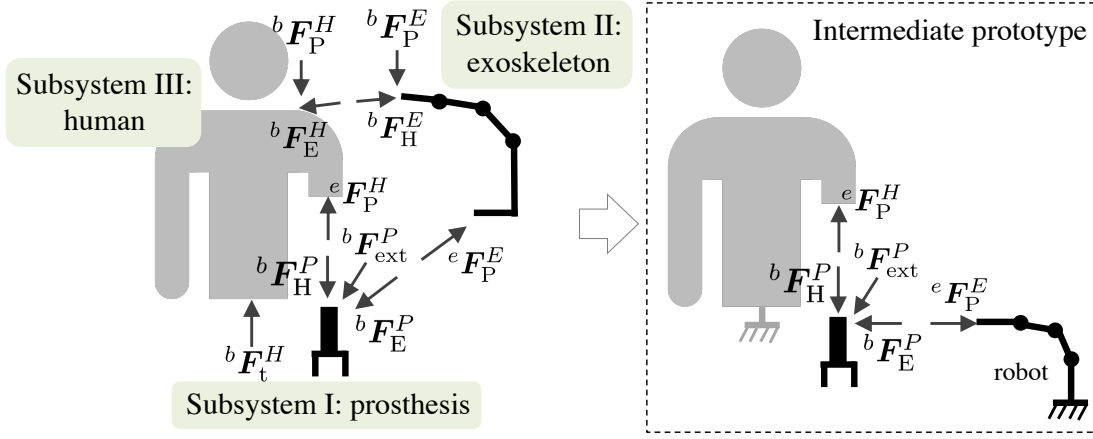


Figure 8.2: Subsystems of exo-prosthesis and intermediate prototype. © 2019 IEEE [268]

expressed in world coordinates. The equations of motion are

$$\begin{aligned}
 & \underbrace{\begin{pmatrix} M_{bb}(\mathbf{q}) & M_{bj}(\mathbf{q}) \\ M_{jb}(\mathbf{q}) & M_{jj}(\mathbf{q}) \end{pmatrix}}_{\mathbf{M}(\mathbf{q})} \underbrace{\begin{pmatrix} \ddot{\mathbf{x}}_b \\ \ddot{\mathbf{q}}_j \end{pmatrix}}_{\ddot{\mathbf{q}}} + \underbrace{\begin{pmatrix} \mathbf{c}_b(\mathbf{q}, \dot{\mathbf{q}}) \\ \mathbf{c}_j(\mathbf{q}, \dot{\mathbf{q}}) \end{pmatrix}}_{\mathbf{c}(\mathbf{q}, \dot{\mathbf{q}})} + \underbrace{\begin{pmatrix} \mathbf{g}_b(\mathbf{q}) \\ \mathbf{g}_j(\mathbf{q}) \end{pmatrix}}_{\mathbf{g}(\mathbf{q})} \\
 & = \begin{pmatrix} {}^b\mathbf{F}_H^P \\ \boldsymbol{\tau}_{j,m} \end{pmatrix} - \begin{pmatrix} \mathbf{0} \\ \boldsymbol{\tau}_{j,f} \end{pmatrix} + \begin{pmatrix} {}^b\mathbf{F}_E^P \\ \mathbf{0} \end{pmatrix} + \begin{pmatrix} {}^b\mathbf{F}_{\text{ext}}^P \\ \boldsymbol{\tau}_{j,\text{ext}} \end{pmatrix}, \quad (8.1)
 \end{aligned}$$

where subscript “P” points to prosthesis related quantities, and the base and joint entries are denoted with “b” and “j”, respectively. $\mathbf{M}(\mathbf{q}) \in \mathbb{R}^{n \times n}$ denotes the floating base inertia matrix, $\mathbf{c}(\mathbf{q}, \dot{\mathbf{q}}) \in \mathbb{R}^n$ the Coriolis and centrifugal forces and $\mathbf{g}(\mathbf{q}) \in \mathbb{R}^n$ the gravitational forces. The system is driven by the joint actuator torques $\boldsymbol{\tau}_{j,m} \in \mathbb{R}^{n_j}$ and by the human residual limb interaction wrench ${}^b\mathbf{F}_H^P \in \mathbb{R}^6$, see Fig. 8.2. Furthermore, $\boldsymbol{\tau}_{j,f} \in \mathbb{R}^{n_j}$ denotes the joint friction vector, ${}^b\mathbf{F}_E^P$ the exoskeleton interaction wrench, and ${}^b\mathbf{F}_{\text{ext}}^P \in \mathbb{R}^6$, $\boldsymbol{\tau}_{j,\text{ext}} \in \mathbb{R}^{n_j}$ external wrench and joint torques, respectively.

Exoskeleton The floating-base configuration of a redundant exoskeleton in task-space is represented by the state $\mathbf{y} = (\mathbf{y}_b^\top \ \mathbf{y}_e^\top)^\top$, where $\mathbf{y}_b \in \mathbb{R}^6$ denotes the base position and orientation, and $\mathbf{y}_e \in \mathbb{R}^6$ denotes the Cartesian end-effector coordinates. The floating-base task-space dynamics [272] may be written with as

$$\begin{aligned}
 & \underbrace{\begin{pmatrix} \boldsymbol{\Lambda}_{bb}(\mathbf{y}) & \boldsymbol{\Lambda}_{be}(\mathbf{y}) \\ \boldsymbol{\Lambda}_{eb}(\mathbf{y}) & \boldsymbol{\Lambda}_{ee}(\mathbf{y}) \end{pmatrix}}_{\boldsymbol{\Lambda}(\mathbf{y})} \underbrace{\begin{pmatrix} \ddot{\mathbf{y}}_b \\ \ddot{\mathbf{y}}_e \end{pmatrix}}_{\ddot{\mathbf{y}}} + \underbrace{\begin{pmatrix} \boldsymbol{\mu}_b(\mathbf{y}, \dot{\mathbf{y}}) \\ \boldsymbol{\mu}_e(\mathbf{y}, \dot{\mathbf{y}}) \end{pmatrix}}_{\boldsymbol{\mu}(\mathbf{y}, \dot{\mathbf{y}})} + \underbrace{\begin{pmatrix} \boldsymbol{\rho}_b(\mathbf{y}) \\ \boldsymbol{\rho}_e(\mathbf{y}) \end{pmatrix}}_{\boldsymbol{\rho}(\mathbf{y})} \\
 & = \begin{pmatrix} \mathbf{0} \\ {}^e\mathbf{F}_c^E \end{pmatrix} + \begin{pmatrix} {}^b\mathbf{F}_H^E \\ \mathbf{0} \end{pmatrix} + \begin{pmatrix} {}^b\mathbf{F}_P^E \\ {}^e\mathbf{F}_P^E \end{pmatrix} - \begin{pmatrix} \mathbf{0} \\ {}^e\mathbf{F}_f^E \end{pmatrix}, \quad (8.2)
 \end{aligned}$$

where subscript “E” points to exoskeleton related quantities, and the base and end-effector entries are denoted with “b” and “e”, respectively. The Cartesian mass matrix, the centrifugal and Coriolis terms, and gravitational forces are denoted by $\mathbf{\Lambda}(\mathbf{y}) \in \mathbb{R}^{12 \times 12}$, $\boldsymbol{\mu}(\mathbf{y}, \dot{\mathbf{y}}) \in \mathbb{R}^{12}$, $\boldsymbol{\rho}(\mathbf{y}) \in \mathbb{R}^{12}$, respectively. The interaction wrenches ${}^e\mathbf{F}_c^E$, ${}^{b/e}\mathbf{F}_P^E$, ${}^b\mathbf{F}_H^E \in \mathbb{R}^6$ correspond to the exoskeleton control input, the interaction with the connected prosthesis and human, respectively, see Fig. 8.2. Friction forces are lumped as ${}^e\mathbf{F}_f^E \in \mathbb{R}^6$. Exoskeleton related wrenches ${}^{b/e}\mathbf{F}^E$ and velocities $\dot{\mathbf{y}}_{b/e}$ are expressed in the frames associated with b / e, respectively.

Human residual limb The floating-base configuration of a human residual limb in task-space is represented by the state $\mathbf{z} = (\mathbf{z}_b^\top \ \mathbf{z}_e^\top)^\top$, where $\mathbf{z}_b \in \mathbb{R}^6$ denotes the Cartesian base position and orientation, and $\mathbf{z}_e \in \mathbb{R}^6$ denotes the residual limb end-effector coordinates. Similar to (8.2) the task-space dynamics can be written as

$$\begin{aligned} & \underbrace{\begin{pmatrix} \mathbf{\Gamma}_{bb}(\mathbf{z}) & \mathbf{\Gamma}_{be}(\mathbf{z}) \\ \mathbf{\Gamma}_{eb}(\mathbf{z}) & \mathbf{\Gamma}_{ee}(\mathbf{z}) \end{pmatrix}}_{\mathbf{\Gamma}(\mathbf{z})} \underbrace{\begin{pmatrix} \ddot{\mathbf{z}}_b \\ \ddot{\mathbf{z}}_e \end{pmatrix}}_{\ddot{\mathbf{z}}} + \underbrace{\begin{pmatrix} \boldsymbol{\psi}_b(\mathbf{z}, \dot{\mathbf{z}}) \\ \boldsymbol{\psi}_e(\mathbf{z}, \dot{\mathbf{z}}) \end{pmatrix}}_{\boldsymbol{\psi}(\mathbf{z}, \dot{\mathbf{z}})} + \underbrace{\begin{pmatrix} \boldsymbol{\eta}_b(\mathbf{z}) \\ \boldsymbol{\eta}_e(\mathbf{z}) \end{pmatrix}}_{\boldsymbol{\eta}(\mathbf{z})} \\ & = \begin{pmatrix} {}^b\mathbf{F}_t^H \\ {}^e\mathbf{F}_m^H \end{pmatrix} + \begin{pmatrix} {}^b\mathbf{F}_E^H \\ \mathbf{0} \end{pmatrix} + \begin{pmatrix} {}^b\mathbf{F}_P^H \\ {}^e\mathbf{F}_P^H \end{pmatrix}, \end{aligned} \quad (8.3)$$

where subscript “H” points to human related quantities, and the base and residual limb end-effector entries are denoted with “b” and “e”, respectively. The Cartesian mass matrix, the centrifugal and Coriolis terms, and gravitational forces are denoted by $\mathbf{\Gamma}(\mathbf{z}) \in \mathbb{R}^{12 \times 12}$, $\boldsymbol{\psi}(\mathbf{z}, \dot{\mathbf{z}}) \in \mathbb{R}^{12}$, $\boldsymbol{\eta}(\mathbf{z}) \in \mathbb{R}^{12}$, respectively. ${}^e\mathbf{F}_m^H$ denotes human upper-limb muscle forces, and ${}^b\mathbf{F}_t^H \in \mathbb{R}^6$ denotes the human body wrench associated to the torso, see Fig. 8.2. ${}^b\mathbf{F}_E^H$, ${}^{b/e}\mathbf{F}_P^H \in \mathbb{R}^6$ correspond to the interaction with the exoskeleton and the prosthesis, respectively. Human related wrenches \mathbf{F}^H and velocities $\dot{\mathbf{z}}_{b/e}$ are expressed in the frames associated with b / e, respectively.

Coupled system The bases of the exoskeleton and human are rigidly connected. The prosthesis base is rigidly mounted to the end-effector of the exoskeleton. The exoskeleton base frame is assumed to correspond to the human base frame, thus $\mathbf{y}_b = \mathbf{z}_b$. The exoskeleton end-effector frame coincides with the prosthesis base frame, thus $\mathbf{y}_e = \mathbf{x}_b$.

The coupling between the human residual limb and the prosthesis base is approximated by introducing a visco-elastic coupling (see Fig. 8.2)

$${}^e\mathbf{F}_P^H = \mathbf{K}_v(\mathbf{z}_e - \mathbf{x}_b) + \mathbf{D}_v(\dot{\mathbf{x}}_b - \dot{\mathbf{z}}_e), \quad (8.4)$$

$${}^b\mathbf{F}_H^P = -{}^e\mathbf{F}_P^H, \quad (8.5)$$

where $\mathbf{D}_v, \mathbf{K}_v \in \mathbb{R}^{6 \times 6}$ are the coupling damping and stiffness matrix.

Merging (8.1) to (8.5) lead to the hybrid exo-prosthesis system dynamics. The state space equation with state vector $\boldsymbol{\zeta} = (\mathbf{z}_b^\top \ \mathbf{z}_e^\top \ \mathbf{x}_b^\top \ \mathbf{q}_j^\top \ \dot{\mathbf{z}}_b^\top \ \dot{\mathbf{z}}_e^\top \ \dot{\mathbf{x}}_b^\top \ \dot{\mathbf{q}}_j^\top)^\top$ is given by (8.6).

$$\begin{aligned}
& \text{hybrid system matrix} \\
\begin{pmatrix} \dot{z}_b \\ \dot{z}_e \\ \dot{x}_b \\ \dot{q}_j \\ \ddot{z}_b \\ \ddot{z}_e \\ \ddot{x}_b \\ \ddot{q}_j \end{pmatrix} &= \begin{pmatrix} \mathbf{0} & I \\ M_*^{-1} \begin{pmatrix} \mathbf{0} & \mathbf{0} & \mathbf{0} & \mathbf{0} \\ \mathbf{0} & -\mathbf{K}_v & \mathbf{K}_v & \mathbf{0} \\ \mathbf{0} & \mathbf{K}_v & -\mathbf{K}_v & \mathbf{0} \\ \mathbf{0} & \mathbf{0} & \mathbf{0} & \mathbf{0} \end{pmatrix} & M_*^{-1} \begin{pmatrix} \mathbf{0} & \mathbf{0} & \mathbf{0} & \mathbf{0} \\ \mathbf{0} & -\mathbf{D}_v & \mathbf{D}_v & \mathbf{0} \\ \mathbf{0} & \mathbf{D}_v & -\mathbf{D}_v & \mathbf{0} \\ \mathbf{0} & \mathbf{0} & \mathbf{0} & \mathbf{0} \end{pmatrix} \end{pmatrix} \begin{pmatrix} z_b \\ z_e \\ x_b \\ q_j \\ \dot{z}_b \\ \dot{z}_e \\ \dot{x}_b \\ \dot{q}_j \end{pmatrix} \\
&+ \begin{pmatrix} \mathbf{0} \\ \mathbf{0} \\ \mathbf{0} \\ \mathbf{0} \\ M_*^{-1} \begin{pmatrix} {}^b \mathbf{F}_e^{\bar{H}} \\ {}^e \mathbf{F}_m^H \\ {}^e \mathbf{F}_c^E \\ \boldsymbol{\tau}_{j,m} \end{pmatrix} \end{pmatrix} + \begin{pmatrix} \mathbf{0} \\ \mathbf{0} \\ \mathbf{0} \\ \mathbf{0} \\ M_*^{-1} \begin{pmatrix} -\boldsymbol{\psi}_b - \boldsymbol{\mu}_b - \boldsymbol{\eta}_b - \boldsymbol{\rho}_b \\ -\boldsymbol{\psi}_e - \boldsymbol{\eta}_e \\ -\mathbf{F}_{E_e,f} - \mathbf{c}_b - \boldsymbol{\mu}_e - \mathbf{g}_b - \boldsymbol{\rho}_e \\ -\boldsymbol{\tau}_{j,f} - \mathbf{c}_j - \mathbf{g}_j \end{pmatrix} \end{pmatrix} \\
&\quad \text{control input} \quad \text{Coriolis, centrifugal, gravitation and friction terms} \\
&+ \begin{pmatrix} \mathbf{0} \\ \mathbf{0} \\ \mathbf{0} \\ \mathbf{0} \\ M_*^{-1} \begin{pmatrix} \mathbf{0} \\ \mathbf{0} \\ {}^b \mathbf{F}_{\text{ext}}^P \\ \boldsymbol{\tau}_{P_j,\text{ext}} \end{pmatrix} \end{pmatrix} \\
&\quad \text{external forces}
\end{aligned} \tag{8.6}$$

I denotes the identity matrix and

$$M_* = \begin{pmatrix} \boldsymbol{\Gamma}_{bb} + \boldsymbol{\Lambda}_{bb} & \boldsymbol{\Gamma}_{be} & \boldsymbol{\Lambda}_{be} & \mathbf{0} \\ \boldsymbol{\Gamma}_{eb} & \boldsymbol{\Gamma}_{ee} & \mathbf{0} & \mathbf{0} \\ \boldsymbol{\Lambda}_{eb} & \mathbf{0} & M_{bb} + \boldsymbol{\Lambda}_{ee} & M_{bj} \end{pmatrix}.$$

Robot-based system In this work, the exoskeleton is emulated by a robot, see Fig. 8.2. For now, the subsystems human and robot are assumed to have a fixed base, meaning the human thorax and the robot base are fixed in space and are not able to move. The prosthesis is assumed to have a floating base, however, its base is rigidly connected to the end-effector of the robot and is therefore not completely free to move in space. For sake of brevity, the robot base frame corresponds to the world frame, and the robot

end-effector frame is defined to be the prosthesis base frame. For this new system the reduced state vector is

$$\boldsymbol{\sigma} = \left(\mathbf{z}_e^\top \quad \mathbf{x}_b^\top \quad \mathbf{q}_j^\top \quad \dot{\mathbf{z}}_e^\top \quad \dot{\mathbf{x}}_b^\top \quad \dot{\mathbf{q}}_j^\top \right)^\top,$$

and the rest of the model changes accordingly, cf. (8.6).

8.1.1.2 Experimental validation testbed

The exoskeleton replacement by a robot allows an early validation of a simplified system dynamics as well as the implementation and evaluation of the semi-autonomous control methods. Fig. 8.3 depicts the system architecture of the current prototype.

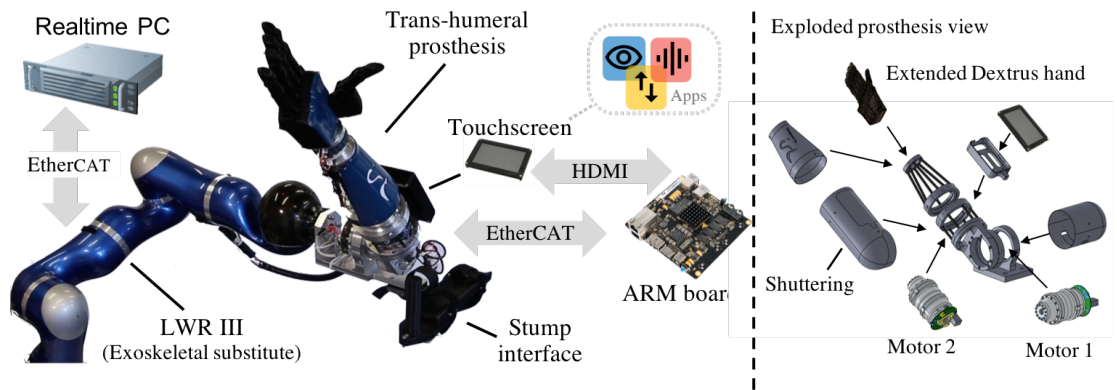


Figure 8.3: Intermediate prototype: semi-autonomous robot-based exo-prosthesis (left), and mechatronic architecture of prosthesis (right). ©2019 IEEE [268]

It consists of a soft-robotics enhanced 2 DoF transhumeral prosthesis that is mechanically mounted to the end-effector of an LWR III [121], emulating the future exoskeleton in first approximation. This step is justified for two reasons. First, from a functional point of view, both variants compensate the weight of the prosthesis and the user is relieved from it. (Note here that in the robot-based version, the prosthesis weight is transferred via the robot into the floor. In the future target system, the weight is diverted to the human body, and then into the floor, via the exoskeleton, see Fig. 8.2. This more complex dynamics require further analysis.) Second, both provide information about the position, velocity and acceleration of the human residual limb that can be of further use. *Clearly, several challenges such as careful weight balancing still have to be solved on the way to a fully integrated, wearable exo-prosthesis system.*

Transhumeral prosthesis design The design of the new 2 DoF elbow prosthesis follows three main principles: use of *light-weight materials*, a *modular mechanical structure* and, in terms of control, the extension of *soft-robotics methods* to the class of exoprosthetic systems. However, note that the current prosthesis version is not yet fully optimized and significant potentials for further weight reduction are possible.

Mechatronic architecture Fig. 8.3 shows the mechatronic architecture of the prosthesis. It can be separated into an actuated *elbow-* and *forearm-joint*, and a fixed *wrist-joint*. A 2 DoF wrist is currently under development [273]. Both actuators (motor 1 and 2, each max. 30 Nm) are equipped with joint-torque sensors for soft-prosthetics control, including collision handling. An aluminium plate serves as the base of the system and interface to the environment. For now, it is designed to be mounted to a LWR III that compensates the prosthesis gravity forces. The used hand is an improved version of the Dextrus Hand [274]. Finally, a 5"-touch display grants the user access to a novel app-based software system.

Software and communication architecture Fig. 8.3 depicts the overall software and communication architecture. The software for the prosthesis including the user app system runs mainly on a *BeagleBoard-X15* [275] (based on a TI Sitara AM 5728 SoC, integrating a dual-core ARM Cortex-A15 processor operated at 1.5 GHz). The high-level user app interface is implemented using the Robot Operating System (ROS). The low-level joint controller runs at 1 kHz in realtime using EtherCAT.

EMG interface The *Myo armband* [276] placed on the upper arm serves as EMG user input and mainly measures the muscle activation of *musculus biceps brachii* (BIC) and *musculus triceps brachii* (TRI). Four upper arm muscle gestures are trained using an SVM with radial basis kernel function, see Table 8.1.

Table 8.1: Trained gestures using the *Myo armband*. ©2019 IEEE [268]

gesture state g_s	muscle contraction
0	arm relaxed
1	BIC contracted
2	TRI contracted
3	BIC+TRI contracted

Prosthetic app interface The prosthesis is equipped with a touchscreen that grants the user access to a variety of apps. In this work, three basic apps are introduced: *sequential control* and two *semi-autonomous power grasping* apps that are fed either by a) kinesthetically taught postures or b) 3D vision input.

Low-level control This work focus on the control of the emulation system only. As a preliminary solution, the robot shall compensate for the gravity of the prosthesis while the prosthesis is equipped with compliance control fed by trajectories, see Fig. 8.4.

Robot control One goal of the exoskeleton (or robot) is to compensate gravitational effects of the prosthesis to release the human residual limb. Therefore, the robot control

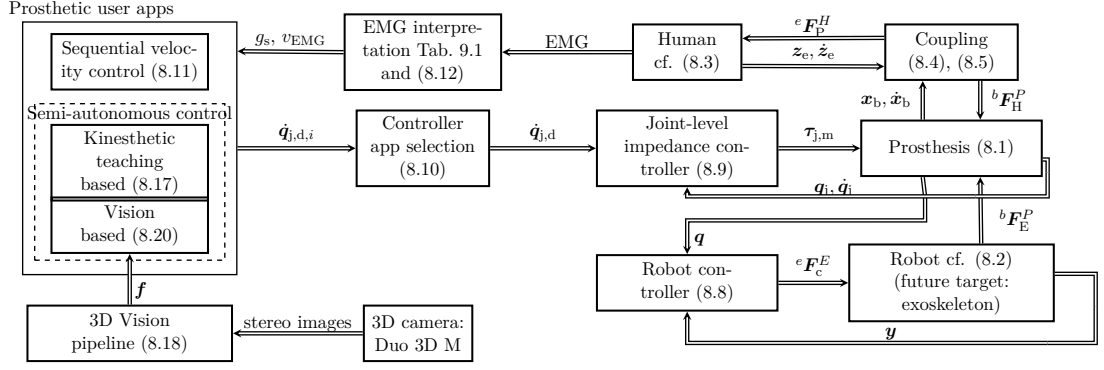


Figure 8.4: Block diagram of the intermediate exo-prosthesis system with semi-autonomous coordinated control. ©2019 IEEE [268]

input in (8.2) is chosen to be

$${}^e \mathbf{F}_c^E = {}^e \hat{\mathbf{F}}_f^E + \hat{\mathbf{g}}_b(\mathbf{q}) + \hat{\boldsymbol{\rho}}_e(\mathbf{y}), \quad (8.8)$$

where the accent $\hat{\cdot}$ denotes the model of the corresponding term. Assuming $\mathbf{c} \ll \mathbf{g}$ and $\boldsymbol{\mu} \ll \boldsymbol{\rho}$, the terms $\hat{\mathbf{c}}_b$ and $\hat{\boldsymbol{\mu}}_e$ in (8.1) and (8.2) are neglected for simplicity.

Prosthesis impedance control The compliant behavior of the prosthesis is rendered by a *joint level impedance controller* with feed-forward control

$$\begin{aligned} \boldsymbol{\tau}_{j,m} = & \mathbf{K}(\mathbf{q}_{j,d} - \mathbf{q}_j) + \mathbf{D}(\dot{\mathbf{q}}_{j,d} - \dot{\mathbf{q}}_j) + \hat{\mathbf{g}}_j(\mathbf{q}) + \hat{\mathbf{c}}_j(\mathbf{q}_j, \dot{\mathbf{q}}_j) \\ & + \hat{\mathbf{M}}_{jj}(\mathbf{q}_{j,d})\ddot{\mathbf{q}}_{j,d} + \hat{\boldsymbol{\tau}}_{j,f}(\dot{\mathbf{q}}_j), \end{aligned} \quad (8.9)$$

where $\mathbf{K} \in \mathbb{R}^{n_j \times n_j}$ is the desired joint stiffness matrix. The damping matrix $\mathbf{D} \in \mathbb{R}^{n_j \times n_j}$ is calculated according to the factorization damping design approach from [254]. The gravitational, Coriolis, inertial and friction effects $\hat{\mathbf{g}}_j$, $\hat{\mathbf{c}}_j$, $\hat{\mathbf{M}}_{jj}$ and $\hat{\boldsymbol{\tau}}_{j,f}$ are compensated using identified model data to ensure good tracking of the desired trajectory $\mathbf{q}_{j,d}$, $\dot{\mathbf{q}}_{j,d}$ and $\ddot{\mathbf{q}}_{j,d}$.

8.1.2 Prosthetic user apps

A *prosthetic user app* generates task-dependent velocity profiles based on different methods such as kinesthetic teaching, 3D object tracking or sequential control, driving the compensated prosthesis. The desired joint velocity $\dot{\mathbf{q}}_{j,d}$ in (8.9) is selected from n_a tasks via

$$\dot{\mathbf{q}}_{j,d} = \mathbf{S} \left[\dot{\mathbf{q}}_{j,d,1}^\top \cdots \dot{\mathbf{q}}_{j,d,n_a}^\top \right]^\top, \quad (8.10)$$

where $\mathbf{S} \in \mathbb{R}^{n_j \times (n_a n_j)}$ is the app selection matrix. The desired velocity provided by the i th app is denoted by $\dot{\mathbf{q}}_{j,d,i}$.

8.1.3 Sequential velocity control

This control mode was implemented for comparison. It integrates the desired velocities driven by the EMG system by

$$\dot{\mathbf{q}}_{j,d,3} := \mathbf{s}^\top \dot{\mathbf{q}}_{j,d,\max} v_{emg}, \quad (8.11)$$

where $\dot{\mathbf{q}}_{j,d,\max}$ is the constant maximum link velocity vector. However, only one joint $j \in [1, \dots, n_j]$ is moved at the same time, which is selected by the n_j -dimensional unitary selection vector \mathbf{s} . The user may switch between individual joints by executing a predefined EMG gesture (contracting both BRI+TRI, see $g_s = 3$ in Table 8.1). The normalized EMG-driven velocity is defined as

$$v_{EMG} = \max(\min((p_{BIC} - p_{TRI})c_0, 1), -1) \in [-1, 1], \quad (8.12)$$

where $p_{BIC/TRI}$ denote the respective logarithmic probability of the BRI and/or TRI being classified as contracted. These probabilities correlate with the EMG activation level, assuming fully contracted muscles during gesture training phase. For example, if the user starts to contract BRI ($g_s = 1$) a positive analog signal v_{emg} is generated. If the user contracts TRI ($g_s = 2$), v_{emg} gets negative. $c_0 \approx \frac{1}{5}$ is an empirically determined scalar value used to normalize the logarithmic probabilities to 1. The sequential control mode serves as reference to evaluate the coordinated control scheme introduced next.

8.1.4 Velocity control based on kinesthetic teaching

In the first approach the user kinesthetically teaches two target poses \mathbf{x}_{e1} and \mathbf{x}_{e2} for a reaching task. The controller is designed to stabilize the target pose and reject human movement disturbances that do not match the task to be executed. Noticeably, instead of moving joints laboriously and counter-intuitively in a sequential fashion, the system is now able to smoothly transit between changing goal configurations through activating discrete EMG gestures. This means, the user can toggle between \mathbf{x}_{e1} and \mathbf{x}_{e2} by activating muscles according to $g_s = 3$, see Table 8.1. The transition is realized by simple position and orientation error integration. Starting from the differential kinematics

$$\dot{\mathbf{x}}_e = \mathbf{J}_g(\mathbf{q}_j)\dot{\mathbf{q}}_j = \begin{pmatrix} \mathbf{J}_t \\ \mathbf{J}_r \end{pmatrix} \dot{\mathbf{q}}_j, \quad (8.13)$$

where $\mathbf{x}_e \in \mathbb{R}^6$ is the pose of the prosthesis end-effector. The geometric Jacobian \mathbf{J}_g can be split into a translational and rotational part such that $\mathbf{J}_g = [\mathbf{J}_t^\top \ \mathbf{J}_r^\top]^\top$. The differential inverse kinematics results into

$$\dot{\mathbf{q}}_j = \mathbf{J}_g^{-1}(\mathbf{q}_j)\dot{\mathbf{x}}_e = \mathbf{J}_g^{-1}(\mathbf{q}_j) \begin{pmatrix} \dot{\mathbf{r}}_e \\ \boldsymbol{\omega} \end{pmatrix}, \quad (8.14)$$

where $\dot{\mathbf{r}}_e$ and $\boldsymbol{\omega}$ denote the Cartesian translational and angular velocities. The proposed coordinated prosthesis velocity control law is

$$\dot{\mathbf{q}}_j := \mathbf{J}_g^\#(\mathbf{q}_j) \begin{pmatrix} \Delta \mathbf{r}_e \\ \mathbf{m} \end{pmatrix}, \quad (8.15)$$

where $\mathbf{J}_g^\#(\mathbf{q}_j)$ is the Moore-Penrose-Inverse of the Jacobian. The position error $\Delta \mathbf{r}_e = \mathbf{r}_{e,d} - \mathbf{r}_e$ (where $\mathbf{r}_{e,d}$ denotes the kinesthetically taught position) of the prosthesis end-effector is interpreted as the incremental desired Cartesian velocity. \mathbf{m} is the Cartesian moment necessary to achieve a desired orientation [277]. Note that the pseudo-inverse is generated from

$$\begin{pmatrix} \Delta \mathbf{q}_{j,t} \\ \Delta \mathbf{q}_{j,r} \end{pmatrix} = \begin{pmatrix} \mathbf{J}_t^\# \Delta \mathbf{r}_e \\ \mathbf{J}_r^\# \mathbf{m} \end{pmatrix}. \quad (8.16)$$

Finally, the desired velocity becomes

$$\dot{\mathbf{q}}_{j,d,1} := \Delta \mathbf{q}_{j,t} + \Delta \mathbf{q}_{j,r}. \quad (8.17)$$

This motion law regulates the prosthesis end-effector to point to the originally taught-in pose \mathbf{x}_{e1} or \mathbf{x}_{e2} .

8.1.5 Velocity control based on 3D vision

In addition, the permanently kinesthetically programmed poses (see Sec. 8.1.4) can be replaced by the visual tracking of objects. Prosthesis servo control could regulate the optimal grasping pose based on image data.

In this work, the stereo camera *Duo3D M* [278] was utilized, see Fig. 8.5. The implemented 3D vision pipeline segments point clouds in regions of interests. Then it classifies these regions against a set of pre-trained objects. If an object is found, the

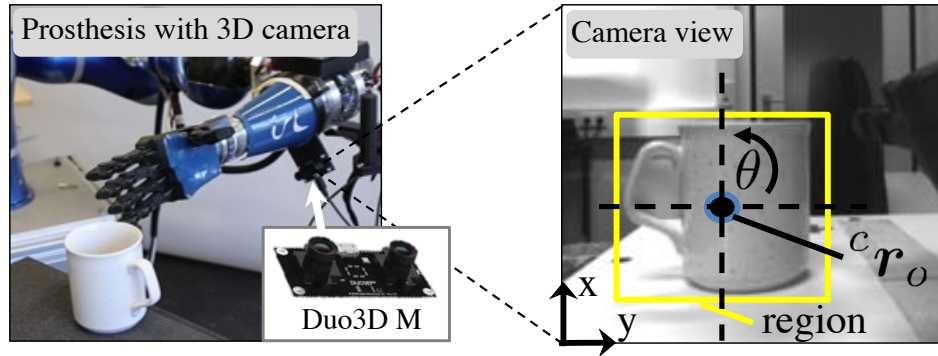


Figure 8.5: Prosthesis equipped with 3D camera (left) and exemplary result of a detected coffee mug via the vision pipeline (right). © 2019 IEEE [268]

pipeline continuously provides the feature vector

$$\mathbf{f} := \left({}^c \mathbf{r}_o^T \quad \theta \mathbf{u}^T \quad \kappa \right)^T, \quad (8.18)$$

where ${}^c \mathbf{r}_o$ is the translational and the $\theta \mathbf{u}$ the rotational part of the object location in camera coordinates, see Fig. 8.5. κ is the classification confidence. A more detailed description of the developed 3D vision pipeline lies outside the scope of this work.

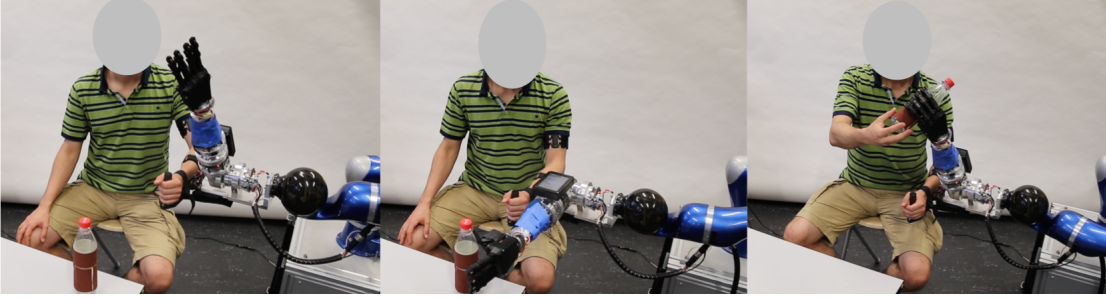


Figure 8.6: Experimental task sequences: Start (left), grasp bottle (middle), lift up and take bottle. ©2019 IEEE [268]

For visual tracking the position-based visual servoing approach (PBVS) from [279] was used. The control law expressed in camera space is defined as $\mathbf{v}_c = -\mathbf{\Omega}\mathbf{L}^\# \mathbf{e}$, where \mathbf{v}_c denotes the desired camera velocity, $\mathbf{L}^\#$ is the Moore-Penrose-Inverse of the interaction matrix, $\mathbf{\Omega}$ the control gain matrix and \mathbf{e} the control error. The control law becomes

$$\mathbf{v}_c = -\mathbf{\Omega} \begin{pmatrix} ({}^c\mathbf{r}_{o,d} - {}^c\mathbf{r}_o) + (\theta - \theta_d)[{}^c\mathbf{r}_o]_x \mathbf{u} \\ (\theta - \theta_d)\mathbf{u} \end{pmatrix}, \quad (8.19)$$

where $[{}^c\mathbf{r}_o]_x$ is the skew-symmetric matrix representation of ${}^c\mathbf{r}_o$ and $\theta_d\mathbf{u}$ the desired orientation. The control gain matrix is defined as $\mathbf{\Omega} = \text{diag}(\gamma_t^T \ \gamma_r^T)$, where $\gamma_t = \gamma_t\kappa(1 \ 1 \ 1)^T$ and $\gamma_r = \gamma_r\kappa(0 \ 0 \ 1)^T$. γ_t/γ_r denote constant positive gain parameters. Segmented objects with larger κ have a more reliable pose estimate, avoiding tracking of weakly classified objects. Finally, desired joint velocities simply become

$$\dot{\mathbf{q}}_{j,d,2} = \mathbf{J}_c^\# \mathbf{v}_c. \quad (8.20)$$

8.2 Results

For first evaluation of the semi-autonomous controls based on the intermediate prototype, a basic reaching grasping task was conducted with one male healthy subject (age 30). All human experimentation was conducted in conformity with the Helsinki Declaration.

Experimental protocol The experimental task is composed of three steps, starting from a predefined initial configuration: 1) grasp a bottle that is placed on a table in front of the subject, 2) lift up the bottle and 3) take the bottle with the right hand, see Fig. 8.6. The task is executed in three setups: A) without prosthesis (for reference), with the proposed exo-prosthesis prototype in B) *sequential* and C) *coordinated (based on kinesthetic teaching)* control mode. Eight trials were conducted for each setup. The EMG interface was used with the exo-prosthesis prototype in both control modes. In addition, the app-interface was used to kinesthetically teach the *grasp bottle* and *take bottle* pose, see Fig. 8.6. During task execution, the subjects were seated. Prior to the experiment, the subject had only very little experience (≈ 10 minutes) with the system.

8 From sequential to semi-autonomous control

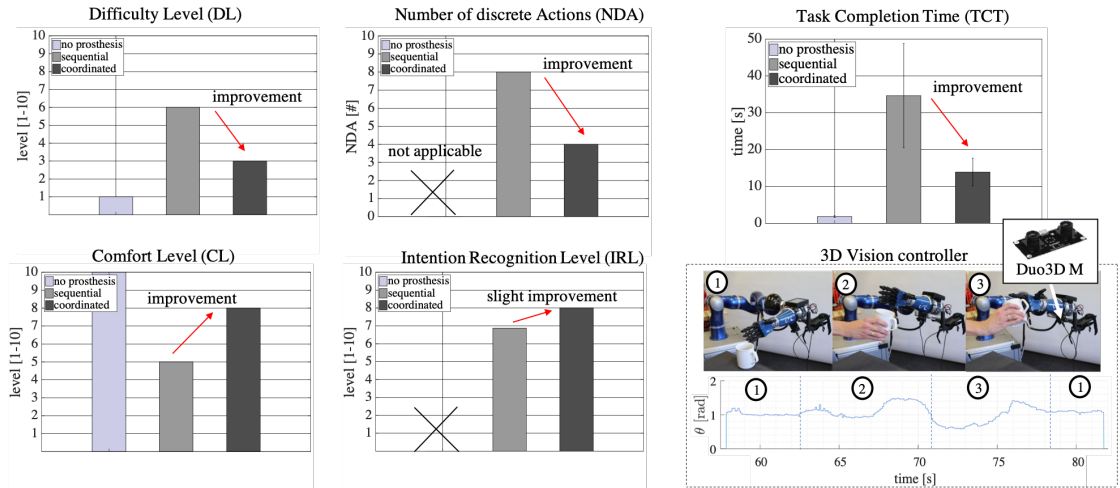


Figure 8.7: Experiments with an unimpaired subject, and 3D vision controller performance during tracking of a coffee mug. © 2019 IEEE [268]

Research question and evaluation metrics Specifically, this work attempts to answer the question whether the coordinated control strategy helps to reduce the level of user guidance difficulty and increase the speed in contrast to classical sequential control. Five metrics are used to evaluate the system and help answer the question:

- Task Completion Time (TCT)
- Number of Discrete User Actions (NDA)
- Comfort Level (CL)
Scale: very uncomfortable (1) to very comfortable (10)
- Intention Recognition Level (IRL):
Scale: inadequate (1) to very good (10)
- Difficulty Level (DL)
Scale: very easy (1) to very difficult (10)

After each trial, the subjects were asked to rate these metrics on a scale, see Fig. 8.7.

The orientation θ for a randomly moved coffee mug is shown in Fig. 8.7 (bottom-right). The overall tracking performance is also shown in the video attachment.

8.3 Conclusion

This chapter presented the concept of semi-autonomous soft-robotics based exo-prosthetics based on [129], which aims at leveraging the advantages from the different disciplines and mark a step towards next-generation intuitive-to-use upper-limb prosthetic systems. For this system class the full hybrid human-exoskeleton-prosthesis dynamics model was

formulated. A robot-based prototype was built to enable early implementation and experimental validation of basic semi-autonomous controls. The fully integrated target system can be designed and built. So far, the developed controls are either based on kinesthetic teaching or visual tracking. First experiments underline that the proposed coordinated control algorithms significantly improve the ease of use in solving basic reaching and grasping tasks. In future work, a highly integrated lightweight system, including a fully integrated exoskeleton with evaluated mechanical interfacing concept will be developed. Also, more comprehensive user studies over this wider set of coordinated control laws, including the proposed vision controller, will be conducted. Additionally, the system will be equipped with reflexive sensitive behaviors.

9 Synergy complement control

Humans replaced lost or non-developed body limbs for millennia with technical counterparts, namely prostheses. The presumably first powered upper limb prosthesis dates back to a patent from Germany in 1915 [160, 161]. Since then, many powered mechanical systems have developed for a broad spectrum of amputations degrees with continuously improved mechanics. With the emergence of myoelectric upper limb prostheses around 1950 [162, 163, 164], significant efforts have been made to improve and enhance the operability of such systems by myoelectric controls with sequential control as today’s commercial standard [13, 280, 281, 282, 283, 284, 285]. It often involves a finite state machine, allowing the user to select and control single joints at a time using direct Electromyography (EMG)-based proportional control. Unused joints are locked, and a muscle co-contraction incites switching to the next one [286]. However, due to the limitations of myoelectric control, such as muscle fatigue, electrode displacement, difficulties in decoding complex patterns or dealing with coordinated joint movements [14], an interest in limb-driven control concepts emerged [187]. Here, the residual limb (RL) movement rather than muscle activation measurements is used as a continuous control input for the device. Several RL-driven methods exist for upper limb prostheses that are still considered to be basic and primarily focus on simulation, virtual reality, or single DoF elbow coordination (e.g., [188, 189, 187]). At its core, they share one fundamental idea: simultaneously learn the coordination between the upper and lower arm for a wide spectrum of possible motion variants from captured human movement examples (templates). For this, regression techniques are applied involving linear regression such as Principal Components Analysis (PCA) [190, 187, 191] or non-linear regression such as Artificial Neural Networks (ANN), Radial Basis Function Networks (RBFN), or Locally Weighted Regression (LWR) [192, 193, 194, 187, 195, 191, 196, 197, 198, 189, 188]. However, the mapping between low dimensional upper arm movement and high dimensional total limb movement is highly underdetermined. In addition, different lower arm motions should be possible even if the residual limb’s movement pattern is similar. Existing methods cannot address this. Therefore, these methods output prosthesis motions that are inaccurate, not smooth (jerky), are of unnatural shape, and often uncomfortably delayed [187]; in sum, still quite far from solving the original problem. This complex, high-dimensional coordination problem cannot be accurately solved by treating it as a data-driven black-box problem. A further critical limitation of current approaches is the lack of environmental context, leading to the inability to systematically deal with changing tasks or targets. More context information and autonomy are required for limb-driven methods to be useful for amputees. Therefore, a significant gap remains calling for alternative methods [187]. This work presents the new RL-driven method Synergy Complement Control (SCC) that inherently deals with complex multi-DoF motions and

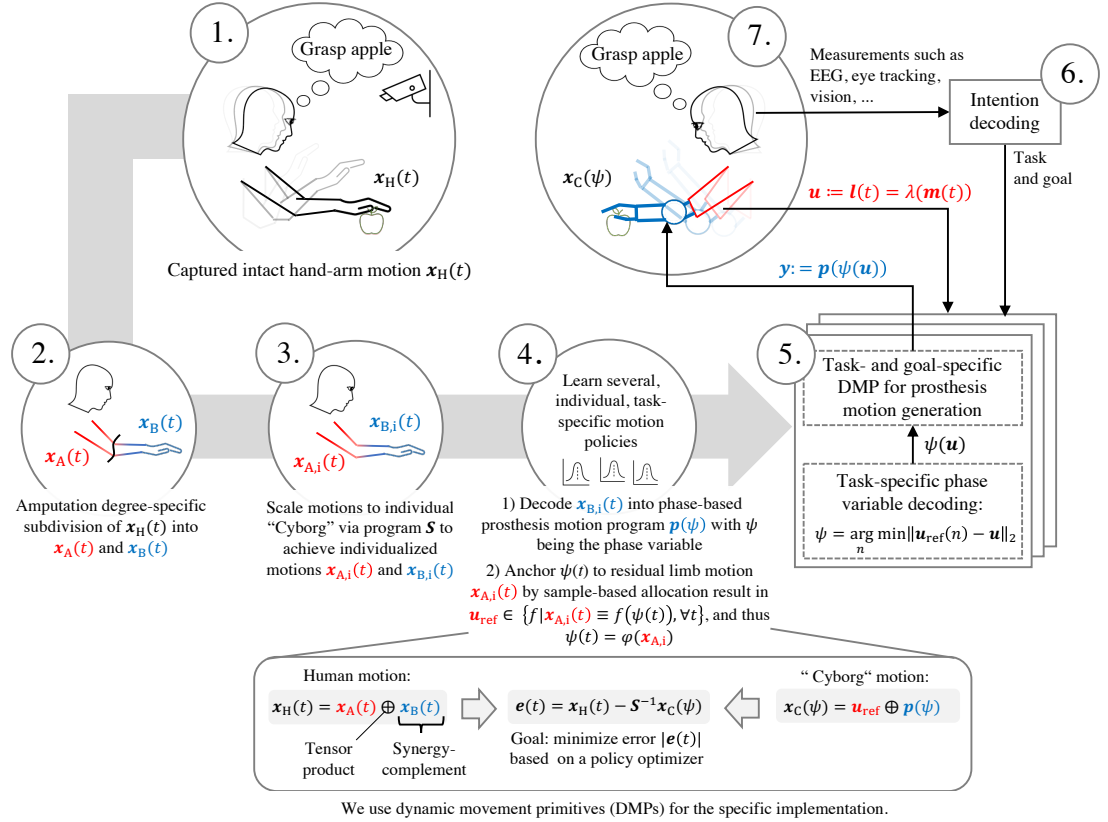


Figure 9.1: Workflow of proposed method in seven steps. The RL position $\mathbf{l}(t) = \lambda(\mathbf{m}(t))$ —which results from the muscle activation $\mathbf{m}(t)$ —drives the prosthetic motion $\mathbf{p}(\psi)$ via the phase variable ψ .

changing tasks and target locations, and outputs RL-coordinated complementary prosthetic trajectories of human-like shape and are smooth and delay-free. Fig. 9.1 shows the workflow of the SCC method. Throughout this work, a transhumeral amputation is assumed (cf. step 2 in Fig. 9.1).

9.1 General framing

The SCC method is designed by framing a reach-and-grasp problem within a new dual-task structure (Fig. 9.2). This hypothesis looks at the problem from a robotics task-space perspective. The problem is divided into three phases (reach, grasp, and post grasp) and into two sub-tasks, one performed by the arm and the other by the hand. While several works consider only the kinematic and grasp force level, this work extends this idea to include arm compensating forces. The arm reaches for the object ($\dot{\mathbf{x}}_{\text{arm}} = \dot{\mathbf{x}}_{\text{reach}}$), while the hand prepares to grasp ($\dot{\mathbf{x}}_{\text{hand}} = \dot{\mathbf{x}}_{\text{pre}}$). Neither hand grasp forces ($\mathbf{F}_{\text{hand}} = \mathbf{0}$) nor arm feed-forward compensation forces ($\mathbf{F}_{\text{arm}} = \mathbf{0}$) are commanded, which are required

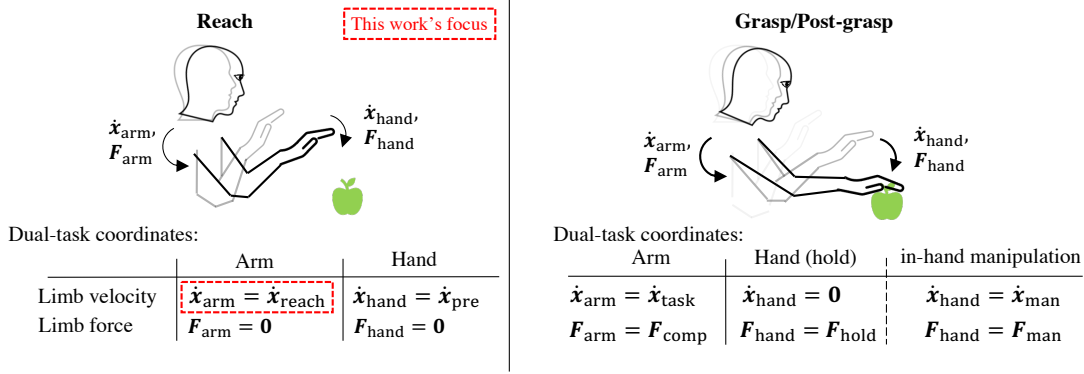


Figure 9.2: Dual-task structure of reach and grasp task.

to compensate the object. After the hand grasped the object, it either holds ($\dot{\mathbf{x}}_{\text{hand}} = \mathbf{0}$, $\mathbf{F}_{\text{hand}} = \mathbf{F}_{\text{hold}}$) or manipulates ($\dot{\mathbf{x}}_{\text{hand}} = \dot{\mathbf{x}}_{\text{man}}$, $\mathbf{F}_{\text{hand}} = \mathbf{F}_{\text{man}}$) it. The arm performs the task (e.g., lifting) ($\dot{\mathbf{x}}_{\text{arm}} = \dot{\mathbf{x}}_{\text{task}}$) and compensates the object ($\mathbf{F}_{\text{arm}} = \mathbf{F}_{\text{comp}}$). This work, however, focuses on a simplified version of the whole problem, namely arm reaching movements. Arm compensating forces are neglected, while grasping is simplified to the states “open” and “close”.

9.2 Concept

The concept of SCC can be explained in seven steps as shown in Fig. 9.1. In the first step, a full hand-arm motion $\mathbf{x}_{\text{H}}(t)$ for task T is obtained from experiments with unimpaired subjects performing activities of daily living. In this work, two *intransitive* tasks, in which subjects lifted their right arm to perform a “stop” and “block light source” gesture, are considered. Furthermore, three *transitive* tasks that involved hand-object interactions such as grasping an apple, a book, and a bottle are included. In the second step, the intact motion $\mathbf{x}_{\text{H}}(t)$ is subdivided according to the amputation level into $\mathbf{x}_{\text{A}}(t)$ and $\mathbf{x}_{\text{B}}(t)$. Throughout this work, a transhumeral amputation is assumed. Thus, one obtains a motion corresponding to the RL $\mathbf{x}_{\text{A}}(t)$ and the corresponding synergy complement $\mathbf{x}_{\text{B}}(t)$. In the third step, motions $\mathbf{x}_{\text{A}}(t)$ and $\mathbf{x}_{\text{B}}(t)$ are scaled to the individual cyborg resulting in the individualized motions $\mathbf{x}_{\text{A},i}(t)$ and $\mathbf{x}_{\text{B},i}(t)$. In the fourth step, the individualized reference motion $\mathbf{x}_{\text{B},i}(t)$ is decoded into a phase-based prosthesis motion program $\mathbf{p}(\psi)$ with ψ being the phase variable. For the specific implementation, dynamic movement primitives (DMPs) are used (9.8)(9.10). A DMP is a system of differential equations that can be used to model trajectories. Furthermore, $\psi(t)$ is anchored to the RL reference motion $\mathbf{u}_{\text{ref}} = \mathbf{x}_{\text{A},i}(t)$ by sample-based allocation resulting in $\psi(\mathbf{u}_{\text{ref}})$. In the fifth step, the measured RL position $\mathbf{u} := \mathbf{l}(\mathbf{m}(t)) \in \mathbb{R}^3$ (which is determined by muscle activation $\mathbf{m}(t)$) is online matched to the task-specific reference trajectory \mathbf{u}_{ref} and a continuous phase variable $\psi(\mathbf{u}) \in [0, 1]$ (9.15) is online generated. A value of $\psi = 1$ means that \mathbf{u} corresponds to the start position of \mathbf{u}_{ref} , whereas if $\psi = 0$ means that \mathbf{u} reached the end position of \mathbf{u}_{ref} . The task-specific prosthesis motion program $\mathbf{p}(\psi)$ is

now online generated using the DMP, where ψ is the input. Thus, $\mathbf{p}(\psi)$ is fully driven by $\mathbf{l}(\mathbf{m}(t))$. The SCC method also enables seamless transit between tasks. In step six, the user’s intention is decoded based on eye-tracking and motion-tracking measurements. It outputs the intended task to be solved and also the goal pose related to the corresponding object. If the user switches a task or goal, the corresponding reference motion \mathbf{u}_{ref} and DMP are loaded. In summary (step seven), this framework leads to a cyborg movement $\mathbf{x}_C(t)$ that corresponds to a natural synergistically coordinated movement of an entire arm.

9.3 Methods

9.3.1 Synergy dataset

Human template motions are taken from the dataset presented in Chapter 7 [267]. This dataset contains multi-modal measurements such as Cartesian marker trajectories of shoulder-arm movements from six right-handed, male, and unimpaired human subjects (age 30 ± 5.81). They performed 30 table-top activities of daily living (in [234] this dataset is analyzed for kinematic and muscular synergies). This work considers two *intransitive* tasks (no objects involved) and three *transitive* tasks (hand-object interactions) for validation purposes. In the intransitive tasks, the subjects lifted their right arm from a relaxed pose on the table to perform the daily-life gestures “Block light source” and “Stop gesture”. The transitive tasks involve hand-object interactions such as “Grasp an apple”, “Grasp a bottle” and “Grasp a book from shelf”. These tasks were considered suitable to demonstrate the proposed method for two reasons. First, they involve complex multi-DoF arm movements (including the upper arm, forearm, and wrist rotation). Second, the prosthetic hand can grasp the objects (i.e., apple, bottle, book).

9.3.2 Participants

The experiments took place at the Munich Institute of Robotics and Machine Intelligence of Technical University Munich (TUM). All experiments were conducted according to the principles in the Declaration of Helsinki. The unimpaired subject and the amputee gave their written informed consent prior to participating in the study. The amputee was female and had a right-arm transradial arm amputation (>1 years).

9.3.3 Experimental protocol

Three experiments were conducted with the unimpaired subject denoted as (i) “reach and grasp”, (ii) “inter-task transitioning”, and (iii) “goal change within a task”. A brief training session was conducted before the start of each experiment. The first experiment included the two intransitive and the three transitive tasks (see “Synergy dataset” section). The experiment always started from the same pre-defined start pose and ended as soon as the hand touched the object (transitive tasks) or reached the final goal pose (intransitive tasks). Each task was repeated four times. The second experiment

included the three transitive tasks with the following task sequence. Starting from the initial pose, the user was instructed to (1) grasp the object, (2) return to the start pose with the object in hand, (3) place the object back at its original place, and then (4) return to the start pose. Each task was repeated four times. The third experiment included an additional “ball grasp” task from the human synergy database. Three balls of the same size were located at the default goal and two other locations. The user was instructed to (1) look at a ball, (2) reach and grasp the ball, (3) put the ball into a ball bucket and (4) return to the start pose. This experiment was repeated three times.

The experiment with the amputee was designed in analogy with the unimpaired subject’s “inter-task transitioning” experiment. However, two of the three transitive tasks were implemented in VR. The amputee was instructed to follow the same task sequence, repeating the experiment four times.

9.3.4 Exo-Prosthesis

The presented approach is experimentally validated on an *exo-prosthesis* system [129, 268] (Fig. 9.3a). In this work, our latest developed system is used. Briefly, the system is composed of a three DoF exoskeleton, a four DoF prosthesis, and a prosthetic hand (Fig. 9.3a). The exoskeleton—used to compensate the weight of the prosthesis—is carried by the user, while the RL is mechanically fixed to it (see highlighted red-colored part in Fig. 9.3a). In this work, the exoskeleton is used for three reasons: (i) compensating the prosthesis dynamics, (ii) enabling accurate RL position sensing, and (iii) helping the carrier to focus on the actual task. The novel prosthesis (blue colored in Fig. 9.3a) includes elbow and forearm rotation, and a two DoF tendon-driven wrist for flexion/extension and radial/ulnar deviation. To the end-effector of the prosthesis, the *SoftHand Pro* is attached. This robust prosthetic hand is designed for grasping and soft manipulation based on hand synergies [287]. Furthermore, a *Myo armband* (Thalnic Labs Inc., USA) [288] serves as electromyographic user input to control the hand.

The human-coupled exo-prosthesis system can be described as a serial-chain floating-base system such as

$$\mathbf{M}(\boldsymbol{\theta})\ddot{\boldsymbol{\theta}} + \mathbf{c}(\boldsymbol{\theta}, \dot{\boldsymbol{\theta}}) + \mathbf{g}(\boldsymbol{\theta}) = \boldsymbol{\tau}_m - \boldsymbol{\tau}_f + \boldsymbol{\tau}_{\text{ext}} + \mathbf{J}_c^\top(\boldsymbol{\theta})\mathbf{F}_c, \quad (9.1)$$

$$\mathbf{F}_c = \mathbf{h}(\mathbf{x}_l - \mathbf{x}_c, \dot{\mathbf{x}}_l - \dot{\mathbf{x}}_c), \quad (9.2)$$

where $\boldsymbol{\theta} = (\mathbf{x}_b^\top \ \mathbf{q}_{\text{exo}}^\top \ \mathbf{q}_p^\top)^\top$ denotes the generalized coordinates, and indexes “b”, “exo” and “p” mark the base, exoskeleton and prosthesis entries, respectively. The base coordinates $\mathbf{x}_b = (\mathbf{r}_b^\top \ \boldsymbol{\varphi}_b^\top)^\top$ are composed of the Cartesian base position $\mathbf{r}_b \in \mathbb{R}^3$ and the Euler angle base rotation $\boldsymbol{\varphi}_b \in \mathbb{R}^3$. The joint angles of the 3 DoF exoskeleton and 4 DoF prosthesis are denoted by $\mathbf{q}_{\text{exo}} \in \mathbb{R}^3$ and $\mathbf{q}_p \in \mathbb{R}^4$, respectively. The matrix $\mathbf{M}(\boldsymbol{\theta}) \in \mathbb{R}^{13 \times 13}$ accounts for inertia. Coriolis and gravity effects are explained, respectively, by $\mathbf{c}(\boldsymbol{\theta}, \dot{\boldsymbol{\theta}}) \in \mathbb{R}^{13}$ and $\mathbf{g}(\boldsymbol{\theta}) = (\mathbf{g}_b^\top(\boldsymbol{\theta}) \ \mathbf{g}_{\text{exo}}^\top(\boldsymbol{\theta}) \ \mathbf{g}_p^\top(\boldsymbol{\theta}))^\top$, where $\mathbf{g}_b(\boldsymbol{\theta}) \in \mathbb{R}^6$, $\mathbf{g}_{\text{exo}}(\boldsymbol{\theta}) \in \mathbb{R}^3$ and $\mathbf{g}_p(\boldsymbol{\theta}) \in \mathbb{R}^4$. Frictional effects are denoted by $\boldsymbol{\tau}_f = (\mathbf{0}^\top \ \boldsymbol{\tau}_{f,\text{exo}}^\top \ \boldsymbol{\tau}_{f,p}^\top)^\top$, where $\boldsymbol{\tau}_{f,\text{exo}} \in \mathbb{R}^3$ and $\boldsymbol{\tau}_{f,p} \in \mathbb{R}^4$. Commanded motor torques are denoted by $\boldsymbol{\tau}_{m,\text{exo}} \in \mathbb{R}^3$ and $\boldsymbol{\tau}_{m,p} \in \mathbb{R}^3$, while the exoskeleton base is mechanically fixed to the human torso,

9 Synergy complement control

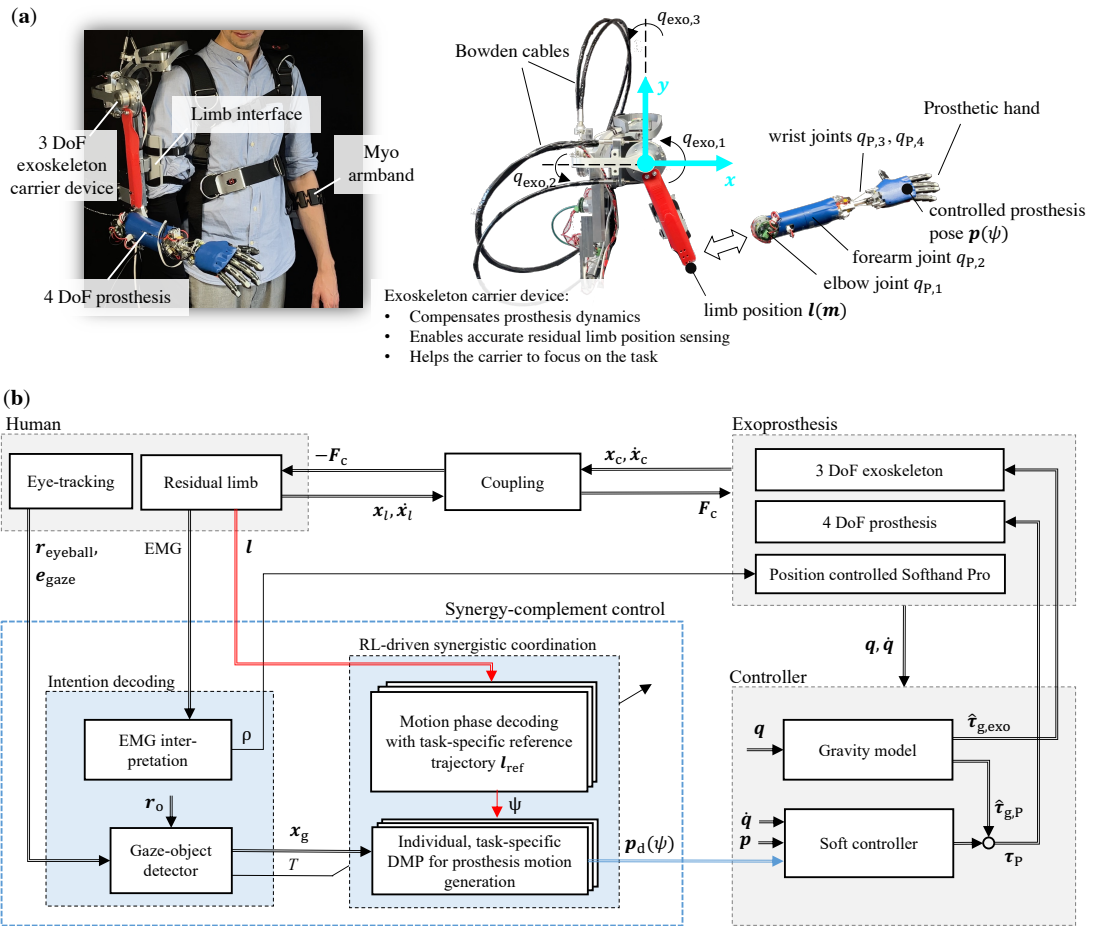


Figure 9.3: Control diagram. (a) Prosthesis testbed with exoskeleton support. (b) Overall control diagram of proposed method.

here expressed by the interaction wrench $\mathbf{F}_{\text{torso}} \in \mathbb{R}^6$. Such forces are summarized in the vector $\boldsymbol{\tau}_m = (\mathbf{F}_{\text{torso}}^\top \ \boldsymbol{\tau}_{m,\text{exo}}^\top \ \boldsymbol{\tau}_{m,\text{p}}^\top)^\top$. External forces, except for the RL coupling, are denoted by $\boldsymbol{\tau}_{\text{ext}} \in \mathbb{R}^{13}$. The human RL is mechanically connected to the system at $\mathbf{x}_c \in \mathbb{R}^6$ (cf. Fig. 9.3a) and the corresponding Jacobian is $\mathbf{J}_c(\boldsymbol{\theta}) \in \mathbb{R}^{6 \times 13}$. The RL pose is denoted by $\mathbf{x}_1 = (\mathbf{l}^\top \ \boldsymbol{\varphi}_1^\top)^\top$, where $\mathbf{l} \in \mathbb{R}^3$ is the Cartesian limb position and $\boldsymbol{\varphi}_1 \in \mathbb{R}^3$ is the Euler angle limb rotation. In this work, a very stiff connection between the RL and the exoskeleton is assumed, thus $\mathbf{x}_1 \approx \mathbf{x}_c$. Note that the full human embodied exo-prosthesis dynamics is given in [268].

9.3.5 Soft controller used with SCC

The prosthesis control law is defined as

$$\boldsymbol{\tau}_{m,\text{p}} = \mathbf{J}^\top(\mathbf{q}) \begin{pmatrix} \mathbf{K}_t(\mathbf{r}_{\text{p,d}} - \mathbf{r}_{\text{p}}) \\ \mathbf{J}_\omega^{-\top}(\boldsymbol{\varphi})\mathbf{K}_r\boldsymbol{\varphi} \end{pmatrix} + \mathbf{D}\dot{\mathbf{q}}_{\text{p}} + \hat{\mathbf{g}}_{\text{p}} + \hat{\boldsymbol{\tau}}_{\text{f,p}}, \quad (9.3)$$

where $\mathbf{r}_{\text{p,d}}, \mathbf{r}_{\text{p}} \in \mathbb{R}^3$ denote the desired and current Cartesian position of the prosthetic hand (cf. Fig. 9.3b), respectively. $\boldsymbol{\varphi} \in \mathbb{R}^3$ is the orientation difference in Euler angle representation, and $\mathbf{J}_\omega \in \mathbb{R}^{3 \times 3}$ is the Jacobian between Euler angle velocities and angular velocities [289]. The diagonal matrices $\mathbf{K}_t, \mathbf{K}_r \in \mathbb{R}^{3 \times 3}$ denote the translational and rotational stiffness matrices, respectively, and $\mathbf{D} \in \mathbb{R}^{4 \times 4}$ is the damping matrix. Furthermore, $\hat{\mathbf{g}}_{\text{p}}, \hat{\boldsymbol{\tau}}_{\text{f,p}}$ denote the estimates of gravitational and frictional effects.

The exoskeleton is used to compensate for its own weight as well as the weight of the prosthesis. The feed-forward control law, applied to the exoskeleton part, is defined as

$$\boldsymbol{\tau}_{m,\text{exo}} = \hat{\mathbf{g}}_{\text{exo}} + \hat{\boldsymbol{\tau}}_{\text{f,exo}}, \quad (9.4)$$

where $\hat{\mathbf{g}}_{\text{exo}}$ and $\hat{\boldsymbol{\tau}}_{\text{f,exo}}$ denote the estimates of $\mathbf{g}_{\text{exo}}(\boldsymbol{\theta})$ and $\boldsymbol{\tau}_{\text{f,exo}}$, respectively.

In the experiments with SCC, the exoskeleton is controlled in gravity compensation mode (9.4), and the prosthesis follows the control law defined in (9.3). The control parameters of (9.3) are empirically determined based on a full simulation of the exo-prosthesis system. They are chosen to be $\mathbf{K}_t = 125 \text{ N/m } \mathbf{I}_{3 \times 3}$, $\mathbf{K}_r = 25 \text{ N/rad } \mathbf{I}_{3 \times 3}$, where $\mathbf{I}_{3 \times 3} \in \mathbb{R}^{3 \times 3}$ denotes a identity matrix.

9.3.6 EMG-based sequential control

For the experiments based on sequential control, a joint-level impedance controller is applied, which is defined as

$$\boldsymbol{\tau}_{m,\text{p}} = \mathbf{K}_j(\mathbf{q}_{\text{p,d}} - \mathbf{q}_{\text{p}}) + \mathbf{D}_j(\dot{\mathbf{q}}_{\text{p,d}} - \dot{\mathbf{q}}_{\text{p}}) + \hat{\mathbf{g}}_{\text{p}} + \hat{\boldsymbol{\tau}}_{\text{f,p}}, \quad (9.5)$$

where $\mathbf{K}_j \in \mathbb{R}^{4 \times 4}$ and $\mathbf{D}_j \in \mathbb{R}^{4 \times 4}$ denote the joint stiffness and damping matrix, respectively. The desired joint position is calculated as

$$\mathbf{q}_{\text{p,d}} = \int \mathbf{K}_v \mathbf{s}(j, g_s) dt + \mathbf{q}_{\text{p}0}, \quad (9.6)$$

Table 9.1: Gestures recognized by the *Myo armband*.

Gesture state	Gesture
g_{s0}	double tap
g_{s1}	wave in
g_{s2}	wave out
g_{s3}	rest

where t denotes time, $\mathbf{K}_v \in \mathbb{R}^{4 \times 4}$ is a diagonal gain matrix, and $\mathbf{q}_{p0} = \text{const.} \in \mathbb{R}^4$ is the initial joint position. The i -th element of $\mathbf{s}(j, g_s) \in \mathbb{R}^4$ is defined as

$$s_i = \begin{cases} 0 \text{ rad/s,} & i \neq j \\ +1 \text{ rad/s,} & g_s = g_{s1} \wedge j = i \\ -1 \text{ rad/s,} & g_s = g_{s2} \wedge j = i \\ 0 \text{ rad/s,} & g_s = g_{s3} \wedge j = i \end{cases}, \quad i \in \{1, 2, 3, 4\}, \quad (9.7)$$

where the gesture $g_s \in \{g_{s0}, g_{s1}, g_{s2}, g_{s3}\}$ is derived from the EMG-interface (see Tab. 9.1 for a full list of gestures). Joint number j , which determines the manipulation of the i -th element of $\mathbf{s}(j, g_s)$, is the output of a state-machine. The user sequentially switches through the joints via the EMG-interface by executing gesture $g_s = g_{s0}$ and then controls its velocity by gestures $g_s = g_{s1}$, $g_s = g_{s2}$ or $g_s = g_{s3}$. Note that one further joint is added to actuate the SoftHand Pro.

9.3.7 Human template encoding

For the specific implementation, the Dynamic Movement Primitive (DMP) framework of [290, 291] is used to generate a desired position $\mathbf{r}_d(t) \in \mathbb{R}^3$ and orientation $a(t)$ (expressed as quaternion throughout this chapter) to feed the controller in (9.3). A DMP is essentially a nonlinear system that, for the positional part, can be written as [290]

$$\ddot{\mathbf{r}}_d = \mathbf{A}_p(\mathbf{r}_g - \mathbf{r}_d) - \mathbf{B}_p\dot{\mathbf{r}}_d - \mathbf{A}_p(\mathbf{r}_g - \mathbf{r}_0)\psi + \mathbf{A}_p\mathbf{f}_p(\psi), \quad (9.8)$$

where $\mathbf{r}_0, \mathbf{r}_g \in \mathbb{R}^3$ is the starting and goal position, respectively. The positive definite and diagonal matrices $\mathbf{A}_p, \mathbf{B}_p \in \mathbb{R}^{3 \times 3}$ denote stiffness and damping, respectively. A forcing term is defined as

$$\mathbf{f}_p(\psi) = \frac{\sum_i \Omega_i(\psi) \mathbf{w}_i}{\sum_i \Omega_i(\psi)} \psi, \quad (9.9)$$

where $\Omega_i(\psi) = \exp(-h_i(\psi - c_i)^2)$ is a Gaussian function with h_i, c_i being its width and center, respectively. The parameter vector $\mathbf{w}_i \in \mathbb{R}^3$ is learned for a desired trajectory based on linear regression (cf. [290]). In this work, the hand position trajectories $\mathbf{r}_{B,i}$ of task T ($\mathbf{r}_{B,i}$ is the positional component of $\mathbf{x}_{B,i}$ in Fig. 9.1) are learned that were extracted from the synergy dataset (see ‘‘Synergy dataset’’ section).

A quaternion-based DMP, as for the orientation part, can be written as [291, 290]

$$\dot{\boldsymbol{\omega}} = 2\mathbf{A}_o\Delta(\log(a_g * \bar{a})) - \mathbf{B}_o\boldsymbol{\omega} - 2\mathbf{A}_o\Delta(\log(a_g * \bar{a}_0))\psi + \mathbf{A}_o\mathbf{f}_o(\psi) \quad (9.10)$$

$$\dot{a} = \frac{1}{2}\nabla(\boldsymbol{\omega}) * a \quad (9.11)$$

where the output orientation is expressed as the unit quaternion $a = a_0 + na_1 + ma_2 + ka_3$, and $1, n, m, k$ denote the quaternion basis. The starting and goal quaternion is denoted by a_0 and a_g , respectively. The positive, definite, and diagonal stiffness and damping matrices are denoted, respectively, by $\mathbf{A}_o, \mathbf{B}_o \in \mathbb{R}^{3 \times 3}$. $\boldsymbol{\omega} \in \mathbb{R}^3$ denotes angular velocity, and $\mathbf{f}_o(\psi)$ (cf. (9.9)) is a nonlinear forcing term. The operators $\bar{\cdot}, *, \log(\cdot)$ and $\exp(\cdot)$ denote the quaternion conjugation, product, logarithm, and exponential function, respectively. Furthermore, the following operators are introduced

$$\Delta(b) := (b_1, b_2, b_3)^\top \quad (9.12)$$

$$\nabla(\mathbf{z}) = 0 + mz_1 + nz_2 + kz_3 \quad (9.13)$$

where $b = 0 + mb_1 + nb_2 + kb_3$ denotes a non-real quaternion and $\mathbf{z} = (z_1, z_2, z_3)^\top$. For the integration of (9.11) the following formula is used [291]

$$a(t + \delta t) = \exp\left(\frac{1}{2}\delta t\nabla(\boldsymbol{\omega})\right) * a(t), \quad (9.14)$$

where δt denotes the time step. Corresponding to the learned position, the hand orientation trajectory $a_{B,i}$ of task T is learned ($a_{B,i}$ is the orientation component of $\mathbf{x}_{B,i}$ in Fig. 9.1).

9.3.8 Phase variable decoding

The motion phase is obtained via the following optimization problem

$$\psi(t) = \arg \min_x \|\mathbf{u}_{\text{ref}}(x) - \mathbf{u}\|_2, \quad \text{subject to } 0 \leq x \leq 1, \quad (9.15)$$

where $\mathbf{u} := \mathbf{l}(\mathbf{m}(t)) \in \mathbb{R}^3$ denotes the current RL position (as a result of muscle activation $\mathbf{m}(t)$) and $\mathbf{u}_{\text{ref}} := \mathbf{r}_{A,i}$ is the reference limb trajectory of task T obtained from the synergy dataset ($\mathbf{r}_{A,i}$ is the position component of $\mathbf{x}_{A,i}$ in Fig. 9.1).

9.3.9 Intention decoding

9.3.9.1 EMG interpretation

For implementation purpose, the *Myo armband* [288], placed on the lower left arm, serves as EMG user input and measures lower arm muscle activation via eight electrodes. This work uses four built-in gestures (Tab. 9.1) to control the SoftHand Pro, and also to realize the sequential control mode (see ‘‘Sequential control’’ section). The SoftHand’s pose $\rho \in [0, 1]$ (if $\rho = 0$ hand is opened, if $\rho = 1$ hand is closed) is controlled in analogy to (9.6) and (9.7). Briefly, as long as g_{s1} is active the hand closes, and opens if the user activates g_{s2} , while the hand remains in the current position if g_{s3} is recognized. During gesture execution, the elbow angle is positioned at 0 degrees.

9.3.9.2 Gaze-object detector

The Euclidean distance between the i -th object and the object-related eye-focus is calculated by

$$d_i(t) = \|\mathbf{r}_{\text{eye},i}(t) - \mathbf{r}_{\text{o},i}(t)\|_2, \quad (9.16)$$

$$\mathbf{r}_{\text{eye},i}(t) = \mathbf{r}_{\text{eyeball}}(t) + \|\mathbf{r}_{\text{o},i} - \mathbf{r}_{\text{eyeball}}(t)\|_2 \mathbf{e}_{\text{gaze}}(t) \quad (9.17)$$

where $\mathbf{r}_{\text{o},i}(t) \in \mathbb{R}^3$ is the measured position of the i -th object, $\mathbf{r}_{\text{eyeball}}(t) \in \mathbb{R}^3$ denotes the measured position of the eyeball, and $\mathbf{e}_{\text{gaze}}(t) \in \mathbb{R}^3$ is the measured gaze direction vector. Object i is selected if $d_i(t) < 5$ cm. In this work, the object is only allowed to be switched if $\psi(t) = 1$ (i.e. the RL is in the start position).

The motion capture system is utilized to also adapt the goal position of an object online. The calculated goal position is

$$\mathbf{r}_g := \mathbf{r}_M + \mathbf{R}_{MM} \mathbf{r}_g, \quad (9.18)$$

where ${}_M \mathbf{r}_g \in \mathbb{R}^3$ is the measured position of the object expressed in the motion capture frame $\{M\}$. The position vector $\mathbf{r}_M \in \mathbb{R}^3$ denotes the base position of frame $\{M\}$ expressed in exo-prosthesis base frame, while $\mathbf{R}_M \in \text{SO}(3)$ denotes its rotation.

Apparatus

A *Dikablis eye-tracker* (Ergoneers Group, Germany) was used to track eye movements of the subject. A motion capture system with sixteen infrared *Vicon Vero* cameras (Vicon Motion Systems Ltd, UK) tracked the Cartesian positions of passive reflected markers at 200 Hz to track the position of the objects and subjects.

9.4 Results

9.4.1 Residual limb-prosthesis coordination

Figure 9.4 shows an image sequence with corresponding time series of the RL-prosthesis coordination for an exemplar reaching template movement, which was computationally designed. The time series is divided into six periods. In period I, the user is in the pose and does not move (Fig. 9.4-I). In period II, the RL moves forward (cf. measured RL position l_x), while the phase variable ψ starts to drop. In consequence, the prosthesis adapts its position p_y and orientation α_x to follow the synergy complementary motion. In period III, the user stops moving the RL, which causes ψ and, thus, p_y and α_x to remain constant (Fig. 9.4-III). It shows that the RL solely drives the prosthesis movement. In period IV, the user continues to move the RL leading to a further drop of ψ . Correspondingly, the prosthesis is lifted and rotated to finally reach the goal pose in period V (Fig. 9.4-V). In contrast, the final configuration with SCC turned off is shown in the top right image in Fig. 9.4. In period VI, the movement is reverted. The RL moves backward, leading ψ to increase again, which drives the prosthesis backward

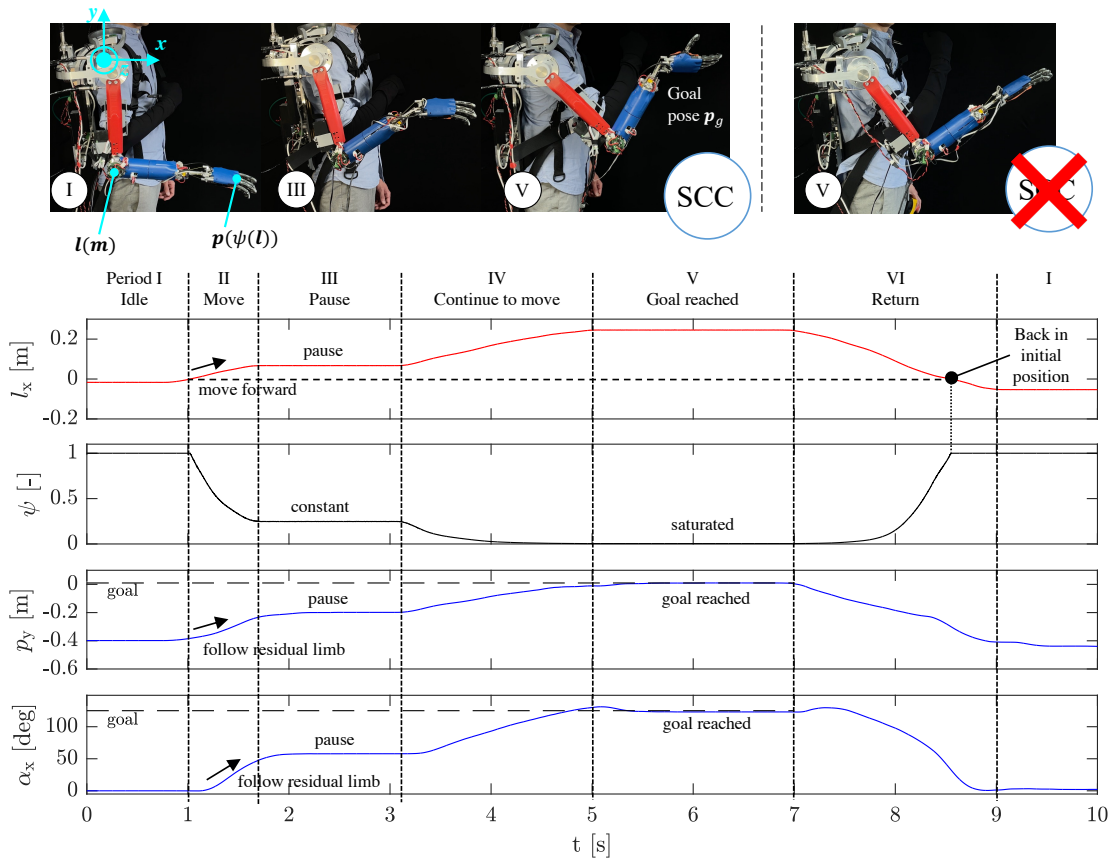


Figure 9.4: RL-prosthesis coordination for an exemplar reaching movement. Time-series of measured RL position l_x , phase variable ψ (9.15), prosthetic position p_y and prosthetic orientation α_x (angle around x -axis).

to the initial configuration. Notice in period VI that the user pulls the RL beyond the initial position. In this case, the phase variable remains at $\psi = 1$, ensuring that the prosthesis remains in its initial position.

9.4.2 Reach and grasps tasks

The SCC method is demonstrated based on two pure reaching tasks (*intransitive* tasks) (Fig. 9.5) and three reach and grasp tasks, which involve hand-object interaction (*transitive* tasks) (Fig. 9.6). All movements were learned from human templates.

Figure 9.5 shows an image sequence of the template movement and a corresponding representative “cyborg” movement for each *reaching* task, respectively. The start pose is shown in the first image, the finale pose in the third and the second images shows an intermediate state. The goal of “Block light source” (Fig. 9.5a) is to protect the eyes from the center light originating from direction \mathbf{o} , while keeping a distance of $\approx 0.1\text{m}$ from the face with the hand/prosthesis. This task is reliably executed with 100 % success rate (4 out of 4 trials) close to average human speed (Fig. 9.10a).

The goal of “Stop gesture” (Fig. 9.5b) is to signal an agent who approaches at velocity \mathbf{v} to stop by extending the arm and presenting the palm in his direction. This task is reliably executed with 100 % success rate (4 out of 4 trials) close to average human speed (Fig. 9.10a). It shows that with the proposed SCC method, lost reaching abilities are reliably recovered.

Figure 9.6 shows an image sequence of the template movement and a corresponding representative “cyborg” movement for each *reach and grasp* task, respectively. The goal of all three tasks is to reach and grasp the object, i.e., the apple (Fig. 9.6a), the bottle (Fig. 9.6b) or the book (Fig. 9.6c) at location \mathbf{x}_g from direction \mathbf{o} under the constraint not to collide with the table. All three objects are reliably grasped with each 100 % success rate (4 out of 4 trials) with the speed shown in (Fig. 9.10a). It shows that based on the proposed SCC method, more complex grasping tasks are reliably recovered. The accompanying video attachment shows the full experiment of representative trials.

9.4.3 Inter-task transitioning

Figure 9.7 shows the experimental setup, the task sequence, and time series for the inter-task transition experiment. The “cyborg” is seated in front of a table on which three objects, a book (Task 1), an apple (Task 2) and a bottle (Task 3) are placed and to be grasped (same template motions as in Fig. 9.6 are applied). Eye-tracking glasses are used to track the gaze, while a motion tracking system keeps track of the objects. The user was instructed to grasp the objects in a freely chosen order by following the “Task sequence” (see the lower box in Figure 9.7). The user can activate a *Task-Transition-Request* (TTR) by looking at the desired object for 1 second. A TTR is only accepted in this work if the RL is in the start position (i.e., phase variable $\psi = 1$). A valid TTR triggers a *Context Transition* in which both (i) the task-related RL reference motion and (ii) the task-related DMP with goal pose \mathbf{p}_g are loaded.

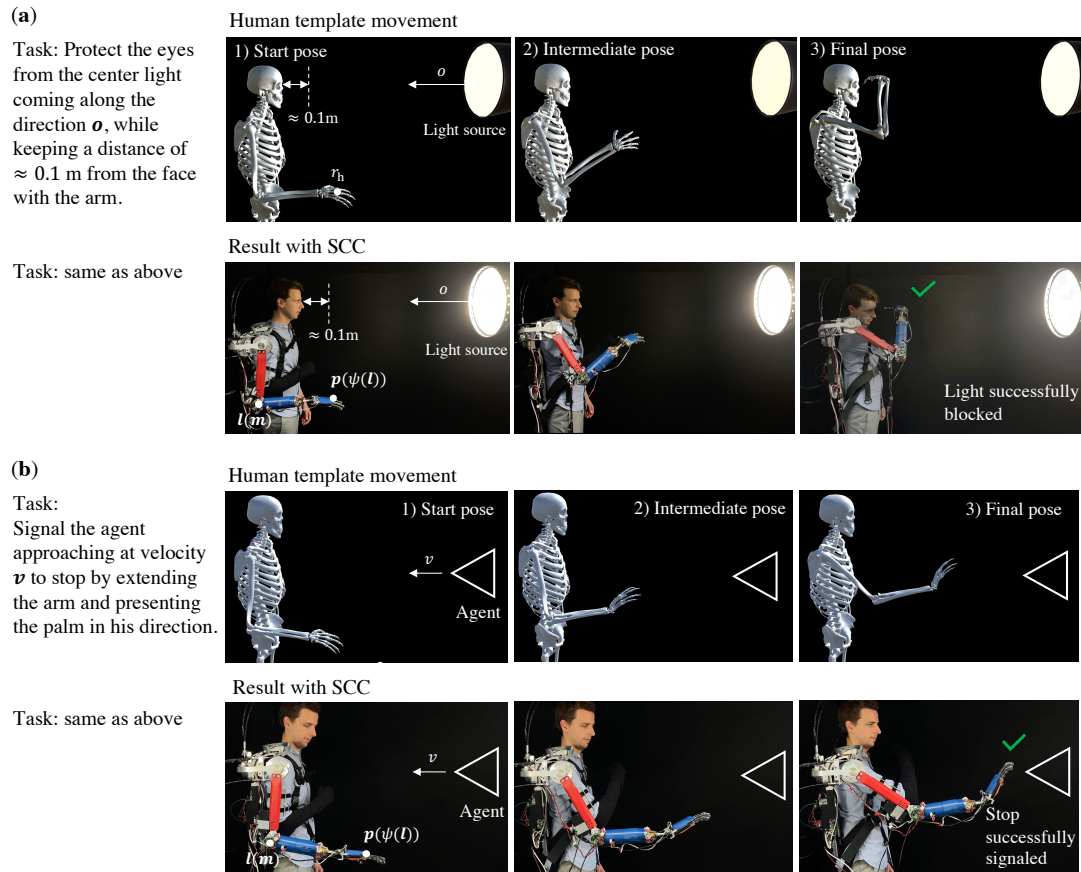


Figure 9.5: Recovered reaching skills using SCC. (a) Block light source. (b) Stop gesture.

9 Synergy complement control

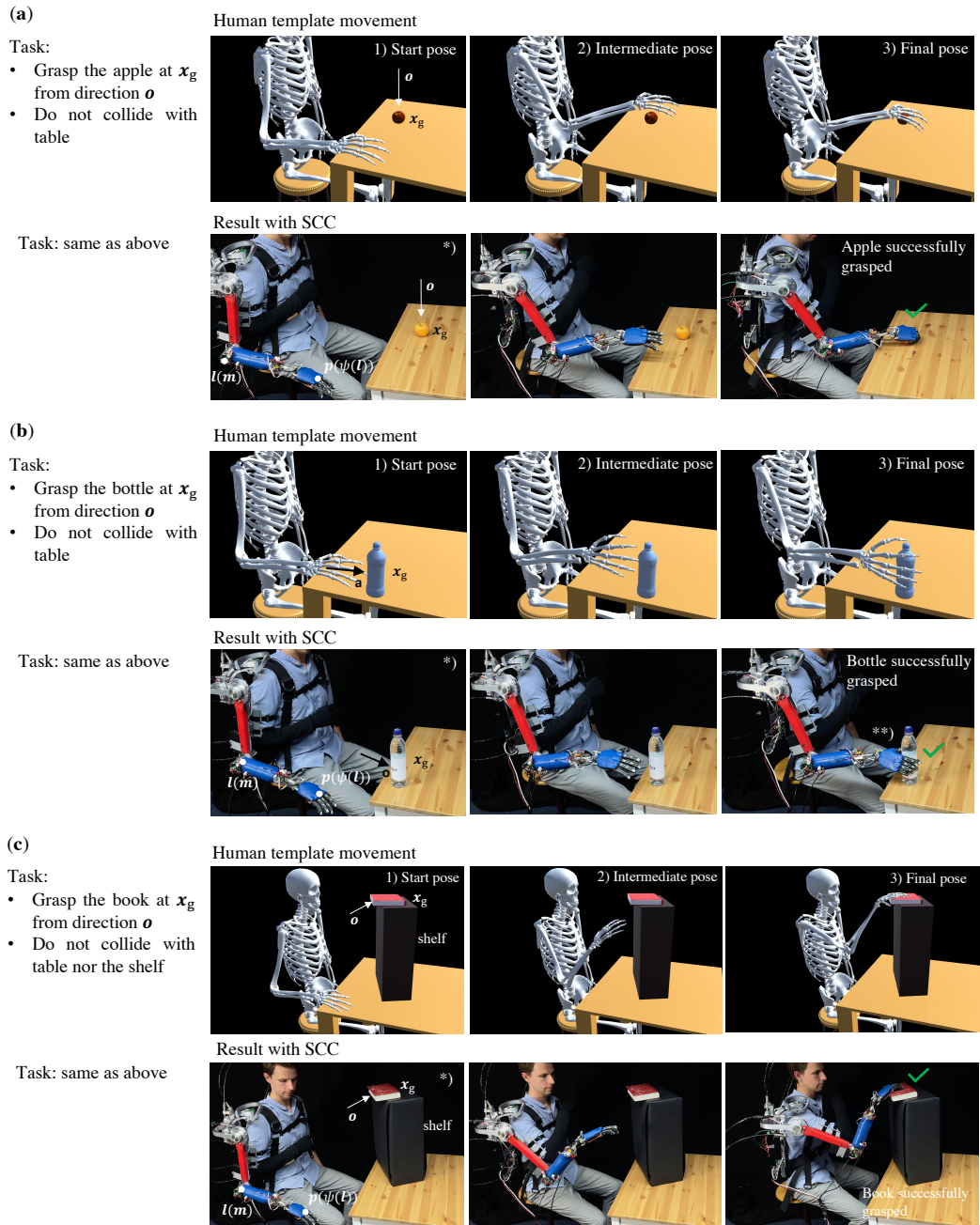


Figure 9.6: Recovered reach and grasp skills using SCC. **(a)** Reach and grasp an apple. **(b)** Reach and grasp a bottle **(c)** Reach and grasp a book. *) Due to the size of the subject and the system, the start pose was taken in front of the table. **) To ensure a firm grip with the prosthetic hand, the goal pose was adjusted compared to the template.

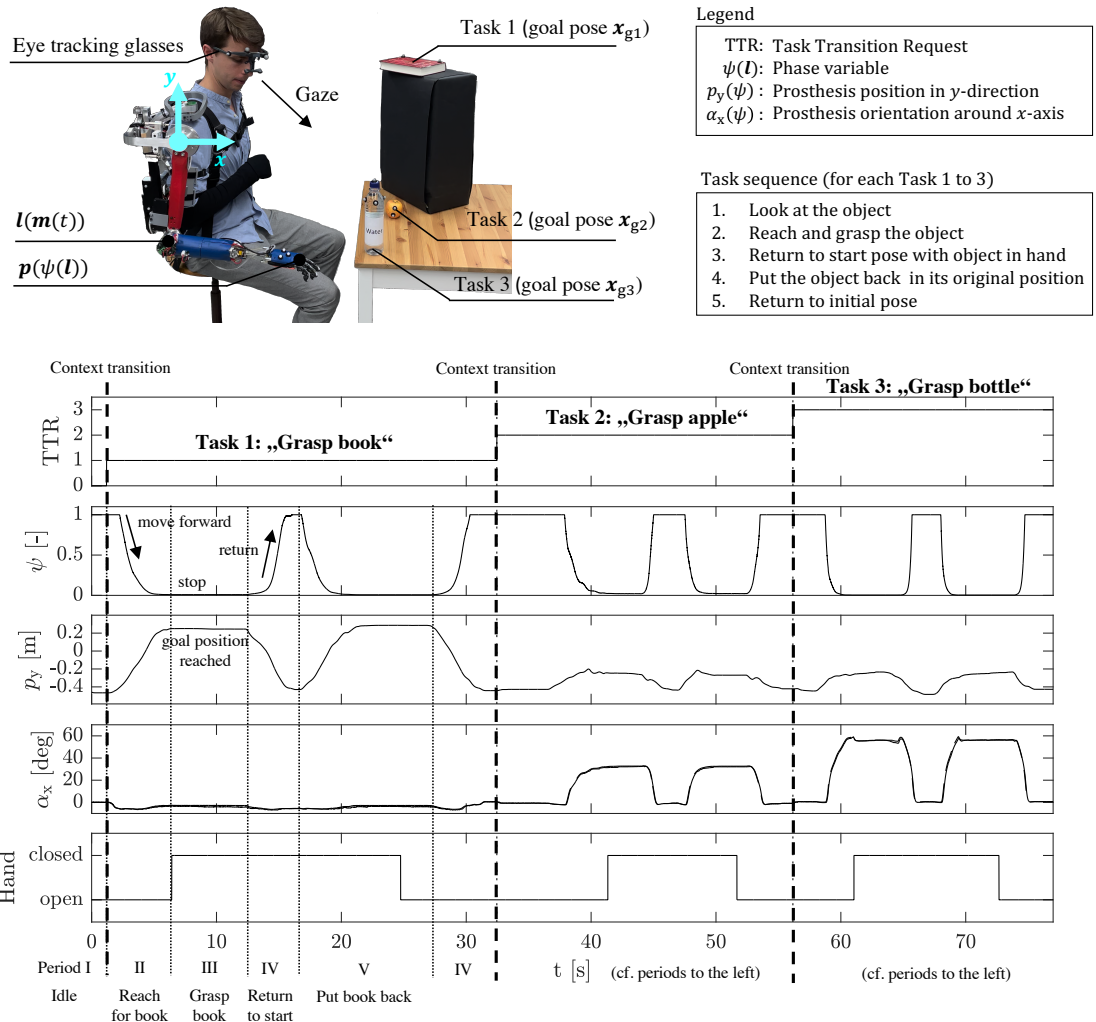


Figure 9.7: Inter-task transitioning.

The procedure is divided into five periods. In period I, the cyborg is in the initial pose and does not move. He then moves his gaze on the book, which causes a TTR for grasping the book. The corresponding RL reference motion and the DMP with goal pose \mathbf{p}_{g1} is loaded. In period II he reaches for the book causing the phase variable ψ to drop, and the prosthesis to adapt its position p_y and orientation α_x accordingly. In period III, the user closes the prosthetic hand via the *myo armband*, which is attached to his lower left arm (for more details, refer to the “Materials and Methods” section). In period IV he returns to the start pose while holding the book with his prosthetic hand. In period V he places the book back at its original location and returns to the start pose to complete the task sequence. Next, he focuses on the apple, and the procedure repeats. All three objects are reliably grasped following this sequence with each 100% success rate (4 out of 4 trials) with speed shown in (Fig. 9.10b). The results show that the proposed SCC method allows users to transit between different tasks seamlessly.

9.4.4 Goal changes within a task

Figure 9.8 shows the experimental setup, the task sequence, and time series for this experiment. The experimental setup remains the same compared to the inter-task transitioning experiment. Another human template motion is used in this experiment: a ball is grasped from the table. The red colored ball is placed at the default goal $\mathbf{x}_{g,def}$. The blue and yellow colored balls are placed at different goals \mathbf{x}_{g1} and \mathbf{x}_{g2} , respectively. The positions are measured by a motion capture system, and subsequently transformed to the exo-prosthesis base frame (cf. (9.18)). The procedure is divided into five periods. In period I, the cyborg is in the initial pose and does not move. He then moves his gaze on the red ball, which causes a TTR. The corresponding RL reference motion \mathbf{u}_{ref} and the DMP with goal pose $\mathbf{x}_{g,def}$ is loaded. In period II the user reaches for the red ball causing the phase variable ψ to drop and the prosthesis to reach the default goal position. In period III, the user grasps the ball with the prosthetic hand. In period IV he places the ball in the ball bucket and then returns to the start position (period V). Next, he focuses on the blue ball (located in the middle). The goal gets updated to \mathbf{x}_{g1} , and the procedure repeats. It shows that the proposed SCC method generalizes to new goal poses.

9.4.5 Pilot study with amputee

A pilot study with an amputee operating a fully operational digital twin of the prosthesis with SCC in Virtual Reality (VR) is conducted in analogy to the “inter-task transitioning” experiment with the unimpaired subject. The amputee’s head, thorax, and arm motions are tracked via the motion tracking system, while the VR headset track the gaze. The amputee was instructed to follow the task sequence depicted in Fig. 9.7 for the “grasp an apple” and “grasp a book” (in this order). The experiment was repeated four times. Figure 9.9a and Fig. 9.9b show image sequences of an exemplary trial for the two tasks, while Figure 9.9c shows the corresponding time series. Analog to Fig. 9.7, the time series is divided into five periods. In period I, the amputee is in the initial

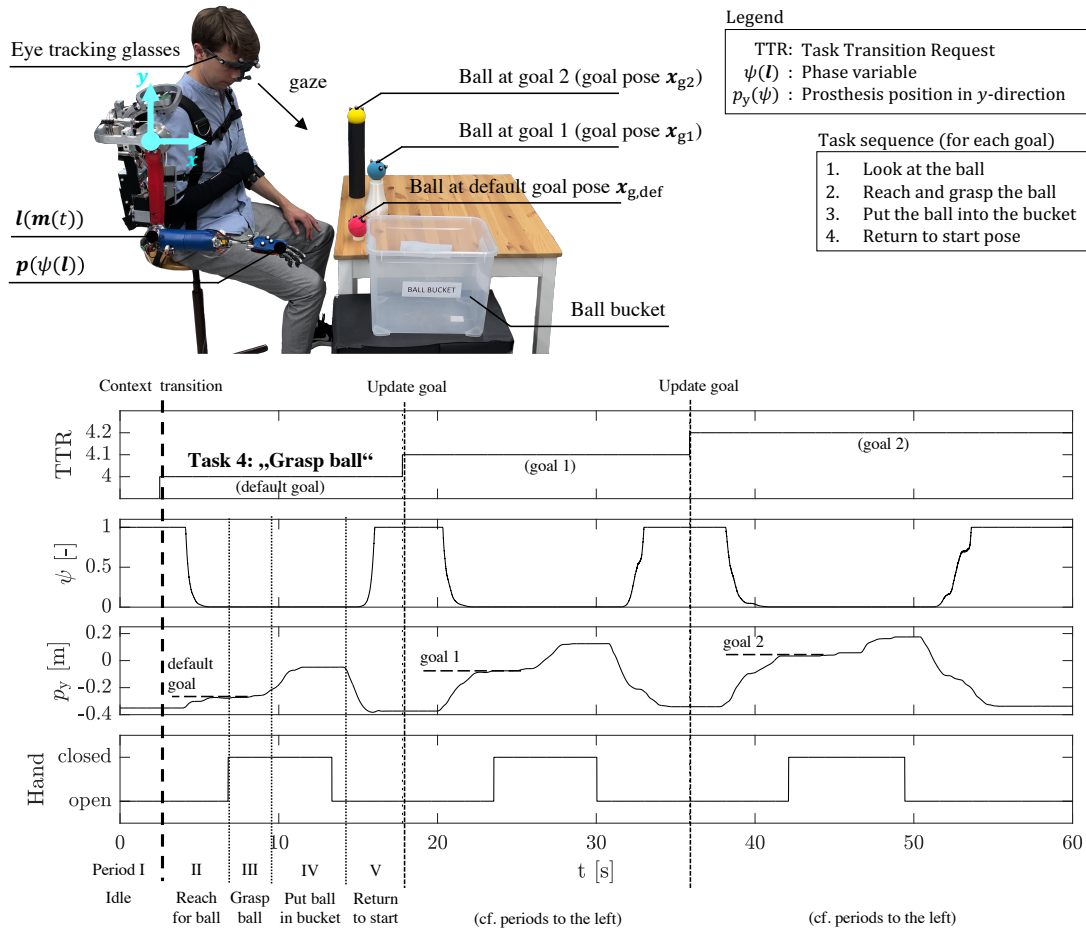


Figure 9.8: Goal change within a task.

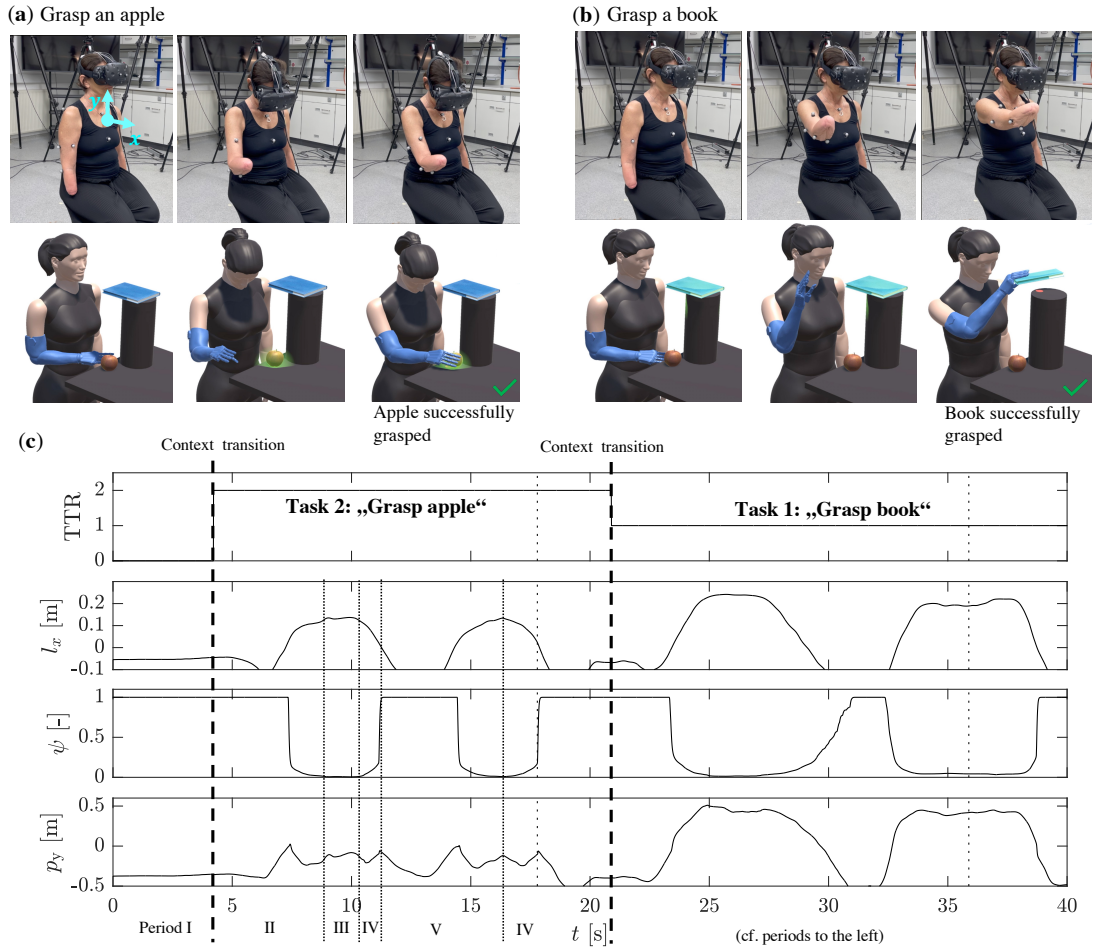


Figure 9.9: Amputee performing two tasks with SCC. (a) Image sequence of grasp an apple. (b) Image sequence of grasp a book. (c) Representative time series of both tasks. TTR denotes a Task Transition Request, l_x is the RL position in x -direction, ψ is the phase variable, and p_y denotes the prosthesis position in y -direction.

pose and does not move. She then moves her gaze on the apple, which causes a TTR; the corresponding RL reference motion and the DMP with goal pose \mathbf{x}_{g1} is loaded. She then reaches for the apple (period II), causing the phase variable ψ to drop and the prosthesis to adapt its position p_y accordingly. In period III, the apple is grasped. For simplification, the hand closes automatically if the distance between hand and object drops below a distance of 5 cm in the VR environment. In period IV she returns to the start pose while holding the apple in hand. In period V she places the apple back at its original location and returns to the start pose. Next, she focuses on the book, and the procedure repeats.

The time duration for the reaching movement (from the start position to hand-on-object) in Fig. 9.10a shows that the amputee performed similarly to the experiments with the human with preserved arm. The time duration for the whole task (see task sequence in Fig. 9.7) in Fig. 9.10b shows that the amputee performed similarly to the human with preserved arm for the “grasp an apple” task. However, it also shows that the amputee performed the “grasp a book” task faster.

9.4.6 SCC versus sequential control

In order to compare the proposed SCC method with classical control approaches, a sequential control mode that follows the control law defined in (9.5) was implemented. Briefly, based on a state-machine, the user can sequentially switch between single joints and control their velocity via an EMG-interface attached to the left lower arm (Fig. 9.3a, Tab. 9.1). The user is instructed to conduct the two reaching tasks (Fig. 9.5) and the three reach and grasp tasks (Fig. 9.6) by following the task sequence (same task sequence as depicted in Fig. 9.7):

- i) starting from the initial configuration,
- ii) grasp the object by controlling the prosthetic hand via the EMG interface,
- iii) return to the initial configuration while holding the object,
- iv) place the object back to its original location, and
- v) return to the starting pose.

In the case of the reaching tasks, the user was instructed to return to the starting pose after dwelling in the goal configuration about 1 second. Each task was repeated four times with the sequential control mode and SCC. Figure 9.10 shows the box plots of time duration for each task, respectively. In this plot, also human data from six healthy subjects who repeated each task three times is added for comparison. This initial comparison indicates that the proposed SCC method is much faster than the classical sequential control mode.

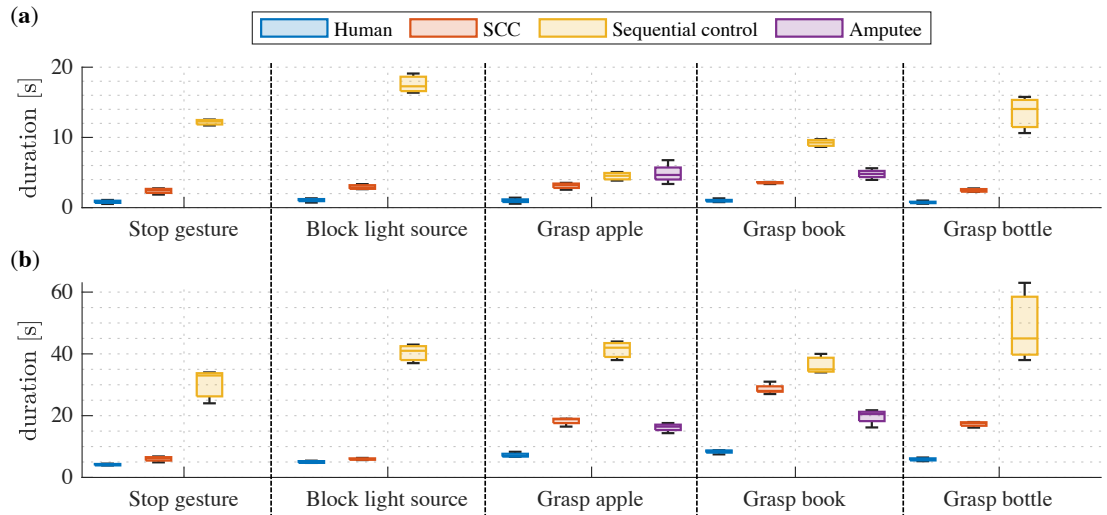


Figure 9.10: Duration comparison between methods. (a) Box-plots of duration from start pose to hand-on-object (transitive tasks) or to final goal pose (intransitive tasks). (b) Box-plots of duration for entire *task-sequence* (which is depicted in Fig. 9.7).

9.5 Discussion

Existing limb-driven methods simultaneously learn a wide spectrum of possible motions from stump to entire arm motions from human templates, relying on linear or non-linear regression techniques [192, 193, 194, 187, 195, 191, 196, 197, 198, 189, 188]. However, the mapping between low dimensional stump movement and high dimensional total limb movement is highly underdetermined. Consequently, these methods output prosthesis motions that are inaccurate, not smooth (jerky), are of unnatural shape, and often delayed [187]. In this work, the synergy complement control framework was introduced to overcome these drawbacks fundamentally.

Results on the exemplar reaching movement show that the RL purely drives the prosthesis movement. Unnatural EMG-based control that is accompanied by non-robust EMG measurements [14] are omitted for the prosthesis arm movement generation. However, this does not mean that EMG measurements are or should be avoided entirely. For example, grasping objects with the prosthetic hand is still solved via EMG measurement in this work. Although focusing on trajectory tracking, the SCC framework shall be extended to adapt the impedance setting of the prostheses and the grasping force in the future. EMG measurements will play a central role here.

The unimpaired subject solved the reaching tasks using SCC with 100% success rate and close to human speed. It shows that this method reliably generates the complementary synergy movement. Visual inspection of the generated prosthesis trajectories reveals that they are smooth and achieve the goals accurately. Compared to existing methods that output inaccurate prosthesis positions because of the inherent underdetermination in the learning approach, with SCC, the accuracy problem is reduced to a simple

tracking problem and is governed by controller performance. The unimpaired subject solved all three reach and grasp tasks with 100% success rate. It confirms that the SCC method reliably generates smooth synergy-complementary movements for more complex grasping tasks. However, the time duration of reaching (Fig. 9.10A) and especially for whole task completion (Fig. 9.10B) is still higher compared to human performance. The bulky exo-prosthesis system may have prevented the subject from performing the reaching movement more quickly. The larger time duration for the whole task completion may be also explained by the time-consuming grasping procedure (see accompanying video attachment). Extended algorithms that result in faster task completion should be implemented in the future. A further key advantage of SCC is that it can adapt to deviating goals and transits between tasks, as shown in the experiments with the unimpaired subject and the amputee. The comparison with the sequential control mode indicates that *reaching* tasks and *reach and grasp* tasks can be solved much faster with SCC. Furthermore, the pilot study with the amputee confirms that the SCC method also works with potential users.

A limitation of all RL-driven prosthesis control methods is that the prosthesis cannot be controlled if no RL motion is involved, for example, when the lower arm needs to be positioned without moving the RL. Furthermore, the comparison with the sequential control requires more subjects, trials, and perhaps other control methods to prove that SCC is superior to them. It also applies to the pilot study with the amputee. Future work will include a large-scale user study with amputees, including a thorough analysis of body compensation strategies [191]. Also, more relevant tasks will be included. Here, the intention recognition algorithms will be extended with vision-based scene understanding and also with other sensing interfaces [292]. Moreover, the SCC method will be extended to manipulate more modalities such as impedance.

In summary, this work presented a new robust RL-driven control method, SCC, that copes with the disadvantages of existing methods. The key advantages, such as reliability (i.e., high task success rates), the transition between tasks, and goal updates, were experimentally validated using a novel four DoF prosthesis. Furthermore, a pilot study with an amputee and a comparison with conventional sequential control indicate a great benefit of this method for prosthesis wearers in the future.

10 Conclusion

10.1 Summary

This thesis took an interdisciplinary approach between human (Part I), robotics (Part II) and prosthetics research (Part III). The overall goal was to deepen the understanding of human protective reflexes and arm coordination to design human-inspired protective robot/prosthesis reflexes and derive coordinated control schemes for upper limb prostheses. In the following, the thesis' works, goals G1 to G3, and research questions Q1 to Q6 (Sec. 1.1) are summarized.

Part I investigated human upper limb reflexes and motor coordination in response to noxious stimuli. Two studies were presented in total. The first study (Chapter 2) investigated how stimulus' physical characteristics such as shape, speed, or temperature modulate the kinematic and dynamic reflex responses in the neuromusculoskeletal system (Q1). It was the first attempt to shed light on this open question through a case study. Human finger reflexes elicited by mechanical and temperature stimuli with varying properties at kinematic and muscular levels were studied. Analyzing the subject's motor reactions unveiled a 5-phase reflex launch sequence that changes with shape, speed, and temperature of the stimulus and habituation. Chapter 3 dealt with the question of how humans coordinate their arm movements to avoid concurrent pain sources (Q2). Subjects needed to withdraw the arm to avoid a slap on the hand while simultaneously avoiding an elbow obstacle with noxious electrical stimulation. Results show that humans do not simply regulate the retraction of the hand alone to avoid both the original threatening source and the collision with the obstacle. However, they use the degrees of freedom of their upper limb — in a highly coordinated manner. Here, subject-specific motor strategies were used to modify the joint movement coordination to avoid hitting the obstacle with the elbow at the cost of increasing the risk of hand slap. The findings also revealed that humans adopt a conservative strategy and plan the movement according to the worst-case scenario as if assuming an obstacle in all trials. Understanding the motor strategies that humans develop to prevent damage, pain and injury adds to the understanding of motor control and may provide insight into the implementation of artificial pain mechanisms for robots in the future.

Part II presented protective robot reflexes. Chapter 5 introduced the concept of an artificial Robot Nervous System as a novel way of unifying multi-modal physical stimuli sensation with robot pain-reflex movements. This work focused on the formalization of robot pain, based on insights from human pain research, as an interpretation of tactile sensation (Q3). Specifically, pain signals were used to adapt a pain-based impedance controller's equilibrium position, stiffness, and feed-forward torque. The scheme was experimentally validated with the KUKA LWR4+ for simulated and real physical collisions

using the BioTac sensor. Also, the framework was successfully applied to a pneumatically actuated prosthesis finger testbed. Chapter 6 presented the first protective robot finger reflexes that are superhuman. In particular, it remained unclear from previous works which sensory configuration may achieve superhuman performance (Q4). To address this, this work introduced novel human-inspired robot reflex algorithms based on the aRNS framework and evaluated them with a custom-developed robot finger testbed. While the human remained superior in temperature reaction, touch reflex performance was superhuman with an unconventional configuration of proprioceptive forces and link segment acceleration. It also shows that the traditional tactile sensing or proprioceptive arrangements are suboptimal, though having the potential to be superhuman.

Part III introduced novel coordinated upper-limb prosthesis control schemes. Chapter 8 introduced the first robot-based prototype of a semi-autonomous upper-limb exo-prosthesis, unifying exoskeletons and prostheses. The exoskeleton provides the residual limb's kinematic data to enable the design of more intelligent coordinated control concepts (Q5). In contrast to established standard sequential strategies, all joints are moved simultaneously according to the desired task. Combined with an app-based configuration framework, goals were set by the user via kinesthetic teaching or autonomously via 3D computer vision. Chapter 9 introduced a novel control framework denoted synergy complement control (Q6). It allows a prosthesis to complement residual limb movements autonomously, while human arm coordination in everyday tasks, presented in Chapter 7 supported the design. With SCC, the human-prosthesis system naturally renders intended movements for its carrier and adapts online to new tasks.

In a nutshell, this thesis introduced self-protective reflexes for soft-controlled robots and prostheses inspired by analyzing human withdrawal reflexes on a single finger and coordinated arm level. Complementary to that and next to basic semi-autonomous coordinated control schemes, human arm coordination of daily life tasks helped design the novel residual limb-driven control framework SCC.

Table 10.1 evaluates research questions Q1 to Q6 and goals G1 to G3. It can be concluded that the research questions have been answered, and this thesis has achieved all goals G1 to G3. Certainly, the case study on human finger reflexes (Q1) needs further verification by a subsequent study including more subjects to generalize the results and generate mathematical models. Table 10.1 also shows future work related to the other research questions.

10.2 Impact and future work

In conclusion, on a scientific level, the development of reflex and coordinated motor controls for articulated structures have the potential to become an integral part of standard controller design for complex (semi-)autonomous systems in the future. Also, the proposed reflex-paradigms will further advance towards whole body reflex frameworks, opening up new directions for humanoid research. It will systematically treat physical disturbances and responses even for these complex systems. Furthermore, neuroscience research on motor coordination and protective reflexes provides new impulses. The pre-

Table 10.1: Evaluation of the research questions and goals from Sec. 1.1 with future work.

Goals and research questions	Chapter	Answered?	Future work
Q1 How do stimulus's physical characteristics modulate the reflex response on a kinematic and muscular level?	2	(✓)	Large-scale user study & design of mathematical reflex models
Q2 How do humans coordinate their arm movements to avoid concurrent pain sources?	3	✓	Investigate underlying motor control principles
Q3 How can human-inspired robot reflexes be designed to achieve self-protective behaviors?	5	✓	Extend framework, e.g. to avoid self-collisions
Q4 Are the insights from the human reflex studies transferable to robot reflexes and which specific sensory setup enables the best robot reflex performance?	2,6	✓	Consider alternative sensors such as vision-based sensors
Q5 How can new semi-autonomous coordinated control schemes for upper limb prostheses be achieved?	8	✓	Comprehensive user studies
Q6 How can upper-limb prosthesis control be reconciled with natural, coordinated motor control in humans?	7,9	✓	Comprehensive user studies
G1 Deepen the understanding of human upper limb withdrawal reflexes and coordination in response to noxious stimuli.	2,3	✓	
G2 Develop human-inspired self-protective reflexes for robots and prostheses.	5,6	✓	
G3 Develop new coordinated control methods for upper-limb prosthesis.	7,8,9	✓	

sented human experiments may serve others as a template for subsequent evolutions and transfer to other systems of interest.

The next generation of soft-controlled robots and prostheses benefits mainly on a technological level. Enhanced self-protection and safer interaction capabilities will become

10 Conclusion

universally available. Gained insights from human motor coordination and protective reflexes analysis revealed still unconventional configuration of proprioceptive forces and link segment acceleration suitable for low-level perception. The proposed combination of user intention, human body residual motions, controls, and autonomous behaviors with human-inspired reflexes can affect other assistive technologies such as mechatronic exoskeletons and avatars. Furthermore, the results of measuring and understanding human upper-limb protective reflexes can be helpful for numerous medical applications, diagnostic purposes, and fundamental human injury and pain research and treatment.

List of Figures

1.1	Examples of soft robotic and prosthetic systems.	1
1.2	Scientific objectives of this thesis.	3
1.3	The thesis' contributions to state of the art and structure.	13
1.4	Impressions from the work carried out in Part I.	21
2.1	Protective reflexes in humans.	23
2.2	Human reflex case study.	25
2.3	Reflex launch sequence.	29
2.4	Effect of stimulus shape and speed.	31
2.5	Effect of stimulus temperature, and finger retraction and habituation.	32
3.1	Schematic of experiment.	36
3.2	Protocol sequence and measurements.	38
3.3	Raw data of representative subjects from each group.	42
3.4	Results on hand behavior.	44
3.5	Results on elbow behavior.	45
3.6	Results on shoulder behavior.	46
3.7	Impressions from the work carried out in Part II.	57
5.1	Dynamics of a collision between a controlled robot and a collision object.	61
5.2	Collision between a controlled robot and a collision object including the aRNS.	62
5.3	Mechanical model of the proposed nervous robot-tissue.	63
5.4	Modeling aRN firing as a finite-state machine.	63
5.5	Cumulated spike signals of aRN-types.	66
5.6	Pain reflex graph.	71
5.7	\mathbf{q}_d -adaptation for single contact for different \mathbf{k}_q and \ddot{q}_r	73
5.8	\mathbf{K}_d -adaptation for repetitive contacts for different \mathbf{k}_K and \ddot{K}_r	74
5.9	Contribution of $r(\delta)$ and r_v to τ_p -adaptation for given \mathbf{k}_τ	75
5.10	Experimental setup consisting of KUKA LWR4+ equipped with BioTac sensor and controlled by the aRNS.	76
5.11	Physical collision for the KUKA LWR4+ equipped with the aRNS/BioTac and a human finger that applies varying pressure.	77
5.12	Experimental setup.	78
5.13	Contact types of the experiment shown in Fig. 5.14.	79
5.14	aRNS reflex responses.	79
5.15	Humanoid reflex stack.	80

LIST OF FIGURES

5.16	Collisions with the Atlas robot.	80
6.1	Protective reflexes in humans and robots.	84
6.2	Robot finger testbed.	85
6.3	Robot versus human protective reflexes.	90
6.4	Impressions from the work carried out in Part III.	97
7.1	Schematic experimental setup.	100
7.2	Anatomical landmarks.	103
8.1	Towards a semi-autonomous exo-prosthesis system.	106
8.2	Subsystems of exo-prosthesis and intermediate prototype.	107
8.3	Intermediate robot-based exo-prosthesis prototype.	110
8.4	Block diagram of the robot-based system with semi-autonomous coordinated control.	112
8.5	Prosthesis equipped with 3D camera (left) and exemplary result of a detected coffee mug via the vision pipeline (right).	114
8.6	Experimental task sequences.	115
8.7	Experiments with an unimpaired subject, and 3D vision controller performance during tracking of a coffee mug.	116
9.1	Workflow of SCC in seven steps.	120
9.2	Dual-task structure of reach and grasp task.	121
9.3	Control diagram prosthesis testbed and SCC.	124
9.4	RL-prosthesis coordination for an exemplar reaching movement.	129
9.5	Recovered reaching skills using SCC.	131
9.6	Recovered reach and grasp skills using SCC.	132
9.7	Inter-task transitioning.	133
9.8	Goal change within a task.	135
9.9	Amputee performing two tasks with SCC.	136
9.10	Duration comparison between methods.	138

List of Tables

1.1	Human upper-limb neuromechanics, motor control and protective reflexes.	6
1.2	Samples of state of the art of upper limb prostheses and control	9
2.1	Explanations of Phase I to V (see Fig. 2.3).	30
2.2	Parameters used in the thermal model.	30
3.1	Failure ratios f (3.3).	43
3.2	Reaction time Δt_r (3.2).	43
3.3	Results of linear regression in Fig 3.5 and Fig 3.6.	47
5.1	Robot pain classes and corresponding reaction strategies.	68
5.2	Gain vectors and parameters for collision between BioTac and human finger.	75
6.1	Human and robotic finger parameters.	89
6.2	Performance metrics.	91
7.1	The intransitive and transitive daily-life tasks.	101
7.2	The tool-mediated daily-life tasks.	102
7.3	List of measured muscles.	104
8.1	Trained gestures using the Myo armband.	111
9.1	Gestures recognized by the <i>Myo armband</i>	126
10.1	Evaluation of the research questions and goals.	143

Bibliography

- [1] A. Albu-Schäffer, C. Ott, and G. Hirzinger, “A unified passivity-based control framework for position, torque and impedance control of flexible joint robots,” *The International Journal of Robotics Research*, vol. 26, no. 1, pp. 23–39, 2007.
- [2] B. Vanderborght, A. Albu-Schäffer, A. Bicchi, E. Burdet, D. G. Caldwell, R. Carloni, M. G. Catalano, O. Eiberger, W. Friedl, G. Ganesh, M. Garabini, M. Grebenstein, G. Grioli, S. Haddadin, H. Hoppner, A. Jafari, M. Laffranchi, D. Lefeber, F. Petit, S. Stramigioli, N. G. Tsagarakis, M. V. Damme, R. V. Ham, L. C. Visser, and S. Wolf, “Variable impedance actuators: A review,” *Robotics and Autonomous Systems*, 2013.
- [3] A. Albu-Schäffer, S. Haddadin, C. Ott, A. Stemmer, T. Wimböck, and G. Hirzinger, “The dlr lightweight robot: design and control concepts for robots in human environment,” *Industrial Robot*, vol. 34, no. Iss 5, pp. 376 – 385, 2007.
- [4] S. Haddadin, *Towards Safe Robots*, ser. Springer Tracts in Advanced Robotics. Springer Berlin Heidelberg, 2014, no. 90.
- [5] S. Haddadin, A. De Luca, and A. Albu-Schäffer, “Robot collisions: A survey on detection, isolation, and identification,” *IEEE Transactions on Robotics*, vol. 33, no. 6, pp. 1292–1312, 2017.
- [6] F. E. GmbH. The robot system: Franka emika robot. [Online]. Available: <https://franka.de/robot-system>
- [7] qb robotics. qb robotics softhands. [Online]. Available: <https://qbrobotics.com>
- [8] M. Catalano, G. Grioli, E. Farnioli, A. Serio, C. Piazza, and A. Bicchi, “Adaptive synergies for the design and control of the pisa/iit softhand,” *The International Journal of Robotics Research*, vol. 33, no. 5, pp. 768–782, 2014.
- [9] A. Whitman. Modular prosthetic limb. [Online]. Available: <https://www.jhuapl.edu/prosthetics>
- [10] M. Bridges, M. Para, and M. Mashner, “Control system architecture for the modular prosthetic limb,” *JHAPLTD*, vol. 30, no. 3, 2011.
- [11] Ottobock. Ottobock prostheses. [Online]. Available: <https://www.ottobock.com/en/>

BIBLIOGRAPHY

- [12] F. M. Control. Utah arms. [Online]. Available: <https://www.utaharm.com/product-utah-arm-options/>
- [13] P. A. Parker and R. N. Scott, "Myoelectric control of prostheses," *Journal of Critical Reviews in Biomedical Engineering*, vol. 13, no. 4, pp. 283–310, 1986.
- [14] C. Castellini, P. Artemiadis, M. Wininger, A. Ajoudani, M. Alimusaj, A. Bicchi, B. Caputo, W. Craelius, S. Dosen, K. Englehart, D. Farina, A. Gijsberts, S. B. Godfrey, L. Hargrove, M. Ison, T. Kuiken, M. Marković, P. M. Pilarski, R. Rupp, and E. Scheme, "Proceedings of the first workshop on Peripheral Machine Interfaces: going beyond traditional surface electromyography," *Front Neurobot*, vol. 8, p. 22, 2014.
- [15] J. Hanson and H. E. Huxley, "Structural basis of the cross-striations in muscle," *Nature*, vol. 172, no. 4377, pp. 530–532, 1953.
- [16] J. R. Cram and G. S. Kasman, *Introduction to Surface Electromyography*. Aspen Publishers, Inc., 1998.
- [17] D. E. Rassier, B. R. MacIntosh, and W. Herzog, "Length dependence of active force production in skeletal muscle," *Journal of Applied Physiology*, vol. 86, no. 5, pp. 1445–1457, 1999.
- [18] W. Linke and G. Pfitzer, "Kontraktionsmechanismen," in *Physiologie des Menschen mit Pathophysiologie*, 30th ed., R. F. Schmidt and F. Lang, Eds. Springer Medizin Verlag, 2007, ch. 6, pp. 111–139.
- [19] J. Hescheler, "Quergestreifte muskulatur," in *Physiologie*, 5th ed., E.-J. Speckmann, J. Hescheler, and R. Köhling, Eds. Urban & Fischer Verlag, Elsevier GmbH, 2008, ch. 4.2.2, pp. 174–195.
- [20] M. Blix, "Die länge und die spannung des muskels," *Skandinavisches Archiv für Physiologie*, vol. 3, pp. 295–318, 1891.
- [21] —, "Die länge und die spannung des muskels," *Skandinavisches Archiv für Physiologie*, vol. 4, pp. 399–409, 1893.
- [22] —, "Die länge und die spannung des muskels," *Skandinavisches Archiv für Physiologie*, vol. 5, pp. 149–206, 1894.
- [23] A. V. Hill, "The heat of shortening and the dynamic constants of muscle," *Proceedings of the Royal Society of London. Series B, Biological Sciences*, vol. 126, no. 843, pp. 136–195, 1938.
- [24] —, "The series elastic component of muscle," *Proceedings of the Royal Society of London B: Biological Sciences*, vol. 137, no. 887, pp. 273–280, 1950.
- [25] —, "The mechanics of active muscle," *Proceedings of the Royal Society of London B: Biological Sciences*, vol. 141, no. 902, pp. 104–117, 1953.

- [26] H. Hatze, "A myocybernetic control model of skeletal muscle," *Biological Cybernetics*, vol. 25, pp. 103–119, 1977.
- [27] J. M. Winters and L. Stark, "Estimated mechanical properties of synergistic muscles involved in movements of a variety of human joints," *Journal of Biomechanics*, vol. 21, no. 12, pp. 1027–1041, 1988.
- [28] J. M. Winters, "An improved muscle-reflex actuator for use in large-scale neuromusculoskeletal models," *Annals of Biomedical Engineering*, vol. 23, pp. 359–374, 1995.
- [29] G. K. Cole, A. J. van den Bogert, W. Herzog, and K. G. M. Gerritsen, "Modelling of force production in skeletal muscle undergoing stretch," *Journal of Biomechanics*, vol. 29, no. 8, pp. 1091–1104, 1996.
- [30] D. G. Lloyd and T. F. Besier, "An emg-driven musculoskeletal model to estimate muscle force and knee joint movements in vivo," *Journal of Biomechanics*, vol. 36, pp. 765–776, 2002.
- [31] E. Cavallaro, J. Rosen, J. C. Perry, S. Burns, and B. Hannaford, "Hill-based model as a myoprocessor for a neural concontrol powered exoskeleton arm - parameters optimization," in *IEEE International Conference on Robotics and Automation*, Barcelona, Spain, 2005.
- [32] E. E. Cavallaro, J. Rosen, J. C. Perry, and S. Burns, "Real-time myoprocessors for a neural controlled powered exoskeleton arm," *IEEE Transactions on Biomedical Engineering*, vol. 53, no. 11, pp. 2387–2396, 2006.
- [33] D. G. Thelen, F. C. Anderson, and S. L. Delp, "Generating dynamic simulation of movement using computed muscle control," *Journal of Biomechanics*, vol. 36, pp. 321–328, 2003.
- [34] D. G. Thelen and F. C. Anderson, "Using computed muscle control to generate forward dynamic simulation of human walking from experimental data," *Journal of Biomechanics*, vol. 39, pp. 1107–1115, 2006.
- [35] H. Gomi and R. Osu, "Task-dependent viscoelasticity of human multijoint arm and its spatial characteristics for interaction with environments," *Journal of Neuroscience*, vol. 18, no. 21, pp. 8965–8978, 1998.
- [36] M. G. Pandy, "Computer modeling and simulation of human movement," *Annu. Rev. Biomed. Eng.*, vol. 3, pp. 245–273, 2001.
- [37] K. P. Tee, E. Burdet, C. M. Chew, and T. E. Milner, "A model of force and impedance in human arm movements," *Biological Cybernetics*, vol. 90, pp. 368–375, 2004.

BIBLIOGRAPHY

- [38] J. Rosen, J. C. Perry, N. Manning, S. Burns, and B. Hannaford, "The human arm kinematics and dynamics during daily activities - toward a 7 dof upper limb powered exoskeleton," in *IEEE International Conference on Advanced Robotics*, Seattle, WA, USA, 2005, pp. 532–539.
- [39] A. Erdemir, S. McLean, W. Herzog, and A. J. van den Bogert, "Model-based estimation of muscle force exerted during movements," *Clinical Biomechanics*, vol. 22, pp. 131–154, 2007.
- [40] R. Shadmehr and M. A. Arbib, "A mathematical analysis of the force-stiffness characteristics of muscles in control of a single joint system," *Biological Cybernetics*, vol. 66, pp. 463–477, 1992.
- [41] P. Pigeon, L. Yahia, and A. G. Feldman, "Moment arms and length of human upper limb muscles as function of joint angles," *Journal of Biomechanics*, vol. 29, no. 10, pp. 1365–1370, 1996.
- [42] B. A. Garner and M. G. Pandy, "The obstacle-set method for representing muscle paths in musculoskeletal models," *Computer Methods in Biomechanics and Biomedical Engineering*, vol. 3, pp. 1–30, 2000.
- [43] ———, "Musculoskeletal model of the upper limb based on the visible human male dataset," *Computer Methods in Biomechanics and Biomedical Engineering*, vol. 4, pp. 93–126, 2001.
- [44] N. Hogan, "Impedance control: An approach to manipulation: Part i - theory, part ii - implementation, part iii - applications," *Journal of Dynamic Systems, Measurement, and Control*, vol. 107, pp. 1–24, 1985.
- [45] W. M. Murray, S. L. Delp, and T. S. Buchanan, "Variation of muscle moment arms with elbow and forearm position," *Journal of Biomechanics*, vol. 28, no. 5, pp. 513–525, 1995.
- [46] D. K. Kuechle, S. R. Newman, E. Itoi, G. L. Niebur, and B. F. Morrey, "The relevance of the moment arm of shoulder muscles with respect to axial rotation of the glenohumeral joint in four positions," *Clinical Biomechanics*, vol. 15, pp. 322–329, 1997.
- [47] A. K. Bremer, G. R. Sennwald, P. Favre, and H. A. C. Jacob, "Moment arms of forearm rotators," *Clinical Biomechanics*, vol. 21, pp. 683–691, 2005.
- [48] D. C. Ackland, P. Pak, M. Richardson, and M. G. Pandy, "Moment arms of the muscles crossing the anatomical shoulder," *Journal of Anatomy*, vol. 213, pp. 383–390, 2008.
- [49] D. C. Ackland and M. G. Pandy, "Moment arms of the shoulder muscles during axial rotation," *Journal of Orthopaedic Research*, vol. 29, pp. 658–667, 2011.

- [50] M. A. Shermann, A. Seth, and Delp, “What is a moment arm? calculating muscle effectiveness in biomechanical models using generalized coordinates,” in *International Design Engineering Technical Conferences and Computers and Information in Engineering Conference*, vol. 7B, Portland, Oregon, USA, August 2013.
- [51] M. Jäntschi, “Non-linear control strategies for musculoskeletal robots,” Ph.D. dissertation, Technische Universität München, 2014.
- [52] B. A. Garner and M. G. Pandy, “Estimation of musculotendon properties in the human upper limb,” *Annals of Biomedical Engineering*, vol. 31, pp. 207–220, 2003.
- [53] W. Herzog, “Distribution problem in biomechanics,” in *Encyclopedia of Neuroscience*, M. D. Binder, N. Hirokawa, and U. Windhorst, Eds. Springer-Verlag Berlin Heidelberg, 2009, pp. 983–985.
- [54] S. R. Hammer, A. Seth, and S. L. Delp, “Muscle contributions to propulsion and support during running,” *Journal of Biomechanics*, vol. 43, pp. 2709–2716, 2010.
- [55] B. A. Garner and M. G. Pandy, “A kinematic model of the upper limb based on the visible human project (vhp) image dataset.” *Computer methods in biomechanics and biomedical engineering*, vol. 2, pp. 107–124, 1999.
- [56] E. V. Biryukova, A. Roby-Brami, A. A. Frolov, and M. Mokhtari, “Kinematics of human arm reconstructed from spatial tracking system recordings,” *Journal of Biomechanics*, vol. 33, pp. 985–995, 2000.
- [57] T. H. Schiebler and H.-W. Korf, “Extremitäten,” in *Anatomie: Histologie, Entwicklungsgeschichte, makroskopische und mikroskopische Anatomie, Topographie*. Steinkopff Verlag, 2007, ch. 12, pp. 450–580.
- [58] M. Veber, T. Bajd, and M. Munih, “Assessing joint angles in human hand via optical tracking device and calibrating instrumented glove,” *Meccanica*, vol. 42, no. 5, pp. 451–463, 2007.
- [59] P. Cerveri, E. D. Momi, N. Lopomo, G. Baud-Bovy, R. M. L. Barros, and G. Ferrigno, “Finger kinematic modeling and real-time hand motion estimation,” *Annals of Biomedical Engineering*, vol. 35, no. 11, pp. 1989–2002, 2007.
- [60] C. D. Metcalf, S. V. Notley, P. H. Chappell, J. H. Burridge, and V. T. Yule, “Validation and application of a computational model for wrist and hand movements using surface markers,” *IEEE Transactions on Biomedical Engineering*, vol. 55, no. 3, pp. 1199–1210, 2008.
- [61] R. Nataraj and Z.-M. Li, “Integration of marker and force data to compute three-dimensional joint moments of the thumb and index finger jigits during pinch,” *Computer Methods in Biomechanics and Biomedical Engineering*, vol. 18, no. 16, pp. 592–606, 2015.

BIBLIOGRAPHY

- [62] L. Vigouroux, M. Domalain, and E. Berton, “Effect of object width on muscle and joint forces during thumb–index finger grasping,” *Journal of Applied Biomechanics*, vol. 27, pp. 173–180, 2011.
- [63] X. Zhang, S.-W. Lee, and P. Braido, “Determining finger segmental centers of rotation in flexion–extension based on surface marker measurement,” *Journal of Biomechanics*, vol. 36, p. 1097–1102, 2003.
- [64] J. R. Cook, N. A. Baker, R. Cham, E. Hale, and M. S. Redfern, “Measurements of wrist and finger postures: A comparison of goniometric and motion capture techniques,” *Journal of Applied Biomechanics*, vol. 23, pp. 70–78, 2007.
- [65] A. D. Speirs, C. F. Small, J. T. Bryant, D. R. Pichora, and B. Y. Zee, “Three-dimensional metacarpophalangeal joint kinematics using two markers on the phalanx,” *Journal of Engineering in Medicine*, vol. 2015, no. 4, pp. 415–419, 2001.
- [66] F. Cordella, L. Zollo, A. Salerno, D. Accoto, E. Guglielmelli, and B. Siciliano, “Human hand motion analysis and synthesis of optimal power grasps for a robotic hand,” *International Journal of Advanced Robotic Systems*, vol. 11, p. 1, 2014.
- [67] R. Nataraj and Z.-M. Li, “Robust identification of three-dimensional thumb and index finger kinematics with a minimal set of markers,” *Journal of Biomedical Engineering*, vol. 135, no. 9, pp. 091 002–091 002–9, 2013.
- [68] E. Burdet, D. W. Franklin, and T. E. Milner, *Human Robotics: Neuromechanics and Motor Control*. MIT Press Ltd, 2013.
- [69] R. F. Kirsch, D. Boskov, W. Z. Rymer, R. E. Center, M. H. M. Center, and O. H. Cleveland, “Muscle stiffness during transient and continuous movements of catmuscle: perturbation characteristics and physiological relevance,” *IEEE Transactions on Biomedical Engineering*, vol. 41, no. 8, pp. 758–770, Aug 1994.
- [70] R. Shadmehr and F. A. Mussa-Ivaldi, “Adaptive representation of dynamics during learning of a motor task,” *Journal of Neuroscience*, vol. 14, no. 5, pp. 3208–3224, 1994.
- [71] M. A. Smith, A. Ghazizadeh, and R. Shadmehr, “Interacting adaptive processes with different timescales underlie short-term motor learning,” *PLOS Biology*, vol. 4, no. 6, 2006.
- [72] D. W. Franklin, U. So, E. Burdet, and M. Kawato, “Visual feedback is not necessary for the learning of novel dynamics,” *PLOS Biology*, vol. 2, no. 12, p. e1336, 2007.
- [73] E. Burdet, R. Osu, D. W. Franklin, T. E. Milner, and M. Kawato, “The central nervous system stabilizes unstable dynamics by learning optimal impedance,” *Nature*, vol. 414, pp. 446–449, 2001.

- [74] A. Kadiallah, G. Liaw, M. Kawato, and E. Burdet, “Impedance control is selectively tuned to multiple directions of movement,” *Journal of Neurophysiology*, vol. 106, no. 5, pp. 2737–2748, 2011.
- [75] D. W. Franklin, G. Liaw, T. E. Milner, R. Osu, E. Burdet, and M. Kawato, “End-point stiffness of the arm is directionally tuned to instability in the environment,” *Journal of Neurophysiology*, vol. 27, no. 29, pp. 7705–7716, 2007.
- [76] D. W. Franklin and D. M. Wolpert, “Computational mechanisms of sensorimotor control,” *Neuron*, vol. 72, no. 3, pp. 425–442, 2011.
- [77] K. P. Tee, D. W. Franklin, M. Kawato, T. E. Milner, and E. Burdet, “Concurrent adaptation of force and impedance in the redundant muscle system,” *Biological Cybernetics*, vol. 102, pp. 31–44, 2010.
- [78] E. Burdet and A. Codourey, “Evaluation of parametric and nonparametric nonlinear adaptive controllers,” *Robotica*, vol. 16, no. 1, pp. 59–73, 1998.
- [79] R. C. Miall, D. J. Weir, D. M. Wolpert, and J. F. Stein, “Is the cerebellum a smith predictor?” *Journal of Motor Behavior*, vol. 25, no. 3, pp. 203–216, 1993.
- [80] R. C. Miall and D. M. Wolpert, “The cerebellum as a predictive model of the motor system: a smith predictor hypothesis,” in *Neural Control of Movement*, W. R. Ferrell and U. Proske, Eds. Plenum Press, 1995, pp. 215–222.
- [81] P. van der Smagt and G. Hirzinger, “The cerebellum as computed torque model,” in *Fourth International Conference on Knowledge-Based Intelligent Engineering Systems and Allied Technologies*, Brighton, UK, Aug 2000.
- [82] N. Bhushan and R. Shadmehr, “Computational nature of human adaptive control during learning of reaching movements in force field,” *Biological Cybernetics*, vol. 81, pp. 39–60, 1999.
- [83] M. Kawato, “Internal models for motor control and trajectory planning,” *Current Opinion in Neurobiology*, vol. 9, no. 6, pp. 718–727, 1999.
- [84] I. Kurtzer, J. A. Pruszynski, and S. H. Scott, “Long-latency reflexes of the human arm reflect an internal model of limb dynamics,” *Current Biology*, vol. 18, no. 6, pp. 449–453, 2008.
- [85] S. H. Scott, “Optimal feedback control and the neural basis of volitional motor control,” *Nature*, vol. 5, pp. 534–546, 2004.
- [86] ———, “The computational and neural basis of voluntary motor control and planning,” *Trends in Cognitive Sciences*, vol. 16, no. 11, pp. 541–549, 2012.
- [87] H. A. H. Jongen, J. J. Denier van der Gon, and C. C. A. M. Gielen, “Activation of human arm muscles during flexion/extension and supination/pronation tasks: a theory on muscle coordination,” *Biological Cybernetics*, vol. 61, pp. 1–9, 1989.

BIBLIOGRAPHY

- [88] A. de Rugy, G. E. Loeb, and T. J. Carroll, "Are muscle synergies useful for neural control?" *Front. Comput. Neurosci.*, vol. 7, 2013.
- [89] A. d'Avella and F. Lacquaniti, "Control of reaching movements by muscle synergy combinations," *Front. Comput. Neurosci.*, vol. 7, 2013.
- [90] A. d'Avella, A. Portone, L. Fernandez, and F. Lacquaniti, "Control of fast-reaching movements by muscle synergy combinations," *Journal of Neuroscience*, vol. 26, no. 30, pp. 7791–7810, 2006.
- [91] M. F. Bear, B. W. Connors, and M. A. Paradiso, "Das somatosensorische system," in *Neurowissenschaften*, 3rd ed., A. K. Engel, Ed. Springer Spektrum, 2007, ch. 12, pp. 427–469.
- [92] C. S. Sherrington, "Flexion-reflex of the limb, crossed extension- reflex and reflex stepping and standing," *J Physiol*, pp. 28–121, 1910.
- [93] E. Kugelberg, "Demonstration of a and c fibre components in the babinski plantar response and the pathological flexion reflex," *Brain*, vol. 71, no. 3, pp. 304–19, 1948.
- [94] E. Kugelberg, K. Eklund, and L. Grimby, "An electromyographic study of the nociceptive reflexes of the lower limb. mechanism of the plantar responses," *Brain*, vol. 83, pp. 394–410, 1960.
- [95] N. Eckert and Z. A. Riley, "The nociceptive withdrawal reflex does not adapt to joint position change and short-term motor practice," *F1000Research*, vol. 2, p. 158, 2013.
- [96] C. L. Peterson, Z. A. Riley, E. T. Krepkovich, W. M. Murray, and J. Perreault, "Withdrawal reflexes in the upper limb adapt to arm posture and stimulus location," *Muscle & Nerve*, vol. 49, no. 5, pp. 716–723, 2014.
- [97] K. E. Hagbarth, "Excitatory and inhibitory skin areas for flexor and extensor motoneurons," *Acta Physiol Scand Suppl*, vol. 26, no. 94, pp. 1–58, 1952.
- [98] ———, "Spinal withdrawal reflexes in the human lower limbs," *J. Neurol. Neurosurg. Psychiat.*, vol. 23, p. 222, 1960.
- [99] R. W. Clarke and J. Harris, "The organization of motor response to noxious stimuli," *Brain Research Reviews*, vol. 46, pp. 163–172, 2004.
- [100] M. K. Floeter, C. Gerloff, J. Kouri, and M. Hallett, "Cutaneous withdrawal reflexes of the upper extremity," *Muscle and Nerve*, vol. 21, no. 5, pp. 591–598, 1998.
- [101] M. Kofler, P. Fuhr, A. A. Leis, F. X. Glocker, M. F. Kronenberge, J. Wissele, and I. Stetkarovaf, "Modulation of upper extremity motor evoked potentials by cutaneous afferents in humans," *Clinical Neurophysiology*, vol. 112, pp. 1053–1063, 2001.

- [102] R. Don, F. Pierelli, A. Ranavolo, M. Serrao, M. Mangone, M. Paoloni, A. Cacchio, G. Sandrini, and V. Santilli, "Modulation of spinal inhibitory reflex responses to cutaneous nociceptive stimuli during upper limb movement," *European Journal of Neuroscience*, vol. 28, pp. 559–568, 2008.
- [103] A. A. Leis, D. S. Stokic, P. Fuhr., M. Kofler, M. F. Kronenberg, J. Wissel, F. X. Glocker, C. Seifert, and I. Stetkarova, "Nociceptive fingertip stimulation inhibits synergistic motoneuron pools in the human upper limb," *Neurology*, vol. 55, no. 9, pp. 1305–1309, 2000.
- [104] K. E. Hagbarth and B. L. Finer, *The Plasticity of Human Withdrawal Reflexes to Noxious Skin Stimuli in Lower Limbs*. Elsevier Publishing Company, 1963, ch. Progress in Brain Research, Volume 1, Brain Mechanisms, pp. 65–81.
- [105] M. Hugon, *New Developments in Electromyography and Clinical Neurophysiology*. Karger, 1973, vol. 3, ch. Exteroceptive reflexes to stimulation of the sural nerve in normal man, pp. 713–729.
- [106] K. Kanda and H. Sato, "Reflex responses of human thigh muscles to non-noxious sural stimulation during stepping," *Brain Research*, vol. 288, no. 1-2, pp. 378–380, 1983, kan83.
- [107] J. Duysens, A. Tax, M. Trippel, and V. Dietz, "Increased amplitude of cutaneous reflexes during human running as compared to standing," *Brain Research*, vol. 613, pp. 230–238, 1993.
- [108] M. Serrao, F. Pierelli, R. Don, A. Ranavolo, A. Cacchio, A. Curra, G. Sandrini, M. Frascarelli, and V. Santilli, "Kinematic and electromyographic study of the nociceptive withdrawal reflex in the upper limbs during rest and movement." *The Journal of Neuroscience*, vol. 26, pp. 3505–13, Mar 2006.
- [109] E. G. Spaich, J. Emborg, T. Collet, L. Arendt-Nielsen, and O. K. Andersen, "Withdrawal reflex responses evoked by repetitive painful stimulation delivered on the sole of the foot during late stance: site, phase, and frequency modulation," *Experimental Brain Research*, vol. 194, pp. 359–368, 2009.
- [110] J. Schouenborg, H.-R. Weng, and H. Holmberg, "Modular organization of spinal reflexes: a new hypothesis," *News Physiological Sciences*, vol. 9, pp. 261–265, 1994.
- [111] O. K. Andersen, F. A. Sonnenborg, and L. Arendt-Nielsen, "Modular organization of human leg withdrawal reflexes elicited by electrical stimulation of the foot sole," *Muscle Nerve*, vol. 22, pp. 1520–1530, 1999.
- [112] F. A. Sonnenborg, O. K. Andersen, L. Arendt-Nielsen, and R.-D. Treede, "Withdrawal reflex organisation to electrical stimulation of the dorsal foot in humans," *Experimental Brain Research*, vol. 136, pp. 303–312, 2001.

BIBLIOGRAPHY

- [113] J. Schouenborg, “Modular organisation and spinal somatosensory imprinting,” *Brain Research Reviews*, vol. 40, pp. 80–91, 2002.
- [114] B. B. Edin and J. H. Abbs, “Finger movement responses of cutaneous mechanoreceptors in the dorsal skin of the human hand,” *B. B. Edin and J. H. Abbs*, vol. 65, no. 3, pp. 657–669, 1991.
- [115] Z. Riley, E. T. Krepkovich, E. C. Mayland, W. M. Murray, and E. J. Perreault, “Flexion-withdrawal reflexes in the upper-limb adapt to the position of the limb.” in *Annual Conference of the American Society of Biomechanics*, 2009.
- [116] T. S. Dahl, E. A. Swere, and A. Palmer, “Touch-triggered withdrawal reflexes for safer robots,” in *New Frontiers in Human–Robot Interaction*, K. Dautenhahn and J. Saunders, Eds. John Benjamins Publishing Company, 2011, ch. Touch-Triggered Withdrawal Reflexes for Safer Robots, pp. 281–304.
- [117] J. M. Winters, “Hill-based muscle models: a systems engineering perspective,” in *Multiple muscle systems: biomechanics and movement organization*, J. M. Winters and S. L. Woo, Eds. Springer-Verlag, 1990, ch. 5, pp. 69–93.
- [118] R. C. Miall, D. J. Weir, D. M. Wolpert, and J. F. Stein, “Is the cerebellum a smith predictor?” *Journal of Motor Behavior*, vol. 25, no. 3, pp. 203–216, 1993.
- [119] S. Haddadin and E. Croft, *Physical Human–Robot Interaction*. Cham: Springer International Publishing, 2016, pp. 1835–1874. [Online]. Available: https://doi.org/10.1007/978-3-319-32552-1_69
- [120] W. Townsend and J. Salisbury, “Mechanical design for whole-arm manipulation,” in *Robots and Biological Systems*. Springer, 1993.
- [121] A. Albu-Schäffer, S. Haddadin, C. Ott, A. Stemmer, T. Wimböck, and G. Hirzinger, “The DLR lightweight robot - lightweight design and soft robotics control concepts for robots in human environments,” *Industrial Robot Journal*, vol. 34, no. 5, pp. 376–385, 2007.
- [122] G. Hirzinger, J. Butterfaß, M. Fischer, M. Grebenstein, M. Hahnle, H. Liu, I. Schaefer, and N. Sporer, “A mechatronics approach to the design of light-weight arms and multi-fingered hands,” *IEEE International Conference on Robotics and Automation*, 2000.
- [123] Y. Yamada, Y. Hirasawa, S. Huang, Y. Umetani, and K. Suita, “Human-robot contact in the safeguarding space,” *IEEE/ASME Transactions on Mechatronics*, vol. 2, no. 4, pp. 230–236, 1997.
- [124] B. Vanderborght, B. Verrelst, R. Van Ham, M. Van Damme, D. Lefeber, B. M. Y. Duran, and P. Beyl, “Exploiting natural dynamics to reduce energy consumption by controlling the compliance of soft actuators,” *The International Journal of Robotics Research*, vol. 25, no. 4, pp. 343–358, 2006.

- [125] A. Albu-Schäffer, O. Eiberger, M. Grebenstein, S. Haddadin, C. Ott, T. Wimböck, S. Wolf, and G. Hirzinger, “Soft robotics: From torque feedback controlled lightweight robots to intrinsically compliant systems,” *IEEE Robotics and Automation Magazine: Special Issue on Adaptable Compliance/Variable Stiffness for Robotic Applications*, vol. 15, no. 3, pp. 20 – 30, 2008.
- [126] R. van Ham, T. Sugar, B. Vanderborght, K. Hollander, and D. Lefeber, “Compliant actuator designs: Review of actuators with passive adjustable compliance/controltable stiffness for robotic applications,” *IEEE Robotics and Automation Magazine*, vol. 16, no. 3, pp. 81–94, 2009.
- [127] J. Craig and M. Raibert, “A systematic method for hybrid position/force control of a manipulator,” *IEEE International Computer Software and Applications Conference*, 1979.
- [128] C. Ott, *Cartesian Impedance Control of Redundant and Flexible-Joint Robots*. Springer Publishing Company, Incorporated, 2008.
- [129] S. Haddadin, “Prosthesis,” Germany Patent PCT/EP2017/059 699, 2017.
- [130] E. Shahriari, A. Kramberger, A. Gams, A. Ude, and S. Haddadin, “Adapting to contacts: Energy tanks and task energy for passivity-based dynamic movement primitives,” in *IEEE/RAS International Conference on Humanoid Robotics*, 2017, pp. 136–142.
- [131] C. Yang, G. Ganesh, S. Haddadin, S. Parusel, A. Albu-Schaeffer, and E. Burdet, “Human-like adaptation of force and impedance in stable and unstable interactions,” *IEEE Transactions on Robotics*, vol. 27, no. 5, pp. 918–930, 2011.
- [132] S. Takakura, T. Murakami, and K. Ohnishi, “An approach to collision detection and recovery motion in industrial robot,” in *Annual Conference of IEEE Industrial Electronics Society, Philadelphia, USA*, 1989, pp. 421–426.
- [133] K. Kosuge, T. Matsumoto, and S. Morinaga, “Collision detection system for manipulator based on adaptive control scheme,” *Transactions of the Society of Instrument and Control Engineers*, vol. 4, no. 39, pp. 552–558, 2003.
- [134] M. Strohmayer, “Artificial skin in robotics,” Master’s thesis, Karlsruhe Institute of Technology, 2012.
- [135] R. S. Dahiya, P. Mittendorfer, M. Valle, G. Cheng, and V. J. Lumelsky, “Directions toward effective utilization of tactile skin: A review,” *IEEE Sensors Journal*, vol. 13, no. 11, pp. 4121–4138, 2013.
- [136] A. De Luca and R. Mattone, “Actuator failure detection and isolation using generalized momenta,” in *IEEE International Conference on Robotics and Automation*, vol. 1, 2003, pp. 634–639 vol.1.

BIBLIOGRAPHY

- [137] J. Vorndamme, M. Schappler, and S. Haddadin, “Collision detection, isolation and identification for humanoids,” in *IEEE International Conference on Robotics and Automation*, 2017.
- [138] S. Haddadin, A. Albu-Schäffer, A. De Luca, and G. Hirzinger, “Collision detection and reaction: A contribution to safe physical human-robot interaction,” in *IEEE International Conference on Intelligent Robots and Systems*, 2008, pp. 3356–3363.
- [139] A. De Luca and L. Ferrajoli, “Exploiting robot redundancy in collision detection and reaction,” in *IEEE/RSJ International Conference on Intelligent Robots and Systems*, 2008, pp. 3299–3305.
- [140] S. Parusel, S. Haddadin, and A. Albu-Schäffer, “Modular state-based behavior control for safe human-robot interaction: A lightweight control architecture for a lightweight robot,” in *IEEE International Conference on Robotics and Automation*, 2011, pp. 4298–4305.
- [141] Q. H. Q. Huang and Y. Nakamura, “Sensory reflex control for humanoid walking,” *IEEE Transactions on Robotics*, vol. 21, no. 5, pp. 977–984, 2005.
- [142] R. Kratz, S. Klug, M. Stelzer, and O. von Stryk, “Biologically inspired reflex based stabilization control of a humanoid robot with artificial sma muscles,” in *IEEE International Conference on Robotics and Biomimetics*, 2006, pp. 1089–1094.
- [143] S. Yakovenko, V. Gritsenko, and A. Prochazka, “Contribution of stretch reflexes to locomotor control: a modeling study,” *Biological Cybernetics*, vol. 90, no. 2, pp. 146–155, 2004.
- [144] T. Tanikawa, Y. Masuda, and M. Ishikawa, “A reciprocal excitatory reflex between extensors reproduces the prolongation of stance phase in walking cats: Analysis on a robotic platform,” *Frontiers in Neurorobotics*, vol. 15, p. 36, 2021.
- [145] M. M. Williamson, “Postural primitives: Interactive behavior for a humanoid robot arm,” *Society for Adaptive Behaviour*, 1996.
- [146] S. Yigit, C. Burghart, and H. Woern, “Applying reflexes to enhance safe human-robot-co-operation with humanlike robot arm,” *International Symposium on Robotics*, pp. 1–6, 2004.
- [147] T. S. Dahl and A. Paraschos, “A force-distance model of humanoid arm withdrawal reflexes,” in *Advances in Autonomous Robotics*, 2012, pp. 13–24.
- [148] T. Kröger and F. M. Wahl, “Online trajectory generation: Basic concepts for instantaneous reactions to unforeseen events,” *IEEE Transactions on Robotics*, vol. 26, no. 1, pp. 94–111, 2010.
- [149] A. De Luca, A. Albu-Schäffer, S. Haddadin, and G. Hirzinger, “Collision detection and safe reaction with the dlr-iii lightweight manipulator arm,” in *IEEE International Conference on Intelligent Robots and Systems*, 2006, pp. 1623–1630.

- [150] S. Haddadin, F. Huber, and A. Albu-Schäffer, “Optimal control for exploiting the natural dynamics of variable stiffness robots,” in *IEEE International Conference on Robotics and Automation*, 2012, pp. 3347–3354.
- [151] S. Ivaldi, “From humans to hhumanoid: a study on optimal motor control for the icub,” Ph.D. dissertation, Italian Institute of Technology & University of Genova, Italy, 2011.
- [152] Elbow components. [Online]. Available: <https://professionals.ottobockus.com/media/pdf/646D626-EN-04-1411w.pdf>
- [153] Utha arm 3. [Online]. Available: <http://www.utaharm.com/index.php>
- [154] Boston digital arm systems for adults. [Online]. Available: <http://www.liberatingtech.com/>
- [155] Dynamic arm. [Online]. Available: <http://www.ottobock.de/prothetik/armprothetik/systemuebersicht/dynamic-arm-prothesenellenbogen/>
- [156] Prosthesis for running activities. [Online]. Available: <http://www.ottobockus.com/prosthetics/lower-limb-prosthetics/solution-overview/above-knee-fitness-prosthesis/>
- [157] J. Burck, J. Bigelow, and S. Harshbarger, “Revolutionizing prosthetics: Systems engineering challenges and opportunities,” *Johns Hopkins APL Technical Digest (JHAPLTD)*, vol. 30, no. 3, 2011.
- [158] M. Johannes, J. Bigelow, J. Burck, S. Harshbarger, M. Kozlowski, and T. Van Doren, “An overview of the developmental process for the modular prosthetic limb,” *JHAPLTD*, vol. 30, no. 3, 2011.
- [159] C. Moran, “Revolutionizing prosthetics 2009 modular prosthetic limb – body interface: Overview of the prosthetic socket development,” *Johns Hopkins APL Technical Digest*, vol. 30, no. 3, pp. 204 – 249, 2011.
- [160] D. S. Childress, “Historical aspects of powered limb prostheses,” *Clinical Prosthetics and Orthotics*, vol. 9, no. 1, pp. 2–13, 1985.
- [161] M. Borchardt, K. Hartmann, R. Leymann, and S. Schlesinger, *Ersatzglieder und Arbeitshilfen: Für Kriegsbeschädigte und Unfallverletzte*. Springer-Verlag, 2013.
- [162] W. Sauter, “Myoelektrische, durch mikroschaltungen gesteuerte prothesensysteme für die obere extremität,” in *Amputationschirurgie und Rehabilitation*. Springer, 1985, pp. 373–391.
- [163] C. K. Battye, A. Nightingale, and J. Whillis, “The use of myo-electric currents in the operation of prostheses,” *The Journal of Bone and Joint Surgery. British volume*, vol. 37-B, no. 3, pp. 506–510, Aug. 1955.

BIBLIOGRAPHY

- [164] N. Berger and C. R. Huppert, "The use of electrical and mechanical muscular forces for the control of an electrical prosthesis." *The American journal of occupational therapy*, vol. 6, no. 3, p. 110, 1952.
- [165] T. Schiebler and H. Korf, *Anatomie - Histologie, Entwicklungsgeschichte, makroskopische und mikroskopische Anatomie, Topographie*, 10th ed. Steinkopff Verlag, 2007.
- [166] R. Bartlett, *Introduction to Sports Biomechanics: Analysing Human Movement*, 2nd ed. Routledge, Taylor & Francis Group, Abingdon, 2007.
- [167] K. Kiguchi and E. Horikawa, "A study on human upper-limb muscles activities during daily upper-limb motions," *International Journal of Bioelectromagnetism*, vol. 12, no. 2, pp. 54 – 61, 2010.
- [168] N. Klopčar and J. Lenarčič, "Kinematic model for determination of human arm reachable workspace," *Meccanica*, vol. 40, pp. 203 – 219, 2005.
- [169] K. Abdel-Malek, J. Yang, R. Brand, and E. Tanbour, "Towards understanding the workspace of human limbs," *Ergonomics*, vol. 47, no. 13, pp. 1386 – 1405, 2004.
- [170] M. Mihelj, "Human arm kinematics for robot based rehabilitation," *Robotica*, vol. 24, no. 3, pp. 377 – 383, May 2006.
- [171] J. Burck, J. Bigelow, and S. Harshbarger, "Revolutionizing prosthetics: Systems engineering challenges and opportunities," *Johns Hopkins APL Technical Digest*, vol. 30, no. 3, 2011.
- [172] M. Bridges, M. Para, and M. Mashner, "Control system architecture for the modular prosthetic limb," *Johns Hopkins APL Technical Digest*, vol. 30, no. 3, 2011.
- [173] M. Johannes, J. Bigelow, J. Burck, S. Harshbarger, M. Kozłowski, and T. Van Doren, "An overview of the developmental process for the modular prosthetic limb," *Johns Hopkins APL Technical Digest*, vol. 30, no. 3, 2011.
- [174] W. Zhang, Q. Huang, D. Jia, H. Xin, M. Li, and K. Li, "Mechanical design of a light weight and high stiffness humanoid arm of bhr-03," in *IEEE International Conference on Robotics and Biomimetics*, Guilin, China, December 19 -23 2009.
- [175] T. McGee, M. Para, K. Katyal, and M. Johannes, "Demonstration of force feedback control on the modular prosthetic limb," in *Systems, Man, and Cybernetics*. San Diego, CA, USA: IEEE, October 5-8 2014.
- [176] Z. Khokhar, Z. Xiao, and C. Menon, "Surface emg pattern recognition for real-time control of a wrist exoskeleton," *BioMedical Engineering OnLine*, vol. 9, no. 41, pp. 1 – 17, 2010.

- [177] B. Peerdeman, D. Boere, H. Witteveen, R. Huis in Veld, H. Hermens, S. Stramigioli, H. Rietman, P. Veltink, and S. Misra, “Myoelectric forearm prostheses; state of the art from a user-centered perspective,” *Journal of Rehabilitation Research and Development*, vol. 48, no. 6, pp. 719 – 738, 2011.
- [178] C. Castellini, P. Artemiadis, M. Wininger, A. Ajoudani, M. Alimusaj, A. Bicci, W. Caputo, B. Craelius, S. Dosen, K. Engelhart, D. Farina, A. Gijssberts, S. Godfrey, L. Hargrove, M. Ison, T. Kuiken, M. Markovic, P. Pilarski, R. Rupp, and E. Scheme, “Proceedings of the first workshop on peripheral machine interfaces: going beyond traditional surface electromyography,” *Frontiers in Neurorobotics*, vol. 8, no. 22, pp. 1 – 17, 2014.
- [179] M. Ortiz-Catalan, B. Håkansson, and R. Brånemark, “Real-time and simultaneous control of artificial limbs based on pattern recognition algorithms,” *IEEE Transactions on Neural Systems and Rehabilitation Engineering*, vol. 22, no. 4, pp. 756 – 764, 2014.
- [180] S. Bitzer and P. van der Smagt, “Learning EMG control of a robotic hand: towards active prostheses,” in *IEEE International Conference on Robotics and Automation*, 2006, pp. 2819–2823.
- [181] C. Castellini and P. van der Smagt, “Surface emg in advanced hand prosthetics,” *Biological cybernetics*, vol. 100, no. 1, pp. 35–47, 2009.
- [182] D. Farina, N. Jiang, H. Rehbaum, A. Holobar, B. Graimann, H. Dietl, and O. C. Aszmann, “The extraction of neural information from the surface EMG for the control of upper-limb prostheses: Emerging avenues and challenges,” *IEEE Transactions on Neural Systems and Rehabilitation Engineering*, vol. 22, no. 4, pp. 797–809, Jul. 2014.
- [183] N. Jiang, S. Dosen, K.-R. Muller, and D. Farina, “Myoelectric control of artificial limbs—is there a need to change focus?[in the spotlight],” *IEEE Signal Processing Magazine*, vol. 29, no. 5, pp. 152–150, 2012.
- [184] J. Cheesborough, L. Smith, T. Kuiken, and G. Dumanian, “Targeted muscle reinnervation and advanced prosthetic arms,” *Seminars in Plastic Surgery*, vol. 29, no. 01, pp. 062–072, Feb. 2015.
- [185] L. R. Hochberg, D. Bacher, B. Jarosiewicz, N. Y. Masse, J. D. Simeral, J. Vogel, S. Haddadin, J. Liu, S. S. Cash, P. Van Der Smagt *et al.*, “Reach and grasp by people with tetraplegia using a neurally controlled robotic arm,” *Nature*, vol. 485, no. 7398, pp. 372–375, 2012.
- [186] J. Vogel, S. Haddadin, B. Jarosiewicz, J. D. Simeral, D. Bacher, L. R. Hochberg, J. P. Donoghue, and P. van der Smagt, “An assistive decision-and-control architecture for force-sensitive hand–arm systems driven by human–machine interfaces,” *The International Journal of Robotics Research*, vol. 34, no. 6, pp. 763–780, 2015.

BIBLIOGRAPHY

- [187] M. Legrand, M. Merad, E. de Montalivet, A. Roby-Brami, and N. Jarrassé, “Movement-based control for upper-limb prosthetics: Is the regression technique the key to a robust and accurate control?” *Frontiers in Neurorobotics*, vol. 12, p. 41, 2018.
- [188] S. Iftime, L. Egsgaard, and M. Popović, “Automatic determination of synergies by radial basis function artificial neural networks for the control of a neural prosthesis,” *IEEE Transactions on Neural Systems and Rehabilitation Engineering*, vol. 13, pp. 482–9, 01 2006.
- [189] M. Farokhzadi, A. Maleki, A. Fallah, and S. Rashidi, “Online estimation of elbow joint angle using upper arm acceleration: A movement partitioning approach,” *Journal of Biomedical Physics and Engineering*, vol. 7, pp. 305–314, 09 2017.
- [190] H. Vallery and M. Buss, “Complementary limb motion estimation based on interjoint coordination using principal components analysis,” in *IEEE International Conference on Control Applications*, vol. 1-4, Nov 2006, pp. 933 – 938.
- [191] M. LEGRAND, “Upper limb prostheses control based on user’s body compensations,” Theses, Sorbonne Université, Mar. 2021. [Online]. Available: <https://tel.archives-ouvertes.fr/tel-03360709>
- [192] R. R. Kaliki, R. Davoodi, and G. E. Loeb, “Evaluation of a noninvasive command scheme for upper-limb prostheses in a virtual reality reach and grasp task,” *IEEE Transactions on Biomedical Engineering*, vol. 60, no. 3, pp. 792–802, Mar 2013.
- [193] —, “Prediction of distal arm posture in 3-d space from shoulder movements for control of upper limb prostheses,” *Proceedings of the IEEE*, vol. 96, no. 7, pp. 1217–1225, 2008.
- [194] M. Merad, A. Roby-Brami, and N. Jarrassé, “Towards the implementation of natural prosthetic elbow motion using upper limb joint coordination,” in *IEEE International Conference on Biomedical Robotics and Biomechatronics*, 2016, pp. 821–826.
- [195] M. Merad, É. de Montalivet, A. Touillet, N. Martinet, A. Roby-Brami, and N. Jarrassé, “Can we achieve intuitive prosthetic elbow control based on healthy upper limb motor strategies?” *Frontiers in Neurorobotics*, vol. 12, Feb. 2018.
- [196] M. Popovic and D. Popovic, “Cloning biological synergies improves control of elbow neuroprostheses,” *IEEE Engineering in Medicine and Biology Magazine*, vol. 20, no. 1, pp. 74–81, 2001.
- [197] B. Mijovic, M. Popović, and D. Popović, “Synergistic control of forearm based on accelerometer data and artificial neural networks,” *Brazilian Journal of Medical and Biological Research*, vol. 41, pp. 389–97, June 2008.

- [198] N. Alshammary, D. Bennett, and M. Goldfarb, “Efficacy of coordinating shoulder and elbow motion in a myoelectric transhumeral prosthesis in reaching tasks,” in *IEEE International Conference on Robotics and Automation*, May 2016, pp. 3723–3728.
- [199] J. Kühn, T. Hu, A. Tödtheide, E. Pozo Fortunić, E. Jensen, and S. Haddadin, “Approaching asimov’s 3rd law: Superhuman protective robot reflexes for touch and heat,” *Science Robotics*, *submitted*, Dec 2021.
- [200] J. Kühn, C. Bagnato, E. Burdet, and S. Haddadin, “Arm movement adaptation to concurrent pain constraints,” *Scientific Reports (Springer Nature)*, vol. 11, no. 1, p. 6792, 2021.
- [201] E. Martin and R. Hine, *A Dictionary of Biology*. Oxford University Press, 2008.
- [202] M. F. Bear, B. W. Connors, and M. A. Paradiso, *Neuroscience - Exploring the Brain*. Lippincott Williams & Wilkins, 2007.
- [203] M. J. Caterina, M. A. Schumacher, M. Tominaga, T. A. Rosen, J. D. Levine, and D. Julius, “The capsaicin receptor: a heat-activated ion channel in the pain pathway.” *Nature*, vol. 389, pp. 816–24, Oct 1997.
- [204] B. Coste, J. Mathur, M. Schmidt, T. J. Earley, S. Ranade, M. J. Petrus, A. E. Dubin, and A. Patapoutian, “Piezo1 and piezo2 are essential components of distinct mechanically activated cation channels.” *Science (New York, N.Y.)*, vol. 330, pp. 55–60, Oct 2010.
- [205] S.-H. Woo, V. Lukacs, J. C. de Nooij, D. Zaytseva, C. R. Criddle, A. Francisco, T. M. Jessell, K. A. Wilkinson, and A. Patapoutian, “Piezo2 is the principal mechanotransduction channel for proprioception.” *Nature neuroscience*, vol. 18, pp. 1756–62, Dec 2015.
- [206] E. P. Zehr and C. Haridas, “Modulation of cutaneous reflexes in arm muscles during walking: further evidence of similar control mechanisms for rhythmic human arm and leg movements.” *Experimental Brain Research*, vol. 149, pp. 260–6, Mar 2003.
- [207] R. C. Oldfield, “The assessment and analysis of handedness: The edinburgh inventory,” *Neuropsychologia*, vol. 9, pp. 97–113, 1970.
- [208] H. J. Hermens, B. Freriks, C. Disselhorst-Klug, and G. Rau, “Development of recommendations for semg sensors and sensor placement procedures.” *Journal of Electromyography and Kinesiology*, vol. 10, pp. 361–74, Oct 2000.
- [209] N. Hogan, “Impedance control: An approach to manipulation,” in *1984 American Control Conference*, 1984, pp. 304–313.
- [210] H.-N. Ho and L. Jones, “Thermal model for hand-object interactions,” in *IEEE International Symposium on Haptic Interfaces for Virtual Environment and Teleoperator Systems*, April 2006, pp. 461–467.

BIBLIOGRAPHY

- [211] L. A. Jones and H.-N. Ho, “Warm or cool, large or small? the challenge of thermal displays,” *IEEE Transactions on Haptics*, vol. 1, no. 1, pp. 53–70, 2008.
- [212] *Footwear, leather and imitation leather goods manufacturing machines - Shoe and leather presses - Safety requirements DIN EN 12203*, DIN Deutsches Institut für Normung e.V. Std., Jul. 2010.
- [213] J. W. Valvano, *Tissue Thermal Properties and Perfusion*, A. J. Welch and M. J. C. Van Gemert, Eds. Springer US, 1995.
- [214] M. L. Cohen, “Measurement of the thermal properties of human skin. a review,” *Journal of Investigative Dermatology*, vol. 69, no. 3, pp. 333–338, 1977.
- [215] M. Kittelmann, L. Adolph, A. Michel, R. P. M. Schüte, and S. Sommer, “Handbuch gefährdungsbeurteilung - teil 2,” Bundesanstalt für Arbeitsschutz und Arbeitsmedizin, Tech. Rep., Feb. 2021.
- [216] J. Duysens, M. Trippel, G. A. Horstmann, and V. Dietz, “Gating and reversal of reflexes in ankle muscles during human walking.” *Experimental brain research*, vol. 82, pp. 351–8, 1990.
- [217] G. Sandrini, M. Serrao, P. Rossi, A. Romaniello, G. Cruccu, and J. C. Willer, “The lower limb flexion reflex in humans.” *Progress in neurobiology*, vol. 77, pp. 353–95, Dec 2005.
- [218] E. P. Zehr and R. Chua, “Modulation of human cutaneous reflexes during rhythmic cyclical arm movement.” *Experimental brain research*, vol. 135, pp. 241–50, Nov 2000.
- [219] M. K. Floeter, C. Gerloff, J. Kouri, and M. Hallett, “Cutaneous withdrawal reflexes of the upper extremity,” *Muscle and nerve*, 1998.
- [220] J. A. Pruszynski, I. Kurtzer, and S. H. Scott, “The long-latency reflex is composed of at least two functionally independent processes.” *Journal of neurophysiology*, vol. 106, pp. 449–59, Jul 2011.
- [221] T. Hu, J. Kühn, and S. Haddadin, “Forward and inverse dynamics modeling of human shoulder-arm musculoskeletal system with scapulothoracic constraint,” *Computer Methods in Biomechanics and Biomedical Engineering*, vol. 23, no. 11, pp. 785–803, 2020.
- [222] R. Melzack and K. Casey, *Sensory, Motivational, and Central Control Determinants of Pain*. Charles C. Thomas, Jan 1968, pp. 423–439.
- [223] S. N. Raja, D. B. Carr, M. Cohen, N. B. Finnerup, H. Flor, S. Gibson, F. J. Keefe, J. S. Mogil, M. Ringkamp, K. A. Sluka, X.-J. Song, B. Stevens, M. D. Sullivan, P. R. Tutelman, T. Ushida, and K. Vader, “The revised international association for the study of pain definition of pain: concepts, challenges, and compromises.” *Pain*, May 2020.

- [224] H. Breivik, P. C. Borchgrevink, S. M. Allen, L. A. Rosseland, L. Romundstad, E. K. Breivik Hals, G. Kvarstein, and A. Stubhaug, “Assessment of pain,” *BJA: British Journal of Anaesthesia*, vol. 101, no. 1, pp. 17–24, May 2008.
- [225] D. C. Turk and R. Melzack, *Handbook of pain assessment*. Guilford Press, 2011.
- [226] G. Hawker, S. Mian, T. Kenozerska, and M. French, “Measures of adult pain: Visual analog scale for pain (vas pain), numeric rating scale for pain (nrs pain), mcgill pain questionnaire (mpq), short-form mcgill pain questionnaire (sf-mpq), chronic pain grade scale (cpgs), short form-36 bodily pain scale (sf-36 bps), and measure of intermittent and constant osteoarthritis pain (icoap).” *Arthritis Care Res (Hoboken)*, vol. 63, pp. 240–252, 2011.
- [227] J. Willer, “Comparative study of perceived pain and nociceptive flexion reflex in man,” *Pain*, vol. 3, pp. 69–80, 1977.
- [228] J. C. Pinheiro and D. M. Bates, *Mixed-Effects Models in S and S-PLUS*. Springer, New York, NY, 2000.
- [229] B. Winter, *Linear models and linear mixed effects models in R with linguistic applications*, Cornell University, 2013.
- [230] E. R. Kandel, J. H. Schwartz, and T. M. Jessell, *Principles of neural science*. New York: McGraw-Hill, Health Professions Division, 2000.
- [231] C. Bagnato, A. Takagi, and E. Burdet, “Artificial nociception and motor responses to pain, for humans and robots.” *International Conference of the IEEE Engineering in Medicine and Biology Society.*, vol. 2015, pp. 7402–5, 2015.
- [232] G. Ganesh, M. Haruno, M. Kawato, and E. Burdet, “Motor memory and local minimization of error and effort, not global optimization, determine motor behavior,” *Journal of Neurophysiology*, vol. 104, no. 1, pp. 382–390, 2010.
- [233] A. Maselli, A. Dhawan, M. Russo, B. Cesqui, F. Lacquaniti, and A. d’Avella, “A whole body characterization of individual strategies, gender differences, and common styles in overarm throwing,” *Journal of Neurophysiology*, vol. 122, no. 6, pp. 2486–2503, 2019.
- [234] T. Hu, J. Kühn, and S. Haddadin, “Identification of human shoulder-arm kinematic and muscular synergies during daily-life manipulation tasks,” in *IEEE International Conference on Biomedical Robotics and Biomechatronics*, Aug 2018, pp. 1011–1018.
- [235] Z. Zhang, D. Guo, M. E. Huber, S.-W. Park, and D. Sternad, “Exploiting the geometry of the solution space to reduce sensitivity to neuromotor noise.” *PLOS computational biology*, vol. 14, p. e1006013, Feb 2018.

BIBLIOGRAPHY

- [236] N. Lelis-Torres, H. Ugrinowitsch, T. Apolinário-Souza, R. N. Benda, and G. M. Lage, “Task engagement and mental workload involved in variation and repetition of a motor skill,” *Scientific Reports*, vol. 7, no. 1, p. 14764, 2017.
- [237] E. Vassena, M. Silvetti, C. N. Boehler, E. Achten, W. Fias, and T. Verguts, “Overlapping neural systems represent cognitive effort and reward anticipation,” *PLOS ONE*, vol. 9, no. 3, pp. 1–9, Mar. 2014.
- [238] A. Ploghaus, I. Tracey, J. S. Gati, S. Clare, R. S. Menon, P. M. Matthews, and J. N. Rawlins, “Dissociating pain from its anticipation in the human brain.” *Science (New York, N.Y.)*, vol. 284, pp. 1979–1981, Jun 1999.
- [239] C. Villemure and M. C. Bushnell, “Mood influences supraspinal pain processing separately from attention.” *The Journal of neuroscience*, vol. 29, pp. 705–15, Jan 2009.
- [240] C. Sprenger, F. Eippert, J. Finsterbusch, U. Bingel, M. Rose, and C. Büchel, “Attention modulates spinal cord responses to pain.” *Current biology: CB*, vol. 22, pp. 1019–1022, Jun 2012.
- [241] C. Bagnato, “Influence of pain on human sensorimotor control and learning,” Ph.D. dissertation, Imperial College London, 2017.
- [242] A. O. de Berker, R. B. Rutledge, C. Mathys, L. Marshall, G. F. Cross, R. J. Dolan, and S. Bestmann, “Computations of uncertainty mediate acute stress responses in humans,” *Nature Communications*, vol. 7, no. 1, p. 10996, 2016.
- [243] R. Martens and D. M. Landers, “Motor performance under stress: a test of the inverted-u hypothesis.” *Journal of personality and social psychology*, vol. 16, pp. 29–37, Sep 1970.
- [244] V. D. Tourassis and M. H. Ang, “Task decoupling in robot manipulators,” *Journal of Intelligent and Robotic Systems*, vol. 14, no. 3, pp. 283–302, 1995.
- [245] O. Khatib, L. Sentis, J. Park, and J. Warren, “Whole-body dynamic behavior and control of human-like robots,” *International Journal of Humanoid Robotics*, vol. 1, pp. 29–43, 2004.
- [246] J. Merel, M. Botvinick, and G. Wayne, “Hierarchical motor control in mammals and machines,” *Nature Communications*, vol. 10, no. 1, p. 5489, 2019.
- [247] R. Brooks, “A robust layered control system for a mobile robot,” *IEEE Journal on Robotics and Automation*, vol. 2, no. 1, pp. 14–23, March 1986.
- [248] D. J. S. Mattos, M. L. Latash, E. Park, J. Kuhl, and J. P. Scholz, “Unpredictable elbow joint perturbation during reaching results in multijoint motor equivalence,” *Journal of Neurophysiology*, vol. 106, no. 3, pp. 1424–1436, 2011.

- [249] S. Grillner, P. Wallèn, K. Saitoh, A. Kozlov, and B. Robertson, “Neural bases of goal-directed locomotion in vertebrates—an overview.” *Brain research reviews*, vol. 57, pp. 2–12, Jan 2008.
- [250] I. Asimov, *Runaround*. Doubleday, 1950.
- [251] J. Kühn and S. Haddadin, “An artificial robot nervous system to teach robots how to feel pain and reflexively react to potentially damaging contacts,” *IEEE Robotics and Automation Letters*, vol. 2, no. 1, pp. 72–79, Jan 2016.
- [252] J. Kühn, J. Vorndamme, M. Schappler, and S. Haddadin, “Humanoid collision reflex sequences based on an artificial robot nervous system including contact location and direction,” in *IEEE International Conference on Robotics and Automation, Workshop on Legged Robot Falling: Fall Detection, Damage Prevention, and Recovery Actions*, 2016.
- [253] A. Tödtheide, J. Kühn, and S. Haddadin, “Proprio- and exteroceptive reflexes for a pneumatically actuated finger based on the artificial robot nervous system,” in *IEEE International Conference on Robotics and Automation, Workshop on “The robotic sense of touch: from sensing to understanding”*, 2017.
- [254] A. Albu-Schaffer, C. Ott, U. Frese, and G. Hirzinger, “Cartesian impedance control of redundant robots: recent results with the dlr-light-weight-arms,” in *IEEE International Conference on Robotics and Automation*, vol. 3, Sept 2003, pp. 3704–3709 vol.3.
- [255] M. Zinn, O. Khatib, B. Roth, and J. Salisbury, “Playing it safe – human-friendly robots,” *IEEE Robotics and Automation Magazine*, vol. 11, pp. 12–21, 2002.
- [256] S. Haddadin, A. Albu-Schäffer, and G. Hirzinger, “Safety evaluation of physical human-robot interaction via crash-testing,” in *Robotics: Science and Systems*, vol. 3, 2007, pp. 217–224.
- [257] J.-J. Park, S. Haddadin, J.-B. Song, and A. Albu-Schäffer, “Designing optimally safe robot surface properties for minimizing the stress characteristics of human-robot collisions,” in *IEEE International Conference on Robotics and Automation*, 2011, pp. 5413–5420.
- [258] R. S. Johansson and A. B. Vallbo, “Tactile sensibility in the human hand: Relative and absolute densities of four types of mechanoreceptive units in glabrous skin,” *Journal of Physiology*, vol. 286, pp. 283–300, 1979.
- [259] R. Polianskis, T. Graven-Nielsen, and L. Arendt-Nielsen, “Pressure-pain function in desensitized and hypersensitized muscle and skin assessed by cuff algometry,” *The Journal of Pain*, vol. 3, no. 1, pp. 28–37, February 2002.
- [260] H. Fruhstorfer, T. Mueller, and E. Scheer, “Capillary blood sampling: how much pain is necessary? part2: Relation between penetration depth and puncture pain,” *Practical Diabetes International*, vol. 12, no. 4, pp. 184–185, July/August 1995.

BIBLIOGRAPHY

- [261] M. Hollins, D. Harper, and W. Maixner, “Changes in pain from a repetitive thermal stimulus: The roles of adaptation and sensitization,” *Pain*, vol. 152, no. 7, pp. 1583–1590, March 2011.
- [262] J. A. F. Danfei Xu, Gerald E. Loeb, “Tactile identification of objects using bayesian exploration,” in *International Conference on Robotics and Automation*, 2013.
- [263] A. Toedtheide, T. Lilge, and S. Haddadin, “Antagonistic impedance control for pneumatically actuated robot joints,” *IEEE Robotics and Automation Letters*, vol. 1, no. 1, pp. 161–168, Jan 2016.
- [264] A. de Luca, R. Farina, and P. Lucibello, “On the control of robots with visco-elastic joints,” in *IEEE International Conference on Robotics and Automation*, 2005, pp. 4297–4302.
- [265] L. Tien, A. Albu-Schäffer, A. Luca, and G. Hirzinger, “Friction observer and compensation for control of robots with joint torque measurement,” in *IEEE/RSJ International Conference on Intelligent Robots and Systems, IROS*, Oct 2008, pp. 3789 – 3795.
- [266] R. Kaye and S. Konz, “Volume and surface area of the hand,” *Human Factors Society Annual Meeting*, vol. 30, no. 4, pp. 382–384, 1986.
- [267] G. Averta, F. Barontini, V. Catrambone, S. Haddadin, G. Handjaras, J. Held, T. Hu, E. Jakubowitz, C. Kanzler, J. Kühn, O. Lambercy, A. Leo, A. Obermeier, E. Ricciardi, A. Schwarz, G. Valenza, A. Bicchi, and M. Bianchi, “U-Limb: A multi-modal, multi-center database on arm motion control in healthy and post-stroke conditions,” *GigaScience*, vol. 10, no. 6, Jun. 2021.
- [268] J. Kühn, J. Ringwald, M. Schappler, L. Johannsmeier, and S. Haddadin, “Towards semi-autonomous and soft-robotics enabled upper-limb exoprosthetics: First concepts and robot-based emulation prototype,” in *IEEE International Conference on Robotics and Automation*, May 2019, pp. 9180–9186.
- [269] J. Kühn, A. Tödtheide, E. Pozo Fortunić, T. Hu, E. Jensen, and S. Haddadin, “Seamless limb-driven prostheses: The synergy-complement control approach,” *Science Robotics*, *submitted*, Jan 2022.
- [270] M. Barbero, R. Merletti, and A. Rainoldi, *Atlas of Muscle Innervation Zones: Understanding Surface Electromyography and Its Applications*. Springer-Verlag Italia, 2012.
- [271] A. Verl, A. Albu-Schäffer, O. Brock, and A. Raatz, *Soft Robotics*. Springer, 2015.
- [272] O. Khatib, “A unified approach for motion and force control of robot manipulators: The operational space formulation,” *IEEE Journal of Robotics and Automation*, vol. 3, no. 1, pp. 1115–1120, 1987.

- [273] A. Toedtheide and S. Haddadin, “Cpa-wrist: Compliant pneumatic actuation for antagonistic tendon driven wrists,” *IEEE Robotics and Automation Letters*, vol. 3, 2018.
- [274] Dextrus hand. [Online]. Available: <http://www.openhandproject.org>
- [275] Beagle board. [Online]. Available: <http://elinux.org/Beagleboard:BeagleBoard-X15>
- [276] Myoarmband. [Online]. Available: <https://www.myo.com>
- [277] C. Natale, *Interaction Control of Robot Manipulators*. Springer, 2008.
- [278] Duo3d. [Online]. Available: <https://duo3d.com>
- [279] B. Siciliano and O. Khatib, *Handbook of Robotics*. Springer, 2016, ch. 24. Visual Servoing and Visual Tracking.
- [280] I. Vujaklija, D. Farina, and O. Aszmann, “New developments in prosthetic arm systems,” *Orthopedic Research and Reviews*, vol. Volume 8, pp. 31–39, Jul. 2016.
- [281] T. Lenzi, J. Lipsey, and J. W. Sensinger, “The RIC arm—a small anthropomorphic transhumeral prosthesis,” *IEEE/ASME Transactions on Mechatronics*, vol. 21, no. 6, pp. 2660–2671, Dec. 2016.
- [282] C. Toledo, A. Simon, R. Munoz, A. Vera, L. Leija, and L. Hargrove, “A comparison of direct and pattern recognition control for a two degree-of-freedom above elbow virtual prosthesis,” in *International Conference of the IEEE Engineering in Medicine and Biology Society*, Aug. 2012.
- [283] N. A. Alshammary, D. A. Bennett, and M. Goldfarb, “Synergistic elbow control for a myoelectric transhumeral prosthesis,” *IEEE Transactions on Neural Systems and Rehabilitation Engineering*, vol. 26, no. 2, pp. 468–476, Feb. 2018.
- [284] C. Laurettili, A. Davalli, R. Sacchetti, E. Guglielmelli, and L. Zollo, “Fusion of mimu and emg signals for the control of trans-humeral prostheses,” in *IEEE International Conference on Biomedical Robotics and Biomechatronics (BioRob)*. IEEE, 2016, pp. 1123–1128.
- [285] R. Garcia-Rosas, Y. Tan, D. Oetomo, and C. Manzie, “On-line synergy identification for personalized active arm prosthesis: a feasibility study,” in *2018 Annual American Control Conference (ACC)*. IEEE, 2018, pp. 514–519.
- [286] R. A. M. Abayasiri, D. K. Madusanka, N. Arachchige, A. Silva, and R. Gopura, “Mobio: A 5 dof trans-humeral robotic prosthesis,” in *2017 International Conference on Rehabilitation Robotics (ICORR)*. IEEE, 2017, pp. 1627–1632.

BIBLIOGRAPHY

- [287] S. B. Godfrey, K. D. Zhao, A. Theuer, M. G. Catalano, M. Bianchi, R. Breighner, D. Bhaskaran, R. Lennon, G. Grioli, M. Santello, A. Bicchi, and K. Andrews, “The soffthand pro: Functional evaluation of a novel, flexible, and robust myoelectric prosthesis,” *PLOS ONE*, vol. 13, no. 10, pp. 1–20, Oct. 2018.
- [288] P. Visconti, F. Gaetani, G. Zappatore, and P. Primiceri, “Technical features and functionalities of myo armband: An overview on related literature and advanced applications of myoelectric armbands mainly focused on arm prostheses,” *International Journal on Smart Sensing and Intelligent Systems*, vol. 11, pp. 1–25, 06 2018.
- [289] W. F. Schindler and C. Natale, *Interaction Control of Robot Manipulators: Six Degrees-of-Freedom Tasks*. Berlin, Heidelberg: Springer-Verlag, 2003.
- [290] H. Hoffmann, P. Pastor, D. Park, and S. Schaal, “Biologically-inspired dynamical systems for movement generation: Automatic real-time goal adaptation and obstacle avoidance,” in *IEEE International Conference on Robotics and Automation*, May 2009, pp. 2587–2592.
- [291] A. Ude, B. Nemeč, T. Petrić, and J. Morimoto, “Orientation in cartesian space dynamic movement primitives,” in *IEEE International Conference on Robotics and Automation*, May 2014, pp. 2997–3004.
- [292] F. Ficuciello, A. Migliozzi, G. Laudante, P. Falco, and B. Siciliano, “Vision-based grasp learning of an anthropomorphic hand-arm system in a synergy-based control framework,” *Science Robotics*, vol. 4, Jan. 2019.